Measurement of ϕ meson production in Cu+Cu collisions at 200 GeV using the PHOBOS detector at RHIC

by

Siarhei Vaurynovich

Bachelor of Science, Moscow Institute of Physics and Technology (2001)
Master of Science, Moscow Institute of Physics and Technology (2003)

Submitted to the Department of Physics
in partial fulfillment of the requirements for the degree of

Doctor of Philosophy

at the

MASSACHUSETTS INSTITUTE OF TECHNOLOGY

May 2012

Author . . . . . .
Department of Physics
May 16, 2012

Certified by . . . . . .
Gunther Roland
Professor of Physics
Thesis Supervisor

Accepted by . . . . . .
Krishna Rajagopal
Associate Head for Education, Physics

Measurement of ϕ meson production in Cu+Cu collisions at 200 GeV using the PHOBOS detector at RHIC

by

Siarhei Vaurynovich

Submitted to the Department of Physics
on May 16, 2012 in partial fulfillment of the
requirements for the degree of
Doctor of Philosophy

Abstract

Strong enhancement of production of strange particles, and in particular of ϕ mesons, in heavy ion collisions of sufficiently high energies has been predicted to be an indication of a formation of a new state of matter, composed of deconfined quarks and gluons and having a property of chiral symmetry, called Quark Gluon Plasma (QGP). Studying production of ϕ mesons is of special interest due to their small cross-section of interaction with non-strange hadrons and due to their long lifetime, which should allow ϕ mesons to decouple from the strongly interacting medium produced in heavy ion collisions early in time and to escape the medium before decaying, thereby preserving information about the conditions in which the mesons were produced.

In addition, the decay properties of ϕ mesons have been predicted to be modified in a hadronic gas medium. The $\phi \rightarrow K^+K^-$ decay is of particular interest since the mass of a ϕ meson in vacuum is very close to the mass of two charged kaons, and consequently, even a small change in the mass or the width of ϕ mesons or in the mass of kaons would have a strong effect on the decay properties.

Measurement of ϕ meson production using the PHOBOS detector at the Relativistic Heavy Ion Collider (RHIC) has proven to be especially challenging due to a small acceptance of the PHOBOS spectrometer and due to a much lower than predicted yield of ϕ mesons in heavy ion collisions at the highest RHIC energy. The measurement required a development of a new tracking algorithm, specifically tailored to reconstruct charged kaons with a high efficiency in a high hit density environment, keeping at the same time the necessary computing time within feasible limits.

Results of a measurement of ϕ meson invariant yield in the rapidity interval $0 < y < 1$ as a function of transverse momentum in Cu+Cu collisions at $\sqrt{s_{\rm NN}}$=200 GeV are presented in various ranges of centrality. The results were used to determine the dN/dy values, the inverse slope parameters T (corresponding to m_T-scaling fits of the invariant yields), and average transverse momentum of ϕ mesons as a function of collision centrality. The PHOBOS results on ϕ meson invariant yield were compared to the corresponding measurements performed by the STAR and the PHENIX collaborations and were found to be compatible with both within the estimated measurement uncertainties. The centrality dependence of the yield of ϕ mesons at mid-rapidity was studied for all of the available data on ϕ meson production in heavy ion collisions at $\sqrt{s_{\rm NN}}$=200 GeV, and it was found that the data are not sufficient to distinguish between the $N_{\rm part}$ and

N_{coll} scaling laws of the yield, thereby making it impossible to tell apart two mechanisms of ϕ meson production: 1) disintegration of a thermalized QGP, and 2) production in the primordial hard scatterings of partons of the collided nuclei. The $\sqrt{s_{\mathrm{NN}}}$ dependence of the inverse slope parameter T was studied for various particle species, showing an evidence of a change in the mechanism of particle production at temperatures and energy densities corresponding to $\sqrt{s_{\mathrm{NN}}} \simeq$4-9 GeV, however no indication of a plateau was found in any of the dependencies in contrast to theoretical predictions. The T versus $\sqrt{s_{\mathrm{NN}}}$ dependence of ϕ mesons was found to have a local maximum at $\sqrt{s_{\mathrm{NN}}} \approx$20 GeV. Invariant yield of ϕ mesons with $p_t < 130$ MeV/c was measured in the 0-60% Cu+Cu collisions at $\sqrt{s_{\mathrm{NN}}}$=200 GeV showing a strong suppression of the yield (by about a factor of $\sim$6 in comparison to an extrapolation to $p_t = 0$ of the PHOBOS results at $p_t > 390$ MeV/c), however, since a full analysis of the systematic errors was not performed for the measurement, the results cannot be considered conclusive. The $\sqrt{s_{\mathrm{NN}}}$ dependence of the yield of ϕ mesons at mid-rapidity was studied separately and with respect to the charged particle multiplicity, showing no indication of any special interval of $\sqrt{s_{\mathrm{NN}}}$ values which could be associated with such a transition (of a QCD matter into a new state) that would produce a noticeable sudden increase in the number of produced ϕ mesons. No evidence of any change in the mean or the width of the ϕ meson invariant mass peak with respect to the vacuum values was observed.

Thesis Supervisor: Gunther Roland
Title: Professor of Physics

This work is dedicated to the people who loved and supported me the most during my study at MIT: my mother Tamara and my beloved Willa.

Contents

1. Introduction

1.1. Fundamental Interactions

The physical world is dynamic. The geometrical position and the state of matter in the observable universe change constantly. The reason the changes occur are interactions of different constituents of matter with each other. Four types of interactions are presently known, namely, gravitational, electromagnetic, weak, and strong.

1.1.1. Gravitational Interaction

Gravitational interaction is experienced between any form of energy. The interaction is of infinite range and is always attractive. It is responsible for the formation and existence of planets, stars, galaxies, and galaxy clusters by pulling together interstellar gas and dust together. Historically, it was the first interaction to be understood, and the first complete theory of gravity is due to Newton [1], who based his work on Kepler's laws published in 1609-1619 and, possibly, got the idea of the gravitational force being inversely proportional to the square of the distance between bodies from Robert Hooke, with whom Newton had exchanged letters on the subject and who accused Newton of plagiarism after the "Principia" was presented to the Royal Society of London. According to the theory, the gravitational force experienced by two bodies with masses m_1 and m_2 separated by distance R is equal to

$$F = G\frac{m_1 m_2}{R^2},$$

where $G = 6.67428 \times 10^{-11}$ N m^2 kg^{-2} is a fundamental constant, defining the strength of the interaction. Newton's theory is valid if the speeds of the interacting bodies are much lower than the speed of light and if the distance between the bodies is much greater than their Schwarzschild radii [2, 3]. A more general theory of gravity, applicable under all the conditions, under which it could be tested experimentally today, was developed by Albert Einstein [4]. The only known deviations from the predictions of Einstein's theory are found on a large scale in the motion of stars in galaxies and the movement of galaxies in clusters, which are commonly explained either by an existence of yet undetected dark matter and dark energy ($\sim 70\%$ and $\sim 25\%$ of all the matter in the universe correspondingly), or with some modifications to the gravitational laws. However, since consistent data on the distribution and mass of the mysterious substances come from different measurements, i.e. gravitational lensing, angular size of the anisotropies in the Cosmic Microwave Background (CMB), baryon acoustic oscillations, distance to re-

mote supernovas, failure to find any discrepancy between the predictions of the Einstein's theory and various experimental measurements at short distances, dark matter and dark energy are postulated by most of the modern cosmological models. To understand the reason of the discrepancy between the distribution and the motion of the detectable matter in the universe and the theory predictions is one of the most interesting and intriguing unsolved problems in physics.

It is worth to mention that gravity is the only basic interaction for which a working quantum theory does not exists at the moment. Which might mean that it is fundamentally different from the other types of interactions, or might be just a reflection of our general inability at the moment to derive the laws of the macroscopic world from basic underlying quantum theories. Since the gravity is much weaker than the other basic interactions, only macroscopic measurements of gravitational effects are performed, which makes it impossible to test validity of any possible candidate of a gravitational quantum theory. Creation of such a theory together with experimental proof of its correctness is another example of a very interesting open question in modern physics.

1.1.2. Electromagnetic Interaction

Electromagnetic interaction is the best understood type of fundamental interactions. It is of infinite range and is responsible for the existence of atoms and molecules as well as their formation from the constituent nuclei and electrons, for the existence and propagation of electromagnetic waves, and for the interaction of the waves with any particles carrying electric charge. The first complete classical theory of the interaction is due to James Maxwell [5], who introduced the famous set of equations describing electromagnetic fields, and used it to predict the existence of electromagnetic waves and to interpret light as one of their examples. Maxwell's equations were the starting point of Einstein's theory of special relativity, and their failure to describe microscopic phenomena, in particular the stability of atoms, led to the creation of the non-relativistic quantum mechanics and, eventually, through the basic works of Paul Dirac [6], Enrico Fermi [7], Hans Bethe [8], Sin-ichirô Tomonaga [9], Julian Schwinger [10, 11], Richard Feynman [12–14], and Freeman Dyson [15, 16] to the creation of the modern theory of the electromagnetic interaction, **Q**uantum **E**lectro**D**ynamics (QED). In the theory, the calculations are done through summation of infinite converging series which is allowed by the fact that the coupling constant of the interaction is significantly smaller than unity (at small momentum transfer $\alpha = e^2/(4\pi\epsilon_0\hbar c) \approx 1/137.0359$). The effective coupling constant α grows with energy but stays much smaller than unity at any energies experimentally achievable today. QED is a $U(1)$ gauge theory, a consequence of which is that there is only one type of gauge bosons in the QED (*photons*) and that photons do not interact with each other in the Leading Order (LO). The theory is a remarkable success, giving extremely precise predictions of experimental data, and was therefore used as an example for building quantum theories of other fundamental interactions.

1.1.3. Weak Interaction

Weak interaction is the sister interaction of the electromagnetic one and is also very well understood. At this moment there are almost no experimental data which are in disagreement with the theory of weak interaction. The interaction is responsible for various radioactive decays and partially for the nuclear fusion reactions inside the stars, mostly through the following processes ${}^1H + {}^1H \rightarrow {}^2H + e^+ + \nu_e$ (light stars), ${}^{15}O \rightarrow {}^{15}N + e^+ + \nu_e$, and ${}^{13}N \rightarrow {}^{13}C + e^+ + \nu_e$ (heavy stars) [17, 18]. The first theory of weak interaction is due to Enrico Fermi [19]. It was a theory of a contact interaction (i.e. zero range) which provided good agreement with experimental data at the low energies accessible at the time. A more complete theory, which unified the electromagnetic and weak interaction and which is valid at all energies tested so far, was created by Sheldon Glashow [20], Abdus Salam [21], and Steven Weinberg [22] (*"GSW theory"*). This spontaneously broken symmetry theory described the electroweak interaction as being mediated by massless photons and massive W and Z bosons, and, consequently, the weak interaction as being of a very short range on the order of $\sim 2\pi\hbar/(cM_{W/Z}) \approx 10^{-17}$ m, where the $M_{W/Z} \sim (80-90)$ GeV is the mass of W and Z bosons. The intrinsic strength of the weak interaction is actually larger than of the electromagnetic one, which can be seen from comparing the coupling constant $\alpha_w \approx 1/29$ to the fine structure constant α (see section 1.1.2 on the preceding page). Later Gerardus 't Hooft showed that the GSW theory is renormalizable [23, 24], which, together with the excellent agreement of the theory predictions with data, made it an example for most of the further attempts to theoretically unify all interactions. The GSW theory is a $U(1) \times SU(2)$ gauge theory in which, as well as in QED, the calculations are done through summation of infinite converging series which is allowed by the fact that the coupling constant of the interaction is significantly smaller than unity and by the large masses of W and Z bosons. The effective coupling constant α_w depends on energy [1] but stays much smaller than unity at any energies experimentally achievable today. The only disagreement of the GSW theory with data at this moment is the yet undiscovered experimentally Higgs boson, which, in the theory, gives masses to all the particles through the interaction with the Higgs field.

1.1.4. Strong Interaction

Strong interaction is named so because it is the strongest of all the fundamental interactions. The interaction is responsible for various nuclear reactions and for holding the nucleons inside of nuclei as well as the nucleon constituents, quarks and gluons, together.

[1] At the energies that were experimentally probed so far, α_w decreases with energy. However, for energies higher than ~1 TeV, the energy dependence of α_w could be either increasing (in the Standard Model) or decreasing (in the super-symmetric theories).

1.1.4.1. Strong Isospin

After James Chadwick discovered the neutron in 1932 [25], it was found out that the masses of the proton and the neutron (*nucleons*) were almost identical and the strength of the strong interaction between any two nucleons was the same. The situation was similar to atomic physics where energy of an atom could be slightly different depending on its spin state. As well, it resembled the observation that some atomic nuclei could have almost the same mass but different charge, i.e. *isobars*. Therefore the same year (1932) Werner Heisenberg introduced the concept of the *isotopic spin* (or just *isospin*) [26] [2], a vector quantity conserved in the strong interactions, theorizing that the proton and the neutron were the same particle with the total isospin of $1/2$ and values of its 3^{rd} projection of $1/2$ and $-1/2$ correspondingly. Other particles discovered afterward were assigned the total isospin and its 3^{rd} projection based on the conservation of the quantity in the strong interaction and based on the number of other particles with almost identical mass. Rotations in the isospin space is an approximate symmetry with respect to the strong interaction, which is violated, as it was understood much later, by the difference in the masses of quarks composing different strongly interacting particles (*hadrons*).

1.1.4.2. Strange Particles

In the early days of particle physics, the only known elementary particles were $e^{\pm}$, p, n, $\pi^{\pm}$, and $\mu^{\pm}$. All of them (except muons) had a well defined position assigned in our understanding of their role in the physical world: protons and neutrons were the constituents of the positively charged atoms nuclei, electrons surrounded the nuclei determining the chemical properties of elements and their physics was governed by the quantum mechanics, and pions were the mediators of the strong interaction holding protons and neutrons together inside nuclei. The proliferation of newly discovered particles started in 1947 with the discovery of K^0 [28]. Soon after that were discovered K^+, Λ, η, ϕ, ω, ρ and many others. Some of the particles (including K^0) appeared *"strange"* to their discoverers, since they were produced abundantly on the typical time scale of $\sim 10^{-23}$ seconds, but decayed without neutrino emission on the time scale of $\sim 10^{-10}$ seconds. This was explained as production of the particles in the strong interaction but decay due to the weak interaction [29]. The first theoretical breakthrough in understanding of the "strange" particles came in 1953 when Tadao Nakano and Kazuhiko Nishijima introduced a new conserved (in the strong interaction) quantum number called *"strangeness"* assigned to the particles [30, 31]. Murray Gell-Mann proposed the same quantum number independently in 1956 [32].

1.1.4.3. Quarks

In 1961 Murray Gell-Mann and Yuval Ne'emam found a way to organize into simple geometrical patterns the scores of known by then particles according to their electrical

[2] The name of the value was actually invented by Eugene Wigner in 1937 [27].

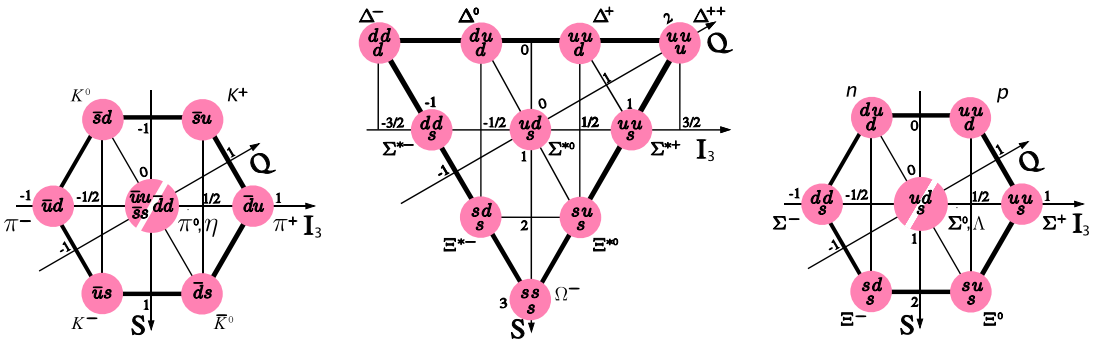

(a) meson octet [33] (b) baryon decuplet [34] (c) baryon octet [35]

Figure 1.1.: A few examples of the geometrical classification of hadrons invented by Murray Gell-Mann and Yuval Ne'emam: (a) pseudoscalar mesons (ground states), (b) completely symmetric flavor states of baryons (ground states), (c) mixed symmetry flavor states of baryons (ground states). See section 1.1.4.3 on the preceding page for details.

charge, strangeness, and the 3rd projection of their isotopic spin (see Fig. 1.1 for some examples) [36]. At the time, all of the ground state baryon decuplet particles but Ω^- (Fig. 1.1(b)) had been found experimentally, therefore when the last member of the decuplet was observed in a laboratory [37], it was considered as a confirmation of the model correctness. In 1964 Murray Gell-Mann [38] and George Zweig [39] independently proposed an interpretation (the *quark model*) of the patterns by surmising that all hadrons are composed of more elementary constituents of three types (u, d, and s) all carrying spin 1/2, which were named *quarks* [3,4]. According to the model, any baryon is composed of three quarks or three antiquarks and any meson is composed of a quark and an antiquark. The quark model had two major problems:

1. it predicted existence of particles with fractional electric charge ($Q_u = +2/3$, $Q_d = -1/3$, and $Q_s = -1/3$), and no such particles had ever been observed in an experiment,

2. some particles (like Δ^{++}, Δ^-, and Ω^-) seemed to violate the Pauli exclusion principle, since according to the quark model they were composed of three quarks in the same state, however according to the quantum field theory no two fermions

[3] This is the modern interpretation of the model. In the beginning, it was customary to consider quarks as purely mathematical objects, since the idea of identifying them with real particles seemed too bold. However, already in his original publication [38], Gell-Mann uses words "baryons can... be constructed from quarks", "mesons are made out of $(q,\bar{q})$...", speculates "about the way quarks would behave if they were physical particles of finite mass", and talks about how "the highest energy accelerators would help to reassure us of non-existance of real quarks".

[4] *Quarks* was the name given to the constituents by Murray Gell-Mann. George Zweig called the particles *aces*.

can be in the same state [40–43] [5].

The 1st of the problems was "resolved" by postulating the quark confinement hypothesis, i.e. by stating that quarks cannot exist outside of hadrons. It is interesting to note that this hypothesis turned out to be notoriously difficult to prove and now, dozens of years later, it has still not been derived from the basic theory of strong interactions [6]. The 2nd problem was solved by introducing a new quantum number assigned to all quarks, called *color*, which could assume three different values, named traditionally as *red*, *green*, and *blue* [44–47]. If all the quarks in the Δ^{++}, Δ^{-}, and Ω^{-} particles are in a different color state, then the Pauli exclusion principle is no longer violated (therefore the minimum number of colors needed is three). The color analogy comes from the fact that all the hadrons are required to be color singlets in the theory of strong interactions, which is a mathematically exact name for "colorless" and in everyday experience red, green, and blue colors, when mixed, give white.

The confirmation of the existence of quarks came from the *deep inelastic scattering* experiments, i.e. from studying high energy scatterings of electrons on nucleons at the Stanford Linear Accelerator Center (SLAC) and from studying scatterings of neutrino beams on nucleons at the European Organization for Nuclear Research (CERN). In the case of electrons on nucleons scattering, the experiments were based on the following general expression of the scattering cross-section (if the energy of incident electrons is significantly lower than the Z-boson mass):

$$\frac{d^2\sigma}{dE'd\Omega} = \left(\frac{\alpha\hbar}{2E\sin^2(\theta/2)}\right)^2 \left[2W_1(q^2,x)\sin^2(\theta/2) + W_2(q^2,x)\cos^2(\theta/2)\right],$$

where E and E' are the energies of the incident and scattered electron correspondingly, θ is the electron scattering angle, $q = p_i - p_f$ is the difference between the initial and final 4-momentum of the electron, p is the proton 4-momentum, $x = -q^2/(2qp)$, and functions $W_1(q^2,x)$ and $W_2(q^2,x)$ depend on the inner structure of a nucleon. It was predicted by James Bjorken that, in the limit of large q^2 and large qp but finite ratio of the two x, functions $W_1(q^2,x)$ and $(qp)W_2(q^2,x)$ depend on x only [48]. The later is true if nucleons are composed of point-like constituents. It was also predicted by Curtis Callan and David Gross that if nucleon constituents have spin 1/2, then in the Bjorken limit also $2xMW_1(q^2,x) = (qp)W_2(q^2,x)/(Mc^2)$, where M is the nucleon mass [49]. Both of the predictions were successfully verified in the SLAC experiments in 1969-1971 [50–53]. The quark model predicts in the Bjorken limit that if $F_2(x) = (qp)W_2(q^2,x)/(Mc^2)$ is compared for scattering of electrons versus scattering of neutrinos on targets containing equal number of protons and neutrons, then

$$\frac{\int \left[F_2^{ep}(x) + F_2^{en}(x)\right] dx}{\int \left[F_2^{\nu p}(x) + F_2^{\nu n}(x)\right] dx} = \frac{Q_u^2 + Q_d^2}{2} = \frac{5}{18},$$

[5] Remember, at that time QED was already proven to be correct (see section 1.1.2 on page 12) and the GSW theory (see section 1.1.3 on page 13), giving exact theoretical predictions, existed.

[6] The problem is considered to be so hard that a mathematically rigorous proof of the confinement is required in one of the Millennium Prize Problems established by the Clay Mathematics Institute (`http://www.claymath.org/millennium/Yang-Mills_Theory/`).

which was confirmed by the "Gargamelle" collaboration results from the neutrino beam experiments at CERN [54], providing the evidence that the electric charges of the nucleon constituents are equal to those of quarks. In addition, the neutrino scattering data was in agreement with the Gross/Llewellyn-Smith and the Adler sum-rules for the quark model with three valence quarks of baryon number 1/3 [55]. As can be seen, the last thing, which had to be confirmed experimentally to identify the proton point-like constituents with quarks, was the color hypothesis. A fundamental idea of the quark model is that hadron production in an e^+e^- annihilation results from a creation of a quark-antiquark pair. If the center of mass energy of the incoming leptons is much smaller than the Z-boson mass, then in the process, the quark-antiquark pair couples directly to the intermediate photon, and the process can be calculated exactly using QED. Therefore, except the cases when the center-of-mass energy E_{cm} is in the vicinity of a resonance, it is expected that

$$R = \frac{\sigma(e^+e^- \to \text{hadrons})}{\sigma(e^+e^- \to \mu^+\mu^-)} = N_{\text{colors}} \cdot \sum_q Q_q^2, \tag{1.1}$$

where the summation is done over all of the quark flavors with $2m_q < E_{\text{cm}}$. The validity of Eq. 1.1 with $N_{\text{colors}} = 3$ was confirmed in the pioneering experiments at Frascati [56–59], Orsay [60], and Novosibirsk [61].

1.1.4.4. Asymptotic Freedom, Confinement, And Quantum Chromodynamics

Significant experimental evidence of quark model correctness and the successful unification of the electromagnetic and the weak interaction within a gauge theory led to application of this kind of theories to the strong interaction as well. In 1973, David Gross, Frank Wilczek, and David Politzer showed that in certain types of gauge theories the coupling constant of the strong interaction between quarks becomes small at short distances, which is known now as *"asymptotic freedom"* [62, 63]. That allowed to explain the experimental results described in section 1.1.4.3, in which the quarks appeared to be approximately free when they were hit with high energy electrons and neutrinos. It also justified theoretically application to the strong interaction of a perturbative expansion of the interaction amplitudes in orders of the coupling constant analogous to the one used in the theory of the electromagnetic and the weak interactions. Asymptotic freedom gradually received a rigorous direct experimental confirmation (see Fig. 1.2 on the next page) in the measurements of the coupling constant of the strong interaction α_s as a function of the momentum transfer q [64]. It is impossible to calculate the precise form of the potential between quarks at the current level of the strong interaction theory, but we know that at large distances, i.e. comparable to or larger than the size of a nucleon, the potential energy of interaction between quarks becomes extremely large, preventing an observation of free quarks [7]. The conventional cartoon picture used to visualize what happens when two quarks, let us consider a meson as an example, are being pulled apart is the following:

[7] For more comments about the quark confinement see page 16.

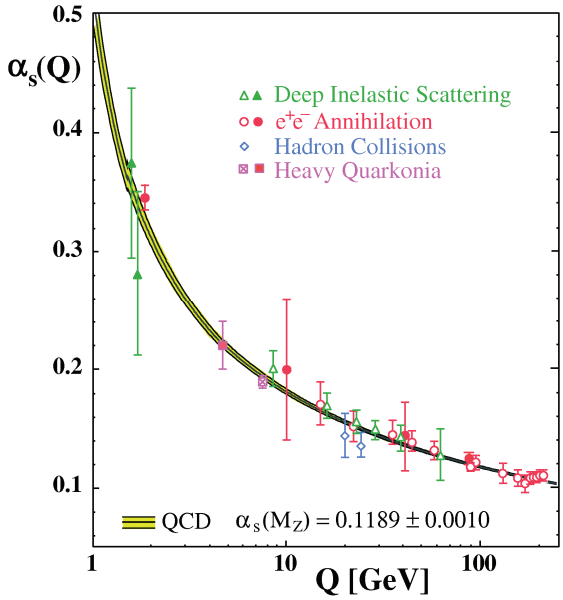

Figure 1.2.: Direct experimental confirmation of the asymptotic freedom in measurements of the coupling constant of the strong interaction α_s as a function of the momentum transfer q. The figure was taken from the arXiv version of Ref. [64].

1. the gluon field, responsible for the strong interaction between the quarks, is mostly concentrated in the region between them and forms something resembling a string or a tube in the space coordinates,

2. it takes some energy to create some extra gluonic fluctuations out of vacuum, therefore to increase the distance between the quarks one needs to perform some work, which is spent to increase the potential energy of the system,

3. at some distance between the quarks, the energy becomes so large that it becomes more energetically economical to create a new quark-antiquark pair out of vacuum than to increase the distance even further, and in the process some of the stored potential energy is used,

4. consequently, by increasing the distance between the quarks, we do not end up having two free quarks but instead create a multitude of new hadrons, each of which confines its own constituent quarks.

The $SU(3)$ gauge theory of the strong interaction was named ***Q**uantum **C**hromo**d**ynamics (QCD)*. The theory was first presented by Harald Fritzsch and Murray Gell-Mann

in 1972 [65] and published in 1973 [66]. According to the findings of Gross, Wilczek, and Politzer, QCD has the property of asymptotic freedom if $11N_c > 2N_f$, where N_c is the number of different colors and N_f is the number of different quark flavors in the theory. As far as we know, $N_c = 3$ (see page 17 for the experimental evidence) and the number of quark flavors discovered so far is $N_f = 6$, which is the 1st evidence of QCD being a valid theory of the strong interaction. As in any gauge theory, the strong interaction between quarks in QCD is mediated by massless vector bosons, called *gluons*. Since QCD is a gauge theory with $SU(3)$ symmetry, there are eight linearly independent gluons possible. The gluons of QCD are not just purely mathematical abstractions of the theory. Some examples of direct experimental evidence of their existence are provided in section 1.1.4.5.

A few further major discoveries, which convinced the scientific community of the correctness of the quark model and QCD as a theory of the strong interaction are the following:

- the agreement between the experimental data and the QCD predictions of logarithmic in q^2 deviations from the Bjorken scaling because of the gluon radiation,
- the discovery of the charm quark in the experiments performed in 1974 at the Brookhaven National Laboratory (BNL) [67] and SLAC [68, 69],
- the discovery of quark jets in 1975 at SLAC [70],
- the discovery the of the bottom quark in 1977 at the Fermi National Accelerator Laboratory (FermiLab) [71],
- the discovery of the top quark at FermiLab [72, 73],
- success of the lattice QCD (see section 1.2.3 on page 24).

The only known problem in our understanding of the strong interaction at this moment is the inability to do the exact calculations at low momentum transfer ($q^2 \lesssim 1$ GeV), while in the asymptotic freedom limit no discrepancies between the theory and the experimental data have been found.

1.1.4.5. Experimental Evidence Of Gluons Existence

The first experimental evidence of gluons existence came from the data on scattering of neutrinos on nucleons at CERN, when it was shown that only ∼50% of a nucleon momentum can be attributed to quarks [55], which means that something (i.e. gluons) carries the rest. The corresponding integral was also evaluated for the SLAC data on electron on nucleons scattering [53], but the CERN group was the first to interpret it as an evidence of gluons existence. However, the observation of three-jet events, first seen in e^+e^- collisions at PETRA in 1979 [74], is commonly regarded as the most direct evidence of gluons existence. Such events are interpreted as the radiation, by one of the final state quarks in the process $e^+e^- \to q\bar{q}$, of a noncollinear gluon carrying a substantial fraction of the collision center-of-mass energy.

1.1.5. Standard Model

The current theory of elementary particles physics (not including the gravitational interaction), called the *Standard Model*, is the GSW theory combined with QCD. While there is plethora of extensions to the Standard Model motivated by requirements of additional symmetries, trying to explain why the strengths of the fundamental interactions are what they are, or having some more exotic motivations, if one focuses on the areas where there are disagreements between the data and the theory, then as can be seen from sections 1.1.1, 1.1.2, 1.1.3, and 1.1.4, the list of the current problems to be solved is the following:

- to explain the *dark matter* and the *dark energy* phenomena, i.e. either to modify the theory in such a way that the data and the theory agree or to detect the mysterious substances in an experiment,
- to detect the Higgs boson in an experiment or to come up with an alternative theory of the electroweak interactions, in which masses of the W and Z bosons are naturally nonvanishing (since the underlying gauge theory of the interaction requires zero masses of the gauge bosons, those are introduced artificially through the spontaneous symmetry breaking, i.e. through the *Higgs mechanism*),
- to understand the low momentum transfer (i.e. $q^2 \lesssim 1$ GeV) strong interactions, since while we can do measurements at such conditions, rigorous theoretical calculations are not possible at the moment.

This thesis is a contribution to solve the last problem on the list above. While the scientific community waits for the theory sector to come up with new ideas about how to do calculations of the strong interactions at all conditions, our understanding of the interactions is guaranteed to improve by studying the low momentum transfer phenomena experimentally, while in parallel providing data on which theorists could test their ideas. As well, this thesis contributes to the experimental study of collective behavior of large number of interacting quarks and gluons in a thermodynamic equilibrium at high temperatures and energy densities.

1.2. QCD Phase Diagram

One way of studying the low momentum transfer sector of QCD is to improve our understanding of the thermodynamic properties of *quark matter*, i.e. of bulk volumes of interacting quarks and gluons in a thermal equilibrium at different values of temperature T and baryon chemical potential μ_B (volume of a system is considered to be infinite here, since in the case of a finite volume it would have to be included into the grand canonical partition function [75], making properties of the system volume dependent, and at a finite volume the system might not undergo a possible phase transition which would otherwise happen at infinite volume [76]). The approach allows one to look at

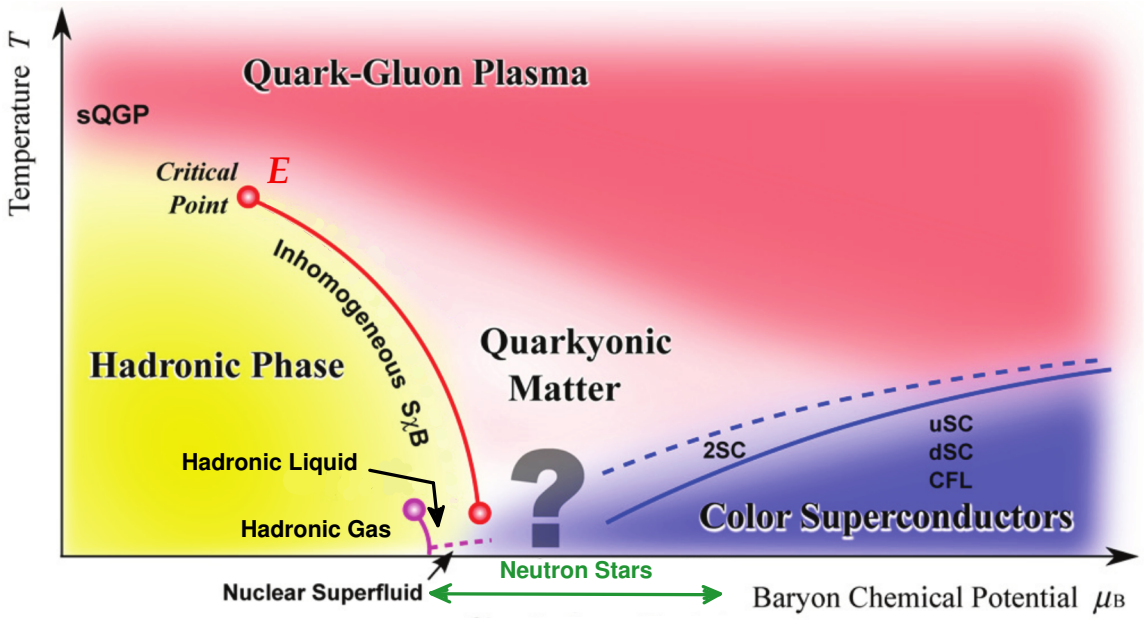

Figure 1.3.: The modern view on the QCD phase diagram. The figure is a modified version of the one taken from Ref. [77].

the problem from a different point of view and is complementary to studying the processes of interest directly, i.e. for example, by studying the fragmentation of parton jets, hadron mass spectrum and quark structure functions, inelastic scatterings at low energies, and such. The set of all the possible thermodynamic parameters (T, μ_B) together with the description of the quark matter properties at each such values of temperature and baryon chemical potential is called the *QCD phase diagram* (see Fig. 1.3). Of course, since temperature is a measure of average kinetic energy per degree of freedom of a system, not all the points on the diagram would correspond to the region of interest, that is to the quark matter in which the interactions between the constituent particles would be dominated by the low momentum transfer processes. At large temperatures ($T \gg 1$ GeV), most of the interactions fall into the domain of asymptotic freedom (see section 1.1.4.4 on page 17) and can be well described theoretically using the perturbative QCD. And at very large temperatures ($T \to \infty$) the kinetic energy of quarks and gluons becomes so much larger than both the energy of their interactions and their rest energy, that the quark matter can be approximated with an ideal relativistic gas of massless particles.

However, studying properties of quark matter in a thermodynamic equilibrium for all values of T and μ_B is of great interest by itself. But even for that purpose, being able to do the low momentum transfer, otherwise called *nonperturbative*, QCD calculations would be a great step forward:

- The first important reason for that is: while we could create in a laboratory small volumes of short-lived extreme states of quark matter (see section 1.3 on page 32),

even if the interactions in the matter are dominated by the perturbative regime of QCD, it is the long lived decay products of the matter which could be detected in an experiment, and since the transformation of the quark matter into the decay products would inevitably proceed at some stage through the low momentum transfer processes, their understanding is crucial for a correct interpretation of experimental data, i.e. for deriving the medium properties from the measurement results.

- And the second reason is that it is always desirable to understand experimental observations (properties of the medium in this case) from the fundamental underlying principles, and for quark matter those are QCD.

Therefore, I believe that the biggest impediment to making more reliable theoretical predictions about the QCD phase diagram at the moment is the current inability to do the nonperturbative calculations in the QCD.

1.2.1. Temperature

In general, *temperature* is a measure of average energy per degree of freedom of a system in a thermodynamic equilibrium. However, the correspondence between the temperature parameter and the energy could be established in different ways. In the nonrelativistic case, the traditional conformity is $\langle E \rangle = \frac{1}{2} k T$. If any two systems are brought into a thermodynamic equilibrium with each other then, by definition, their temperatures are said to be equal. Therefore, temperature of any thermodynamic system S could be determined by bringing it into a thermal contact with another system, for which temperature is easily defined, for example, with an ideal gas of particles without internal degrees of freedom. If the average kinetic energy of the gas particles does not change as a result of the contact, then the temperature of the system S is equal to the gas temperature. At least conceptually, the method allows one to measure the temperature of any system with any required precision. However, while the method is straightforward to implement in the nonrelativistic case, for which the ideal gas microscopic theory is well developed, the situation is more complicated for a relativistic ideal gas, since the distribution of particles over energies in such gas is still under discussion [78]. Therefore, temperature is defined macroscopically as

$$\frac{1}{T} = \left(\frac{\partial S}{\partial E} \right)_N, \quad \text{or} \quad \frac{1}{T} = \left(\frac{\partial S}{\partial E} \right)_V.$$

Both the microscopic and the macroscopic definitions of temperature follow from the same principle, i.e. that in a thermodynamic equilibrium, a system is in such macroscopic state which can be realized with the maximum number of microscopic states. Since temperature is not precisely defined yet microscopically, then macroscopically the situation is the same as well.

However, there exists a number of approximations of the relativistic distribution of particles over their energies and momenta. One of such approximations, called m_T

scaling [79], will be used in this work to extract the temperature of the thermal source of ϕ mesons produced in Cu+Cu collisions at $\sqrt{s_{\rm NN}}$=200 GeV in a narrow range of rapidity (see also sections 5.2.3 on page 95 and 7.2 on page 185):

$$\frac{1}{m_T}\frac{dN}{dm_T} = \text{const}\cdot\exp\left(-\frac{m_T}{T}\right), \tag{1.2}$$

where $m_T = \sqrt{p_T^2 + m^2}$ and p_T is the transverse momentum of a particle with respect to the collision axis. The above distribution is the $m_T \gg T$ limit of the one originally proposed by Rolf Hagedorn [80]:

$$\frac{1}{m_T}\frac{dN}{dm_T} = \text{const}\cdot m_T K_1\left(-\frac{m_T}{T}\right), \tag{1.3}$$

where K_1 is the modified Bessel function.

1.2.2. Chemical Potential

Chemical potential can be assigned to any conserved quantity as the internal energy increase of a system in a thermodynamic equilibrium occurring when the quantity is increased in the system by one unit while the entropy and the volume of the system are kept constant [8]. The *baryon chemical potential* discussed here is associated with the conservation of the *baryon number* (the difference between the number of baryons and anti-baryons in a system) in the strong interactions and is defined as the increase in the internal energy of a system when the number of baryons in it is incremented by one. QCD is a relativistic quantum field theory and therefore

- it does not conserve the number of particles and so the chemical potential cannot be defined non-relativistically as the increase in energy required to increase the number of particles by one,

- the average baryon rest energy has to be taken into account, i.e. $\mu_B = m_B c^2 + \mu'_B$, where μ'_B is the increase in energy of the system associated with an addition of a baryon after it has been created.

Other chemical potentials used to study the QCD phase diagram include the *isospin chemical potential* μ_I and the *strangeness chemical potential* μ_s, corresponding to the conservation of the strong isospin and of the strangeness in the strong interactions correspondingly. All of these chemical potentials can be used on the time scales on the order of ~ 1 fm/c $\simeq 3\times10^{-24}$ s, at which the evolution of a system produced in a heavy-ion collision (see section 1.3 on page 32) is dominated by the strong interaction. As well, one could define the *u-quark* and *d-quark chemical potentials*, then $\mu_I = \frac{1}{2}(\mu_u - \mu_d)$.

[8] Alternatively, chemical potential can be defined as the Gibbs free energy of the system per unit of the conserved quantity.

1.2.3. Lattice QCD

Lattice QCD calculations were pioneered by Kenneth Wilson in 1974 [81], whose work was built upon the same year by John Kogut and Leonard Susskind [82]. It is a numerical way of doing calculations based on the first principles of QCD in which the QCD Lagrangian is discretized on a 4-dimensional (1 time + 3 spacial dimensions) cubic lattice and the theory is formulated using Feynman path integrals. The quark variables are assigned to the sites of the lattice while gluons are defined as 3×3 matrices on the links connecting the neighboring sites (it is a natural assignment since gluons transport color between quarks) [83]. Since results in such a framework are dependent on the distance between the lattice sites (at any non-zero lattice site spacing a, there are additional, proportional to powers of a, non-physical terms in the lattice QCD Lagrangian [84]), the calculations are done for several different lattice discretizations with subsequent extrapolation to a vanishing one, corresponding to the continuous physical space time. If lattice QCD is used to study some thermodynamic property of quark matter, then in addition, all the calculations are done at several values of the lattice volume V, with the following extrapolation to the limit $V \to \infty$. Lattice QCD calculations are very computationally intensive, requiring currently on the order of 1 teraflop-years per publishable result, and the required Central Processing Unit (CPU) time depends strongly on the number of lattice sites and on the assumed quark masses (vanishing and infinite masses calculations being rather easy, while the results for masses close to the physical ones being a challenge). The reason for this is that the computations are done using the Monte Carlo methods, which means that random gluon field configurations (i.e. sets of 3×3 gluon matrices, one per each link between the lattice sites) are generated and used to find an average of an observable of interest. Dynamical quarks enter the calculations implicitly. Since in the averaging procedure every configuration contributes with a weight e^{-S}, where $S = \int \mathscr{L} d^4x$ is the action of the Lagrangian, in practice the configurations are generated with probability e^{-S} to greatly reduce the required computing resources (this method is called the *importance sampling*) [84].

In a sense, the lattice QCD is complementary to the perturbative QCD since while the latter is applicable at high momentum transfers due to the asymptotic freedom (see section 1.1.4.4 on page 17), the former has an ultraviolet cut-off in the momentum space due to the lattice discretization since no phenomena with wavelengths less than $\sim a$ could be studied in the framework. It might seem that the lattice QCD is a universal way to do non-perturbative calculations of the strong interactions. But it is only true for some problems. For example, lattice QCD gives precise calculations of hadron masses even for hadrons made of light constituent quarks [9] [85]. As another example, lattice QCD was successful in establishing that the transition from a hadron gas to the deconfined state (see section 1.2.4 on the facing page) at $\mu_B = 0$ is a crossover [83].

Nevertheless, the lattice approach can be used today to study properties of the quark matter only at $\mu_B \approx 0$ due to the *sign problem* which accompanied such calculations since they were first introduced. At any given $\mu_B \neq 0$, lattice QCD results are not guar-

[9] The calculations are even easier for hadrons composed of heavy flavor quarks, since in that case the problem is largely nonrelativistic and the interaction energy is much smaller than the quarks rest energy.

anteed to converge to the correct ones in the thermodynamic limit ($V \to \infty$) [86]. The essence of the sign problem is that at any $\mu_B \neq 0$, the importance sampling method of speeding up the calculations (see above) is impossible to employ since the action S becomes complex valued and therefore e^{-S} cannot be used as a probability density function of the generated gluon configurations. Because of that, any lattice QCD results at non-vanishing μ_B values rely on extrapolations from the calculations at $\mu_B = 0$.

1.2.4. Quark Gluon Plasma

The first proposal of existence of a state of a quark matter at very high temperatures in which the quarks are "liberated" and not confined inside of hadrons is due to Nicola Cabibbo and is dated from 1975 [87]. The term *Quark Gluon Plasma* was first introduced by Edward Shuryak in 1980 in his attempt to build a theory of a superdense matter from the perturbative QCD point of view [88]. The analogy here is with the regular electromagnetic plasma, which is a gas of electrically charged particles. QGP is in a similar way a gas of charged particles as well, but the charge in this case is the QCD color. From the modern point of view, QGP is a state of quark matter, which occurs at high temperatures (and consequently at high energy densities) - see Fig. 1.3 on page 21. The two independent properties assigned to the state are:

- color and quark deconfinement,
- chiral symmetry restoration.

This thesis is a contribution to the study of QGP properties.

1.2.4.1. Color And Quark Deconfinement

QGP is characterized by quarks and gluons being not confined inside of hadrons, or by, which I think is a better way to explain it, by quarks and gluons not being strongly correlated in spacial coordinates. Intuitively, such state is to be anticipated from the asymptotic freedom property of QCD , i.e. if the strength of the interaction between quarks decreases with energy and at high temperatures the average quark energy is large (temperature is a measure of an average energy per degree of freedom), then at a high enough T the quarks should become not bound to each other since their kinetic energy would exceed the potential energy of their interaction. Another way to put it: the color confinement radius is expected to grow from its typical value of ~ 1 fm at $T = 0$ to infinity as $T \to \infty$. This intuition does not tell anything about how the transition from a finite to an infinite confinement radius occurs, i.e. if the growth is gradual or if there is a phase transition temperature T_c. It is also natural to expect that the transition to the deconfined state occurs at the typical size of a hadron, i.e. at $T \sim 1$ fm=197.33 MeV. Another way to develop an intuition about why a transition into a deconfined state of quark matter exists is the following: a higher temperature corresponds to a higher energy density $u(T) = \frac{1}{2} A\sigma T^4$ of quantum fluctuations popping in and out of existance out of vacuum, where A is the average effective number of degrees of freedom per such

fluctuation (think of a photon gas, for which the energy density is $u(T) = \sigma T^4$, where σ is the Stefan-Boltzmann constant), then since according to the Heisenberg's uncertainty principle $\Delta t \Delta E \sim 2\pi\hbar$ (in a thermal equilibrium $\Delta E \sim \frac{1}{2} k_B T A$ is the average energy of a fluctuation, where k_B is the Boltzmann's constant), one gets $n \sim \frac{u(T)}{\Delta E} \sim \frac{\sigma T^3}{k_B}$ and $\Delta t \sim \frac{2\pi\hbar}{\Delta E} \sim \frac{4\pi\hbar}{k_B T A}$ (n is the spacial density of the quantum fluctuations, and Δt is the their typical lifetime). At high enough temperature, the density of quarks due to the quantum fluctuations should become equal to the density of quarks inside of hadrons and therefore any border between the inside and outside of hadrons is going to disappear, and the two regions will become equivalent. Since in this new state hadrons do not exist anymore, in such quark matter, quarks and gluons move freely in space. Of course from this point of view, different hadrons might disappear at different temperatures depending on their size and the energy density of their interior.

1.2.4.2. Chiral Symmetry

Chirality is the eigenvalue of the γ^5 operator, where $\gamma^5 = i\gamma^0\gamma^1\gamma^2\gamma^3$ is the Dirac 5$^{\text{th}}$ matrix applied on a spinor $u(\vec{p})$ of a spin 1/2 particle. The spinor $u(\vec{p})$ could be separated into two components $u(\vec{p}) = u_R(\vec{p}) + u_L(\vec{p})$, where $u_R(\vec{p}) = 0.5 \cdot (1+\gamma^5)u(\vec{p})$ and $u_L(\vec{p}) = 0.5 \cdot (1-\gamma^5)u(\vec{p})$. Since γ^5 anticommutes with all the other γ-matrices $\{\gamma^5, \gamma^\mu\} = 0$, then the QCD Lagrangian (excluding the $-\frac{1}{16\pi}\mathbf{F}^{\mu\nu} \cdot \mathbf{F}_{\mu\nu}$ free gauge field term) for one quark flavor

$$\mathscr{L} = \left[i\hbar c \bar{\psi}\gamma^\mu \partial_\mu \psi - mc^2 \bar{\psi}\psi \right] - (q\bar{\psi}\gamma^\mu \boldsymbol{\lambda}\psi) \cdot \mathbf{A}_\mu, \tag{1.4}$$

where $\psi = a e^{\frac{i}{\hbar}(Et - \mathbf{pr})} u$, could be separated into the sum of two identical parts for ψ_L and ψ_R (each part can be received from Eq. 1.4 by replacing $\psi \to \psi_L$ and $\psi \to \psi_R$) if $m = 0$ and could not otherwise. Since the Lagrangian for several quark flavors is a sum of Lagrangians for each flavor, the Lagrangian for the two lightest quarks u and d acquires *chiral symmetry* $SU(2)_L \times SU(2)_R$, corresponding to $SU(2)$ flavor rotations of (u_L, d_L) and (u_R, d_R) doublets independently, if the quarks are considered to be massless [86] (for a detailed derivation of this fact see, for example, Ref. [89]). Spontaneous breaking of the symmetry in the QCD ground state generates three massless Goldstone pseudoscalar bosons - the pions, which in turn acquire mass due to the explicit breaking of the chiral symmetry by the non-vanishing quark masses. Thus a test for a chiral symmetry of a state is the absence in it of pions. From a theoretical point of view, the chirally symmetric state is characterized by $\langle\bar{\psi}\psi\rangle = 0$, while in a state in which the symmetry is broken $\langle\bar{\psi}\psi\rangle \neq 0$ and if quark masses are neglected (which is approximately correct for the u and d quarks) the two states are not connected analytically in the (T, μ_B) plane, i.e. there must be a phase transition between them [10] [90].

Chiral symmetry is a notion independent from the deconfinement (see section 1.2.4.1 on the preceding page) and is a property commonly assigned to QGP, since at high temperatures the small current masses of the u and d quarks could be neglected in

[10] By definition $\langle\bar{\psi}\psi\rangle \equiv \langle 0|\bar{\psi}_L\psi_R + \bar{\psi}_R\psi_L|0\rangle$, where $|0\rangle$ is the vacuum state and $\bar{\psi}$ and ψ are the creation and the destruction operators correspondingly. So one can see that the chiral condensate is composed of pairs of left-handed quarks and right-handed anti-quarks and vice verse.

comparison to their total energy [11]. It was shown in lattice QCD calculations at $\mu_B \approx 0$ (see section 1.2.3 on page 24) that the transition temperatures to the chirally symmetric and deconfined states are very close to each other [91] (however, not all the lattice QCD calculations agree with it [92]), that is why it is normally believed that the two phase transitions (or crossovers) happen simultaneously [12], but it is not excluded that at larger μ_B it is not the case [93]. Quarkyonic matter (see section 1.2.7 on page 29) is an example of a proposed thermodynamic state of quarks and gluons, which has both confinement and (possibly) chiral symmetry properties simultaneously [94].

1.2.5. Hadronic States

According to QCD, any physically isolated (by a distance of $\gtrsim$1 fm) lump of matter has to be in a color singlet state. The smallest such lumps possible are three quark (baryons) and quark-antiquark (mesons) combinations, collectively called hadrons (see section 1.1.4 on page 13). All hadronic phases have individual, interacting with each other hadrons as their constituents. The phases are crucial to understand for studying any other part of the QCD phase diagram, since it is hadrons that are experimentally observable products of a decay of any other form of quark matter.

In $T = 0$ and $\mu_B = 0$ corner of the phase diagram is the vacuum (see Fig. 1.3 on page 21). At low T and low μ_B one has a relativistic hadron gas state, which is quite similar to a regular molecular gas. Just like molecules interact with each other in a mixture exchanging energy in collisions and reacting chemically, hadrons scatter in collisions transferring momentum with and without an exchange of quarks (we neglect here the effects of the weak interaction, which can change the quark flavors and reduce the total number of quarks in a system).

As μ_B is increased keeping $T \sim 0$, the hadronic gas undergoes a phase transition into a liquid state [13] [95, 96]. By analogy with a regular liquid-gas, the transition is expected to be of the first order [90], which is also suggested by experimental data [97]. The curve in the (T, μ_B) plane separating the liquid from the gas hadronic states is expected to terminate at a critical point at $T_c = 15 - 20$ MeV [98, 99] and $\mu_{Bc} \simeq 919 - 924$ MeV [77]. However, the effect of nuclei finite volume is expected to spread the critical point over a region in the phase diagram [100]. T_c values have been measured in experiments bombarding nuclear targets with projectiles having energy of about hundreds of MeV per nucleon and are in the range $5 - 10$ MeV [101]. However, experimentally one has to distinguish the *kinetic* and the *emission* [14] temperatures, which are different for a not yet understood reason, with the kinetic temperature being ~ 10 MeV higher [97].

[11] A good familiar analogy, showing a change of properties of a medium at some temperature due to a change in an internal symmetry is the phase transition of a ferromagnet, which changes into a paramagnet above the material Curie temperature.

[12] It is interesting to notice that the absence of pions is a test for chiral symmetry of a quark matter state, but pions also disappear due to the quark (and color) deconfinement. This fact could be used as another argument, that the transitions to the chirally symmetric and deconfined states should happen simultaneously.

[13] The ground states of common atom nuclei are examples of finite volume drops of the liquid.

[14] Also called *chemical* or *internal* temperature.

If the transition from the hadron gas to the hadron liquid is performed such that the corresponding path in the (T, μ_B) plane does not intersect the first order phase transition curve, then the transition will be a *crossover*, which means that no discontinuities will be observed in any thermodynamic quantity.

In the very low temperature region, the hadron (i.e. nucleon) liquid is expected to be in a superfluid state [102, 103]. This is in agreement with experimental data on the long relaxation times of sudden periodic changes in rotational rates of radio pulsars, which cannot be explained assuming presence of viscosity [104, 105]. It is not known if there is a clear transition between the nucleon superfluid and the color superconducting states of quark matter (see section 1.2.6) [77].

1.2.6. Color Superconductors

The first idea about existence of a quark matter phase with quark degrees of freedom at very large density (i.e. the idea of the energy source of quasars being the process of binding of quarks into hadrons) date back to 1965 [106]-1966 [107]. In 1969-1970 it was suggested for the first time by Dmitri Ivanenko and D. F. Kurdgelaidze that quarks might pair to form new quasi-particles of a "quark plasma" as well as the possibility of superconductivity in the cores of very massive stars [108, 109]. For a more detailed history of publications on the subject see, for example, Ref. [110].

From the modern point of view, by analogy with electrons in metals, it is expected that in the low T and large μ_B region of the QCD phase diagram, quarks near their Fermi surface [15] get bound by forming analogs of the Cooper pairs in superconductors. The resulting state of quark matter was named ***C**olor **S**uper**C**onductor (CSC)* (the term was introduced by Bertrand Barrois and Stephen Frautschi [111–113]). However, unlike the regular superconductors, in which there is only one kind of charge carriers (electrons), there are several different quark types distinguished by their flavor and color (in addition, one has to take into account the effect of antiquarks), which creates a possibility of many different pairing patterns, each of which being energetically preferred in different regions of the (T, μ_B) plane leading to a variety of CSC phases. It is an open problem to figure out which pattern is the most stable at any particular values of T and μ_B, except the phase which description follows.

At asymptotically large μ_B, the number density of quarks becomes very large as well, which leads in turn to a small distance between quarks, and therefore the properties of such CSC state could be calculated precisely using perturbative methods due to the asymptotic freedom of QCD. It was shown that at such highest densities, the quark matter exists in the *Color-Flavor Locked (CFL)* phase, in which all quarks of all flavors in the state are bound on equal footing into zero-momentum no-spin Cooper pairs [114]. The name of the phase reflects that the Lagrangian of the state is invariant not under color or

[15] Quarks are fermions and so obey the Pauli exclusion principle, therefore at $T \approx 0$ all the available energy levels are filled up to some some energy, called the *Fermi energy*. The dependence of the energy on particle momentum, called *Fermi surface*, might be non-trivial in some states of matter, for example, for electrons in a crystal.

flavor rotations separately but under simultaneous and opposite color and flavor rotations, so that the two are *locked* together in one symmetry. The matter in the CFL phase is a superfluid and an electromagnetic insulator with broken chiral symmetry [110].

Other possible phases of CSC can be characterized with values of the energy gaps between Cooper paired and unpaired states for different quark flavors (we do not have any reason to believe that different colors have different interaction strengths) [77]. Normally, the effects of quark flavors heavier than s are ignored, since we do not expect to find CSC states where c, b, or t quarks play a significant role in any naturally occurring object. Denoting as Δ_{xy} the energy gap for quark flavors x and y, we get a state uSC if $\Delta_{ds} = 0$ while $\Delta_{ud} \neq 0$, and $\Delta_{us} \neq 0$. States dSC and sSC are defined analogously. Similarly, states $2SCsd$, $2SCsu$, and $2SCud$ (the latter is also called just $2SC$, which stands for *2 flavor superconductor*) are defined as the phases where $\Delta_{sd} \neq 0$, $\Delta_{su} \neq 0$, and $\Delta_{ud} \neq 0$ correspondingly while other energy gaps vanish. If the energy gap for a given pair of flavors is zero, they do not form Cooper pairs. In this classification, the CFL phase corresponds to all three $\Delta_{ds} \neq 0$, $\Delta_{ud} \neq 0$, and $\Delta_{us} \neq 0$.

The only place in the observable universe where CSC could naturally occur is the interior of neutron stars, however it is not know if it actually happens. The theoretical studies of the CSC states, in addition to being of purely fundamental interest, are in search of any experimentally detectable signatures of such occurrence.

1.2.7. Quarkyonic Matter

An existence of a cold dense phase (see also section 1.2.6 on the facing page) called *quarkyonic matter* in the limit of $N_c = \infty$ was predicted by Larry McLerran and Robert Pisarski in 2007 [115]. The phase diagram in the limit resembles the one shown on Fig. 1.3 on page 21, except that the CSC phase is replaced with the quarkyonic one, therefore the new phase could be considered as the CSC limit for the case $N_c = \infty$. All phase transitions in the infinite number of colors limit are of the first order and the critical point does not exist. It is not clear as of today whether the quarkyonic matter persists in some region of the phase diagram as the N_c is reduced to 3 (as in QCD) [77]. Some authors believe that the quarkyonic matter is just the $N_c = \infty$ limit of the regular nuclear liquid (see section 1.2.5 on page 27) [116], which makes it reasonable to suggest that this is what the matter becomes in the case $N_c = 3$. As it was mentioned earlier (see section 1.2.4.2 on page 26), quarkyonic matter could occupy the region on the QCD phase diagram, in which the quark matter is both

1. quark and color confined, and

2. in the state of restored chiral symmetry,

however it is still being investigated whether the 2-nd statement is true. Matter satisfying the two above conditions exists also in the Nambu-Jona-Lasinio with Polyakov loops (PNJL) model [93].

1.2.8. Phase Transitions, Crossovers, And Critical Points

In general, the issue of establishing the location and the type of transitions (i.e. phase transitions and crossovers) between different forms of quark matter is not settled. Our inability to perform neither nonperturbative calculations in QCD nor the lattice QCD studies at nonvanishing μ_B due to the sign problem (see section 1.2.3 on page 24) makes the scientific community to rely on models, which only approximately reflect some properties of the studied systems and have often unknown or ill-defined values of their parameters. Answers received in such model research are model-dependent and vary strongly (including qualitatively) from one model to another. Therefore, I will summarize here the results which are considered to be settled and give a few examples of what might occur elsewhere. It seems, it will be up to the experimental research, such as the lower energy program at RHIC, at the Facility for Antiproton and Ion Research (FAIR) at the **G**esellschaft für **S**chwer**i**onenforschung (GSI) in Darmstadt, and at the **N**uclotron-based **I**on **C**ollider f**A**cility (NICA) at the Joint Institute For Nuclear Research (JINR) in Dubna, to resolve some of the remaining problems by probing properties of quark matter at higher μ_B values, while the current RHIC and the Large Hadron Collider (LHC) heavy ion programs target $\mu_B \approx 0$ and $T > T_c$ region of the QCD phase diagram (see section 1.3 on page 32).

This section focuses mainly on the properties of the transition between the hadronic states (see section 1.2.5 on page 27) and QGP (see section 1.2.4 on page 25) since it is relevant to the experimental study performed for this thesis. Examples of possible CSC states (see section 1.2.6 on page 28) phase diagrams were received by studying the Nambu-Jona-Lasinio (NJL) model [117] and the four-fermion model [118]. Transitions between some of the hadronic states were explained in section 1.2.5 on page 27. Part of the material relevant to the current discussion was already covered above where it fit naturally, and will only be reminded here briefly.

Lattice QCD established that:

- the transition temperatures to the chirally symmetric and deconfined states at $\mu_B = 0$ are very close to each other, that is why it is normally believed that the two transitions happen simultaneously, but it is not excluded that at larger μ_B it is not the case (see section 1.2.4.2 on page 26),

- the transition from hadronic gas to QGP at $\mu_B = 0$ is a crossover (see section 1.2.3 on page 24),

- the *critical temperature* T_c of transition from the hadronic gas state to the QGP at $\mu_B = 0$ in the case of 2 flavors is 171±4 MeV [119] and 173±8 MeV [120], and in the case of 3 flavors is 154 ± 8 MeV [120], with subsequent studies in the case of 2+1 flavors giving 164 ± 2 MeV [121]. The values are approximately in agreement with the hadron resonance gas model, which predicts 176 ± 8 MeV and 185 ± 6 MeV depending on the method [122]. Therefore, the conservative range of possible T_c values is 140-200 MeV.

The conclusions about how the transition from the hadronic states to QGP proceeds at nonvanishing μ_B values depend on a model used for the study. A few examples are provided below. Following the transition line from $\mu_B = 0$, in the NJL and the PNJL (and most of the other chiral [77]) models the crossover changes at some *critical point E* (at which the phase transition is of the 2nd order, see Fig. 1.3 on page 21) into a 1st order phase transition all the way to $T = 0$ [123]. The location of the critical point is predicted in the lattice QCD calculations to be $\mu_{BE} = 360 \pm 40$ MeV and $T_{cE} = 162 \pm 2$ MeV [121], while in a 3 flavor PNJL model the location of the point is at $\mu_{BE} = 313$ MeV and $T_{cE} = 102$ MeV [93]. The discussed critical point emerges from studying the transition between the states with broken and restored chiral symmetries and is independent from the transition between confined and deconfined states, and if the two transitions do not occur simultaneously, the point would be much harder to locate in an experiment [93]. The baryon chemical potential probed in a heavy-ion collision experiment can be decreased by:

- increasing the collision energy [124],
- increasing the collision centrality [124],
- decreasing the absolute value of the rapidity of the considered particles produced in the collision [124, 125]),
- increasing the ion atomic weight [126].

The temperature probed in such an experiment could be increased by:

- increasing the collision energy,
- increasing the collision centrality,
- decreasing the absolute value of the rapidity of the considered particles produced in the collision [125, 127].

The proposed experimental signatures of a proximity to the critical point in the (T, μ_B) plane are:

- minimum in the event-by-event fluctuations of T and μ_B [124, 126],
- maximum in the event-by-event fluctuations of pion multiplicity [124, 126],
- excess in the yield of low p_T pions over thermal distribution [124, 126],
- maximum in the Hanbury-Brown-Twiss (HBT) correlations [124],
- change in the β_T dependence of the $\bar{p}/p$ ratio [128].

However, neither position nor even the existence of the critical point are guaranteed based on the model and the lattice QCD studies and have to be tested experimentally.

There exists also a prediction of a so called *triple point* at $\mu_{BT} = 350 - 400$ MeV and $T_{cT} = 150 - 160$ MeV, where the hadronic states, the QGP and the quarkyonic matter coexist [94]. An example of an even more exotic result is the prediction of two first order transitions ending in two critical points (a *LOFF crystalline phase* is predicted in between the hadronic gas and CSC states on the phase diagram) [129].

1.3. QGP Creation In Heavy Ion Collisions

Experimentally, QGP is studied in high energy collisions of fully ionized atoms of heavy elements [16], which are normally referred to as *heavy ion collisions*. Such studies have been performed for different elements at a variety of collision energies at the Super Proton Synchrotron (SPS) and the LHC at CERN, the Alternating Gradient Synchrotron (AGS) and the RHIC at BNL, and will be performed at the FAIR at GSI, and at the NICA at JINR. The reason of using collisions of heavy nuclei is that it allows to create large volumes [17] of QGP, which permits thermodynamic analysis of the produced system. Not any heavy ion collision leads to QGP creation. Since this thesis studies Cu+Cu collisions at 200 GeV per nucleon pair, the evidence will be provided below that

- the energy density of the produced in such collisions quark matter is enough for a transition into QGP state, and
- the relevant degrees of freedom in the matter are quarks and not hadrons.

1.3.1. Energy Density

The energy density of the quark matter created in a heavy ion collision can be estimated using the approach developed by James Bjorken [18] [130]:

$$\varepsilon = \mathbf{2} \cdot \frac{N}{\mathscr{A}} \frac{dN_{ch}}{dy} \langle E \rangle \frac{3}{2} \frac{1}{2t}, \tag{1.5}$$

where $N/\mathscr{A}$ is the number of colliding nucleons per unit area, dN_{ch}/dy is the multiplicity of charged particles *per colliding nucleon* produced in the collision at rapidity $y \approx 0$, $\langle E \rangle$ is the average particle energy, 3/2 comes from the ratio of average numbers

[16] A fully ionized atom is just its nucleus.

[17] The volume has to be large in comparison to the characteristic length scale of the strong interaction of ~ 1 fm, which is about the size of a nucleon.

[18] I believe that the original formulas (3) and (4) in Ref. [130] of Bjorken are wrong since they are missing factor of 2. The calculation implicitly assumes that all the particles are massless and that $p_z \ll E$ in the central rapidity region, and therefore the rapidity range of particles, which energy is included into the calculation, is $\Delta y = 2 \cdot \max(y) = 2 \cdot \max\left(\frac{1}{2}(\ln(1+p_z/E) - \ln(1-p_z/E))\right) \approx 2 \cdot \max\left(\frac{1}{2} 2p_z/E\right) \approx 2 \cdot \frac{1}{2} 2d/t$. Bjorken's calculation uses 2 times smaller rapidity range. The formula I use has the missing factor of 2 (shown in bold) added to it.

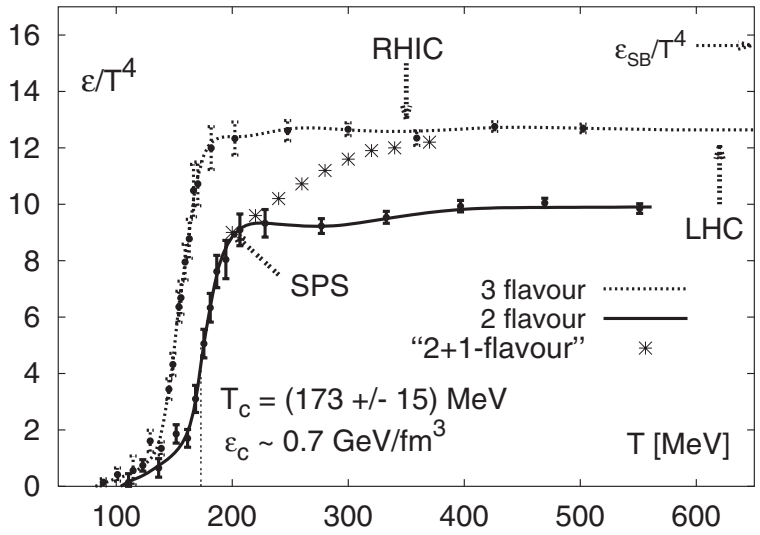

Figure 1.4.: Lattice QCD result on the dependence of the quark matter energy density on temperature. A clear transition from the hadronic state to QGP is visible. The minimal energy density, corresponding to the whole system being in the QGP state, can be estimated from the figure as $\varepsilon_{QGP} \simeq 12.5 \cdot \frac{30}{\pi^2} \cdot \frac{\sigma}{2} T_{\min}^4 \simeq 1.5$ GeV fm^{-3}, where $T_{\min} = 0.175$ GeV and $\sigma = 85.6$ fm^{-3} GeV^{-3} is the *Stefan-Boltzmann* (also called the *radiation*) constant. The Stefan-Boltzmann formula $\varepsilon = \sigma T^4 = g \cdot \frac{\pi^2}{30}(k_B T)^4$ was derived for a photon gas with g=2 (polarization) internal degrees of freedom. The deviation from the formula is due to the facts that in QGP, constituent particles have in addition color and quark flavor quantum numbers and that the particles interact strongly with each other, and so $g \simeq 38$ (if QGP was an ideal gas of 3 quark flavors and 8 gluons states, one would have $g = 47.5$). The rapid increase in the energy density at some critical T_c reflects the rapid increase in the number of degrees of freedom in the system. The figure was adopted from Ref. [134].

of produced neutral to charged particles taken to be 1/2, and t is the time passed since the collision (the calculation is done in natural units, so $c = 1$). Since only particles at mid-rapidity are considered, then $\langle E \rangle \approx \langle E_T \rangle$. Most of the charged particles produced in a heavy ion collision are pions, therefore $\langle E_T \rangle \approx \sqrt{\langle p_T \rangle^2 + m_\pi^2}$. Further consideration will be done for central collisions. By fitting the PHOBOS experiment data on charged hadron p_T spectra in 0-6% Cu+Cu collisions at $\sqrt{s_{\rm NN}}$=200 GeV [131] with an exponential function at low p_T (for example, in the 0-2 GeV range), where most of the particles are produced, one can estimate that $\langle p_T \rangle \approx 0.5$ GeV. In such collisions the multiplicity of charged particles $N \cdot dN_{ch}/dy \approx 185$ [132], where $N = 63$ is the atomic weight of Cu. The radius of a Cu nucleus is $R_{Cu} \approx 1.12 N^{1/3}$ fm [133] and the cross section area $\mathscr{A} = \pi R_{Cu}^2 \approx 62.4$ fm^2.

A few prerequisite remarks are needed before one can estimate the value of the pa-

rameter t in Eq. 1.5. Our goal is to estimate the highest energy density achieved by the quark matter created in a heavy ion collision requiring simultaneously the matter being in a thermodynamic equilibrium. The amount of time τ it takes for the system to achieve such equilibrium (called the *thermalization* or the *equilibration time*) is still under discussion and has large uncertainty. During non-central collisions of nuclei at high energies, a correlation (called the *elliptic flow*) between the number of particles emitted at an azimuthal angle with respect to the plane in which a collision occurs (the *reaction plane*) and the angle itself is predicted [135] and observed in an experiment (see, for example, Ref. [136]). The magnitude of the correlation is well described by the models, which treat the thermalized quark matter as a liquid (the *hydrodynamics models*), assuming that the time τ is 0.25-0.6 fm/c [137–139]. Such short thermalization times are possible to explain in the theory assuming formation of a strongly coupled QGP in heavy ion collisions [140, 141]. However, it is also believed that at such short times the system dynamics is still dominated by the asymptotic freedom domain of the strong interaction and therefore the thermalization times are considered to be too short to be plausible, leading to attempts to increase the theoretical estimates on τ by introducing a weakly coupled evolution time period ($\tau > 2.6$ fm/c if all the equilibration is done in the weak coupling regime) [142], a free streaming stage [138], or by estimating the time directly using the Boltzmann transport equation to be $\tau \sim 1.6$ fm/c [143]. Overall a reasonable estimate is $\tau \sim 1$ fm/c and $t = \tau$, leading to the energy density evaluation of

$$\varepsilon \sim \frac{2}{62.4\ \text{fm}^2} \cdot 185 \cdot \sqrt{(0.5\ \text{GeV})^2 + (0.14\ \text{GeV})^2} \cdot \frac{3}{2} \cdot \frac{1}{2 \cdot 1\ \text{fm}} = 2.3\ \text{GeV fm}^{-3}.$$

It has to be pointed out that Eq. 1.5 is only approximate, since (in addition to the remarks in footnote 18 on page 32) it does not take into account the energy carried by the p_z component of particles and neglects the difference between rapidity and pseudorapidity. A more modern estimate of the energy density is [144]:

$$\varepsilon = \frac{N}{\mathscr{A}} \frac{T_0}{t} \frac{9}{4} \frac{dN_{ch}}{dy} \frac{1}{0.5}, \tag{1.6}$$

where T_0 ($T_0 \approx 0.325$ GeV at RHIC collision energies) is the initial temperature of the thermalized quark matter gives even higher estimate of the initial energy density ($\varepsilon \sim 4.3$ GeV fm^{-3}). Both estimates give the energy density above the minimal value $\varepsilon_0 \simeq 0.5 - 1$ GeV fm^{-3} provided by the lattice QCD calculations at which the transition into QGP occurs (see Fig. 1.4 on the preceding page) [145].

1.3.2. Constituent Quark Scaling Of The Elliptic Flow

The second convincing evidence, that the quark matter produced in heavy ion collisions has quarks and not hadrons as its constituents, comes from the Solenoidal Tracker At RHIC (STAR) [146, 147] and the **P**ioneering **H**igh **E**nergy **N**uclear **I**nteraction e**X**periment (PHENIX) [146] experiments data on the elliptic flow scaling. The data show that for various identified hadrons $v_2/(n_q \cdot \varepsilon)$ is a universal function of KE_T/n_q (see the

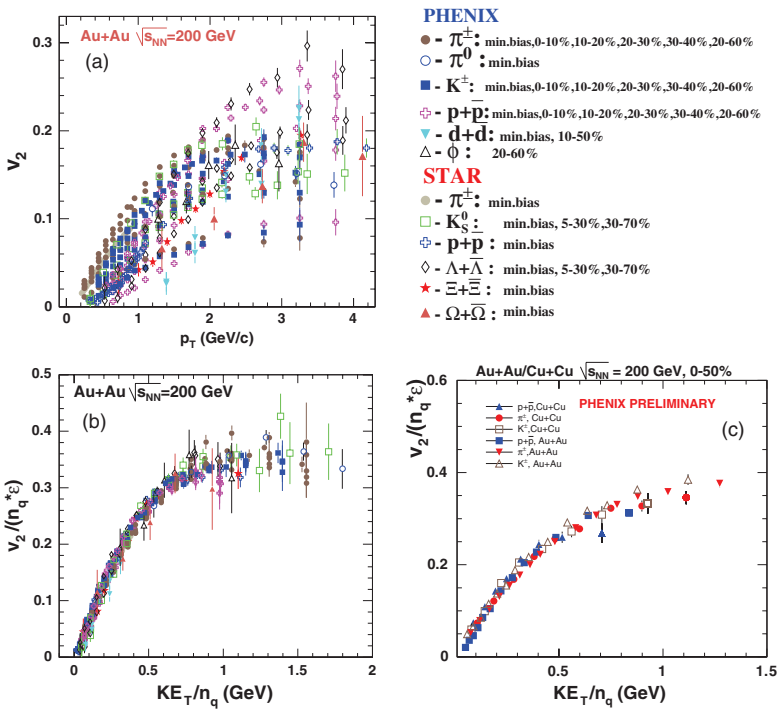

Figure 1.5.: Identified hadron elliptic flow v_2 scaled with the number of constituent quarks n_q and the event eccentricity ε as a function of $KE_T \equiv m_T - m \equiv \sqrt{p_t^2 + m^2} - m$ scaled with n_q. The figure was adopted from Ref. [146].

caption of Fig. 1.5 for definitions of the variables) independent of event centrality, constituent quark content of the hadrons (up to the charmed quark), and size of the collided nuclei (including the Cu+Cu collisions at $\sqrt{s_{\rm NN}}$=200 GeV studied in this thesis). The data can be explained by the quark coalescence model [148], but in the logic of the paper p_T has to be replaced everywhere with E_T (the two are exactly equal for massless quarks, and the later is a good approximation in the chirally symmetric state of QGP), and one has to claim that the p_T values, at which the elliptic flow measurements are done at RHIC, are high enough for the partons propagation to be independent from each other but low enough for the hadron production during the QGP decay to be dominated by the quark coalescence and not by parton fragmentation.

1.4. Strangeness And ϕ Meson Production In QGP

It was predicted by Johann Rafelski and Berndt Müller that strange particles would be produced more abundantly (relative to other hadrons and absolutely) in the QGP state of quark matter in comparison to hadron gas [153–155]. Therefore such abundance, if observed experimentally in heavy ion (in comparison to pp and pA) collisions, could be used as a signature of a transition of the produced matter at some stage of evolution into QGP. The predicted strangeness enhancement was a factor of 10-50 [154]. The

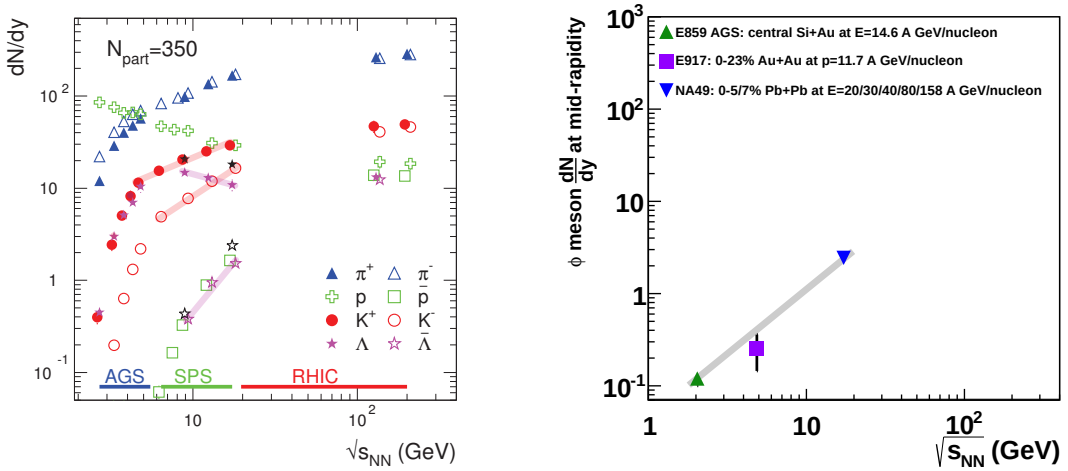

(a) (b)

Figure 1.6.: Compilation of the measured dependencies on $\sqrt{s_{\mathrm{NN}}}$ of various particle yields at mid-rapidity. The lines were added to the figures to indicate the trends exhibited by the data at the highest energies below those at RHIC. As can be seen, the strange particle yields in nucleus-nucleus collisions measured at the AGS and the SPS energies indicate a rise in dN/dy values as a function of $\sqrt{s_{\mathrm{NN}}}$, with the exception of Λ baryons, which have dN/dy values decreasing as a function of $\sqrt{s_{\mathrm{NN}}}$ at the SPS energies. Figure (a) was adopted with modifications from the arXiv version of Ref. [149]. Figure (b) is a compilation of results published in Ref. [150–152] before RHIC started operation (comparison to the measurements performed afterward will be done in section 7.8 on page 222). The comparison on the figures is done between different collision systems. However, almost all of the data points are for Au+Au and Pb+Pb collisions, and the mass of the two nuclei species is very close to each other ($\sim$ 197 versus $\sim$ 207), therefore a rough comparison is justified.

enhancement of ϕ meson (quark content $s\bar{s}$) production would be even higher than for strangeness overall, since it was predicted that $s\bar{s}$ clustering is enhanced (i.e. higher fraction of all strangeness is in $s\bar{s}$ pairs) by a factor $\sim$1-3 if a system created in a heavy ion collision goes through the QGP state versus the situation in which only hadronic gas is formed [156].

The two reasons of the strangeness enhancement are:

1. A much higher density of gluons in QGP in comparison to hadron gas, which leads to increased production of strange quarks through the $gg \rightarrow s\bar{s}$ channel [19] [156]. In hadron gas, gluons are confined inside of the constituent hadrons, which limits the volume occupied by gluons and therefore their average density, and makes the

[19] It is estimated that the $gg \rightarrow s\bar{s}$ channel is responsible for $>$ 90% of the total strangeness production in QGP , while the rest is produced in $q\bar{q}$ annihilations (see Fig. 1.7 on the facing page) [153].

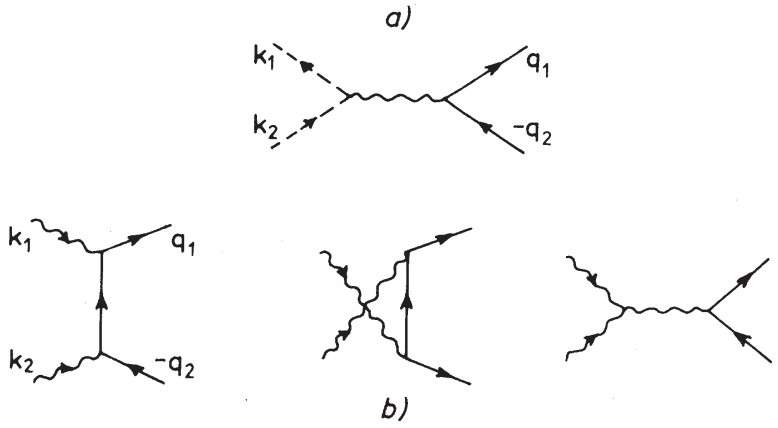

Figure 1.7.: The lowest (tree) level diagrams of the strange quarks production: a) $q\bar{q} \rightarrow s\bar{s}$, b) $g\,g \rightarrow s\bar{s}$. The figure was adopted from Ref. [153].

reaction to be restricted in space in time to the hadron collisions. In addition, the energy density and so the temperature and consequently the gluon density inside of hadrons are lower as well than in the QGP state.

2. The mass of the strange quark is significantly lower in QGP due to the chiral symmetry restoration, which makes it much easier to produce in the state an $s\bar{s}$ pair in a $q\bar{q}$ or $g\,g$ collision. It can be understood the following way [157]. As it was pointed out in section 1.2.4.2 on page 26, chiral condensate is $\langle 0|\bar{\psi}_L\psi_R + \bar{\psi}_R\psi_L|0\rangle$ and if a massless (for example, right-handed) quark propagates through the condensate, it could get annihilated by the ψ_R operator and then $\bar{\psi}_L$ acting on the vacuum $|0\rangle$ would create a left-handed quark, the net result being as if the original quark switched helicity, which is only possible if the quark was massive. Therefore effectively a quark acquires mass in a chiral condensate. Consequently, in a chirally symmetric state (for example, in the QGP) a quark mass is just its *current mass*, and in a chiral condensate the mass is larger and is called the *constituent mass* of the quark.

Trends exhibited by the data on dN/dy of strange particles at mid-rapidity at the AGS and the SPS energies as a function of $\sqrt{s_{\mathrm{NN}}}$ are shown on Fig. 1.6 on the facing page. As can be seen, no such specific range of $\sqrt{s_{\mathrm{NN}}}$ values is visible, which could be associated with a strong enhancement of strangeness production due to formation of QGP at some stage of evolution of a system created in a heavy ion collision, contrary to the theoretical predictions described above. And so, it is an intriguing question to check if strange particle production becomes strongly enhanced at any of the higher collision energies (and at corresponding to them higher energy densities of QCD matter), causing a great interest in an experimental investigation of the strange hadron yields at RHIC.

1.4.1. Statistical Hadronization Model

As it is well known from quantum mechanics, the volume in the phase space (3 spacial and 3 momentum coordinates) occupied by one quantum state, related to a motion of a particle through space along, for example, x-axis, is $\Delta x \Delta p_x = 2\pi\hbar$. For a motion in 3-dimensional space of a particle with g internal degrees of freedom, the total number of states available in the phase space volume $d^3x d^3p$ is

$$d^6N = g\frac{d^3x d^3p}{(2\pi\hbar)^3}.$$

Combining the Quantum Field Theory (QFT) spin-statistics theorem, the requirement that any microscopic quantum state of a given energy can be populated with an equal probability, and the quantum number conservation laws, one gets for an average number of particles per quantum state:

$$n = \frac{1}{\exp\left[(E-\mu)/T\right] \pm 1} \text{ for } \begin{matrix}\text{fermions}\\ \text{bosons}\end{matrix}.$$

Since all quarks are spin-1/2 particles, baryons are combinations of 3 constituent quarks or antiquarks and therefore are fermions, and mesons are constituent quark-antiquark pairs and so are bosons, we get for the expected number of hadrons in a system in the full thermal equilibrium:

$$\frac{d^6N}{d^3x d^3p} = \frac{g}{(2\pi\hbar)^3}\frac{1}{\exp\left[(E-\mu)/T\right] \pm 1} \text{ for } \begin{matrix}\text{baryons}\\ \text{mesons}\end{matrix}.$$

If particles and their antiparticles have $+1$ and -1 unit of some conserved charge correspondingly, then when one calculates the most probable distribution of the particles over the available energy levels taking into account conservation of the charge (and of other conserved quantities, like energy), mathematically the contribution of the charge conservation law to the Lagrange function is $-\mu\left(dN_k^{\text{particles}} - dN_k^{\text{antiparticles}}\right)$, where dN_k is the number of (anti)particles in a small k-th energy range and μ is the Lagrange multiplier, leading to the chemical potentials of particles and antiparticles having opposite signs. From the same mathematics, if the particles have more than one conserved charge (for example, if there are two such charges A and B), then the total chemical potential of the particles is the sum of the chemical potentials associated with each of the charges (i.e. $\mu = \mu_A + \mu_B$). The later means, particularly, that the full chemical potential of a quark is equal to the sum of its baryon chemical potential and its flavor chemical potential [20].

The Statistical Hadronization Model (SHM) adds the following ideas to the basic thermodynamics picture explained above:

[20] Only exactly conserved charges related to the strong interaction are considered here. For example, the regular electric charge and strong isospin chemical potentials could also be considered in a more detailed description.

- The chemical potential of a hadron ($q_1q_2q_3$ for baryons and $q_1\bar{q}_2$ for mesons) is equal to the sum of chemical potentials of its constituent quarks ($\mu=\mu_1+\mu_2+\mu_3$ and $\mu=\mu_1-\mu_2$ correspondingly) [158]. This approximation is exactly correct if the constituent quarks of a hadron do not interact with each other, which in reality is not the case (for example, Δ^0/n, or Δ^+/p have the same quark content but different mass due to different interaction energy between the constituent quarks, therefore their chemical potentials are not the same, however in the SHM approximation their chemical potentials are equal).

- To describe phenomenologically deviations from the full thermodynamic equilibrium, each constituent quark flavor is assigned a *phase space occupancy factor* γ, which is nearly equal to the ratio of the number of quarks of a given flavor in the medium to the one expected for a full equilibrium [159]. The phase space occupancy factor of a hadron is approximated as a product of the factors of its constituent quarks. The occupancy factors of quarks and of their antiquarks are taken to be equal.

And so the number of primary hadrons resulting from the medium decay in the SHM is equal to ($d^3p=4\pi p^2dp$, $\int d^3x=V$, and $E=\sqrt{p^2+m^2}$):

$$N=\frac{gV}{2\pi^2\hbar^3}\int_0^\infty \frac{p^2dp}{(\gamma_1\gamma_2\gamma_3)^{-1}\exp\underbrace{\left[\sqrt{p^2+m^2}/T\pm(\mu_b+\sum_{i=1}^{3}\mu_i^{\text{flavor}})/T\right]}_{\text{"+" for baryons } q_1q_2q_3\text{,"-" for antibaryons } \bar{q}_1\bar{q}_2\bar{q}_3}+1}, \tag{1.7}$$

$$N=\frac{gV}{2\pi^2\hbar^3}\int_0^\infty \frac{p^2dp}{(\gamma_1\gamma_2)^{-1}\exp\underbrace{\left[\sqrt{p^2+m^2}/T-(\mu_1^{\text{flavor}}-\mu_2^{\text{flavor}})/T\right]}_{\text{for mesons } q_1\bar{q}_2}-1}, \tag{1.8}$$

where μ_b is the baryon chemical potential and μ_i^{flavor} is the flavor chemical potential of the i-th quark. The formulas above are convoluted with the relativistic Breit-Wigner distribution around the mass m of a hadron, and since in an experiment one observes the mixture of primary and secondary (resulting from strong decays of other) hadrons, the multiplicities to be compared to the data are found from all the heavier hadron decays as $N_j^{\text{data}}=N_j+\sum_k Br(k\to j)N_k$ [160]. It is normally assumed that the light u and d quarks are in full thermodynamic equilibrium, i.e. $\gamma_u=\gamma_d=1$, while the other model parameters are figured out from a fit of the hadron yields or the hadron yield ratios in data. If the parameters could be estimated beforehand (based on an extrapolation of the fit results of previous measurements), then the SHM could be used to predict the hadron yields for a new experiment. Before RHIC became operational, it was shown, that the SHM is very successful in describing the hadron yields in heavy ion collisions [161–164], as well as in e^+e^- collisions [165], in intermediate energy pp and high energy $p\bar{p}$ collisions [166], and the m_{T}dependence of the yields in intermediate energy πp, pp, Kp,

e^+e^- collisions [167]. It is tempting to explain the agreement between the SHM and the heavy ion data as a formation in the collisions of thermodynamically equilibrated medium with quarks and gluons as constituent particles, which transits into hadron gas once the critical temperature is reached during the medium expansion. However, such unambiguous interpretation assumes that such a medium is formed also in elementary e^+e^- and single hadron collisions, which would require very short thermalization times and could be explained assuming formation of a very strongly coupled medium, but the later is in contradiction with the asymptotic freedom of the QCD at high collision energies. Therefore, the only reliable way to understand the mechanism of particle production in heavy ion collisions at the moment is to study it experimentally. It is interesting to note, that even though it is not possible to predict reliably strange particle yields using the SHM at any new collision energy, crude estimates show that strong enhancement of the yields at the highest RHIC energy based on the model parameters at the AGS and the SPS energies is not excluded (see Fig. 1.8 on the next page).

1.4.2. ϕ Meson As A Probe Of QGP

1.4.2.1. ϕ Meson Decay Time

For a particle decaying mainly through the strong interaction, ϕ mesons have a long lifetime of $\tau = 1/\Gamma_\phi = 1/4.26$ MeV$\simeq$ 46.3 fm/c (the typical time of such decays is $\sim$ 1 fm/c) [169]. The long life of ϕ mesons is due to the combination of the following two factors:

- Decays of the ϕ meson into non strange mesons (see Fig. 1.9(a) for an example) are suppressed due to the OZI [39, 170–172] rule, since they require the $s\bar{s}$ pair to annihilate first into high energy gluons (the gluons have to be energetic enough to be able to produce the decay product mesons), which then couple to several $q\bar{q}$ pairs - the constituent quarks of the final state mesons. However at high transferred momentum the coupling of the gluons to quarks is weak (the QCD asymptotic freedom) and therefore such decays are suppressed.

- Decays of the ϕ meson into kaons (see Fig. 1.9(b)) are the OZI rule allowed, since in that case all the initial state quarks exist also in the final state (there is no pure gluon stage in the lowest order Feynman QCD diagram) and since the mass of the ϕ meson ($m_\phi \simeq 1019.455$ MeV) is very close to a mass of two kaons ($m_{K^+K^-} \simeq 987.354$ MeV, $m_{K^0\bar{K}^0} \simeq 995.228$ MeV) [169], all virtual gluons are of low momentum and therefore with strong coupling to quarks. However, due to this closeness of mass, the phase space available to the decay product kaons is very small, and therefore the decay channels $\phi \to K^+K^-$ and $\phi \to K^0\bar{K}^0$ are suppressed as well.

1.4.2.2. ϕ Meson Interaction Cross-Section

Before the beginning of the heavy ion programs at the AGS (started in 1986) and the SPS (heavy ion injector available as well in 1986), there existed two different points of view

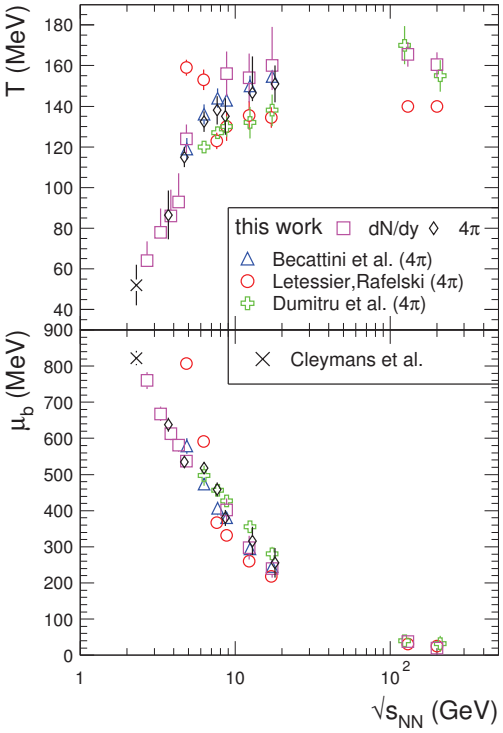

Figure 1.8.: The figure shows the dependencies on $\sqrt{s_{\rm NN}}$ of temperature T and of baryon chemical potential μ_B found by fitting heavy ion collision data using SHM [149]. Even though the model is able to describe particle yields well in various high energy collisions (see section 1.4.1 on page 38), it is not straightforward to use the model to predict strangeness production as a function of $\sqrt{s_{\rm NN}}$ in heavy ion collisions (of fixed centrality and fixed atomic weight) to check if the production is strongly enhanced in some specific range of $\sqrt{s_{\rm NN}}$ values due to formation of QGP at some stage of evolution of matter created in the collisions. We have reasons to believe (based on the trend exhibited by the total multiplicity of produced particles as a function of $\sqrt{s_{\rm NN}}$ at lower energies) that at very high $\sqrt{s_{\rm NN}}$ values the total number of produced particles has to be large in comparison to the number of nucleons (the total baryon number) in the collided nuclei and so μ_B must have a very small positive value. We also know that the extracted T values should approximate the chemical freeze-out temperature (see footnote 6 on page 192), which in turn cannot exceed T_c (140-200 MeV, see section 1.2.8 on page 30). However, since T and μ_B (as well as γ-factors and $\mu_i^{\rm flavor}$) are extracted in SHM by fitting experimental data, it is not possible to say for sure based on the low energy behavior what the parameters should be at the RHIC energies, namely, based on the knowledge of the T and μ_B values at the AGS and the SPS energies, one can only estimate that baryons/mesons with $m \sim 1$ GeV (for example, ϕ mesons) could be enhanced by any factor in the range from 1 to 50/10 if the highest SPS energy is compared to the highest RHIC energy (in the estimate, all the γ-factors were set to unity and all $\mu^{\rm flavor}$ were set to zero, and as a consequence this crude estimate is independent of the constituent quark content of hadrons).

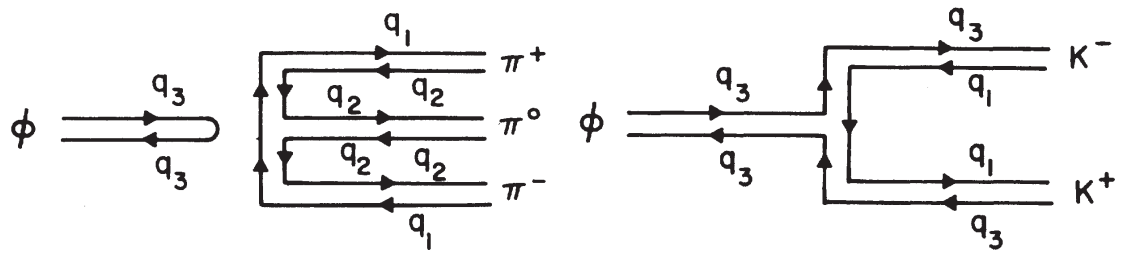

(a) $\phi \to \pi^+\pi^0\pi^-$ is forbidden by the OZI rule

(b) $\phi \to K^+K^-$ is the OZI rule allowed but slowed down by the small phase space available to the decay products

Figure 1.9.: The OZI rule forbidden (a) and allowed (b) strong decays of the ϕ meson. The figures were adopted from [168]. (see section 1.4.2 on page 40 for details).

on the probability of interactions of the ϕ meson with high temperature hadronic gas medium:

- Asher Shor argued in 1985 that due to the restrictions on the interactions imposed by the OZI rule, ϕ mesons would not scatter significantly at the hadronic gas stage of the evolution of a system created in a heavy ion collision after they are produced in a decaying QGP [173]. The total scattering cross-section was measured in a photoproduction experiment on a liquid H_2 target to be ∼7.7-8.7 mb [174], of which ∼8-14% is due to scattering and the rest is due to the absorption $\phi N \to YK$, where K is a kaon and Y is a strange hyperon [173]. Numerically, it means that random ϕ meson would get absorbed in a 7 fm radius nucleus with a probability ∼30% and scattered with a probability ∼3-5%. Combined with the long life of ϕ mesons, it means that ϕ mesons of high enough momentum would be able to escape the hot hadronic gas medium retaining the information about the conditions at which they were produced. This picture assumed that the observable in an experiment ϕ mesons are produced in coalescence of strange quarks in QGP decay.

- In the other point of view [156], it is argued that since the mass of a ϕ meson is very close to the mass of two kaons, it is essentially a $K\bar{K}$ cluster, which would frequently participate in quark exchange reactions during collisions with other hadrons, therefore the number of ϕ mesons would be just somewhat (factor of ∼1-3, due to an enhanced $s\bar{s}$ clustering) higher than in an equilibrated hadron gas with enhanced strange quark content. That assumes that a large fraction of

observable in an experiment ϕ mesons would be produced not in a QGP decay, but at the hadron gas stage of evolution of a system created in a heavy ion collision.

The total cross-section $\sigma_{\phi N}$ of interaction of ϕ mesons with a nucleon target has been studied as well in other photoproduction experiments. Here one has to distinguish *coherent* (where the target is essentially a nucleon in free space, like the hydrogen target in Ref. [174] mentioned above, which is achieved by using targets with very low atomic mass $A \sim 1$) and *incoherent* (where targets with large A are used to study photoproduction on an in nuclear medium target nucleon) photoproduction. If $\sigma_{\phi N}$ is the same in free space and in nuclear medium, then the total cross-section of ϕ meson photoproduction on a nuclear target σ_A would be approximately proportional to A, since $\sigma_{\phi N}$ in free space is small. And if $\sigma_{\phi N}$ in nuclear medium is larger than in free space, then significant fraction of ϕ mesons would be absorbed in target nuclei and σ_A would grow slower than $\sigma_A \propto A$. Incoherent ϕ meson photoproduction experiments showed a large increase (by a factor ~ 4) of $\sigma_{\phi N}$ inside nuclear medium [175, 176] [21]. The results of such experiments cannot directly be used in interpretation of heavy ion collision data since the temperature inside a nucleus is much lower (≤ 10 MeV) and the medium is composed mostly of nucleons and pions only. However, they prove that in-medium effects on a ϕ meson, and in particular on $\sigma_{\phi N}$, are significant. Such effects can only be reliably studied experimentally at the moment, including figuring out which of the two points of view on the ϕ meson scattering cross-section in high temperature hadronic gas medium is correct.

1.4.3. In-Medium Effects On The ϕ Meson

Since about the beginning of 1980's, many QCD sum rules [177], lattice QCD , and model based calculations of modifications of *hadron properties (i.e. the mass, width, branching ratios, and rate interactions with other hadrons)* in a QCD medium at high temperatures have been done, starting with the work which studied the change in the position and width of the ρ-meson [178]. Such modifications are predicted to occur either in heavy ion collisions, that do not lead to a creation of a QGP, or at the mixed [22] and the hadron gas stages of the evolution of a system created in the collisions. The in-medium effects could also offer an alternative (i.e. not requiring QGP formation) explanation for the difference in hadron yields between elementary (i.e. e^+e^-, pp, and $p\bar{p}$) and heavy ion collisions. This section aims to review the calculations for the ϕ meson and to point out the advantages of searching for the modifications experimentally on the example of ϕ mesons, and, in particular, of using the $\phi \to K^+K^-$ decay channel for the purpose.

[21] The increase is from $\sim$8 mb [174] to 35^{+17}_{-11} mb [175]. In addition, an optical model interpretation of the Ref. [175] data gives $23 \leq \sigma_{\phi N} \leq 63$ mb [176].

[22] "Mixed" stage means that hadrons coexist with free quarks and gluons.

1.4.3.1. Change Of Mass Of The ϕ Meson

Study of the $\phi \rightarrow K^+K^-$ decay channel is especially interesting since the ϕ meson mass ($\approx$1.019 GeV) is very close to the sum of masses of the decay products ($2m_K \approx$0.987 GeV). Therefore even a small change in the mass of ϕ mesons or kaons, while submerged into a hot medium, would have a strong effect on the decay properties [179–181]. For example, if at some temperature the ϕ meson mass is smaller than the sum of K^+ and K^- masses, then the $\phi \rightarrow K^+K^-$ decay would not be observed for ϕ mesons decaying inside the medium. As it was pointed out above (see section 1.4.2.1 on page 40), ϕ meson has a long lifetime of $\simeq$ 46.3 fm, which would allow it to escape the medium created in a heavy ion collision (see section 1.4.2.2 on page 40). However, it was also alternatively predicted that the lifetime of the hadronic fireball, created in such a collision would be of the same scale, allowing a significant fraction of ϕ mesons to decay inside the medium [179, 182, 183]. In particular, the time the fireball spends near (assumed to be a 1st order) transition temperature between QGP and hadronic gas was estimated from hydrodynamical calculations with transverse flow to be $\sim$ 10 fm/c [184, 185]. If the mass of ϕ mesons in matter stays above the sum of K^+ and K^- masses, then a second ϕ peak could be observed in the $\phi \rightarrow K^+K^-$ decay channel, similar to the one predicted in the dilepton channel [184–186], where the low and high mass peaks correspond to ϕ mesons decaying inside and outside of the medium correspondingly. The presence of the lower invariant mass ϕ meson peak and its transverse momentum dependence were proposed as a signature of a transition of matter into QGP in heavy ion collisions and as a way to determine experimentally the transition temperature between QGP and hadronic gas correspondingly [184, 185].

It was argued in section 1.4.2.2 on page 40 that an enhanced ϕ meson production in heavy ion collisions is a signature of QGP formation, however the enhancement could also be explained by the in hot hadronic gas changes of the ϕ meson and kaon masses as well as of the kaon production cross-section [188], and so by studying the ϕ meson peak experimentally the two alternative scenarios could be probed. If, in fact, both ideas are correct, i.e. a system created in a heavy ion collision goes through the QGP phase during its evolution and the ϕ mesons mass is reduced in a medium (see Fig. 1.10 on the next page), then it is energetically easier to create them, which combined with an enhanced strangeness production at the QGP stage (see section 1.4 on page 35), would lead to a dramatic enhancement of the observed ϕ meson yield [187].

A simple way to explain [182] why the masses of hadrons at high temperatures were expected to be reduced, is to think in terms of the naive constituent quark model. In the model the mass of a hadron is just the sums of masses of its constituent quarks. As it was pointed out in section 1.4 on page 35 on the example of the strange quark, the masses of quarks are significantly lower in QGP (equal to their current masses) due to the chiral symmetry restoration, in comparison to hadronic gas (equal to their constituent masses). Therefore, the closer the temperature of a hadronic gas is to the transition temperature to QGP, the lower the masses of all hadrons are expected to be.

However, there are predictions of an increase of the ϕ meson mass in a hot hadronic environment as well [189].

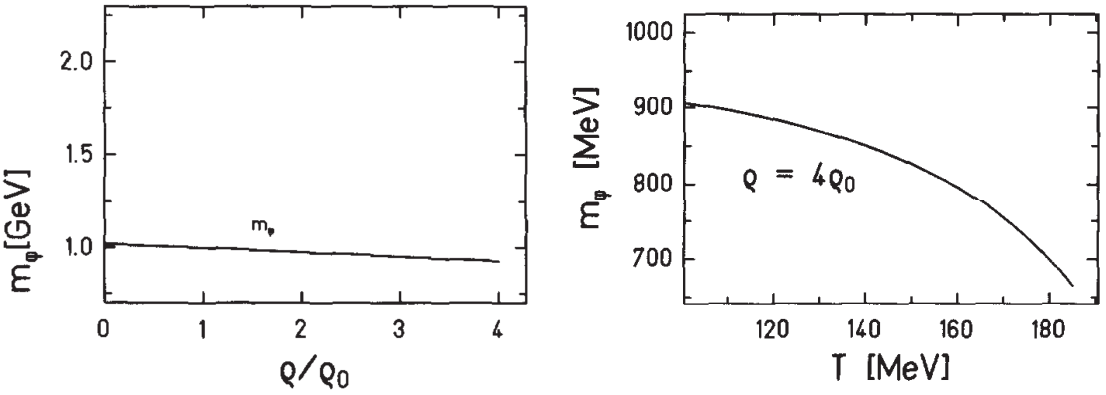

(a) medium density dependence of the ϕ meson (b) temperature dependence of the ϕ meson mass mass at $T = 0$

Figure 1.10.: One example of a prediction [187] of the ϕ meson mass dependence on the medium density (a) and temperature (b) calculated using the QCD sum rules, where ϱ is the medium density and ϱ_0 is the density of normal nuclear matter. See section 1.4.3 on page 43 for details.

1.4.3.2. Change Of Width Of The ϕ Meson

The width of hadrons in a medium is expected to be modified due to interactions (collisions) with the environment (other hadrons or quarks). In such interactions (for example, $\phi + \pi \rightarrow K\bar{K}$) a hadron could be converted to another hadron. Therefore the interactions add extra channels through which a hadron can get destructed and created and consequently changing the hadron width if the initial chemical composition of the hadron gas into which the hadron is submerged is not in a chemical equilibrium [180, 190, 191]. That leads to a situation when even particles, which are stable in vacuum, could get destroyed at some rate in a QCD medium, and so would have a non-vanishing width. The density and the composition of a thermodynamically equilibrated medium, into which a hadron is submerged, determine the rate and the type of interactions of the hadron with its environment and are a function the medium temperature, leading to a temperature dependence of the hadron width.

It is important to distinguish the decay width of a hadron, which effects the observed width of the invariant mass distribution of the hadron decay products, and the collisional (or scattering) width, which just effects the rates of destruction and creation of the hadron in a medium. The later width was explained in the previous paragraph. What follows describes the effects on the observed decay width of a hadron.

Another effect, which can cause broadening of the ϕ meson peak, is a reduction in the momentum resolution of the ϕ decay products due to their scattering on the medium constituent particles.

As well, the so called *stimulated decay* processes in matter contribute to increasing of

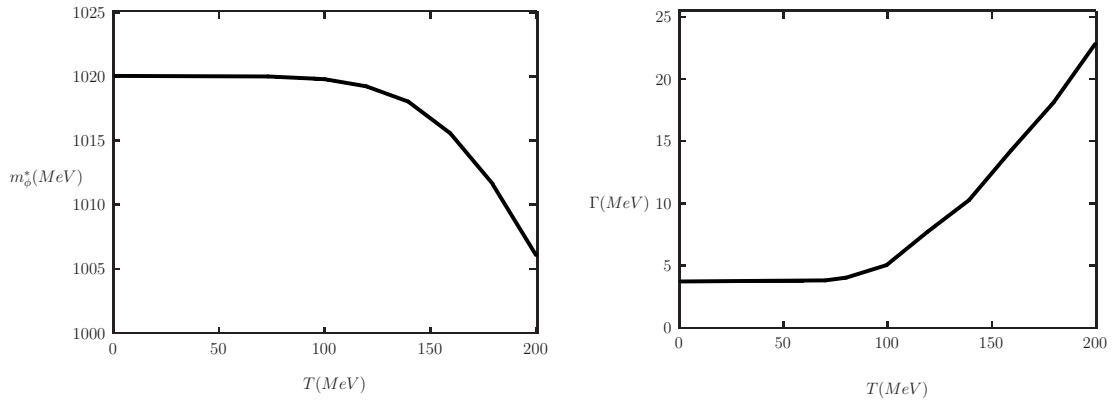

(a) Temperature dependence of the ϕ mass (b) Temperature dependence of the ϕ decay width

Figure 1.11.: An example of a prediction of temperature dependence of ϕ meson mass and width [181]. The lines were made thicker on the plots for better visibility.

hadron widths in matter [190].

In addition, the mass of a hadron and/or of its decay products might change in a medium, and the process might both decrease and increase the hadron width (due to a change in the available phase space for all/some of the hadron decays channels), competing with or enhancing the changes in width mentioned above. However the final predicted effect is an increase (up to a factor of 2-8 near T_c) [181–183, 186, 191] (see also Fig. 1.11) of the ϕ meson width at nonvanishing temperatures.

Different decay channel widths of a hadron might be modified by a different factor, and if some decay channel width is only a small fraction of the total decay width, its modification might be better studied by a comparison of its branching ratio with respect to other channels or, which is the same thing, one could study relative yields of the hadron measured using different decay channels.

It is important to notice that an increase of ϕ mesons decay width in a medium means that they would decay at a faster rate, have shorter mean lifetime $\tau = 1/\Gamma_\phi$, and therefore have an increased probability to decay inside the medium, which in turn would make it easier to observe the effect in an experiment despite the long lifetime of ϕ mesons in vacuum (see section 1.4.2.1 on page 40).

1.4.3.3. Change Of Symmetry Of The ϕ Meson Peak

Another possibility is a change in the symmetry of the ϕ meson peak, studied through the $\phi \to K^+K^-$ decay channel. It was predicted based on experimentally measured forward scattering amplitudes that the ϕ meson peak would become asymmetric at high temperatures due to a difference in in-medium potentials of K^+ and K^- (daughter K^+ getting a higher share of the ϕ meson decay energy than K^-) as well as due to a

change in momentum of charged kaons as they escape the medium (K^+ being accelerated, while K^- being slowed down) [183].

1.4.3.4. Experimental Evidence Of ϕ Meson In Medium Modifications

Experimental evidence of a significant increase in a normal nuclear matter of the total cross-section of interaction of ϕ mesons with nucleons was given in section 1.4.2.2 on page 40.

KEK-PS E325 collaboration studied modifications of ϕ meson mass and width at normal nuclear density using the $\phi \rightarrow e^+e^-$ decay channel [192]. The results indicate a decrease of the ϕ meson mass by $3.4^{+0.6}_{-0.7}$% and an increase in both the total $\Gamma^{\text{tot}}_{\phi}$ and partial decay width of the $\phi \rightarrow e^+e^-$ channel Γ^{ee}_{ϕ} by a factor of $3.6^{+1.8}_{-1.2}$.

The above results demonstrate that in-medium modifications of ϕ meson properties are not a pure theoretical speculation, but are effects which are studied experimentally.

1.5. Goals Of This Thesis

The first goal of this thesis is to measure the invariant yield of ϕ meson production in Cu+Cu collisions at $\sqrt{s_{\text{NN}}}$=200 GeV as a function of transverse momentum and collision centrality, including the very low p_t^{ϕ} <130 MeV region not reachable by any other experiment. The measurement will be used to extract dN/dy of ϕ mesons near mid-rapidity and their effective temperature T using Eq. 1.2 on page 23 as a function of collision centrality. The dependence of the parameters as a function $\sqrt{s_{\text{NN}}}$ will be studied. The yield of ϕ mesons and the ratio of the yield to the yield of all charged particles will be compared for different $\sqrt{s_{\text{NN}}}$ values.

The second goal is to search for in-medium modifications of ϕ meson decay properties using $\phi \rightarrow K^+K^-$ channel, looking for evidence of any changes in ϕ meson mass, width and peak symmetry.

2. The PHOBOS Experiment

The data on Cu+Cu collisions at $\sqrt{s_{\rm NN}}$=200 GeV used for the measurements performed in this thesis were taken by the PHOBOS detector at RHIC in 2005. The collisions were provided by the RHIC-AGS accelerator complex. Information from the following sub-detectors of PHOBOS was utilized in the data analysis: 1) *the spectrometer* - a set of silicon pad detectors (used for a reconstruction of charged particles trajectories) placed in a magnetic field created by a dipole magnet, 2) *the octagon* - an other set of silicon pad detectors (used for a determination of event centrality), 3) *Time Zero* and *Paddle counters* as well as *Zero Degree Calorimeters* (used for the collision triggering).

2.1. Relativistic Heavy Ion Collider

RHIC is a heavy ion and longitudinally polarized proton-proton collider constructed with a budget of ∼$620M at BNL in 1991-1999 in Upton, NY, USA with the original idea dating back to 1983 and R&D work starting in 1987 [193]. First collisions delivered by RHIC (on June 12, 2000) were those of Au+Au at $\sqrt{s_{\rm NN}}$=56 GeV. Since then experiments were performed colliding Au+Au, Cu+Cu, d+Au and polarized protons at energies of $\sqrt{s_{\rm NN}}$=7.7-500 GeV [194]. Operation at a range of energies allows to study properties of the quark matter as a function of energy density. pp collisions data provide a reference for the heavy ion collision measurements, as they allow to study mostly primary collisions between quarks and gluons only with little contamination by secondary interactions between the produced particles. In addition, being able to collide particles at and below the RHIC injection energy provides connection to results from the preceding experiments. Data on the collision events were taken by four physics detectors: **B**road **RA**nge **H**adron **M**agnetic **S**pectrometers (BRAHMS) [195], PHENIX [196], PHOBOS [197], and STAR [198].

The initial source of particles for RHIC is provided by a tandem Van de Graaff accelerator for heavy ion beams and by a linac for polarized protons. Focusing on heavy ions, the input negatively charged ions for the Van de Graaff accelerator are provided by a pulsed *sputter source* [199], in which C^{+5} ions hit a target of material, which nuclei are intended for the final acceleration in RHIC, producing a beam of negatively ($Q=-1$) charged ions. Let us consider the heaviest ions, which RHIC can accelerate, Au^{+79} as an example [200]. The Au^{-1} ions are accelerated in the Van de Graaff accelerator from ground to a +14 MV potential in a static electric field and then collided with a 2 μg/cm^2 carbon *stripping foil* [201]. In in the process the Au^{-1} ions acquire a positive charge $Q=+12$, and are accelerated further (back to ground potential) at the second stage of the Van de Graaff accelerator to energy of ∼ 1 MeV/nucleon. At the exit from the Van

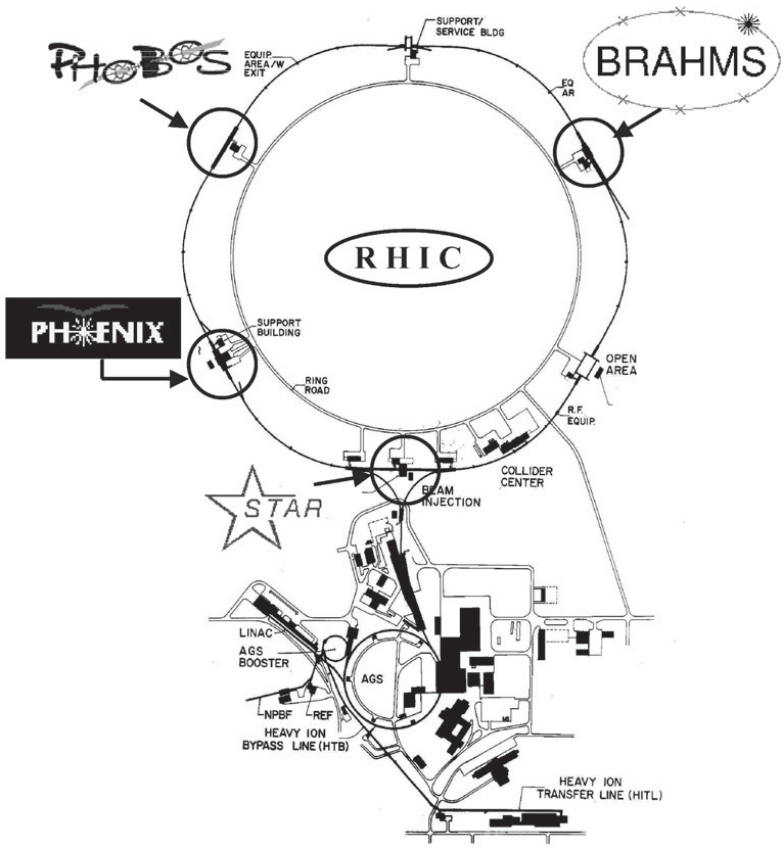

Figure 2.1.: Scheme of the RHIC accelerator complex. The figure was adopted from Ref. [193].

de Graaff accelerator the gold ions are stripped of electrons again by a 8 $\mu g/cm^2$ carbon foil to have a charge $Q = +32$. After that the ions travel a $\sim$ 850 m transfer line to the Booster Synchrotron, where they are accelerated to the energy of 95 MeV/nucleon and at the exit are stripped of electrons again by a 24.2 mg/cm^2 carbon foil or a combination of 6.4 mg/cm^2 aluminum foil followed by 9.2 mg/cm^2 vitreous carbon foil. The charge of the ions after that is $Q = +77$ and they are helium like having only two K-shell electrons left. High vacuum provided by the booster is important for the functioning of the whole RHIC complex, since it allowed to switch from the maximum accelerated nucleus charge of +14 (Si) to the of +79 (Au) [202] and to increase the intensity of the beams delivered to the AGS [203]. The AGS accelerates the ions further to 8.86 GeV/nucleon and at the exit a 522 mg/cm^2 Al_2O_3 or a 48.9 mg/cm^2 tungsten stripping foil removes the remaining 2 electrons, leaving bare gold nuclei entering the RHIC.

RHIC is a two-ring superconducting collider with a circumference of $\sim$3.8 km. The RHIC rings have a hexagonal shape (see Fig. 2.1). The intersection points of the two counter rotating in the same horizontal plane (the clockwise "blue" and the counter-clockwise "yellow") beams are located in the middle of the hexagon sides (the $\sim$ 277 m long straight sectors). The beams are controlled with 1740 NbTi superconducting mag-

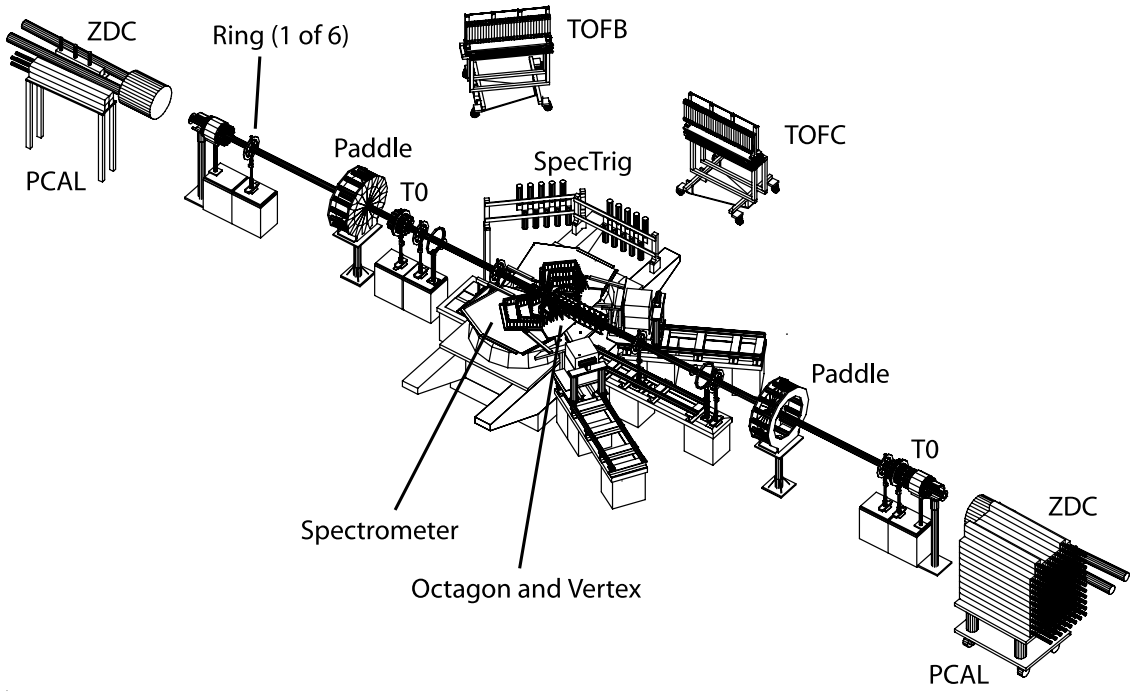

Figure 2.2.: Schematic PHOBOS detector setup in 2003.

nets (dipole ones are used for bending a beam, quadrupole and sextupole ones are used for focusing it) operating in forced-flow helium at a design temperature of ~ 4.6 K with dipole magnets in the arc sections of RHIC providing 3.45 T field [204]. RHIC is able to provide average collision luminosities of $\gtrsim 10^{30}$ cm^2 s^{-1} during heavy ion runs [194]. It accelerates the particles in groups, called *bunches*, each bunch consisting of $\sim 10^9$ nuclei for Au^{+79}, with higher bunch multiplicities possible for lighter ions [200].

2.2. PHOBOS Detector

PHOBOS detector consisted of four main parts: multiplicity detectors (see section 2.2.5.2), vertex detectors (see section 2.2.5.1), silicon magnetic spectrometer (see section 2.2.5.3), trigger and centrality measurement detectors (see sections 2.2.2, 2.2.3), and 2.2.4). The detector design goals were measurement of particles near mid-rapidity ($0 \leq \eta \leq 2$), particle identification for $p_T \leq 1$ GeV/c, and optimized detection of low p_T particles [205]. An other design goal was a high acceptance for two-particle measurements, however this goal was not achieved, since the PHOBOS spectrometer allows analysis of only 1-2% of all produced particles, which means that the acceptance for two particle decays (like $\phi \rightarrow K^+K^-$) is $\sim 10^{-4}$, and that is the main reason why the measurement done in this thesis turned out to be so technically difficult to perform using data from the PHOBOS detector (see section 5.1 on page 89).

This section describes the PHOBOS detectors used in the data analysis performed for this thesis. Information about other parts of the PHOBOS experiment hardware can be

found elsewhere [205].

2.2.1. Coordinate System

PHOBOS detector coordinate system was chosen in such a way that the z-axis is oriented along the rotational symmetry axis of the RHIC beam pipe (which is a 76 mm in diameter $\approx$ 1.0 mm thick Be tube [1] in the 12 m region near the PHOBOS detectors). The x-axis is oriented horizontally pointing towards the TOFB, TOFC, and SpecTrig detectors (see Fig. 2.2 on the preceding page), and the y-axis is oriented vertically upward with respect to the floor level in the PHOBOS detector area of the RHIC tunnel (see Fig. 2.2 on the previous page). The origin of the system was chosen with respect to the spectrometer sensors in the nominal interaction point as shown on Fig. 2.10 on page 61.

2.2.2. Paddle Counters

These are 2 circular shaped plastic scintillator counters [2], each split into 16 "paddle" shaped sectors centered at the beam pipe perpendicular to it (see Fig. 2.3(a) on the facing page). Each paddle sector is a module consisting from a plastic scintillator slab near the beam pipe, followed by a light guide connected to a **P**hoto**m**ultiplier **T**ube (PMT). Each PMT is covered in black epoxy for light tightness, wrapped in a 2 mm mu-metal magnetic shield and attached to the structure with a silicon elastometer. All the scintillators and light guides are wrapped in a layer of aluminum and a layer of black vinyl.

The paddle detectors were located at $z = \pm 3.21$ m around the center of the PHOBOS detector coordinate system (see section 2.2.1). The counters covered 94% of the solid angle corresponding to $3 < |\eta| < 4.5$ region in pseudorapidity and $0 < |\phi| < 2\pi$ region in azimuthal angle, and served as the primary collision trigger (see section 4.1). The detector timing resolution was $\sim$ 1 ns, the signal-to-noise ratio was about 20:1, and energy resolution for one Minimum Ionizing Particle (MIP) (energy loss $\Delta E = 1.7$ MeV) of $\sigma_E/\Delta E$=45%. While the energy and time resolution of each individual scintillator was about $\sigma_E/\Delta E$=11-14% and 300-400 ps correspondingly.

Calibration. The time calibration [208] of the counters was performed by a comparison of event vertex z-coordinates determined from

- the difference in time between the signals from the two paddle detectors (the same idea as the one explained in section 4.1.2.3 on page 73),
- the hit positions in the silicon sensors (see section 4.3 on page 75).

The *pedestal peak* of a paddle detector module is the distribution of signals it produces in the absence of any external influence (i.e. without any particles hitting it) due to various sources of noise. The energy calibration of the detectors was performed for each paddle module separately by adjusting the voltage supplied to the module PMT

[1] Contradicting information about the beam pipe dimensions is given in Ref. [205, 206]. The former cites the tube exterior diameter to be 10 cm.

[2] The detectors are denoted as "Paddle" on Fig. 2.2 on the previous page.

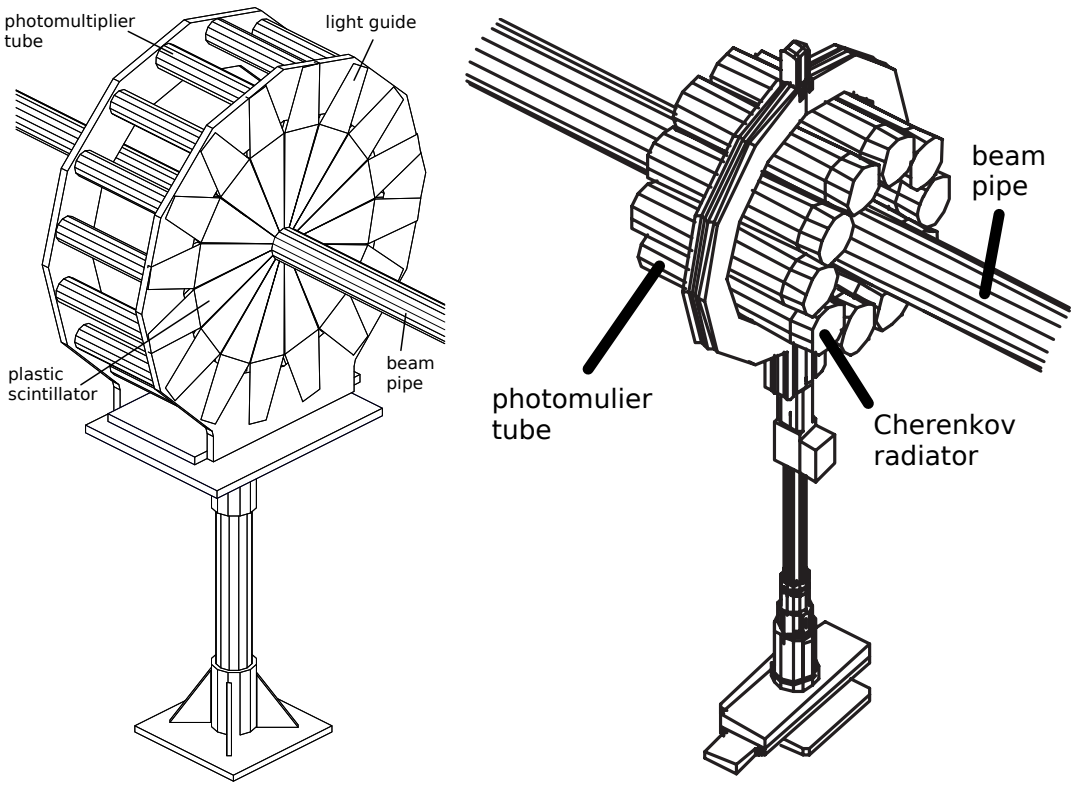

(a) Paddle counter detector

(b) T0 counter detector

Figure 2.3.: (a) Paddle counter detector. (b) T0 counter detector. The figures were adopted from Ref. [206] and Ref. [207] correspondingly. See sections 2.2.2 and 2.2.4 for details.

in such a way, that the number of Analog-to-Digital Converter (ADC) channels between the mean of the pedestal peak and the one MIP peak is equal to a fixed number (50), with subsequent subtraction from an observed signal of the ADC channel number corresponding to the mean of the pedestal peak. Both calibrations were done separately for every data taking run to ensure the stability of the signals from the paddle detectors.

More information about PHOBOS scintillator counters can be found in Ref. [206].

2.2.3. Zero Degree Calorimeters

ZDC are hadronic calorimeters located at $z = \pm 18.5$ m, which is further from the PHOBOS nominal interaction point than positions of two RHIC DX dipole magnets, that bend the beams of collided particles away from the straight path marked by the z-axis (see section 2.2.1 on the preceding page and Fig. 2.4 on the following page). The purpose of the calorimeters is to detect neutral beam fragments (mostly neutrons) and to measure their energy. For collisions at $\sqrt{s_{\mathrm{NN}}}$=200 GeV, such fragments diverge by less

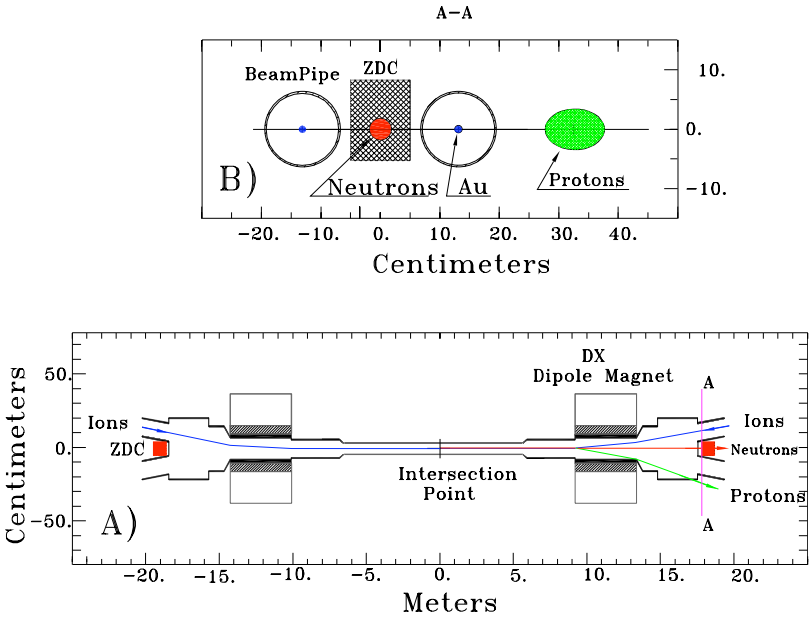

Figure 2.4.: Position of ZDC when viewed in the transverse plane (top) and from above the beam pipe (bottom). The figure was adopted from Ref. [209].

than 2 mrad from 0° defined by the beam axis [209], hence the name of the detectors. The contribution of other produced particles and secondaries to the energy deposited in ZDC is negligible.

Each ZDC is made of three calorimeters, each of which is a sandwich of 27 tungsten 5 mm thick plates and ribbons of 20 optical 0.5 mm in diameter fibers. The difference from a more typical hadronic calorimeter design (where scintillators are sandwiched in between layers of converter material) is that the fibers in ZDC collect Čerenkov light. The reason of the later design choice that a calorimeter of the same size allows to sample a higher fraction of an hadronic shower. The refractive index n of the optical fibers is such that the Čerenkov radiation is emitted at angle θ (defined by $\cos\theta = (n\beta)^{-1}$) equal to 45° for $\beta = 1$ particles, and therefore the fibers are oriented at this angle with respect to the beam direction as shown on Fig. 2.5 on the next page. The light collected by the fibers is converted by a PMT into an electrical pulse, which height is used as a measure of the energy deposited in ZDC by neutral beam fragments, and so could be used as an experiment independent way to determine centrality of a nuclear collision (the ZDC were made identical for all RHIC detectors). A coincidence requirement on the arrival time of the pulses from both ZDC was used as a collision trigger (see section 4.1.2.2 on page 71), and so could also be used to determine the luminosity delivered to PHOBOS by RHIC.

The energy and timing resolution of the ZDC are $\sigma_E/E \leq 20\%$ and $\sigma_t \leq 150$ ps correspondingly. The radiation tolerance was found to be >500 kRad, while the dose delivered to ZDC by RHIC was estimated to be 10 kRad/year, ensuring long useful lifetime of the calorimeters. The efficiency of the ZDC was determined to be $\geq 99.5\%$ [210]. More

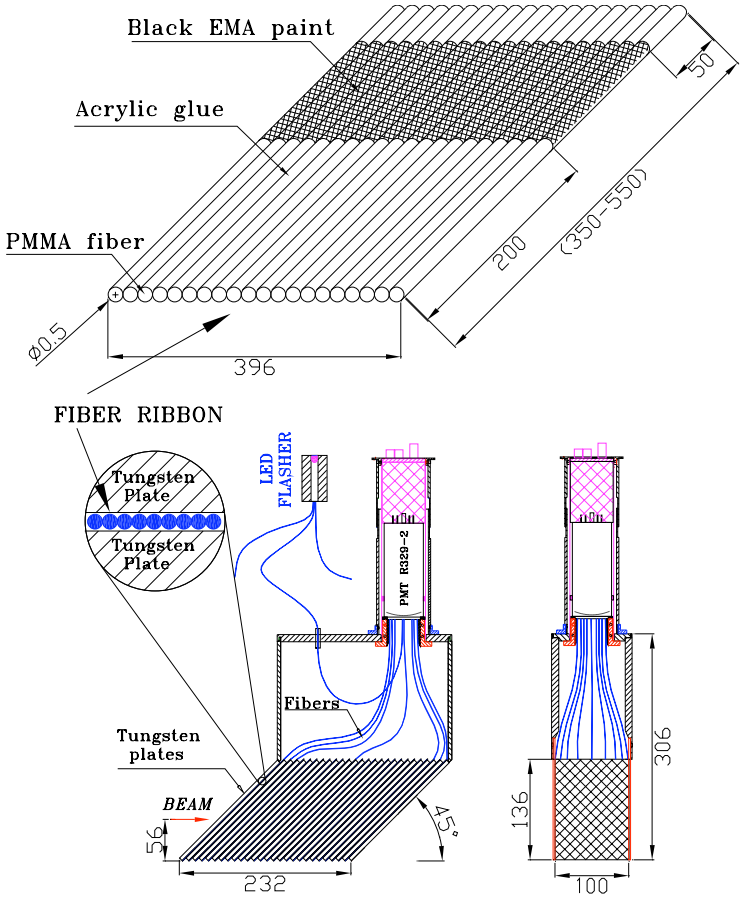

Figure 2.5.: ZDC module design. All dimensions shown are in mm. The figure was adopted from Ref. [209].

information about ZDC can be found in Ref. [209, 211].

2.2.4. Time Zero Detectors

Time Zero Detector (T0) counters are two Čerenkov detectors located at $z = \pm 5.4$ m, each of which is made of ten 25 mm thickness 50 mm diameter cylindrical acrylic Čerenkov radiators coupled to fast PMT (see Fig. 2.3(b) on page 53). The radiators and PMT are arranged on a 151 mm diameter circle around the beam pipe.

The purpose of the detectors is to provide a very fast estimate on the z-coordinate of a collision vertex, which then can be used by the Data Acquisition (DAQ) system to decide if information about the event should read from the other detectors and saved for an off-line analysis. The reason of the vertex selection is that due to the PHOBOS detectors geometry only events in a rather narrow range of vertex z-coordinates (-35 cm$\leq v_z \leq$+15 cm) could be used to extract useful information about the physical laws governing the dynamics of a high energy nuclear collision.

T0 counters have an intrinsic time resolution of 110 ps [205]. The time calibration of

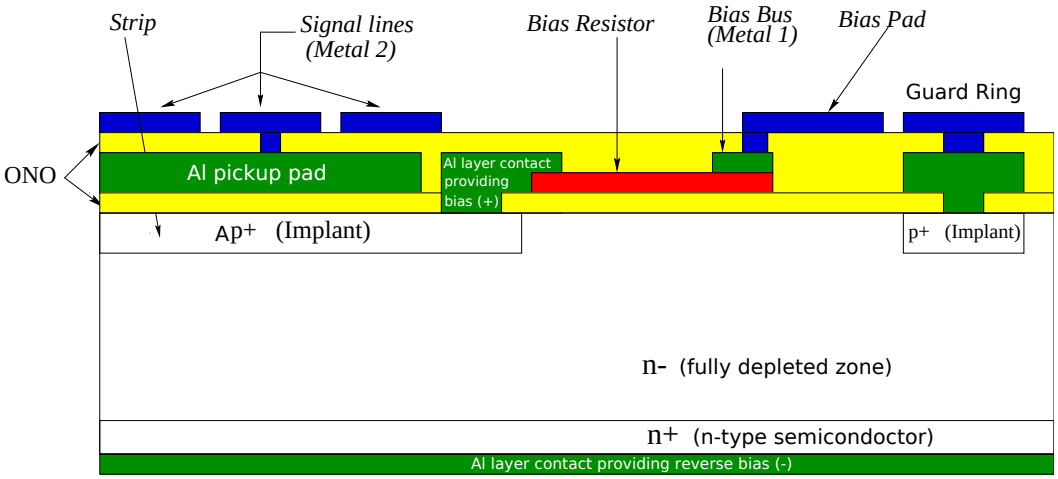

Figure 2.6.: Schematic cross-section of one pad of PHOBOS silicon detectors. The figure was adopted with comments from Ref. [213]. See section 2.2.5 for details.

the counters was performed the same way as for the paddle detectors (see section 2.2.2 on page 52). The difference in time of arrival of pulses from the detectors is used to calculate collision vertex z-coordinate with a resolution from ≈1 cm to 8 cm depending on the number of charged particles hitting the detectors in a particular event [208]. The pseudorapidity acceptance of the T0 counters covered the range $4.4 < \eta < 4.9$ (and a symmetric range on the negative side) [212].

2.2.5. Silicon Detectors

All the actual physical measurements performed by the PHOBOS experiment, used data from silicon pad detectors. Although nine different wafer types were employed, all the detectors used the same silicon pad design, shown on Fig. 2.6. The base wafer of the detectors is made mostly of silicon, which is a chemical element with 4 valence electrons (2 on $s-$ and 2 on $d-$shells). The normal conductivity of pure silicon is somewhere in between metals and isolators and is rather low. To increase the conductivity one can add to the silicon impurities of an element with 3 valence electrons (for example, boron) or with 5 valence electrons (for example, arsenic). Atoms (ions), with 4 electrons in the outer unfilled shell are in a lower energy state than both with 3 and with 5 electrons. Therefore, when in silicon environment, it is energetically preferable for a boron atom to add one electron by taking it away from a silicon atom (boron atoms have smaller atomic number and so have smaller radius of their outer electron shells and lower energy of electrons in the shells, and therefore, even though silicon loses one of its 4 outer electrons, the total energy of the two atoms is reduced). Similarly, since arsenic atoms are larger than silicon ones, the energetically more preferred state is for the arsenic to give up one of its outer electrons, which becomes conductive, leaving only 4 electrons

on its outer shell. A boron doped silicon becomes what is called a *p-type* semiconductor, since it leaves positively charged silicon ions, which charge is mobile (an electron from a neutral silicon atom can jump to a silicon ion, effectively moving the ion charge from the later to the former), while the negative charges of boron ions are (mostly) stationary. An arsenic doped silicon is called a *n-type* semiconductor, since its mobile charge carriers are negatively charged electrons, while its positively charged arsenic ions are (mostly) stationary. A gapless contact between a p-type and n-type semiconductors is called a *p-n junction*. When such a contact is made, positive charges (also called *holes*, since they are equivalent to missing electrons) from the p-type semiconductor diffuse due to the Brownian motion into the n-type semiconductor. Similarly, negative charges from the n-type semiconductor diffuse into the p-type semiconductor. In the region, in which diffusion took place, the positive mobile charges recombine with negative ones, forming a region depleted of free charge carriers (a *depletion zone*). However, on both sides of the region a stationary electric charge gets accumulated, which leads to formation of an electric field (the same way as in a two plate capacitor), that is strong enough to stop further diffusion. By applying an external electric field (*bias*) perpendicular to the p-n junction one can either push the mobile charge carriers further from one semiconductor to an other, or to reduce such charge penetration, thereby increasing (*reverse bias*) or decreasing (*forward bias*) the width of the depletion zone correspondingly. If a charged particle traverses the depletion zone, it ionizes the material, producing conducting electrons and holes. Under the influence of the total electric field (the internal field of the diffused charge carries and applied external one), some fraction of the charges gets swept and creates a charge pulse, which can be registered. The integral of the pulse is then proportional to the energy loss by the particle in the material.

In case of PHOBOS silicon detectors with the wafer thickness distribution shown on Fig. 2.8 on page 59, a reverse bias of about 70 V [213] is applied allowing to create a depletion zone in almost the whole volume of ~ 320 μm thick silicon pads. The bias is applied between the "Bias Pad" (through a "Bias Bus" and a polysilicon (red) 1-10 MΩ "Bias resistor") and an aluminum (green) layer covering the n-type zone marked as "n+" (see Fig. 2.6 on the preceding page). The depletion zone is marked as "n-" and the p-type zone is shown as "Ap+". The p-type zone is capacitively coupled to an aluminum "pickup pad" through a 0.2 μm layer of Oxide-Nitride-Oxide (ONO) (yellow) [205]. The "pickup pad" is isolated (by a thick 1.2 μm layer of ONO) from the metal "Signal lines", carrying signals from one column of pads to a readout electronics chip at the edge of a silicon sensor (of course, the pickup pad is not isolated from its own signal line). The isolation of pickup pads from the signal lines is needed to minimize capacitive coupling of the pads to the lines carrying signals from other pads. Not more than 3% of defective pads per sensor were allowed during tests of silicon detectors. The readout electronics was chosen to allow a very wide range of values from each pad (ionization charge up to 100 MIP). As a final note, in practice the p-n junctions are produced by doping the whole volume of a pad with arsenic to produce an n-type semiconductor, and then doping the intended p-type region with even higher concentration of boron.

Calibration. Before signals from any silicon sensor could be used for a data analysis, they need to be calibrated. In the ideal situation, when no particle traverses a pad (also

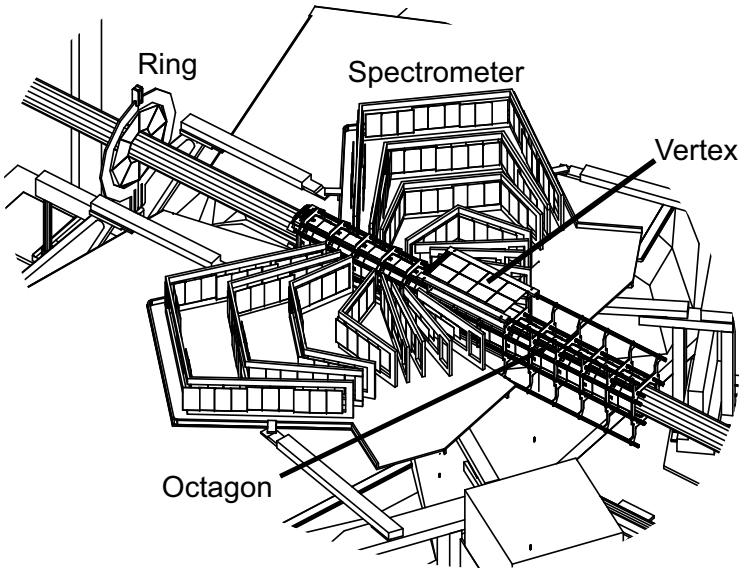

Figure 2.7.: The layout of the PHOBOS silicon detectors near the nominal interaction point [214]. Only one "Ring" detector at $z = +1$ m is shown (other ring detectors were positioned at $z = -1$ m, $z = \pm 2$ m, and $z = \pm 4$ m). Data from ring detectors were not used in this thesis.

called a *channel*) of a silicon detector, the signal detected from the pad should be zero. However, due to a presence of a leakage current and due to a noise in the readout electronics, even in the absence of any external influence, every channel produces a signal, which has a shape of a Gaussian with nonvanishing mean and width. The mean value of the signal is called the *pedestal* of the channel, while the width of the signal distribution is called the *noise* of the channel. The values of the pedestal and of the noise of every silicon channel were measured periodically during the process of taking data. The pedestal value was subtracted during an offline data analysis from all the signals detected from a pad. The typical noise value was taken into account during the hit reconstruction (see sections 4.2 on page 74 and 4.3.1 on page 75) in the silicon detectors by requiring that any detected signal from a pad used to create a hit to be significantly higher than the noise level (after pedestal subtraction). An other correction, that was made to the silicon signals, was due to so called *Common Mode Noise (CMN)*, which is a shift of the signal values in all the channels of the same sensor readout chip caused by a cross talk between different pads. The CMN correction was assigned as a constant value, which was determined separately for every event from the shift from zero of the lowest energy peak in the pedestal subtracted signal values distribution.

Silicon detectors, data from which were used for the measurements performed in this thesis, are described below. Their general layout is shown on Fig. 2.7. More information about PHOBOS silicon detectors can be found in Ref. [205, 213, 215–218].

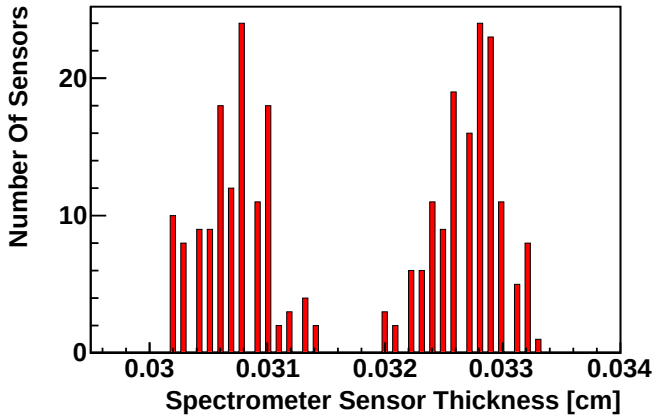

Figure 2.8.: Thicknesses of the PHOBOS spectrometer detectors.

2.2.5.1. Vertex Detectors

The goal of the vertex detectors was to determine the position of an hadron collision vertex in the range -10 cm $\leq v_z \leq +10$ cm with a high precision ($\sigma_{vz} \sim 50-200$ µm [205, 217]) during an offline analysis. They consist of 2 layer of silicon sensors centered above the PHOBOS nominal interaction point, and two such layers are located below it (see Fig. 2.9 on the next page and Fig. 2.7 on the facing page). The layers closer to the beam pipe (the distance to the beam line is 56 mm) consist of 4 sensors ($4_x \times 128_z$ pads each, pad size 0.473 mm × 12.035 mm) and have $|\eta| < 1.54$ coverage at $z = 0$. The layers further from it (the distance to the beam line is 118 mm) consist of 8 sensors ($2_x \times 128_z$ pads each, pad size 0.473 mm × 24.070 mm) and have $|\eta| < 0.92$ coverage at $z = 0$. The azimuthal angle acceptance of both layers is $|\Delta\varphi| < 42.7°$.

2.2.5.2. Octagon Detectors

The primary purpose of the octagon detectors (also called just *octagon*) was to measure the (total and as a function of pseudorapidity) multiplicity of particles produced in an hadron collision. In addition, they were used for studies of 2-particle angular correlations and of magnitude and fluctuations of elliptic flow. However, the only usage of the octagon in this thesis was to determine the centrality of Cu+Cu collisions at $\sqrt{s_{\mathrm{NN}}}$=200 GeV employing the total deposited energy (by charged particles produced in the collisions) in the detectors (see section 4.5 on page 79).

The detectors were composed of 92 silicon sensors positioned on the faces of an octagon shaped (when viewed along the beam line) 1.10 m long barrel centered around $z = 0$ (see Fig. 2.7 on the facing page and Fig. 2.9 on the next page) [197]. The distance between the opposite faces of the barrel was 90 mm. Each sensor had size of 84_z mm × 36_{xy} mm and was subdivided into $30_z \times 4_{xy}$ pads. The octagon acceptance when viewed from the nominal collision point was $|\eta|$<3.1. The overall geometrical acceptance of the octagon was 50% (the detected fraction of all the produced primary charged parti-

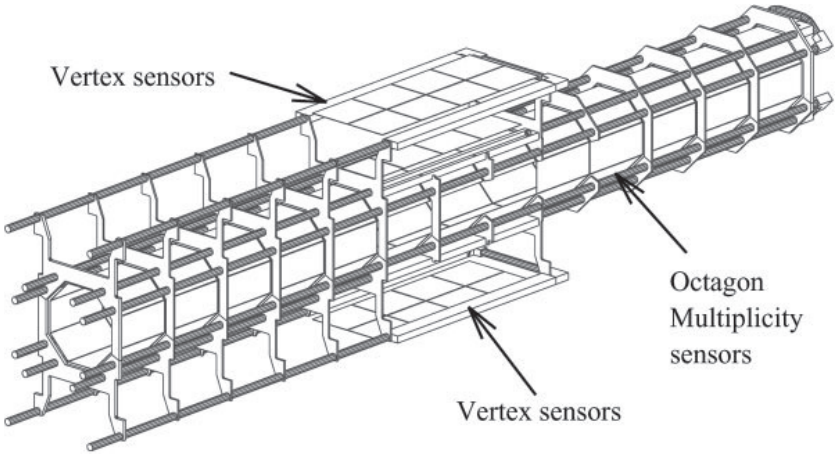

Figure 2.9.: The layout of the PHOBOS vertex and octagon detectors [217].

cles) [219]. Octagon sensors facing the vertex and the spectrometer detectors around $z = 0$ were removed to provide an unobstructed path for particles to the detectors. The fraction of the active area of the octagon detectors (not including the removed sensors) was 89% of the total area. The sensors were mounted on a light aluminum frame, part of which was made of aluminum tubes, through which chilled water was delivered for cool down the readout electronics of the sensors. The frame design goal was to minimize the amount of material through which particles produced in a collision had to traverse thereby undergoing multiple scattering and producing secondary particles. The achieved signal-to-noise ratio in the octagon sensors pads was ∼13:1 [218].

2.2.5.3. Spectrometer

The goal of the PHOBOS spectrometer was to measure with a high precision momentum of the charged particles produced in an hadron collision. The two integral parts of the spectrometer are

- two arms of silicon sensors which were used to locate a set of points on the particle trajectories and to measure the energy lost by the particles in a known amount of material,
- a magnet which was used to bend the paths of the particles by a magnitude depending on their total momenta according to the Lorentz law.

Information about the path of a particle in a known magnetic field allows to determine its momentum. And addition of data on the energy lost by the particle in silicon sensors permits to identify the particle kind (see chapter 5 on page 89).

Spectrometer Sensors The silicon sensors of the PHOBOS spectrometer were arranged in two symmetric with respect to the beam line sets (called *arms*), each of which

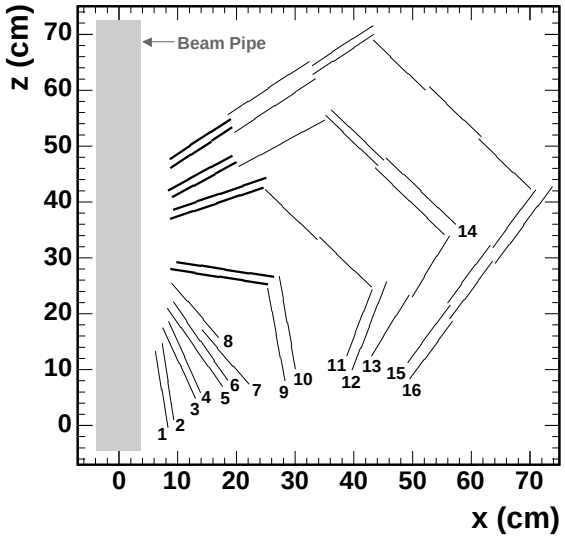

Figure 2.10.: Location of sensors in one arm of the PHOBOS spectrometer. Layer numbers are denoted as referenced in text. Type 3 (see Table 2.1) sensors are shown with thick lines. This figure was adopted from Ref. [212].

consisted of 137 sensors organized into 16 ribbons (called *layers*, see Fig. 2.10). The pattern of the sensor layers positions resembled somewhat legs of a spider having the octagon as its body (see Fig. 2.7 on page 58). Five different sensor designs (see Table 2.1 on the next page) were employed with smaller sensor and pad sizes located closer to the beam pipe and to the nominal interaction point, and the goal of that was to adjust the pad sizes according to the expected relative particle occupancy. The pad sizes are also much smaller in the horizontal direction than along the y-axis since

1. the azimuthal angle acceptance of the PHOBOS spectrometer ($|\Delta\varphi| \lesssim 0.2$ around $\varphi = 0, \pi$) is very small, and therefore a particle has to move essentially in the horizontal plane in order to hit enough sensors to be reconstructable,

2. the PHOBOS magnet produces an almost vertical magnetic field, and therefore the trajectory of a particle mostly has curvature only in the horizontal plane.

Consequently, the momentum of particles could be reconstructed more precisely with finer segmentation of the sensors in the horizontal direction, while the segmentation in the vertical direction only alleviates occupancy of the sensors and provides some information on the azimuthal angle of the particle momentum. While the later is important for studies of particle decays, like the one performed in this thesis, many more measurements performed at PHOBOS only required the knowledge of the transverse momentum of single particles. Therefore, it was decided to reduce the cost of sensors by reducing the vertical segmentation of the spectrometer sensors.

Just as in the octagon, the sensors were mounted on a light weight aluminum frames, with parts of the frames being aluminum tubes circulating water to chill the sensors

Sensor Type	Number of Pads (horiz.×vert.)	Pad Size (mm×mm)	Sensor Placement (layers)
1	70×22	1.000×1.0	1-4
2	100×5	0.427×6.0	5-8
3	64×8	0.667×7.5	9-16, near beam
4	64×4	0.667×15.0	9-12
5	64×4	0.667×19.0	13-16

Table 2.1.: Parameters of PHOBOS spectrometer silicon sensors. Layer numbers are shown on Fig. 2.10 (this table was adopted from Ref. [212]).

readout chips. And again, the goal was to minimize the amount of material in the spectrometer, thereby minimizing multiple scattering and secondary particle production. The frames were mounted on non-conductive carbon-epoxy carrier plates to avoid induction in the plates of eddy currents due to variations in time of the magnetic field or due to vibrations of the plates [197]. The currents would cause strong vibrations of the plates rendering the geometrical sensor positions to be poorly defined. To even further minimize the influence of mechanical vibrations of the magnet on the sensor positions, the carrier plates were supported at 3 points which were not connected mechanically to the spectrometer magnet. With the employed design the sensor positions were known to withing 300 μm. All the spectrometer sensors were placed in a light (to avoid damage to the sensors due to an overload caused by bright light) and air tight enclosure which was continuously flushed with dry nitrogen to ensure the relative humidity of the sensors environment below 10%. The achieved signal-to-background ratio of the sensors was about 18:1 [218].

Magnet The PHOBOS magnet is a room temperature double dipole 45 tonne magnet (see Fig. 2.11 on the facing page), powered by a 115 VDC at 3600 A 342 kW power supply. The distance between the poles of the magnet, where the PHOBOS spectrometer was located, was 158 mm with magnet power off. The two dipoles of the magnet were positioned such that both spectrometer arm plus a magnet dipole combinations were symmetric with respect to the beam line. The maximum magnetic field provided by the magnet was 2.18 T [197]. The exact direction and magnitude of the magnetic field were measured with a precision of $< 0.7\%$ at 15,120 different points and were saved into a file. The geometrical location of each such point was determined with a precision of 150 μm. Three-dimensional linear interpolation was used to estimate the magnetic field vectors in between the points, resulting in the magnetic field map shown on Fig 2.12 on page 64. The PHOBOS magnet was used in 3 different settings: *at the positive and negative polarities* and in the off-state. The difference between the positive and negative polarities was that the direction of the current supplied to the magnet coils was reversed. The magnetic field map was saved only at the positive polarity and it was assumed that at the negative polarity the magnetic field vectors could be found by negating (i.e. mul-

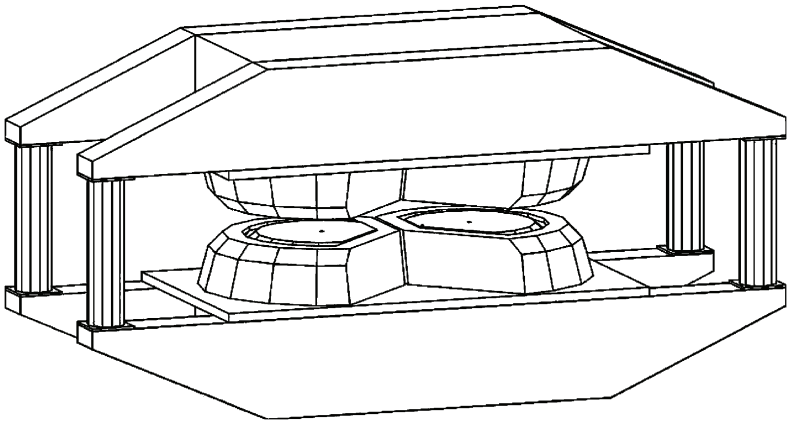

Figure 2.11.: The PHOBOS magnet and its supporting structure. This figure was adopted from Ref. [197].

tiplying by -1) the corresponding vectors at the positive polarity. During the real data taking, the polarity of the PHOBOS magnet was periodically reversed with the goal of having a way to estimate the systematic uncertainties due to an imperfect knowledge of the magnetic field in the PHOBOS detector.

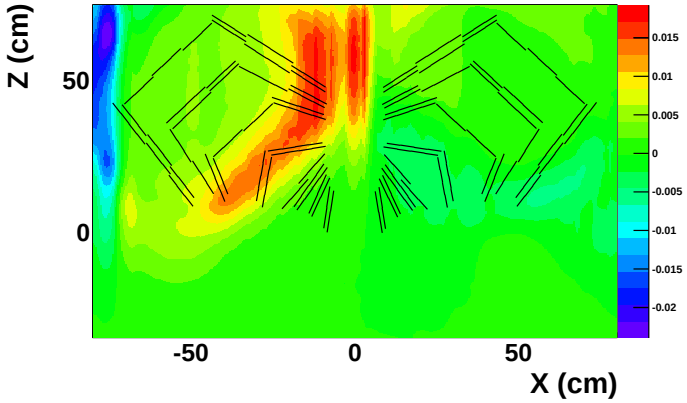

(a) Map of B_x

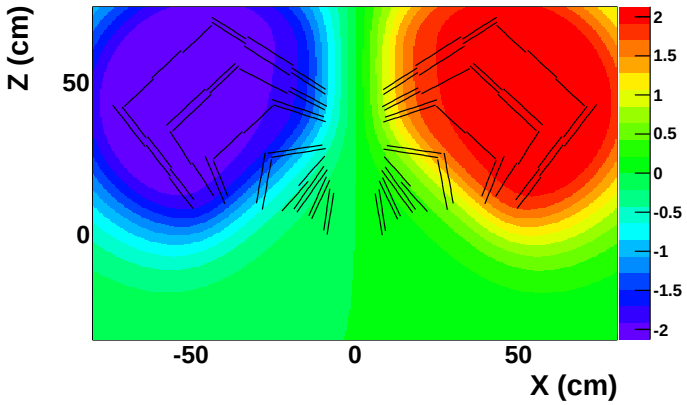

(b) Map of B_y

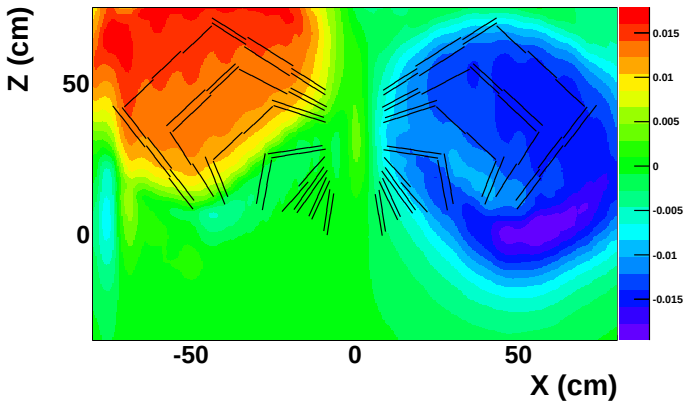

(c) Map of B_z

Figure 2.12.: Map of the PHOBOS magnetic field components in the $y = 0$ plane: (a) B_x, (b) B_y, (c) B_z. The ranges of x and z coordinates are the same as on Fig. 2.10 on page 61 except that the lower bound of the z values was decreased from -7 cm to -35 cm. The magnetic field is measured in Tesla. See section 2.2.5.3 for details.

3. Computing Architecture

3.1. Computing Facility And Software

Most of the computing work performed for the experimental data analysis described in this thesis was done on the dedicated for the PHOBOS experiment part of the RHIC and ATLAS Computing Facility (RACF) at BNL, which consisted of:

- 26 nodes with 16 Gb of Random Access Memory (RAM) and 8 Intel Xeon E5335 CPU cores at 2.00 GHz per node,

- 7 nodes with 16 Gb of RAM and 8 Intel Xeon E5440 CPU cores at 2.83 GHz per node.

In addition, one could use the nodes dedicated to other RHIC experiments as well as those of A Toroidal LHC ApparatuS (ATLAS) at the times when they were idle.

The total time needed to perform the data analysis with such computing resources is estimated at 1.5-2.0 years (after all the analysis algorithms have been developed), of which 8 months were required to perform the particle reconstruction in the used data events (about 4 months for the vertex range $v_z \in [-5,+15]$ cm and about 4 months for the vertex range $v_z \in [-25,-5]$ cm), about 2 months were needed to create the covariance matrices used in the particle reconstruction, a few months were needed to simulate single kaon events to fill efficient enough Hough tables which were also used for the particle reconstruction, with the rest of the time spent for doing various corrections on the raw reconstruction results, running the event mixing algorithm, and making the estimations of the systematic uncertainties.

The data analysis algorithms were designed based on the PHOBOS Analysis Toolkit (also called PHAT, developed by the members of the PHOBOS collaboration), which in turn used extensively the libraries of ROOT [1] (version 5.08/00b). Estimated ∼500,000 lines of new C++ code were written to implement the algorithms of the data analysis described in this thesis. The computing jobs were either run locally on some of the PHOBOS nodes or were submitted to Condor [2], which was installed on all the RACF computers.

[1] http://root.cern.ch

[2] http://research.cs.wisc.edu/condor/

3.2. Parallel Information Processing

This section provides a brief description of a Parallel Information Processing (PIP) system, which was implemented in the beginning of the work on this thesis to optimize some specific data analysis tasks. The situations in which the system provides dramatic advantages over a simple submission of independent computing jobs into some batch job management system (i.e. Condor in our case) are the following:

- If the computing tasks, which need to be performed on different computers, are correlated in such a way that it is impossible to split beforehand the overall computing problem into independent computing jobs. One example of such situation, which was relevant for this thesis, is the implemented event mixing algorithm (see section 6.1.2.4 on page 144), since properties of each new batch of event mixing tasks in the algorithm depended on the overall result of all of the previous tasks and the generation of background entries continued until some specific conditions were satisfied.

- If the overall computing job requires generation of some random entities out of which only a small fraction will be useful in the end. In such case, if the results of each independent computing job are saved on disk before the final selection of needed results, the amount of disk space required could absolutely unfeasible. Moreover, the need to write the results to disk would dramatically slow down the overall process, and writing of large amounts of data simultaneously by multiple jobs increases the risk of hard drive failure and of consequent data loss. Again, the event mixing algorithm implemented for this thesis is a good example of such situation since, by the end of an event mixing job, almost all of the randomly combined pairs of tracks do not satisfy the algorithm requirements and have to be discarded.

- If 1) it is impossible to predict in advance the computing time required to execute each individual task out of a list of such tasks, 2) the time varies dramatically between different tasks, and 3) the tasks requiring large computing resources are organized into random groups on the list. If the list of tasks is simply split into equal size sub-lists, which are submitted as individual computing jobs, then most of the jobs would finish quickly while a few "unlucky" jobs, which got sub-lists composed of (almost) solely of the slowest tasks, would run for a very long time even while there are free computing resources which could be used to aid them. One example of exactly such situation, that was relevant for this thesis, was the generation of the covariance matrices (see section 5.10.4.1 on page 128), which were used for the particle reconstruction. Most of the matrices corresponded to phase space regions outside of the PHOBOS spectrometer acceptance requiring small amount of computing resources to figure that out and to ignore the regions. The regions within the acceptance tend to be near each other, and it is unfeasible to predict the exact shape of the acceptance for any given layer pattern (see section 5.3 on page 98) for which the matrices had to be created. The regions near the

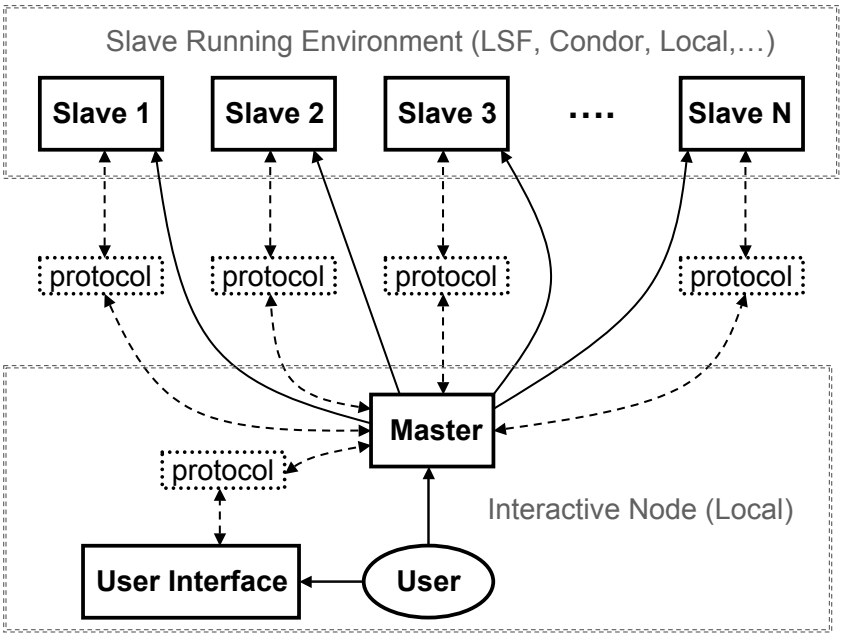

Figure 3.1.: Implementation of the PIP system. Legend: rectangular solid-line boxes represent programs, rectangular double-dashed-line boxes represent environments in which the programs run, the dashed-line double-arrows represent directions in which messages are sent between programs (all the communication is done through a special "protocol" denoted as dotted-line boxes), and if an entity can start a program then a solid-line arrow points from the entity to the program on the diagram. See section 3.2.1 for details.

edge of the detector acceptance are the one which require most of the computing time. Using the PIP system allowed to only give one smallest task (generation of a covariance matrix corresponding to a single phase space bin) to one CPU core at a time, which in tern allowed to utilize all of the available computing resources at (almost) all times thereby not allowing to slow down the whole process by an order of magnitude by a few slow jobs.

3.2.1. Implementation

Implementation of the PIP system is shown schematically on Fig. 3.1. The code implementing the system is independent of a type of processed data and of a kind of analysis performed. For any new type of data one just needs to implement a special class derived from the base class *DataHandler*. Only one specific data-handler class was implemented during the work on this thesis, namely the one which uses ROOT *TTree* objects as data, since an entry of a TTree could a set of numbers, arrays, strings or event objects, and so can be used to describe input and output of an analysis of (pretty much) any complexity. Moreover, the splitting of a TTree into entries is a natural representa-

tion of a list of tasks, which could be divided into sub-lists for a parallel processing on a large number of computers.

The programs, which do the actual processing of lists of tasks, are called *slaves*. In the PIP system the slaves can run in different environments. For any new environment one just needs to implement a special class (a *slave manager*) derived from the base class *NetworkSlaveManagerBase*, which could be done within only a few hours making migration of the system to a new setting very easy. During the work on this thesis, three different slave managers were implemented, namely those which allow to run slaves 1) in Load Sharing Facility (LSF) [3], 2) in Condor, 3) locally (even if an analysis is done locally, the PIP system allows to speed it up greatly, since modern CPUs have multiple cores, which could be all used in parallel; for example, the dedicated PHOBOS nodes have 8 CPU cores each). The slaves could be of two types: independent compiled programs or ROOT macros. To implement a new kind of slave one needs to create a class derived from the base class *NetworkSlave* and implement the following two of its functions: *Initialization* (which determines how to initialize a slave object before it can start processing any tasks) and *Analyze* (which determines what to do with each particular task) [4].

The program, which does all the communication with the slave programs as well as the scheduling of which list of tasks is assigned to which slave, is called *master* [5]. The master implementation is general and does not require any modifications by a user. The user only needs to prepare the overall list of tasks to be processed by the slaves, specify which type of slaves and how many of them need to be created, and then just call the *Analyze* function of the master code. All the communication between the master and the slaves is done through an Internet connection, including sending tasks descriptions to the slaves and receiving the results back. Upon being received by the master, the results are merged in the same order in which their corresponding tasks were provided to the master. It can be chosen whether the slaves should be released after all the tasks assigned to them are complete, and so if multiple lists of tasks need to be analyzed with each list composed based on the results created from the previous lists (as it was the case in the event mixing algorithm), the slaves could be held on standby and ready to receive the next bunch of tasks at any time, eliminating the need to resubmit and to reinitialize the slaves. The master algorithm can also detect crashes of the slave programs, recreate the crashed slaves and to reassign the tasks of the crashed slaves to other slaves, making the data processing very robust. The master code does not require all the slaves to be ready before the data processing can begin, and as soon as at least one slave is available, the analysis starts and finishes successfully. The user can control some of the master parameters even for a running program through a special class *UserInterface*, which can connect to a running master and adjust its parameters or the number of used slaves, make the master to release the slaves and to abort the data processing, and so on.

[3] http://www.platform.com/workload-management/high-performance-computing

[4] One could also implement a function *FixMyself*, which fixes the internal state of a slave in case of a problem, but it is not required.

[5] Implemented as the *NetworkJobDistributor* class.

4. Event Characterization

4.1. Collision Triggers

Any experimental study of some physical process involves reading out some signals from physical detectors. Not all of those readings originate from the physical process under study, since detectors have inherited noise associated with them, and some of the readings might originate from other physical processes, which for a given study constitute "background". Therefore one often has to implement some mechanism to suppress background readings to an acceptable level in order to

- perform a good measurement by increasing its statistical significance
- limit the amount of information saved to storage
- make sure that the information transfer connection between the detectors and the storage as well as the storage writing capacity are not overloaded

For experiments performed on high energy particle colliders, the first and one of the most important steps is to determine if detector readings at any moment of time are produced by a collision of two accelerated particles each originating from the two counter-rotating beams. More details about triggering in the PHOBOS detector in addition to the discussion provided below can be found in Ref. [208].

4.1.1. RHIC Crossing-Clock Gate Triggering

The accelerator of heavy nuclei (RHIC , see section 2.1 on page 49), which supplied collisions for the PHOBOS detector, provided a so called *"crossing-clock gate"* signals, which were issued, when two beam bunches crossed in the PHOBOS detector interaction region. Presence of such a signal was required to consider the detector signals as being produced by a possible collision of two accelerated nuclei.

4.1.2. PHOBOS Detectors Triggering

After that a very fast readout from the following PHOBOS detectors was used to further differentiate accelerated nuclei collisions from the background:

- Paddle Counters – section 2.2.2 on page 52
- Zero Degree Calorimeters – section 2.2.3 on page 53
- T0 Counters – section 2.2.4 on page 55

4.1.2.1. Paddle Counters Triggering

Paddle counter detectors (see section 2.2.2 on page 52) were used as the primary trigger. The advantages of using the paddle counter for triggering are the fast readout time and the large phase space coverage. The trigger has an almost 100% efficiency for central and mid-central events (see Fig. 6.7 on page 152).

Minimum bias triggers. Paddle counters were used for implementing so called *Minimum Bias Triggers* the purpose of which was to record collision events with as large fraction of the total cross section as possible. The triggers only created a small bias (i.e. reduced efficiency) in the very peripheral events. The triggers were implemented by requiring the following conditions:

- *More than two scintillator slats are hit in each paddle array.* This trigger condition was used for high multiplicity collisions, i.e. Au+Au or Cu+Cu .
- *At least one scintillator slat is hit in each paddle array.* This trigger condition was used for low multiplicity collisions, i.e. p+p or p+Au, and as a cross check for the previous trigger condition.

Triggering against collisions with the beam gas. To prevent scattering, energy loss and disintegration of the accelerated nuclei, the accelerator beam pipes were kept under vacuum. Pressure was kept under 10^{-7} Torr for ion beams and under 10^{-6} Torr for proton beams [220] [1]. However some residual gas of molecules and electrons (called *beam gas*) remained [2]. Collision probability of an accelerated nucleus with the molecules was significant in comparison to the collision probability of the accelerated nuclei with each other, making the collisions with the beam gas a major source of background.

To trigger against the events with collisions with beam gas a selection was applied on the time (PdlTDiff) between the signals from the paddle counter detectors, which was required to be less than 5.0 ns, corresponding to selecting collision vertices with $|z| < 75$ cm. The distribution of the PdlTDiff variable is shown on Fig. 4.1 on the facing page. Since the two paddle counters are positioned at $z = \pm 3.21$ m (the distance between them is 6.42 m), if a collision with a beam gas particle occurs at $|z| > 3.21$ m and the momentum direction of the projectile nucleus is towards the counters, then the characteristic time between signals from the counters is 6.42 m / c = 21.4 ns, shown on the figure in yellow and blue. As can be seen, the applied cut on PdlTDiff makes sure that such collisions with beam gas are not recorded [3]. The remaining part of the distribution, shown in green, is a mixture of collisions:

[1] These numbers are the upper threshold limits set in 2001 RHIC run. The pressure strongly depends on the number of accelerated heavy ion bunches in RHIC and on the number of ions per bunch [221]. For example, in the 2000 RHIC run the pressure was kept under $10^{-11} - 10^{-10}$ Torr [222]. The pressure also depended on time and on the geometrical position of a RHIC sector.

[2] In the cold ($\sim$ 5 K) RHIC section 99% of the beam gas pressure is due to helium, while in the warm ($\sim$ 300 K) sections the pressure is created by H_2 ($\sim$ 90%), CO_2 ($\sim$ 5%), and CH_4 ($\sim$ 5%) [222].

[3] If the projectile nucleus momentum direction is away from the paddle counters, no signal is registered in the detectors and such a collision with beam gas is discarded automatically as well.

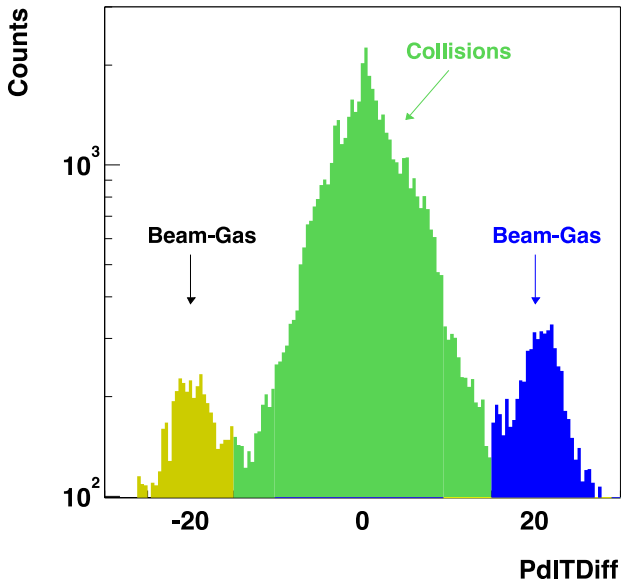

Figure 4.1.: Distribution of time (PdlTDiff) in ns between the signals from the paddle counter detectors [208]. Collisions with beam gas are shown yellow and blue with the characteristic time of 21.4 ns. Shown in green is the mixture of collisions: 1) of accelerated nuclei with each other, and 2) of accelerated nuclei with beam gas occurring in between the paddle counters. The distributions in time are due to 1) a distribution in angle of a collision product particles and the resulting distribution in time it takes for the scintillation light to reach the PMT, 2) a distribution in time it takes for electrons to go through the series of PMT dynodes. See section 4.1.2.1 on the preceding page for details.

1. of accelerated nuclei with each other, and

2. of accelerated nuclei with beam gas occurring in between the paddle counters.

To remove the later type of collisions with beam gas, signals from the ZDC detectors were used (see section 4.1.2.2).

4.1.2.2. ZDC Triggering

As it was discussed in section 2.2.3 on page 53, ZDC detectors were used to measure the total energy of the neutral beam fragments (mostly neutrons). The calorimeters also provided the timing information on the detected energy depositions.

The selection on the time of signals from the paddle counter detectors, discussed in section 4.1.2.1 on the preceding page, not only removed the beam gas collisions occurring outside of the z-coordinate region spanned by the paddle counters, but also restricted the positions of the any accepted collisions to a narrow (in comparison to the distance to the ZDC detectors) range ($|z| < 75$ cm) around the nominal interaction

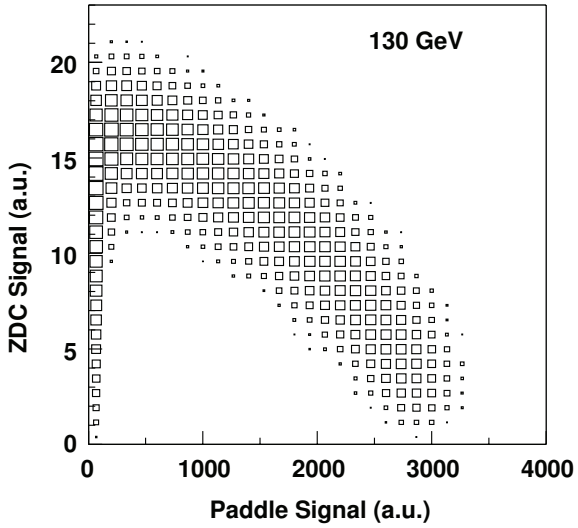

Figure 4.2.: An illustration of the correlation between the signals in the paddle counters and in the ZDC [205]. The sum of the two signal is constant, except for the very peripheral collisions, for which the collided nuclei do not get disintegrated completely, and neutrons not participating in the collisions stay bound inside charged beam fragments, get deviated by the RHIC dipole magnets, and therefore do not produce any signal in the ZDC. The figure was made from $\sqrt{s_{\mathrm{NN}}}$=130 GeV Au+Au collisions data. See section 4.1.2.2 on the previous page for details.

point. If a collision with beam gas occurs withing the range, then a deposition of energy is expected in only one of the ZDC in comparison to such deposition in both of the ZDC for real beam-beam collisions [4]. An exception to the last statement are the very central collisions, in which both of the collided nuclei get disintegrated almost completely leaving few neutral beam fragments (as so no or small signal in ZDC) but with very large energy depositions in the paddle counters (see Fig. 4.2). The time it takes for the neutral beam fragments to reach both ZDC from the nominal collision point is 18.5 m / c = 61.7 ns, hence one gets the selection on the time of the signals from both ZDC shown on Fig. 4.3 on the next page.

Taking into account the considerations just explained, the flow of the triggering decisions (all ZDC signals are used after removal of special *online trigger time calibration events* and after subtraction of the minimum signal produced by the detectors, called the *pedestals*) is shown on Fig. 4.4 on page 74.

As a final note, it is possible that a *double beam gas collision* occurs, which means that within a short time range simultaneously two different beam gas particles are struck by

[4] Collisions with beam gas are fixed target collisions and both the spectator beam fragments and the created particles are produced mostly in the projectile momentum direction. In case of beam-beam collisions the spectating beam fragments and the created particles are produced approximately symmetrically (along the z-axis) with respect to the collision point. The created particles are the ones which produce signals in the paddle counters.

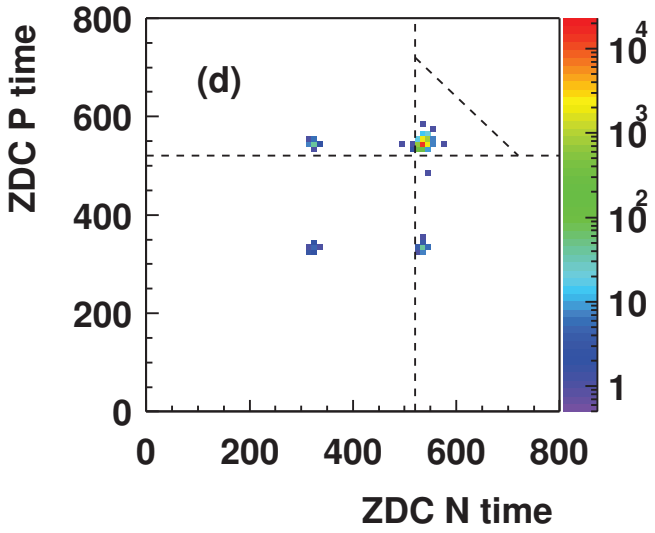

Figure 4.3.: The selected by the ZDC beam-beam collision events are within the triangle region [208]. The deviation of the average selected times from the nominal 61.7 ns is probably because it takes some time (∼10 ns) for signals to be produced in the paddle counters or the T0 counters which serve as a time=0 for the ZDC time measurements. See section 4.1.2.2 on page 71 for details.

two accelerated nuclei, each originating from the two counter-rotating RHIC beams. Such events are accepted by the collision trigger outlined above, provided that both of the collisions occur near the nominal collision point of the PHOBOS detector or just outside the paddle counter detectors on the z-axis (so that the ZDC signal times fall into the accepted time window and both of the paddle counters are struck within 5 ns from each other). However, studies showed that the double beam gas collisions are very rare at the RHIC operating conditions and contribute only about ∼0.2% to the total selected event sample. Moreover, a large fraction of the double beam gas collision events are further removed by the T0 detectors times selection (see section 4.1.2.3) and by the requirement of a successfully reconstructed collision vertex (see section 4.3 on page 75).

4.1.2.3. Time Zero Detector Triggering

As it was already pointed out in section 2.2.4 on page 55, T0 counters were used to provide a very fast estimate on the z-coordinate of a collision vertex (let us denote it as z_v) by measuring the arrival times of signals from both of the detectors. If t_1 and t_2 are such times as measured by the counters positioned at $z = +5.4$ cm $\equiv z_0$ and $z = -5.4$ cm $\equiv -z_0$ correspondingly, then $t_1 = (z_0 - z_v)/c$ and $t_2 = (z_v + z_0)/c$, and therefore $z_v = c(t_2 - t_1)/2$. For the RHIC data taking runs in 2004 and 2005, which includes the time period when the data used in this thesis were obtained, the PHOBOS trigger was set to select events only in the -40 cm $\leq v_z \leq +20$ cm interval.

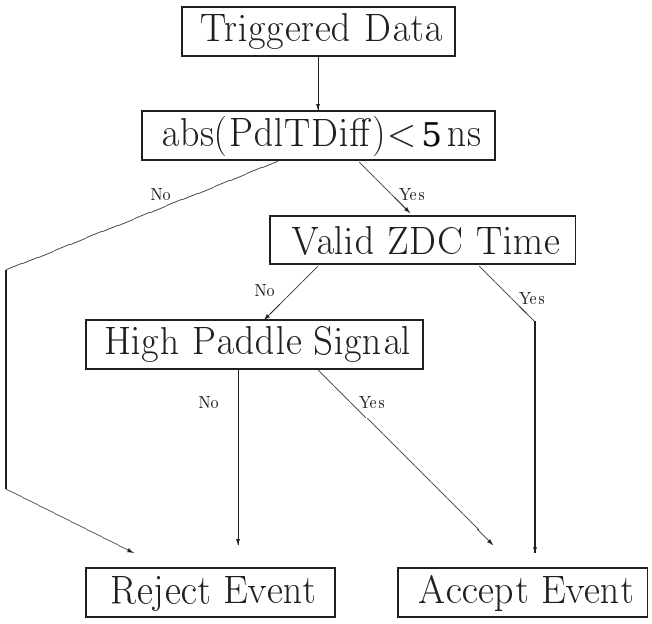

Figure 4.4.: The sequence of the triggering decisions applied on events accepted by the minimum bias trigger (see section 4.1.2.1 on page 70) using the signals from the paddle counters and the ZDC detectors [208]. See section 4.1.2.2 on page 71 for details.

4.2. Hit Reconstruction

A *hit* is by definition an information on the position and the energy loss of a particle in a detector. This section describes the algorithm of hits reconstruction in the spectrometer and the vertex detectors. The hits were used to reconstruct a OneTrackVertex (see section 4.3.2 on page 77) as well as particle trajectories of an event (see chapter 5 on page 89).

The idea of a hit reconstruction is based on the fact that some of the particles produced in a RHIC collision intersect the PHOBOS silicon sensors at a small angle thereby losing energy and producing signals in multiple pads of a silicon sensor, so to reconstruct a hit one needs to add the energy losses in the pads and to reconstruct an average point of intersection of the particle trajectory with the sensor.

Hits were reconstructed in each silicon sensor separately, which means that no two pad signals in different sensors were used to create the same hit. At the first step, all the signals in defective sensor pads were removed from consideration. A pad was considered to be defective if it always produced a zero signal, or always produced a high signal, or had a high noise level. Then, all the pad signals below a noise threshold of $0.15\Delta E_{MIP}$ were removed from consideration as well, where ΔE_{MIP} is the average energy loss in a silicon sensor by a MIP particle at normal incidence. Even though the silicon sensors had somewhat different thicknesses (for spectrometer sensors see Fig. 2.8 on page 59), the ΔE_{MIP} was set to a fixed number of 80 keV. Adding (also called *merging*) of pads

energy losses was only done in pad columns (i.e. along the direction of a finer sensor segmentation) but not in rows. The merging process starts from an edge of a sensor looking for a pad with a signal above the noise threshold. Once such a pad is found, the signals in the subsequent pads are added to the pad signals if they pass the noise threshold cut as well. The merging finishes in one of the following cases:

- the maximum allowed number (equal to 8) of merged pad signals is reached,
- the opposite edge of the sensor is reached,
- a pad removed from consideration is reached.

A hit is created from the merged signals if the total deposited energy of the signals is above the threshold of $0.4\Delta E_{MIP}$ for vertex detectors sensors and of $0.5\Delta E_{MIP}$ for spectrometer sensors. The hit position is the pad signal weighted average of the merged pads positions.

4.3. Vertex Reconstruction

The *vertex* of an event is the geometrical position of the studied nuclear collision. This section describes the two vertex reconstruction algorithms which were used for the data analysis in this thesis.

4.3.1. OctProbMultVertex

The algorithm of OctProbMultVertex reconstruction is summarized briefly below, while a more detailed description can be found in Ref. [219].

The algorithm uses its own definition of hits in the octagon detector and therefore starts with the raw silicon sensors signals. First, all such signals below a threshold of $0.4\Delta E_{MIP}$ (about 3 times the noise level) are removed, where ΔE_{MIP} is the average energy loss in an octagon sensor by a MIP particle at normal incidence. A hit is created either from an isolated single pad signal or from signals in neighboring along the beam direction pads if the total energy loss of the resulting hit exceeds $0.6\Delta E_{MIP}$. For a multiple pad hit it is in addition required that the signals in all the non-boundary pads are greater than 40% of the signal, which would have been produced in the pads by a MIP particle with an angle on incidence compatible with the geometrical size of the hit.

The idea of OctProbMultVertex vertex reconstruction can be summarized as follows. The average energy lost by a charged particle in some material increases with the distance traveled by the particle in the material. A particle hits an octagon silicon sensor at an incident angle, which depends on the distance from the event vertex to the hit point, and since the average path (and therefore the average energy loss) of the particle inside the sensor is determined by the angle, by measuring the energy loss of the particle in the sensor material one could find out the corresponding average distance from the hit point to the event vertex.

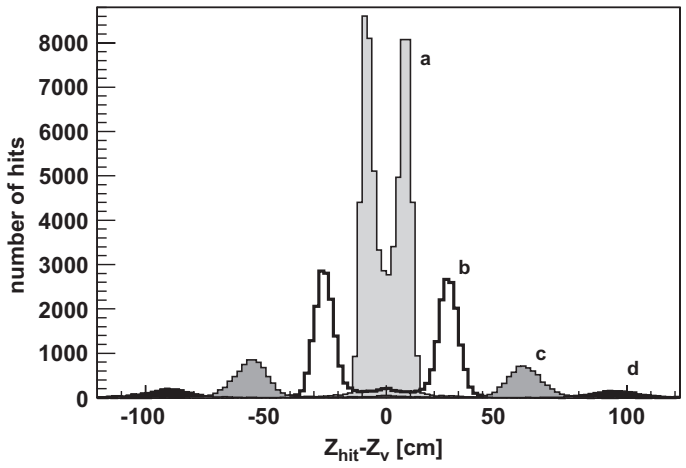

Figure 4.5.: Examples of histograms used in the OctProbMultVertex reconstruction algorithm to estimate the distance from a hit to the collision vertex [219]. Histograms a, b, c, and d correspond to hit energy losses of 2.5, 6, 12, and 25 units of ΔE_{MIP} correspondingly. See section 4.3.1 on the preceding page for details.

The implementation of the reconstruction idea was the following. First, distributions of charged particles hit energy losses in the octagon as a function of $|Z_{hit} - Z_v|$ were studied using GEANT - Detector Description and Simulation Tool (GEANT) [223] simulations (without any detector effects), where Z_{hit} and Z_v are the z-coordinates of a hit and of an event vertex correspondingly. Such distributions were summarized as a set of histograms (one histogram per small energy loss range) similar to those shown on Fig. 4.5. The histograms were properly normalized and parametrized. The z-coordinate of a reconstructed OctProbMultVertex was found using the maximum likelihood method, i.e. a number of different z values were tried, for each of those values a likelihood function was calculated, and the vertex z-coordinate was assigned as the value for which the function is maximized. The likelihood function was the product of the histograms parametrizations calculated for every hit in the octagon, except that if any such parametrization yielded value F smaller than the probability $P_{min} = 0.05$, then P_{min} was used instead of F in the product.

The OctProbMultVertex reconstruction procedure described above resulted in systematically shifted vertex z-coordinates. The shifts were studied again using GEANT simulations as a function of the vertex position and used to correct the reconstructed vertex z-coordinates.

The resolution of the overall OctProbMultVertex reconstruction algorithm is shown on Fig. 4.6 on the facing page as a function of centrality.

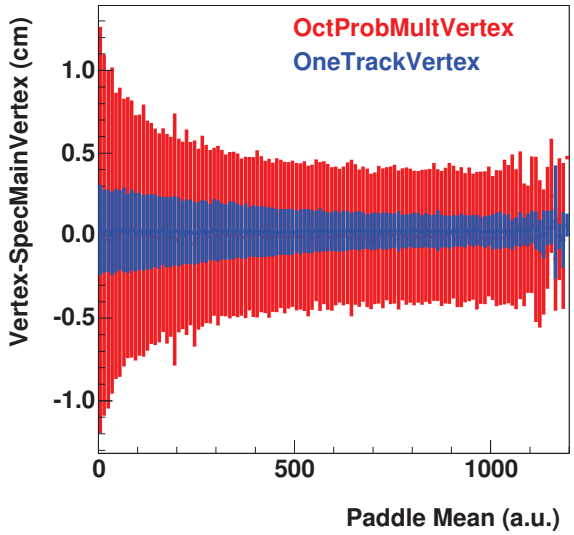

Figure 4.6.: Reconstruction precisions of OneTrackVertex (≈0.13 cm on average) and OctProbMultVertex (≈0.6 cm on average) vertices estimated with respect to the SpecMainVertex of the same event [208]. Regardless of the nature of the SpecMainVertex reconstruction algorithm, the above numbers provide upper limits on the reconstruction precisions of the vertexing algorithms used in this thesis. The efficiencies of the OneTrackVertex and of the OctProbMultVertex reconstruction in Minimum Bias events (see section 4.1.2.1 on page 70) are ∼77% and ∼80% correspondingly. The vertex z-coordinate was restricted to $|z| \leq 10$ cm to make this figure, and to calculate the reconstruction precisions and the efficiencies. It is worth mentioning however that Ref. [219] cites a different average efficiency of the OctProbMultVertex vertex reconstruction, i.e. 90.5% for vertex z-coordinates in the $|z| \leq 60$ cm range. See section 4.3 on page 75 for details.

4.3.2. OneTrackVertex

The reconstruction of OneTrackVertex starts with collecting of hits in the following pairs of silicon layers (see Fig. 2.9 on page 60 and Fig. 2.10 on page 61):

- the 1st and the 2nd layers in the positive spectrometer arm,
- the 1st and the 2nd layers in the negative spectrometer arm,
- the 1st and the 2nd layers of the vertex detectors above the beam pipe,
- the 1st and the 2nd layers of the vertex detectors below the beam pipe,

where for the vertex detectors the 1st layer is the one closer to the beam pipe and the 2nd layer is the one further from it. For each pair of layers the collecting of hits starts from the 1st layer and then goes on in the 2nd layer [5].

[5] with the limitation that not more than 99 hits are collected in total per layer pair

The next step is to loop through all the hits in the 1st and the 2nd layers of each layer pair, draw a straight line through each two hits in different layers within the pair, and find the intersection (let us call it a *vertex candidate*) of each such line with the (y,z) plane for spectrometer layers and with the (x,z) plane for vertex detector layers [6]. Only vertex candidates with $|x| \leq 1$ cm and $|y| \leq 1$ cm are retained.

After that, all the vertex candidates made from the two spectrometer layer pairs are grouped. As well, all the vertex candidates made from the two vertex detector layer pairs are grouped. So, now there are two groups of vertex candidates. Each such group is used to create a separate vertex (called *OneTrackSpecVtx* and *OneTrackVtxVtx* for spectrometer and vertex detectors groups correspondingly) the following way: for each vertex candidate (let us call it V) it is counted how many other vertex candidates there are within the same group not further than 1 cm away from V along the z-axis (let us call S the set of such other vertex candidates plus V, so there is such a set S for every V), and the vertex z-coordinate is assigned as the average z-coordinate of all the vertex candidates in the largest found set S. A vertex created this way is considered to be valid if its $|z| < 100$ cm. The x- and y-coordinates of the vertices are assigned to be zero.

At the last step, it was required that the event already has an OctProbMultVertex (see section 4.3.1 on page 75), and a valid OneTrackSpecVtx or OneTrackVtxVtx (let us call them V_o, V_1, and V_2 correspondingly). If only one of V_1 or V_2 is valid, let us say for the sake of definiteness it is V_1 (the situation for V_2 is analogous), then a valid OneTrackVertex with z-coordinate equal to V_{1Z} is created if and only if $|V_{1Z} - V_{oZ}| < 3$ cm. If both V_1 and V_2 are valid, then it is attempted to create a valid OneTrackVertex (using the same procedure as the one just described) first from V_1, and then from V_2.

The resulting resolution of this vertexing algorithm is shown on Fig. 4.6 on the preceding page.

4.4. Event Selection

The *event selection* discussed here is the set of all conditions imposed on the PHOBOS detector readouts to select only those which corresponded to collisions of two Cu nuclei each originating from a different of the two counter-rotating beams accelerated by RHIC (see section 4.5 on the next page for a detailed definition of a collision). In addition to the conditions imposed by the PHOBOS trigger (see section 4.1 on page 69), the event selection required the following:

- Successfully reconstructed OctProbMultVertex and OneTrackVertex (see section 4.3 on page 75) with the OneTrackVertex being in ranges $[-5,+15]$ cm and $[-25,-5]$ cm for the intermediate ($p_T > 0.39$ GeV/c) and the lowest ($p_T < 0.13$ GeV/c) transverse momentum measurements of the ϕ meson invariant yield correspondingly.
- Events, which were triggered less than 0.5 μs after or 5 μs before an other event, are called *post-pile-up* and *pre-pile-up* correspondingly. Such events were removed from the data analysis.

[6] Only the first 995 such lines are considered.

- A *good L1 timing* of an event means that enough time has past since the preceding event rejected by the PHOBOS trigger to clear all the trigger signals from the readout electronics, which is necessary to make sure that a trigger decision on the current event is not effected by the detector signals produced during the previous event. Only events with a good L1 timing were selected for the data analysis.

- The special *heartbeat* (periodic readouts from all the PHOBOS detectors) and *time calibrator* (designed to calibrate the relative timing delays between different detector channels) events were (of course) not included into the data used for analysis.

The Cu+Cu collision events at $\sqrt{s_{\rm NN}}$=200 GeV used for the data analysis performed in this thesis were recorded by the PHOBOS detector during Run-5 of the RHIC operation, which started on November 23, 2004 and finished on March 7, 2005 [194, 224]. The total number of events passing the event selection and therefore analyzed for this was:

- 77,860,764 : positive magnet polarity, OneTrackVertex in the range $[-5,+15]$ cm,

- 68,267,807 : negative magnet polarity, OneTrackVertex in the range $[-5,+15]$ cm,

- 44,763,144 : positive magnet polarity, OneTrackVertex in the range $[-25,-5]$ cm,

- 42,411,924 : negative magnet polarity, OneTrackVertex in the range $[-25,-5]$ cm.

4.5. Centrality Determination

The *centrality* of a nucleus-nucleus collision is a measure of how many nucleons from each of the two collided nuclei *participated* (or got *wounded*) in the collision. A nucleon *participated* in the collision if it interacted inelastically with an other nucleon from a moving in the opposite direction nucleus, and both such nucleons are called *participants*. The nucleons, which did not participate in the collision, are called *spectators*. See Fig. 4.7 on the following page for an illustration. It is clear that the shorter is the distance (called the *impact parameter*) between the centers of the two collided nuclei in the plane transverse to the collision axis, the higher is the mean number of participants, therefore on average centrality is also a measure of the impact parameter [7].

Alternatively, *centrality* could be defined as a measure of the overall ($N_{\rm ch}$) or at a given value of pseudorapidity ($dN_{\rm ch}/dy$) multiplicity of particles produced in a heavy ion collision. This definition is more relevant for the experimental determination of centrality and would be equivalent to the one given in the previous paragraph if the particle multiplicity was a well defined monotonic function of the number of participants (denoted further as $N_{\rm part}$). The measurements show that the average of both $N_{\rm ch}$ and $dN_{\rm ch}/dy|_{y\approx 0}$ increase with $N_{\rm part}$ [132]. However, since the multiplicities fluctuate at any given $N_{\rm part}$ value, the centrality of a collision depends on how the notion of centrality is defined,

[7] Hence the name centrality, since it a measure of the minimal distance between the centers of the two collided nuclei.

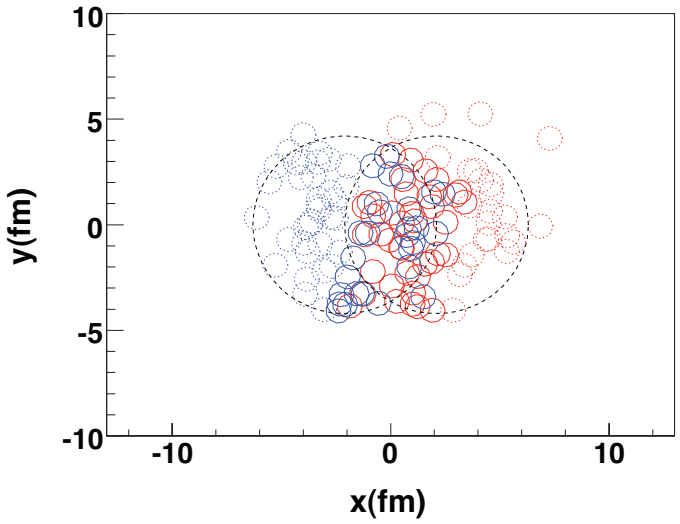

Figure 4.7.: A schematic transverse plane view of a Cu+Cu collision [225]. Nucleons from each of the two collided nuclei, moving in the opposite directions along the z-axis, are shown in red and blue. Nucleons participating in the collision are shown as solid line circles, while the spectators are shown as dotted line circles. The area of the circles is equal to the nucleon-nucleon inelastic cross-section at the collision energy. See section 4.5 on the previous page for details.

and the larger are the fluctuations, the stronger the dependence is. As it was already pointed out above, in the limiting case of no fluctuations, both definitions are equivalent, but in the case of very large fluctuations the two definitions yield uncorrelated quantitative measures of centrality. Other definitions of centrality could be used, most of which (from experience) give similar measures of centrality, which means that the relevant fluctuations are not very large. However, sooner or later, when the precision of measurements of values describing heavy ion collisions becomes high, a rigorous definition of centrality will be required.

Further, by definition, only such nucleus-nucleus interactions will be called *collisions* in which at least one pair of nucleons is wounded, which means that in any collision $N_{\text{part}} \geq 2$.

4.5.1. EOct Variable

The variable *EOct*, used as a measure of centrality of Cu+Cu collisions at $\sqrt{s_{\text{NN}}}$=200 GeV, was defined using the following algorithm:

1. loop over all the hits in the full rows of sensors in the octagon (see section 2.2.5.2 on page 59), which means that hits in the side, the top, and the bottom rows of octagon sensors (that have sensors facing the spectrometer and the vertex detectors removed) are not used in the analysis,

2. divide each hit energy loss by the path length of the particle (which produced the hit) inside the silicon sensor assuming that the particle traveled from OctProbMultVertex (see section 4.3.1 on page 75) to the hit along a straight line,

3. then multiply each hit energy loss by T_o/T_s (where T_o=300 μm, and T_s is the thickness of the sensor in which the hit was produced) and divide each hit energy loss by ΔE_{MIP}=80 keV (see section 4.2 on page 74), which results in all hits energy losses being scaled to the thickness T_o and expressed in units of ΔE_{MIP},

4. sum all such scaled hit energy losses [8].

The assumption here is that the higher the total energy *EOct* deposited in the octagon is, the higher the overall particle multiplicity of an event must be (any fluctuations are ignored in this statement). Therefore indirectly, the multiplicity is the measure of centrality of the event.

The reasons to use only full rows of octagon sensors to calculate *EOct* are:

- to avoid a vertex bias in the centrality determination, since studies [208] showed that if incomplete rows of sensors are used, then *EOct* distribution becomes vertex z-coordinate dependent, which would cause a need of vertex dependent *EOct* cuts,

- to avoid a reaction plane bias in the centrality determination, since if incomplete rows of sensors (causing an asymmetric octagon acceptance) are used, then *EOct* distribution could become reaction plane angle dependent due to the anisotropy (elliptic flow) of the particle distribution over the azimuthal angle, which would induce a necessity of the angle dependent *EOct* cuts.

Note that, by definition, *EOct* is a dimensionless variable.

Octagon Hits Reconstruction. The hits in the octagon used to calculate the *EOct* variable were reconstructed using an algorithm similar to the one described in section 4.2 on page 74 by merging (adding) the raw silicon pad signals of neighboring pads in each sensor separately. The merging was only done along the z-axis, along which the segmentation of sensors is more fine, and so it is possible for a particle to produce signals in several consecutive pads. The merging process started if a pad with an energy loss above the noise threshold of 60 keV was found, then the energy losses in the previous and the following pads [9] (or in just one of the two, if only one passed the selection explained below) were added if after a normalization their energy losses would have fallen in to the range 19.2-60 keV. The normalization just mentioned was done the same way as explained above for hits, which is by

[8] but if any hit energy loss in the sum is greater than $\Delta E_{\max} = 5$ then use $\Delta E_{\max}$ instead

[9] This implicitly means that not more than 3 neighboring pads energy losses could be summed. This restriction comes from considering the geometry of the octagon and estimating that this is the maximum number of consecutive pads, which could be intersected by a single particle traveling along a straight line from a position in a usable for a data analysis range of vertex z-coordinates.

1. dividing a pad energy loss by the path length of the particle (which produced the signal in the pad) inside the silicon sensor assuming that the particle traveled from the OctProbMultVertex (see section 4.3.1 on page 75) of the event to the pad along a straight line,

2. multiplication of the energy loss by T_o/T_s.

If it was estimated that to produce a signal in some pad a particle must have traversed more than one pad but no merging with neighboring pads was done, than such a pad signal was discarded as background. No merging was performed for pads in the pseudorapidity range $|\eta| < 1$. A hit was created from merged hit signals (or from a single pad signal above the noise threshold) if the normalized energy loss of the resulting hit was above 30 keV. Signals in the defective channels (see section 6.3.4 on page 157) of the octagon silicon sensors were not used to create hits.

4.5.2. Centrality Binning

Let us first consider an ideal situation in which triggering and event selection have 100% efficiencies. The case when the efficiencies are nontrivial will be discussed in section 4.5.3. It will be also assumed that the contamination of the event sample with any kind of background events as a result of imperfect triggering and event selection is negligible.

The traditional way (also used in this thesis) to quantitatively characterize centrality of nucleus-nucleus collisions is the following:

1. sort all the events (in the limit of an infinite number of them) in the descending order of the variable X, used as a measure of centrality (in this thesis this variable is *EOct*, see section 4.5.1 on page 80),

2. for every event calculate the percentage of all the events with X larger than of this event - this percentage is the *centrality* of the event.

In reality, one does not have a luxury of an infinite statistics, and so a measurement is performed on events in a given *centrality range* (also called a *centrality bin*), which means all the events with the percentage centrality measure described above in the range are used in the data analysis.

4.5.3. Event Selection Efficiency

The method of event selection efficiency estimation was the same for Cu+Cu and d+Au collisions at $\sqrt{s_{\rm NN}}$=200 GeV [226], and so the method description provided here follows the discussion for the later type of collisions given in Ref. [208].

The (overall and as a function of centrality) efficiency was estimated by matching the shape of *EOct* distributions in data and in Heavy Ion Jet Interaction Generator [227] (HIJING) MC simulations. The MC simulations contain the description of the full collision cross section, and since they provide an accurate description of the data *EOct*

Bin #	% centrality	N_{part}	Bin #	% centrality	N_{part}
17	0-3%	107.945 ± 7.094	8	40-45%	26.569 ± 5.740
16	3-6%	100.747 ± 8.601	7	45-50%	21.605 ± 5.122
15	6-10%	90.917 ± 9.367	6	50-55%	17.184 ± 4.612
14	10-15%	79.095 ± 9.529	5	55-60%	13.557 ± 4.201
13	15-20%	66.989 ± 8.976	4	60-65%	10.670 ± 3.674
12	20-25%	56.633 ± 8.361	3	65-70%	8.138 ± 3.179
11	25-30%	47.533 ± 7.560	2	70-75%	6.258 ± 2.788
10	30-35%	39.611 ± 6.864	1	75-80%	4.884 ± 2.282
9	35-40%	32.746 ± 6.304	0	80-100%	3.224 ± 1.492

Table 4.1.: Centrality bin numbers, the corresponding ranges of fractional cross section, and N_{part} values (which were determined from the PHOBOS HIJING MC simulations) in Cu+Cu collisions at $\sqrt{s_{\text{NN}}}$=200 GeV. The mean N_{part} values and their systematic errors (it is easy to simulate many MC events, and so the statistical errors of the N_{part} values are negligible) in every centrality range were determined separately for the positive and the negative magnet polarities. The N_{part} numbers shown here are the averages of the values found for the two polarities, assuming that all the systematic errors are fully uncorrelated (the case considered in section 7.6.1 on page 208). See section 4.5.3 on the facing page for details.

distribution at high *EOct* values (central events), where the efficiency is expected to be 100%, and so direct comparison between data and MC is possible [10], the efficiency can be estimated by calculating the ratio (data to MC) of normalized *EOct* distributions. The normalization of the distributions was done by:

- Multiplying all the *EOct* values in MC by an appropriate factor close to unity, since the overall scale of the values in data and MC was somewhat different.

- Normalizing the two distributions to the same integral in an interval of the highest *EOct* values.

After that to estimate the average efficiency of the event selection for Cu+Cu collisions in a given range of *EOct* values one just needs to find the ratio (data to MC) of integrals of the distributions in the range. By applying this technique to the full range of *EOct* values, it was found that the overall efficiency for Cu+Cu at $\sqrt{s_{\text{NN}}}$=200 GeV was ϵ_0=84±5%. Knowing the efficiency allowed to estimate the total number N_{tot} of occurred during data taking collisions from the observed one N_{obs} as $N_{\text{tot}} = N_{\text{obs}}/\epsilon_0$.

[10] That is why the *EOct* variable was chosen as a measure of event centrality. The assumption here is that since MC describes the data *EOct* distribution well at high *EOct* values, it does so also at low *EOct* values.

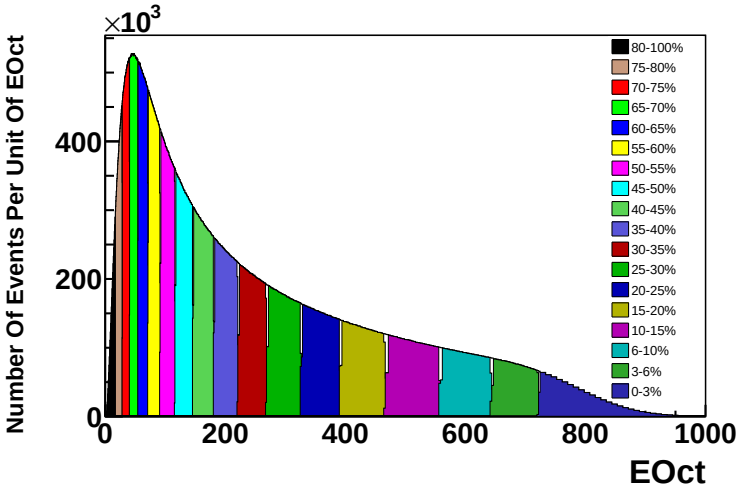

Figure 4.8.: Ranges of *EOct* variable corresponding to the centrality bins used for data analyzes in the PHOBOS experiment. The *EOct* distribution shown corresponds to all events passing the event selection in Cu+Cu at $\sqrt{s_{\mathrm{NN}}}$=200 GeV data collected by the PHOBOS collaboration. See section 4.5.3 on page 82 for details.

Table 4.1 on the previous page shows the list of all centrality ranges used for data analyses by the PHOBOS collaboration. Let us denote the interval of *EOct* values corresponding to the centrality bin $\mathscr{R}_i$ as $\mathscr{I}_i \equiv [EOct_i^{\min}, EOct_i^{\max})$. The interval of *EOct* values corresponding to a centrality range could be determined using the method of induction. This means that one starts with the most central bin of centrality ($\mathscr{R}_{17}$) and uses the following relations:

- $EOct_{17}^{\max} = +\infty$,
- $EOct_{i-1}^{\max} = EOct_i^{\min}$,
- $EOct_i^{\min}$ is chosen such that the number of observed events with *EOct* values in $\mathscr{I}_i$ is equal to

$$N_{\mathrm{tot}} \cdot \epsilon_i \cdot \frac{\Delta\mathscr{P}_i}{100\%},$$

where $\Delta\mathscr{P}_i$ and ϵ_i are the centrality percentage range length [11] and the event selection efficiency corresponding to bin $\mathscr{R}_i$.

The *EOct* intervals resulting from this procedure are shown on Fig. 4.8. Fig. 4.9 and Fig. 4.10 on page 88 demonstrate that the vertex bias of the *EOct* intervals is very small.

[11] $\Delta\mathscr{P}_{17}$=3%, $\Delta\mathscr{P}_{15}$=4%, $\Delta\mathscr{P}_{14}$=4%, etc. See Table 4.1 on the preceding page and section 4.5.2 on page 82.

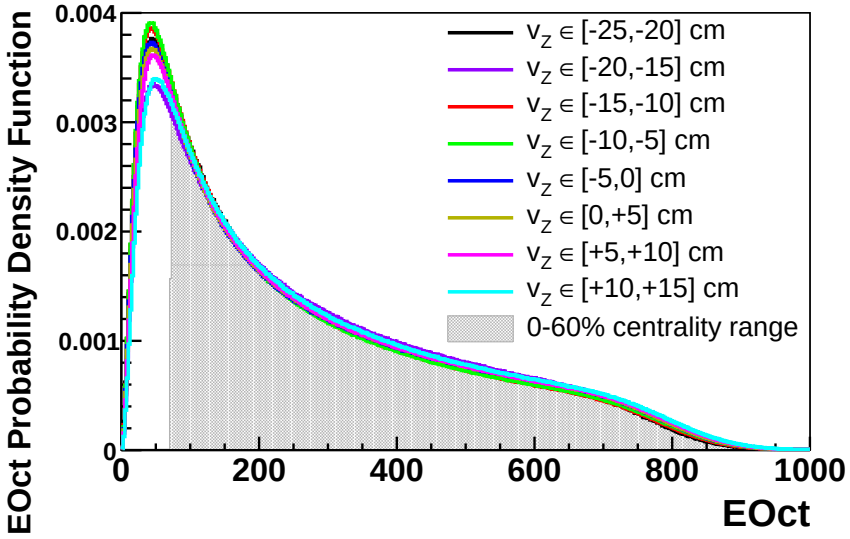

Figure 4.9.: Normalized distributions of *EOct* variable in different OneTrackVertex z-coordinate ranges. As can be seen, there is only very small vertex bias, and even though the centrality ranges selection intervals shown on Fig. 4.8 were found for the $[-10,+10]$ cm OneTrackVertex z-coordinate range, they are applicable to the $[10,15]$ cm range as well within the 0-60% range of centrality used for the data analysis in this thesis. The figure was created for both magnet polarities Cu+Cu $\sqrt{s_{\mathrm{NN}}} = 200$ GeV data passing the event selection, described in section 4.4 on page 78. See section 4.5.3 on page 82 for details.

Calculation of *EOct* variable in MC . The *EOct* variable was calculated somewhat differently in data and in the MC simulations used for the event selection efficiency estimation described above. The difference was the event vertex kind used. As it was pointed out in section 4.5.1 on page 80, in data the reconstructed OctProbMultVertex was used to merge hits in the octagon and to normalize them to the same path length in silicon. In the MC the simulated vertex was utilized to make sure that *EOct* could be calculated for all the events (OctProbMultVertex reconstruction can fail for some events), which is necessary for the simulation to contain the full collision cross section.

4.5.4. Number Of Collisions

An other variable, which can be used as a measure of centrality of a heavy ion collision event, is the *number of collisions* (denoted as N_{coll} or N_{bin}) of nucleons in the event. The average number of collisions corresponding to a given centrality range was calculated using *Glauber MC* simulations [225]. The simulations were performed the following way:

1. The centers of the two collided nuclei were selected randomly with a uniform distribution in the transverse (i.e. xy-coordinates) plane. Let us denote the coor-

Bin #	% centrality	N_{coll}	Bin #	% centrality	N_{coll}
17	0-3%	198.230 ± 16.898	8	40-45%	26.296 ± 5.395
16	3-6%	172.380 ± 16.707	7	45-50%	19.770 ± 4.464
15	6-10%	149.119 ± 16.375	6	50-55%	14.943 ± 3.716
14	10-15%	121.001 ± 14.976	5	55-60%	11.194 ± 3.127
13	15-20%	95.842 ± 12.896	4	60-65%	8.165 ± 2.522
12	20-25%	75.295 ± 11.022	3	65-70%	6.028 ± 2.045
11	25-30%	58.023 ± 9.251	2	70-75%	4.397 ± 1.701
10	30-35%	45.293 ± 7.643	1	75-80%	3.293 ± 1.328
9	35-40%	34.762 ± 6.525	0	80-100%	1.774 ± 0.826

Table 4.2.: Centrality bin numbers, the corresponding ranges of fractional cross section, and N_{coll} values (which were determined from the PHOBOS Glauber MC simulations [225]) in Cu+Cu collisions at $\sqrt{s_{NN}}$=200 GeV. The mean N_{coll} values and their systematic errors (it is easy to simulate many MC events, and so the statistical errors of the N_{coll} values are negligible) in every centrality range were determined separately for the positive and the negative magnet polarities. The N_{coll} numbers shown here are the averages of the values found for the two polarities, assuming that all the systematic errors are fully uncorrelated (the case considered in section 7.6.1 on page 208). See section 4.5.4 on the preceding page for details.

dinates of the centers as (x_1, y_1) and (x_2, y_2). In practice, one fixes $y_1 = y_2 = 0$ fm and chooses $x_1 = -x_2 = b/2$, where the impact parameter b is selected randomly between 0 fm and some maximal value $b_{max} \simeq$20 fm with a distribution $\frac{dN}{db} \propto b$.

2. The nucleon positions of the two collided nuclei were randomly generated with a Woods-Saxon distribution:

$$\rho(r) = \frac{\rho_0}{1 + \exp\left(\frac{r-R}{a}\right)},$$

where r is the distance of a nucleon from the nucleus center and the parameters R=4.2 fm and a=0.596 fm for Cu+Cu collisions. The angular distribution of nucleons with respect to the center of their nucleus was chosen to be isotropic. The normalization parameter ρ_0 is not important in the simulations [12].

3. The two nuclei were then "collided" along the z-axis assuming that all nucleons travel along a straight line (the *eikonal approximation*). A pair of nucleons was considered to have experienced a collision if the distance D between the nucleons in the transverse plane was $D < \sqrt{\sigma_{inel}^{NN}/\pi}$, where σ_{inel}^{NN} is the inelastic cross-section of nucleon-nucleon collisions which can be estimated by measuring it in proton-proton collisions and was chosen to be $\sigma_{inel}^{NN} = 42 \pm 1$ mb at $\sqrt{s_{NN}}$=200 GeV. The

[12] It could be found from $\int_0^\infty \rho(r) d^3 r = A$, where A is the atomic number of a nucleus.

total number of such nucleon collisions was counted and assigned to be the N_{coll} of a simulated event.

The N_{coll} values for Cu+Cu collisions at $\sqrt{s_{\mathrm{NN}}}$=200 GeV resulting from the procedure described above are shown in Table 4.2 on the preceding page for all the centrality ranges used in the PHOBOS experiment.

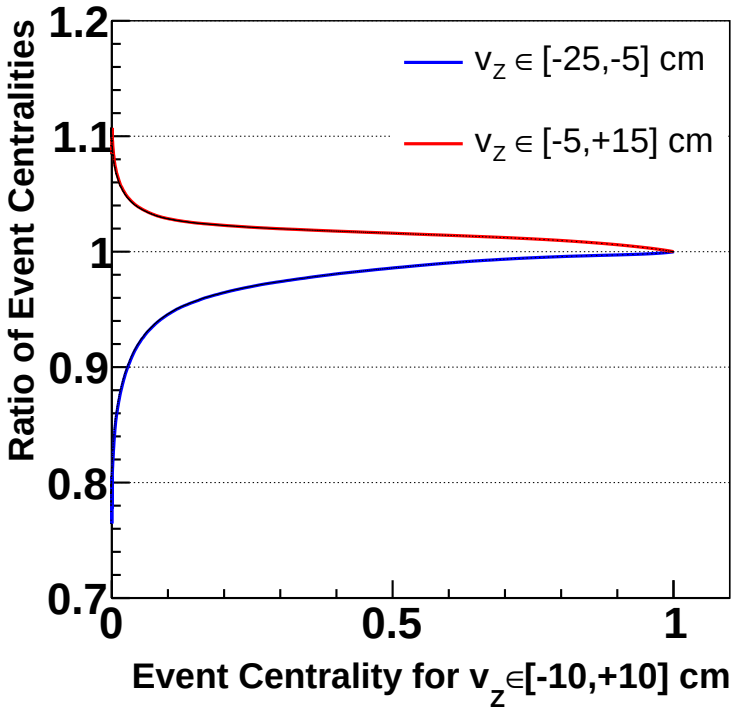

Figure 4.10.: The OneTrackVertex z-coordinate (denoted here as v_z) ranges used for the data analysis in this thesis (namely $v_z \in [-5,+15]$ cm for the ϕ meson $p_t \in [0.39, 1.69]$ GeV/c and $v_z \in [-25,-5]$ cm for the ϕ meson $p_t \leq 0.13$ GeV/c) differed from the nominal range ($v_z \in [-10,+10]$ cm) for which the *EOct* intervals corresponding to centrality ranges shown on Fig. 4.8 were found. That introduces systematic uncertainties on the borders of the centrality ranges in which the ϕ meson invariant yield was measured. This figure illustrates an estimate of the uncertainties. The horizontal axis is the centrality (let us denote it as $\mathscr{C}$) of an event with a given *EOct* value determined using the *EOct* distribution of events with $v_z \in [-10,+10]$ cm. The vertical axis shows the ratio to $\mathscr{C}$ of the event centrality found using the *EOct* distribution of events with a vertex range actually used for the data analysis. As can be seen, the systematic uncertainties on the borders of the used centrality ranges are about $0.3-0.7\%$. See section 4.5.3 on page 82.

5. Particle Reconstruction

5.1. Reconstruction Challenge

Most of the time spent working on the results presented in this thesis was devoted to overcoming the challenges of reconstructing kaons produced in studied Cu+Cu collisions, which is of course the first necessary step of the data analysis since ϕ meson invariant yield was measured through the $\phi \rightarrow K^+K^-$ decay channel (see chapter 6 on page 139). The yield of ϕ mesons is about ~ 100 times smaller than that of pions and about ~ 10 times smaller than that of kaons (see Fig. 5.1), which combined with a small

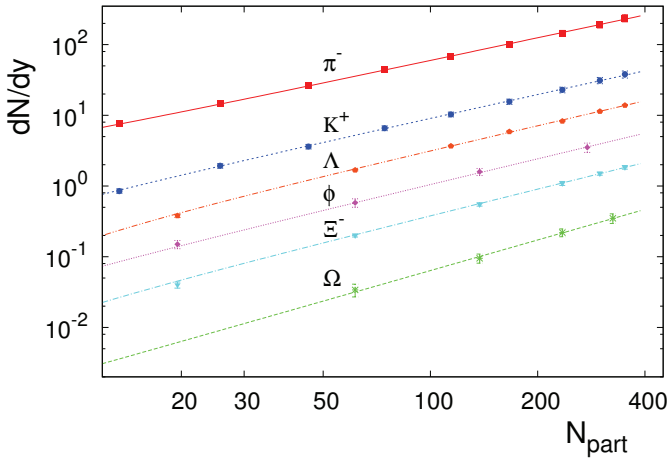

Figure 5.1.: dN/dy of different particle yields measured at midrapidity in Au+Au collisions at $\sqrt{s_{NN}} = 62.4$ GeV [228]. The yield of ϕ mesons is about ~ 100 times smaller than that of pions and about ~ 10 times smaller than that of kaons. Taking into account that the PHOBOS spectrometer allows an analysis of only ~ 0.01 of all particles (see section 2.2 on page 51), the observed raw number of ϕ mesons in PHOBOS data is about 10^4 times lower than for pions and about 10^3 times lower than for kaons.

φ-angle acceptance of the PHOBOS detector and the necessity to find both decay kaons to reconstruct a ϕ meson makes the measurement of the ϕ meson yield a no small feat [1].

[1]The efficiency of ϕ meson reconstruction $eff(\phi)$ is approximately the product of K^+ and K^- reconstruction efficiencies, i.e. $eff(\phi) \approx eff(K^+) \times eff(K^-)$, consequently any reduction in kaon reconstruction efficiency has a quadratic effect on the $eff(\phi)$.

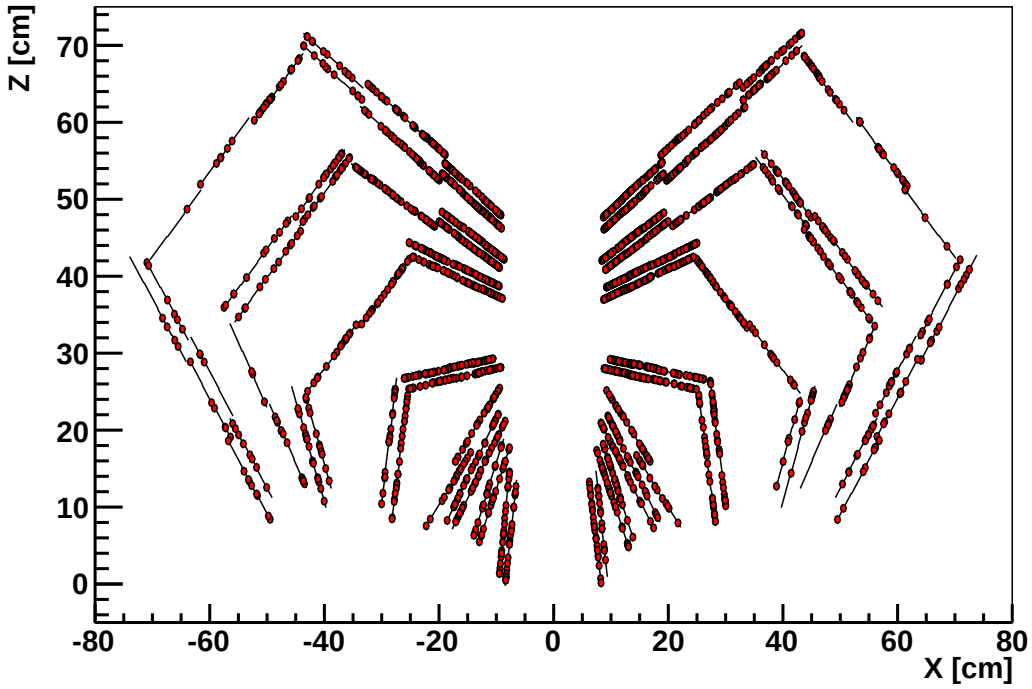

Figure 5.2.: An example of hit positions in a central Cu+Cu 200 GeV event (run 16373, event 122544).

PHOBOS collaboration developed a reconstruction code used for other data analyses, however this code has too low efficiency of kaon reconstruction rendering it insufficient to make the measurement in question. Therefore a specialized kaon reconstruction algorithm was developed for the current work, which addressed the following drawbacks of the standard PHOBOS reconstruction:

1. The standard PHOBOS reconstruction only attempts to find tracks having all of their hits either in the "center" (Fig. 5.3(a)) or in the "wing"(Fig. 5.3(b)) subsets of the spectrometer sensors. It does not use any information from the "forward" (Fig. 5.3(c)) subset of sensors [2], positioned at small angles with respect to the collision axis, where most of the charged particles are produced (see Fig. 5.4). Reconstruction of kaons at low θ angles however not only increases the number of reconstructed ϕ mesons but is critical for making the invariant yield measurement at low p_t^{ϕ}. The standard PHOBOS reconstruction also does not allow to find tracks which have hits in different sensor subsets.

[2]The reason that the standard PHOBOS reconstruction does not use information from the "forward" subset of the spectrometer sensors is that the hit density in those sensors is so high (see Fig. 5.2) that a reconstruction of all tracks (i.e. all particle types with any total momentum value) in this region is not realistic on the current BNL RACF computer farm due to high number of possible hit combinations which need to be considered.

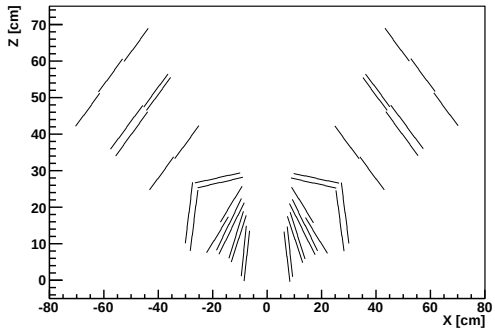

(a) "center" spectrometer sensors

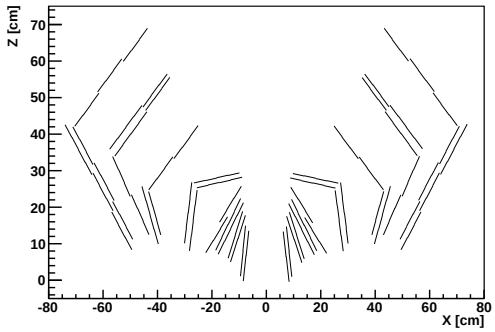

(b) "wing" spectrometer sensors

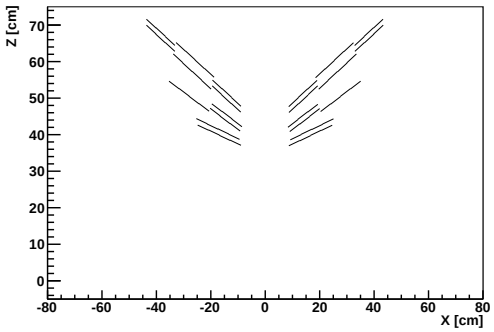

(c) "forward" spectrometer sensors

Figure 5.3.: Standard PHOBOS tracking only reconstructs tracks which have all of their hits either in the "center" (a) or the "wing" (b) subsets of the spectrometer sensors but neither in the "forward" (c) subset nor any mixture of sensors from different sensor subsets.

The specialized kaon reconstruction uses information from *all* the spectrometer sensors and is designed is such a way as to not pose any requirement on the spectrometer sensors subset in which the reconstruction is done [3]. In fact any notion

[3]The exception is that information from sensors in layers 7 and 8 (see Fig. 2.10) is not used. There are two reason why the layers are ignored: 1) the two layers have very small overlap and therefore are essentially one single layer, however in the PHOBOS geometry they are described as two separate layers making their use inconvenient, 2) the layers are positioned in the magnetic field of transitional magnitude, consequently if hits in the layers are included into the "straight" part of tracks (see section 5.7 on page 110), an approximation of the part as a straight line becomes poor, and if hits in the layers are included into the "Hough" part of tracks (see section 5.8 on page 113), then due to a small magnetic field in which the layers are positioned the momentum and angle resolution of the hit pairs containing hits in the layers would be poor leading to compatibility of the pairs with most pairs in other layers, increasing the total number of constructed Hough tracks and leading to a poorer overall resolution of the Hough track parameters. Standard PHOBOS reconstruction does not use information from the spectrometer sensors in layers 7 and 8 either.

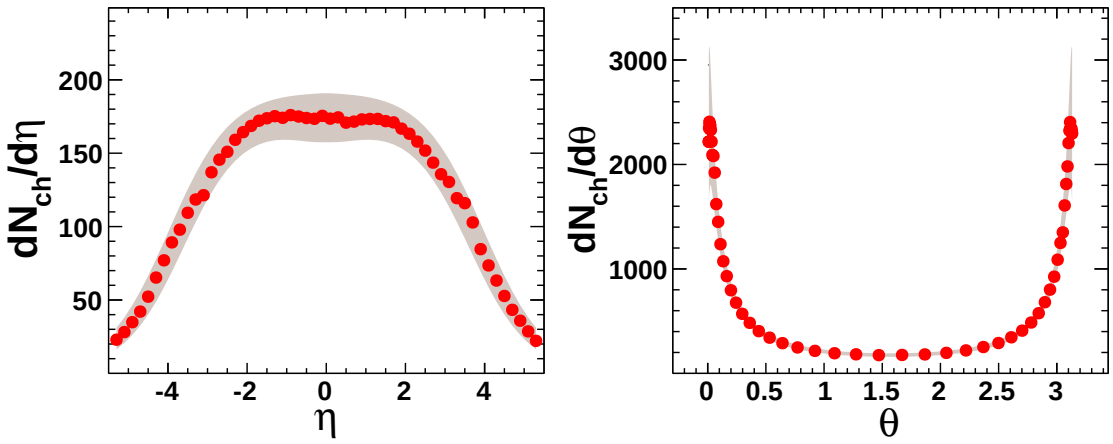

Figure 5.4.: Angular distribution of charged particles produced in Cu+Cu 200 GeV, 3-6% collisions [132]. For other types of collided nuclei as well as for other collision centralities the shape of the distribution is very similar. As one can see, most of the charged particles are produced at small angles with respect to the collision axis.

of a "sensors subset" is not present in the specialized tracking, and any combination of sensors containing a track hits is allowed up to the limits sets by set of layer patterns used for reconstruction (see section 5.3 on page 98).

2. The standard PHOBOS reconstruction only attempts to find tracks with the following layer patterns (see section 5.3.1 on page 98):
   - 1111-1100-1110-1110 ("center" subset of the spectrometer sensors)
   - 1111-1100-1110-1011 ("wing" subset of the spectrometer sensors)

   However, since 1 hit in layers 4-6 was allowed to be not found during reconstruction, the full set of reconstructed layer patterns was:
   - 1111-1100-1110-1110 ("center" subset of the spectrometer sensors)
   - 1110-1100-1110-1110 ("center" subset of the spectrometer sensors)
   - 1111-0100-1110-1110 ("center" subset of the spectrometer sensors)
   - 1111-1000-1110-1110 ("center" subset of the spectrometer sensors)
   - 1111-1100-1110-1011 ("wing" subset of the spectrometer sensors)
   - 1110-1100-1110-1011 ("wing" subset of the spectrometer sensors)
   - 1111-0100-1110-1011 ("wing" subset of the spectrometer sensors)
   - 1111-1000-1110-1011 ("wing" subset of the spectrometer sensors)

   That in particular meant that each reconstructed track was required to have 11-12 successfully assigned hits, which is a rather strict requirement limiting the number of tracks which could potentially be reconstructed.

In the specialized kaon reconstruction the set of allowed layer patterns was extended to include 13 layer patterns for K^+ and 12 layer patterns for K^- reconstruction in positive magnet polarity data (see section 5.3.2 on page 99). For reconstruction of negative magnet polarity data the sets of layer patterns were reversed.

3. The standard PHOBOS reconstruction relies solely on the hit positions in the spectrometer for particle reconstruction. However a charged particle of a given total momentum deposits energy per unit of material thickness (dE/dx) with a distribution around a well defined value when it passes through the silicon spectrometer sensors. All such energies are measured and could be used to check the hits assigned to a given track for:
   - consistency of the energy losses with each other
   - consistency of the energy losses with the track total momentum value and the hypothesis that the track is a kaon (a track total momentum value could be determined using both: hits positions only and hits energy losses only assuming the hypothesis that all the energies were deposited by a kaon, and for successfully reconstructed kaons the two values must be consistent)
   - the average value of energy losses to discard early tracks which could not be identified as kaons with high enough purity using dE/dx vs p method (see section 5.12.2.1 on page 135).

   All the checks were implemented in the specialized kaon reconstruction.

4. Some of the pieces of code from the standard PHOBOS reconstruction which were reused in the specialized kaon reconstruction were directly heavily optimized, to reduce the CPU time required to execute some specific actions. And some parts of the reconstruction were replaced completely with more efficient versions. Some of the notable improvements came from:
   - rewriting the code in such a way that no C++ objects would neither created nor assessed in time critical parts of the track reconstruction
   - rewriting the interpolation of the PHOBOS detector magnetic field map, since the magnetic field information is accessed dozens or hundreds of times per track reconstruction
   - using a more efficient algorithm for χ^2 minimization in the track fitting
   - using smaller number of track parameters minimized during track fitting

5. The standard PHOBOS reconstruction assumed that the straight parts of the tracks are perfectly straight. In the specialized kaon reconstruction it was taken into account that even though the magnetic field magnitude in the area of layers 1-6 is very low, it is not negligible, causing the straight parts of the tracks to have a small curvature, which in turn caused a small systematic shift in the reconstructed value of the θ-angle of the straight tracks. Taking this effect into account allowed

for much stricter selection of matching pairs of straight and Hough tracks (see section 5.9 on page 120).

Overall it was estimated that out of the all kaons originating from ϕ meson decays, that are found by the specialized kaon reconstruction, only $\sim 2\%$ could be found by the standard PHOBOS reconstruction. What follows is a more detailed description of the specialized kaon reconstruction algorithm used for the data analysis.

5.2. Realistic MC Simulation Of ϕ Mesons

The MC simulation is based on previous measurements by other experimental groups and on some insights from the PHOBOS data, having its the goal to simulate

- the yield and the distribution of ϕ mesons production in Cu+Cu 200 GeV collisions in a realistic way
- the PHOBOS detector response to decay products of the ϕ mesons.

The simulation was used to select the set of layer patterns to be used in the specialized kaon reconstruction (see section 5.3.2 on page 99).

The φ-angle distribution of simulated ϕ mesons was uniform in the range $[0, 2\pi]$. It was assumed that the following distributions describing the ϕ meson production are independent:

$$\frac{dN}{d\varphi}, \quad \frac{dN}{dy}, \quad \frac{dN}{dp_t}, \quad \frac{d^2N}{d(\text{CentralityBin})\, dv_z}$$

The details about the employed distributions are explained below.

5.2.1. Distribution Of v_z Versus Centrality Bin Number

Distribution and the yield of ϕ meson production depends on an event centrality (see section 4.5 on page 79) and the PHOBOS detector response to the ϕ mesons decay products depends on the geometrical position of a Cu+Cu collision with the strongest dependence being on the v_z . Therefore a realistic distribution of v_z versus centrality bin number has to be used for simulation of single ϕ meson events.

The distribution was found by reading all of the Cu+Cu 200 GeV events in the PHOBOS data, selecting only those which pass the event selection (see section 4.4 on page 78), and filling a 2D-histogram (200 v_z bins in the -35 cm to +15 cm range) with v_z versus centrality bin number (see section 4.5 on page 79) values. During the MC simulation the pairs of v_z versus centrality bin number values were generated randomly according to the histogram shape (see Fig. 5.5 on the next page).

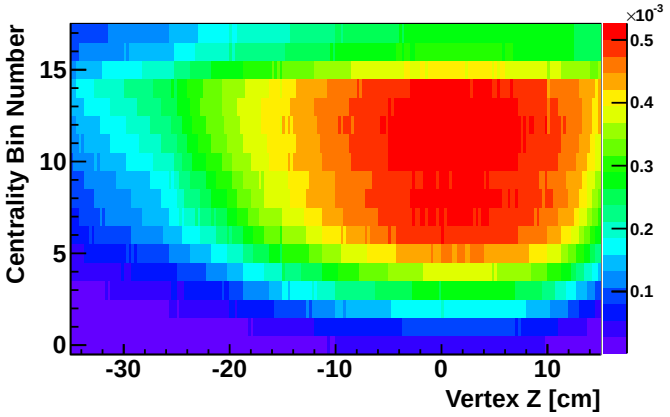

Figure 5.5.: Centrality bin number versus v_z probability density function used for realistic MC simulation of ϕ Mesons in Cu+Cu collisions at $\sqrt{s_{NN}} = 200$ GeV.

5.2.2. Rapidity Distribution Of ϕ Mesons

There is no experimental data on the rapidity distribution of ϕ mesons at RHIC energies. However some insight could be gained from the lower energy data. As can be seen from Fig. 5.6 on the following page, in 40 A GeV, 80 A GeV, and 160 A GeV central Pb+Pb collisions the rapidity distributions of produced K^- and ϕ mesons are Gaussians with about the same width. The measured K^- rapidity density in 0-5% central Au+Au collisions at $\sqrt{s_{NN}} = 200$ GeV has Gaussian shape as well with width of ~ 2.14 units (see Fig. 5.7 on page 97). Therefore assuming that:

- the shapes and the widths of K^- and ϕ meson rapidity distributions in Au+Au collisions at $\sqrt{s_{NN}} = 200$ GeV are the same
- the shapes of ϕ meson rapidity distributions in Cu+Cu and Au+Au collisions at at $\sqrt{s_{NN}} = 200$ GeV are the same
- the width of ϕ meson rapidity distribution is independent of centrality

the rapidity distribution of ϕ mesons in Cu+Cu collisions at $\sqrt{s_{NN}} = 200$ GeV was simulated to be Gaussian with width of 2.14 units at all event centralities.

5.2.3. Transverse Momentum Distribution Of ϕ Mesons

The $m_t = \sqrt{p_t^2 + m_\phi^2}$ dependence of the ϕ meson yield is well described by an exponential function [231, 232]:

$$\frac{1}{2\pi m_t}\frac{d^2N}{dm_t dy} = \frac{dN/dy}{2\pi T(m_\phi + T)} \exp\left(-\frac{m_t - m_\phi}{T}\right), \tag{5.1}$$

where slope T and yield dN/dy are parameters of the distribution, and m_ϕ is the ϕ meson mass. The normalized to unity transverse momentum distribution employed

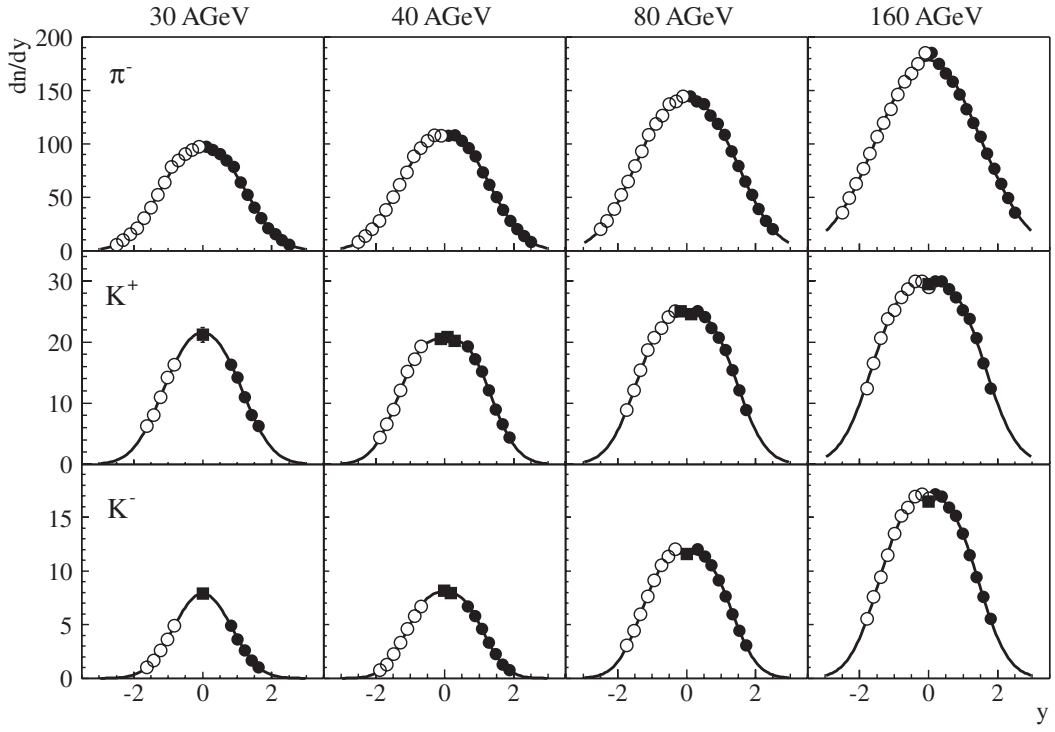

(a) Rapidity distributions of π^-, K^+ and K^- . Filled symbols are measured, open ones are reflected at midrapidity. The solid lines are parametrizations by the sum of two Gaussians displaced symmetrically with respect to midrapidity.

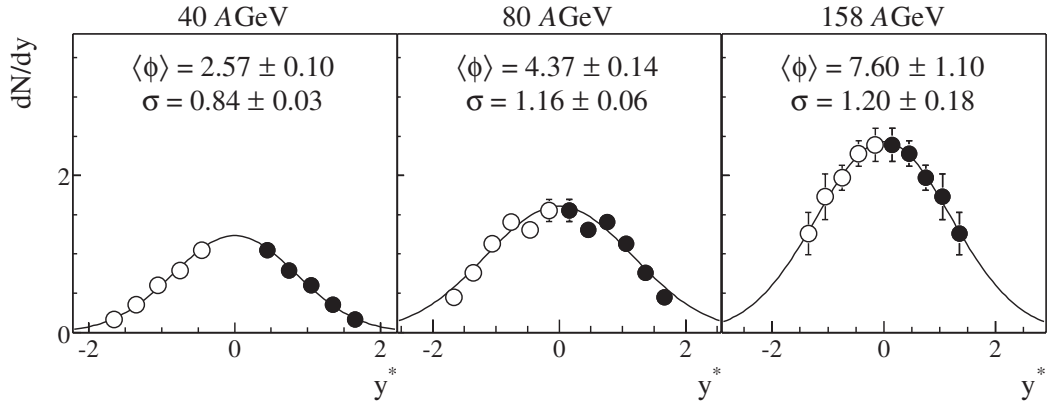

(b) ϕ rapidity distributions. Solid symbols are measured data, open symbols are reflected at midrapidity. The full lines represent Gaussian fits.

Figure 5.6.: In 40 A GeV, 80 A GeV, and 160 A GeV central Pb+Pb collisions the rapidity distributions of produced K^- (a) and ϕ (b) mesons are Gaussians with about the same width [229].

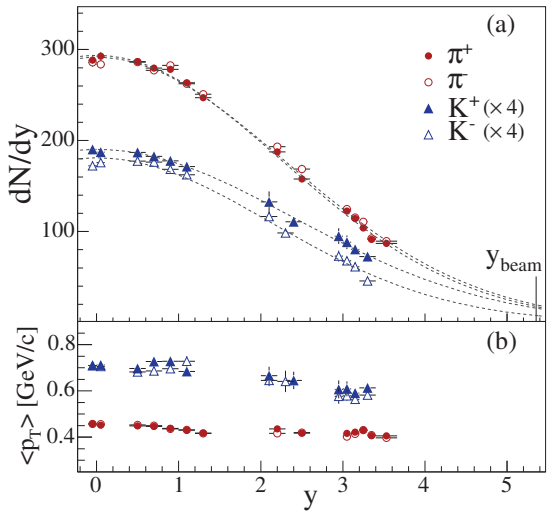

Figure 5.7.: Pion and kaon rapidity densities (a) and their mean transverse momentum $\langle p_T \rangle$ (b) as a function of rapidity as measured in 0-5% central Au+Au collisions at $\sqrt{s_{NN}} = 200$ GeV [230]. The dashed lines in (a) are Gaussian fits to the dN/dy distributions. K^- rapidity distribution has width ~ 2.14 units.

for the realistic MC simulation of ϕ meson production was derived from Eq. 5.1:

$$\frac{dN}{dp_t} = \frac{p_t}{T(T+m_\phi)} \exp\left(-\frac{\sqrt{p_t^2+m_\phi^2}-m_\phi}{T}\right). \tag{5.2}$$

If $\langle p_T \rangle$ is known, Eq. 5.2 could be used to find the corresponding slope parameter T. Parameters dN/dy and $\langle p_T \rangle$ were taken from the STAR collaboration publication on ϕ meson production in Cu+Cu collisions at $\sqrt{s_{NN}} = 200$ GeV[233]. The parameters and the calculated corresponding slope parameter T values are summarized in Table 5.1. Since dN/dy is proportional to N_{part} in Au+Au collisions at $\sqrt{s_{NN}} = 200$ GeV [232], the scaling was assumed to be true in Cu+Cu collisions at $\sqrt{s_{NN}} = 200$ GeV as well, and was used in the 60-100% centrality range to estimate dN/dy by scaling the 50-60% dN/dy value with N_{part} (see Table 4.1 on page 83). The $\langle p_T \rangle$ value (and consequently the slope parameter T) in the centrality ranges 60-100% and 50-60% were approximated to be the same.

5.2.4. Total Number Of ϕ Mesons Per Event

STAR collaboration measured ϕ meson production in the rapidity range $|y^\phi| < 0.5$ [233, 234]. Therefore to estimate the total average number of ϕ mesons produced per event in a given centrality range the dN/dy values in Table 5.1 were divided by the fraction of rapidity distribution (see section 5.2.2 on page 95) contained in the interval $[-0.5, +0.5]$:

% centrality	dN/dy	$\langle p_T \rangle$ (GeV/c)	T (GeV)
0-10	2.3	0.935	0.335
10-20	1.6	0.901	0.318
20-30	1.1	0.897	0.316
30-40	0.7	0.885	0.310
40-50	0.4	0.869	0.302
50-60	0.26	0.852	0.293
60-100	0.26 scaled with N_{part}	0.852	0.293

Table 5.1.: dN/dy and the slope parameter T used in the realistic MC simulation of ϕ meson production.

$$\int_{-0.5}^{+0.5} \frac{1}{\sqrt{2\pi}\cdot 2.14} \exp\left(\frac{-y^2}{2\cdot(2.14)^2}\right) dy \approx 0.185.$$

The resulting quantities were multiplied by 0.492 ($\phi \to K^+K^-$ branching ratio) to estimate the the average numbers N_ϕ of ϕ mesons which decayed into K^+K^- pairs [235] [4]. Finally, the actual number of ϕ mesons in a given event was randomly chosen according to a Poisson distribution with the mean N_ϕ.

5.2.5. Simulating $\phi \to K^+K^-$ Decay

To simulate a $\phi \to K^+K^-$ decay, the following procedure was followed:

1. The ϕ meson boost vector $\vec{v}$ was calculated.
2. The ϕ meson invariant mass was chosen randomly in the range $[2m_K, +\infty]$ according to the Breit-Wigner distribution with the mean $m_\phi = 1.019456$ GeV and the width $\Gamma_\phi = 0.00426$ GeV [236] [5].
3. The ϕ meson was decayed isotropically in to a K^+K^- pair.
4. The daughter kaons were boosted according to the vector $\vec{v}$ to the laboratory reference system.

5.3. Layer Patterns

5.3.1. Layer Patterns Definition

MC simulations (see section 5.2 on page 94) have shown that the probability that a kaon track intersects a given layer of the PHOBOS spectrometer more than once (due to the

[4] Note that the branching ratio listed here is different from the modern value of 0.489 [169], but this is the actual number which was used for the realistic MC simulation of ϕ meson production.

[5] Again, those are the actual values used for the simulation.

track curvature in the magnetic field) is negligible [6]. For this work only kaon tracks with at least 4 hits in layers 1-6 and at least 4 hits in layers 9-16 were reconstructed. The fraction of such tracks that hit the spectrometer sensor layers in order different from the ascending order of the layer numbers (see Fig. 2.10 on page 61) is also negligible. Therefore both types of tracks just mentioned representing a small fraction of all kaon tracks can be safely neglected without any significant reduction in the tracking efficiency. The remaining tracks then can be characterized just by the set of layer numbers which they intersect, which are called *layer patterns* in this work.

It is convenient to represent a layer pattern as an 8-bit binary number with a bit number n equal to 1 (*bit is set*), if tracks with such layer pattern have a hit in the spectrometer layer number n, and equal to 0 (*bit is not set*) otherwise. For example, a track with the layer pattern 1001-0001-0000-0001 has hits in the layers 1, 4, 8, and 16 and does not have any hits in the other spectrometer layers. If layer pattern P_1 has all the bits set, which are set in layer pattern P_2, we say that P_1 *contains* P_2.

5.3.2. Layer Pattern Selection

Once a track layer pattern is chosen, the reconstruction procedure is rather straightforward ideologically: start from the event vertex and add hits one by one in layers with numbers equal to the bit numbers set in the layer pattern in ascending order of the layer numbers. The beginning of a perfect reconstruction procedure would be then to figure out all the possible layer patterns of kaons resulting from ϕ meson decays and to reconstruct all the tracks corresponding to them. However, this approach would be very intensive computationally, since it would require generation of a separate set of covariance matrices (see section 5.10 on page 123) for each such layer pattern and it would require RAM to store the matrices and corresponding track candidate hit combinations during reconstruction, making it unrealistic to execute using the available computing resources at the RACF (see section 3.1 on page 65). Restricting reconstruction to only some subset of the full layer patterns is not a good idea either since it would limit the efficiency of the resulting tracking algorithm.

However, to reconstruct a particle track it is enough to find only some subset of all the hits produced by the particle [7]. Consequently, from the discussion above, it means that it is enough to find hits produced by the particle in a subset of all the layers intersected by the particle trajectory, ignoring intersections with the remaining layers. The resulting track would have a layer pattern which is contained in the layer pattern corresponding to all the intersected layers. Therefore *to construct a maximal efficiency reconstruction*

[6] Due to a small overlap of adjacent sensors in a given layer a particle trajectory can intersect both such sensors. Such cases are not considered a double intersection of a track with a layer. We say that a trajectory intersects a layer more than once if either the distance between some of the intersections is much larger than the typical distance between two adjacent spectrometer sensors or if the integral of incremental changes of trajectory's tangent vector θ-angle between some of the intersections is approximately $\sim 2\pi$.

[7] Although it is not necessary to find all the hits, the more hits are assigned correctly to a given track, the higher the resolution of the particle parameters reconstruction is going to be.

algorithm with a given number of allowed layer patterns, one has to find such a set of layer patterns that at least one of them would be contained in a maximal fraction of all the possible layer patterns of kaons resulting from ϕ meson decays. That is exactly was what done while designing the specialized kaon reconstruction.

Two separate sets of layer patterns were chosen: 13 layer patterns for K^+ and 12 layer patterns for K^- reconstruction in positive magnet polarity data. Since K^+ and K^- have the same mass and opposite charge, if the magnetic field vector direction and a kaon charge are reversed, the kaon trajectory is not altered. Therefore, for reconstruction of negative magnet polarity data the sets of layer patterns were reversed.

The following procedure was followed to select layer pattern sets used for reconstruction:

1. To find out all the possible layer patterns of kaons resulting from ϕ meson decays, a MC simulation (see section 5.2 on page 94) was done of a number of realistically distributed single ϕ mesons, equivalent to the one produced in 10,145,696 real data Cu+Cu 200 GeV events.

2. Only ϕ mesons were selected which decayed into K^+K^- pairs with both kaons:
   - total momentum less than 1.1 GeV
   - dE/dx more than than 1.0 MIP per sensor thickness
   - having at least 4 hits in layers 1-6 and at least 4 hits in layers 9-16 (see Fig. 2.10 on page 61)

3. For every possible K^+ layer pattern, for decays where both kaons originated from the selected ϕ mesons, it was counted how many K^+ trajectories had the layer pattern. Then all such layer patterns were sorted according to the number of the corresponding counts and the fraction (let us call it *"popularity"* in what follows) of K^+ mesons having each layer pattern was calculated. After that each layer pattern binary number representation and the corresponding popularity were printed. Next, starting from the most popular ones, it was assessed which layer patterns could be made equal by ignoring some of the layers. Attempt was made to ignore as little number of layers as possible (mostly 0 or 1). A layer was not allowed to be ignored if after that the requirement on the number of hits, explained in the step 2 would be violated. The layer pattern equal to the selected group of patterns (except the bits corresponding to the ignored layers) was selected to be used in the specialized kaon reconstruction.

4. Step 3 was repeated, this time ignoring all the K^+ layer patterns, which contain the selected one, resulting in a second selected layer pattern[8]. Then step 3 was repeated again, now ignoring all the K^+ layer patterns which contain at least one

[8]We ignore the layer patterns, which contain the selected one, since tracks with such patterns could already be reconstructed using this selected pattern, and the goal is to find such a set of layer patterns, that as big fraction of all K^+ tracks as possible could be reconstructed using at least one of them.

K^+	K^-
1111-1100-1110-1010	1111-1100-1110-1010
0011-1100-1110-1100	0011-1100-1110-1010
0011-1100-1110-1011	1100-1100-1110-1000
1100-1100-1110-1000	0011-1100-1110-1000
1010-1100-1111-0011	1111-1100-1101-0001
0011-1100-1110-1000	1111-1100-0010-1110
1111-1100-1101-0011	1100-1100-1110-1100
1111-1100-0010-1110	1100-1100-1100-1010
1111-1000-1111-1010	1010-1100-1110-0011
1111-1100-1111-0000	1110-1000-1111-1011
0011-1100-1100-1011	1111-1100-1111-0000
1111-1000-1001-0011	0011-1100-0110-1010
0011-1100-1010-1100	

Table 5.2.: Layer patterns used in the specialized kaon reconstruction developed for the data analysis.

of the layer patterns selected so far [9], resulting in one more pattern selected. The processes was iterated until 13 different layer patterns were selected for K^+ reconstruction. It was not required that no two selected layer patterns could contain one in the other - any possible resulting ambiguity between two reconstructed tracks was resolved as described in section 5.12 on page 133.

5. K^- layer patterns to be used in the specialized kaon reconstruction were selected the same way as K^+ ones, i.e. following steps 3 and 4. In total 12 different layer patterns were selected.

The fractions of K^+ and K^- tracks, resulting from decays of ϕ mesons selected in step 2, that could be reconstructed using the selected layer patterns were estimated to be $\sim 97\%$ and $\sim 98\%$. It was also estimated that the fraction of ϕ mesons, passing the just mentioned selection, such that both daughter kaons could be reconstructed using the selected sets of layer patterns, is $\sim 95\%$.

The selected layer patterns are summarized in Table 5.2.

5.4. MC Simulation of Single Kaon Events

Due to the complexity of the PHOBOS detector geometry, theoretical calculation of the amount of scattering and energy losses experienced by K^+ and K^- particles as they travel through the beam pipe and the PHOBOS spectrometer material is a daunting task.

[9] To make the procedure description exact, it has to be mentioned that for one K^+ and one K^- layer pattern no ignoring was done. The layer pattern in both cases was 1100-1100-1110-1000.

However, quantitative knowledge of the amounts for different parameters of kaons was essential for the development of the specialized kaon reconstruction used for the data analysis [10]. A GEANT [223] based MC simulation of single kaon events was employed to get the necessary estimations. The simulation described here was used to develop the straight line tracking (see section 5.7 on page 110), the Hough tracking (see section 5.8 on page 113), and the joining of the two (see section 5.9 on page 120).

The following GEANT parameters were changed from their default values:

"GEN"	=	10	user supplies particle (one particle per event)
"ANNI"	=	0	no positron annihilation
"BREM"	=	2	bremsstrahlung without generation of photon
"COMP"	=	2	Compton scattering without generation of e-
"DCAY"	=	2	decay but ignore secondaries
"DRAY"	=	2	delta ray production without generation of e-
"HADR"	=	2	hadronic interactions without secondaries
"LOSS"	=	3	restricted Landau fluctuations energy losses plus delta ray production
"MULS"	=	2	multiple scattering according to Moliere
"PAIR"	=	2	pair production without generation of e+/e-
"PHOT"	=	2	photoelectric effect without generation of e-

The simulation was performed at discrete positions of v_z in the range [-35,+15] cm with a step of 0.25 cm. All the simulations were done at positive magnet polarity with uniform distributions in the following ranges of the kaon momentum parameters:

$$\varphi \in [-0.2, +0.2], \quad \theta \in [0, \pi], \quad \text{and} \quad 1/p \in [0.02, 10.0]\ (\text{GeV/c})^{-1}. \tag{5.3}$$

K^+ and K^- particles were simulated separately in sets corresponding to each layer pattern (see section 5.3 on page 98) selected to be used in the specialized kaon reconstruction. Once a single kaon event was simulated, it was only saved if the resulting kaon layer pattern contained the layer pattern of the set.

To make sure that a sufficiently high number of kaons is generated for each layer pattern selected to be used in the specialized kaon reconstruction in all the regions of the PHOBOS detector acceptance, the simulation was done in portions. The other important reasons to do the simulation this way were to limit the CPU time and the disk space required. Once a portion of kaon simulations was complete, a ($v_z \times \theta \times 1/p$) 3D-histogram ($20 \times 20 \times 20$ bins) was filled in the ranges of parameters given in Eq.5.3 with one entry per event saved so far. Once the number of entries in a histogram bin reached 100, subsequent kaons which would fall in to the bin in case of a successful layer pattern match were skipped in the next simulation portion.

After completion of every simulation portion, the Hough tracking tables were filled (see section 5.8.2.1 on page 117) using all the single kaon events generated so far and the efficiency of the Hough tracking (see section 5.8 on page 113) was checked. The simulation of single kaon events for a given kaon charge × layer pattern combination was stopped once the efficiency reached $\geq 96\%$ level.

[10] Parameters of a kaon are its origin v_z position and its momentum vector.

5.5. Track Truncated Mean dE/dx

Throughout the current work track dE/dx vs total momentum information was used in different form to identify kaons among other charged particles [11]. This section explains calculation of this energy loss rate in the silicon detectors of the PHOBOS spectrometer.

Theoretically the mean dE/dx can be calculated using the Bethe-Bloch equation [169, 237–240]:

$$-\frac{dE}{dx} = Kz^2\frac{Z}{A}\frac{1}{\beta^2}\left[\frac{1}{2}\ln\frac{2m_e c^2\beta^2\gamma^2 T_{max}}{I^2} - \beta^2 - \frac{\delta(\beta\gamma)}{2}\right], \tag{5.4}$$

where x is the absorber thickness, r_e - the classical electron radius, N_A - Avogadro's number, m_e - electron mass, Z - atomic number of absorber, A - atomic mass of absorber, z - charge of incident particle, $\delta(\beta\gamma)$ - density effect correction to ionization energy loss, I - mean excitation energy, $K = 4\pi N_A r_e^2 m_e c^2 = 0.307075$ MeV g^{-1} cm^2, and T_{max} - maximum kinetic energy which can be transferred to a free electron in a single collision, which can be calculated using the following equation [241]:

$$T_{max} = \frac{2m_e c^2(\beta\gamma)^2}{1 + 2\frac{m_e}{m_K}\sqrt{1+(\beta\gamma)^2} + \left(\frac{m_e}{m_K}\right)^2}. \tag{5.5}$$

However experimentally the mean dE/dx is an ill-defined quantity. This is because the typical thickness of the PHOBOS spectrometer sensors, measuring the energy losses by charged particles, is ~ 0.032 cm (see Fig. 2.8 on page 59). For such thin silicon absorbers the ratio of the average energy loss to T_{max} is well below 0.01 (see Fig. 5.8 on the next page), and therefore the charged kaon energy losses are approximately described by the Landau distribution[241–243], which is highly-skewed with a long tail at high energy loss values due to rare large single collision energy transfers, making the mean of an experimental energy loss distribution subject to large fluctuations and sensitive to cuts and to background[169]. Therefore experimentally instead of the average energy loss, estimators of the most probable dE/dx often are used, which are found as the mean of 50-70% of the lowest dE/dx values in a sample[169].

Hits of a correctly reconstructed track represent a sample of the energy losses by the particle, which produced the hits. If the energy lost by the particle is much lower than its total energy, then with a good approximation all the hit dE/dx values could be thought of as drown from the same Landau distribution convoluted with the energy loss resolution. The reasons one has to deal with dE/dx values and not with the raw energy losses are:

- in general a charged particle intersects different spectrometer sensors at different angles as it propagates through the detector

[11] For the explanation of how dE/dx vs p could be used for kaon identification see section 5.12.2 on page 134.

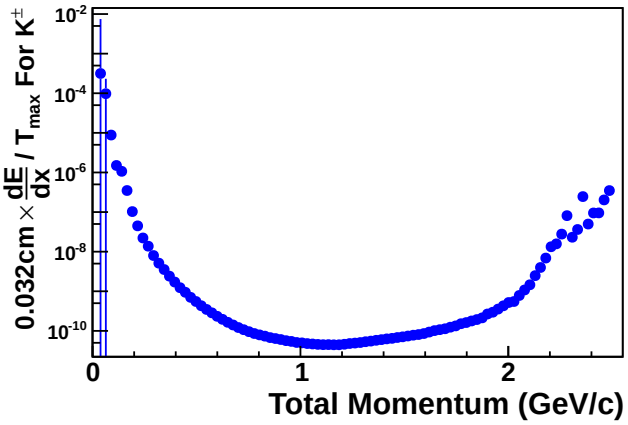

Figure 5.8.: The ratio of the truncated average energy loss (see section 5.5 on the preceding page) by a charged kaon in 0.032 cm of silicon to the maximum energy transfer in one collision as a function of total momentum. The ratio, found by MC simulations of the truncated average energy losses divided by T_{max} calculated using Eq. 5.5 on the previous page, is much lower than ~ 0.01 for all of the reconstructed charged kaons, indicating that the charged kaon energy loss distribution in the PHOBOS spectrometer is well described by the Landau distribution[241]. Note: technically, the truncated average energy loss is different from the mean energy loss by a factor of ~ 1.6, but it does not change the conclusion.

- the PHOBOS spectrometer sensors have different thickness (see Fig. 2.8 on page 59) [12]

and therefore the raw hit energy losses are the integrals of dE/dx over the length of the particle trajectory inside the sensors $\int \frac{dE}{dx} dx$, however it is of interest to sample energy losses by a particle in the same amount of material. It is useful to keep in mind that the goal of finding dE/dx values is to use them for particle identification (see section 5.12.2 on page 134), and so the precision of dE/dx reconstruction has to be just good enough for the purpose. At low total momentum, i.e. $p \leq 0.6$ GeV/c, where a track curvature in the spectrometer magnetic field is the highest, dE/dx distributions of pions, kaons and protons at any given p value are well separated and therefore a lower dE/dx resolution is affordable. At higher total momentum, and consequently at lower track curvature, a track shape approaches that of a straight line. Considering that, the following procedure was used to estimate the length $\mathscr{L}$ of a particle trajectory inside an intersected sensor where it produced a hit $\mathscr{H}$:

1. All the hits of a track containing $\mathscr{H}$ were sorted in ascending order of the layer number (see Fig. 2.10 on page 61).

[12] This fact was not taken into account in the standard PHOBOS reconstruction algorithm.

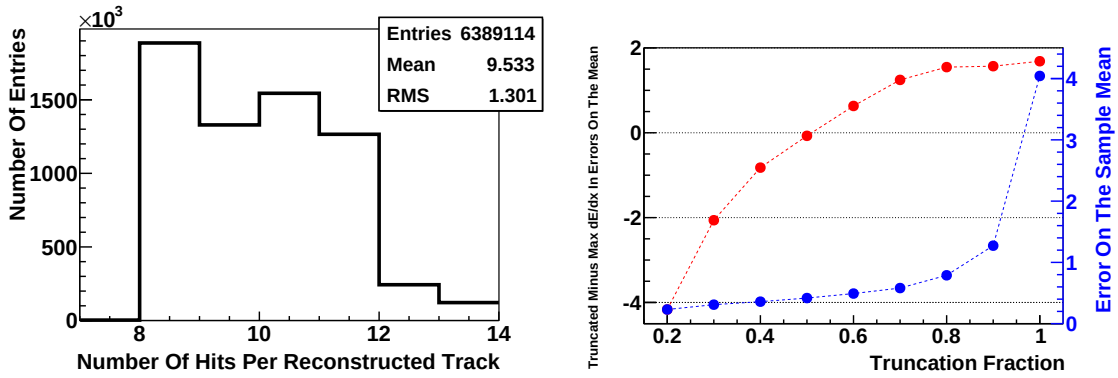

(a) Average number of hits per track ∼ 9.5

(b) Best most probable dE/dx at $\mathscr{T} \sim 50\%$

Figure 5.9.: (a) From MC study of single ϕ mesons embedded into real data events: average number of hits per track is ~ 9.5. (b) The figure shows in red color ((truncated mean dE/dx) - (most probable dE/dx)) divided by (sample error on the mean dE/dx) for 10 hit tracks drawn from a Landau distribution with most probable $dE/dx \sim 10$ and FWHM~ 4. One can see that the a non-shifted estimate on the true most probable dE/dx is achieved at the truncation fraction $\mathscr{T} \sim 50\%$. In blue color the figure shows sample error on the mean dE/dx for a Landau distribution with the same parameters. The error stops decreasing dramatically for truncation fractions $\mathscr{T} \leq 70\%$.

2. The hit $\mathscr{H}$ was connected with the next ($\mathscr{H}_{+1}$) and the previous ($\mathscr{H}_{-1}$) hit on the sorted list with straight lines.

3. The sensor containing hit $\mathscr{H}$ was described with a parallelepiped.

4. $\mathscr{L}$ was estimated as a sum of the lengths of the line segments $\mathscr{H}\mathscr{H}_{+1}$ and $\mathscr{H}\mathscr{H}_{-1}$, contained inside the parallelepiped.

5. If the hit $\mathscr{H}$ was either the first one or the last one on the list, then $\mathscr{L}$ was estimated as the length of the line, containing segment $\mathscr{H}\mathscr{H}_{+1}$ or $\mathscr{H}\mathscr{H}_{-1}$ correspondingly, inside the parallelepiped.

The raw hit $\mathscr{H}$ energy loss ΔE was divided by $\mathscr{L}$ to find dE/dx value corresponding to the hit.

Now that we have dE/dx values for all the hits of a track, it is possible to find an approximation of the track dE/dx. As it was pointed out above, often used estimators of the most probable track dE/dx are found as the mean of 50-70% of the lowest dE/dx values of its hits. In the current work, it was not important to find dE/dx very close to the true most probable dE/dx of a track, rather the goal was to reduce the fluctuations in the value in comparison to the full sample average, and therefore the truncation fraction $\mathscr{T}$ was chosen at 70%. If it was essential for the estimator of a track most probable

dE/dx to be close to the true value, the truncation fraction should have been chosen at 50% (see Fig. 5.9 on the previous page). The procedure of calculating a track truncated mean dE/dx was the following:

1. All track hit dE/dx values were found as described above. The values were subsequently sorted in an ascending order.

2. $\sim$ 70% of the lowest hit dE/dx values were selected. The mean and the Root Mean Square (RMS) of the sample were calculated in units of GeV/cm, which were afterward multiplied by the typical thickness of the PHOBOS spectrometer sensor of 0.032 cm (see Fig. 2.8 on page 59) and divided by 8×10^{-5} GeV/MIP (approximately the energy loss by a MIP in 0.03 cm of silicon).

5.6. Correcting For Data/MC Energy Loss Mismatch

The default PHOBOS MC simulation code does not reproduce correctly the energy losses of charged particles in the spectrometer silicon detectors - the simulated energy losses for kaons are $\sim$ 18.2% higher than those in data. Since the specialized kaon reconstruction checks consistency of a track hit energy losses with the track curvature and applies cuts on the average energy losses of a track hits subsets, the inconsistency of the MC energy losses with data has to be corrected for. Without the correction, the ϕ meson reconstruction efficiency, estimated on MC simulated single ϕ mesons embedded into real data events (see section 6.3.1 on page 150), would be evaluated incorrectly causing a large systematic error in the measurement of the ϕ meson invariant yield.

5.6.1. Kaon Total Momentum Reconstruction Systematic Error

The inconsistency between data and MC energy losses was discovered after the covariance matrices used for track fitting were generated (see section 5.10.4 on page 128), therefore, as it is explained in section 5.10 on page 123, in the final version of the specialized kaon reconstruction only hit positions were fit to estimate the total momentum and θ-angle of kaon tracks. Since MC tracks loose more energy as they propagate through the PHOBOS spectrometer, they are more curved than tracks in data at the same total momentum. Consequently the energy loss mismatch causes the kaon total momentum values to be *overestimated* during reconstruction in data, with a stronger effect at low kaon energies.

Let us estimate the effect of the data/MC energy loss mismatch on the reconstruction of a track total momentum. The energy loss estimations will be given in the format *worst-case-scenario / average*. For the purpose of an approximate effect scale estimation the factor $1/\cos(\alpha) \sim O(1)$, taking into account an angle of intersection of a track with a sensor, will be ignored (systematic error on the total momentum due to the data/MC energy loss mismatch is proportional to $1/\cos(\alpha)$). The average most probable energy lost (calculated as explained in section 5.5 on page 103) by a kaon in one silicon sensor of the PHOBOS spectrometer is about $\sim$ 16 / $\sim$ 1.37 times that of a MIP per 320 μm of

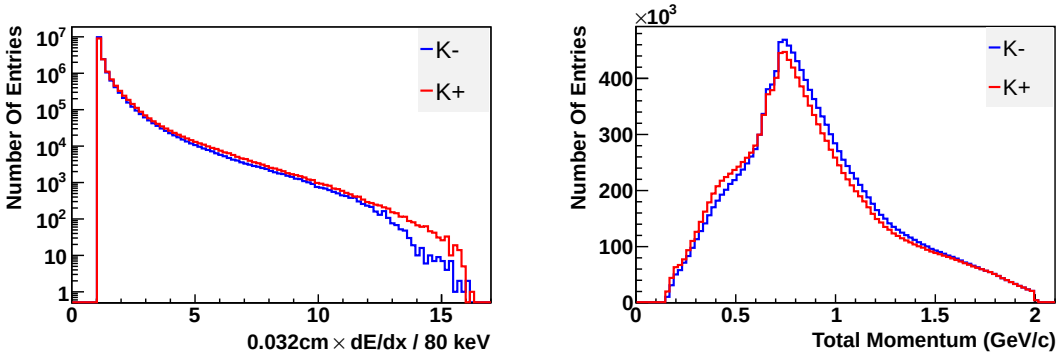

(a) dE/dx: maximal $\sim$ 16, average $\sim$ 1.37 (b) p: minimal $\sim$ 0.15 GeV/c, average $\sim$ 0.87 GeV/c

Figure 5.10.: dE/dx (a) and total momentum (b) of kaons used in the positive magnet polarity data analysis. Kaon dE/dx was scaled to 0.032 cm and MIP energy loss in $\sim$ 300 µm of silicon.

Si (which is $\sim$ 0.04 / $\sim$ 0.0034 GeV/cm) - see Fig. 5.10(a). For a typical silicon detector (thickness $\sim$300 µm) the average energy loss is $\sim$ 1.4 times the most probable one, therefore the average energy lost by a kaon in one silicon sensor is $\sim$ 0.06 / $\sim$ 0.005 GeV/cm. The typical thickness of the PHOBOS spectrometer sensors is $\sim$ 0.032 cm (see Fig. 2.8 on page 59), corresponding to the total energy lost $\sim$ 0.002 / $\sim$ 0.00015 GeV per one silicon sensor. Consequently the total energy lost by a kaon in the $\leq$ 16 layers of the PHOBOS spectrometer (see Fig. 2.10 on page 61) is $\sim$ 0.03 / $\sim$ 0.0026 GeV. Therefore the difference in the energy loss between data and PHOBOS MC is $\sim$ 0.005 / $\sim$ 0.0004 GeV (using factor 0.182 - see section 5.6.2 on the following page), which corresponds to $\sim$ 0.15 / $\sim$ 0.87 GeV/c total momentum kaons (see Fig. 5.10(b)) and systematic error in the track curvature (i.e. total momentum) of $\sim$ 12% / $\sim$ 0.06%). The procedure just described could be applied to the data on a track by track basis with the results shown on Fig. 5.11 on the next page. Now we find that the *worst-case-scenario / average* systematic errors on the kaon total momentum due to the data/MC energy loss mismatch is $\sim$ 5% / $\sim$ 0.08%. Even though the estimation does not take into account the angle of intersection of tracks with spectrometer sensors and does not use the exact number of intersected spectrometer layers, it could be used to get a sense of the size of the effect. As it will be pointed out in section 5.10 on page 123 the average total momentum resolution of the reconstruction procedure (measured on single kaon tracks embedded into real data events) is 3-7% (depending on kaon charge sign and layer pattern used for reconstruction), which shows that for majority of kaon tracks the effect of the data/MC energy loss mismatch is very small in comparison to the momentum reconstruction resolution (the systematic error is larger than 1% for only about $\sim$ 1% of tracks with $p < 0.23$ GeV/c), and therefore can be ignored [13].

[13] In addition to the data/MC energy loss mismatch, there is an other about $\sim$ 4 times larger (than the one just described) total momentum reconstruction systematic error, which arises due to the fact that

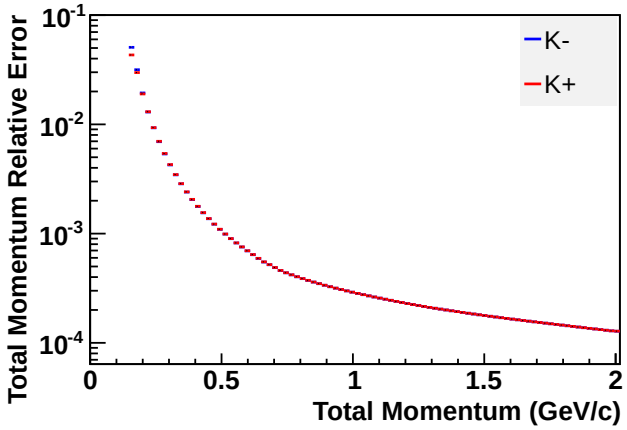

Figure 5.11.: Estimation of the scale of the kaon total momentum reconstruction systematic error, arising due to the mismatch between data and MC energy losses in the PHOBOS spectrometer.

5.6.2. Energy Loss Correction Factor

Kaons are the particles, that are directly reconstructed and identified during the data analysis, therefore the goal of the energy loss correction was to make sure that after the correction the *charged kaons* energy losses in MC would match those in data. However it is not known in advance which hits in data are produced by kaons, and not by some other charged particles. Consequently, the comparison between data and MC energy losses was made between the average most probable energy loss (calculated as explained in section 5.5 on page 103) by kaons reconstructed with the specialized kaon reconstruction algorithm applied on data and on single kaon events simulated by PHOBOS MC with subsequently scaled down energy losses. The comparison was made as a function of kaon reconstructed total momentum.

The energy loss correction can not be applied on the data spectrometer hits to scale their energy losses up since there would be a disagreement left between data and MC on the hit merging level (i.e. when spectrometer hits are created from hit arrays [14]). For example, some hit in MC simulations could have a high enough energy loss to pass a cut on hit energy losses and be added to the hit list, but a hit in data, produced by a particle with the same parameters as in the MC, could fail to satisfy the same cut. An other example, some entry in the MC spectrometer hit arrays could pass a noise removal threshold cut, but the same entry could be withdrawn from the subsequent analysis in data. Therefore, the energy loss correction has to be applied on the raw hit arrays and not on the spectrometer hits.

---

the track model used for track fitting (see section 5.10 on page 123) does not take into account any track energy losses at all. This effect was corrected for as described in section 5.13 on page 135.

[14] *Hit arrays* is the set of data on the energy deposited in all the channels (pads) of all the PHOBOS silicon detectors in a given event (the energy deposition in every channel is listed separately).

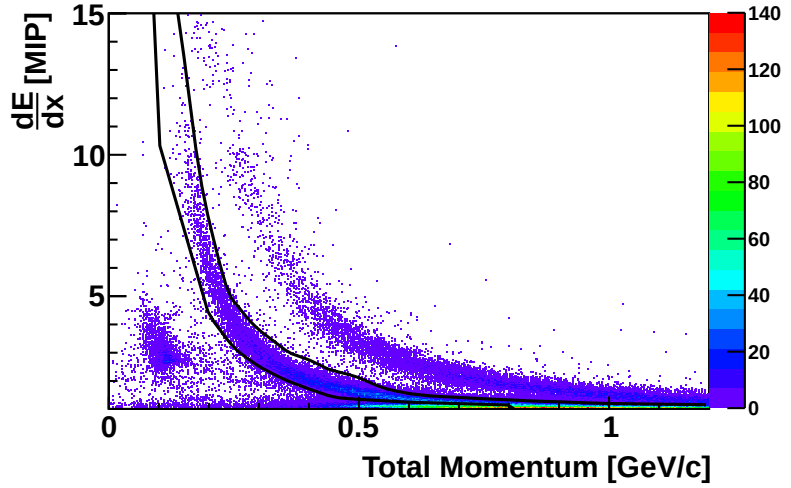

Figure 5.12.: dE/dx vs p cuts used to select kaons in positive magnet polarity data in order to find the scaling factor between MC and data kaon energy losses.

The factor, by which the MC kaon energy losses are higher than in data, was found using the following procedure:

1. Centrality bin number 1 (see Table 4.1 on page 83) data events at positive magnet polarity were reconstructed with the specialized kaon reconstruction algorithm. Very peripheral events were chosen for comparison to MC simulations to reduce as much as possible the probability of assigning to a kaon track a hit produced by an other particle, which is much less likely to happen in a low hit density environment. The kaon track selection and the total momentum correction were applied on the reconstruction results as described in sections 5.12 on page 133 and 5.13 on page 135 with one difference: the dE/dx vs p cuts were significantly more narrow around the kaon maximum in the dE/dx distribution at any given value of total momentum p (see Fig. 5.12). The reason of the tighter cuts was to reduce the fraction of pions and protons in the data kaon sample.

2. For every data kaon track, a single kaon MC event was simulated. The MC kaon vertex position, charge and momentum vector were chosen to be the same as for the reconstructed data kaon.

3. The MC event energy loss hit arrays were scaled down by a constant $\mathscr{C}$ and were used to create spectrometer hits. A track was created from those hits, which matched the hit array entries produced by the MC kaon [15]. If the resulting track layer pattern did not contain the data kaon layer pattern, the MC simulation was

[15] A spectrometer hit was considered to be matching, if it was made form at least one hit array entry, which was produced by the MC kaon.

repeated again, until either the layer pattern condition was satisfied or the maximum of 200 attempts was reached (in which case the data kaon track was omitted from further consideration). In case of success, the resulting MC event was saved.

4. The specialized kaon reconstruction was applied on the saved MC events the same way as it was applied on data.

5. The results of the specialized kaon reconstruction run on data and on MC single kaon events were matched on track by track basis, selecting only MC reconstruction results with the kaon reconstructed with a correct electrical charge.

6. The MC to data ratio of the kaon average most probable energy losses as well as the shapes of the dE/dx distributions in data and MC were compared for different reconstructed total momentum ranges (see Fig. 5.13 on the facing page). The scaling factor $\mathscr{C}$ (defined in step 3) was adjusted until a good agreement between the data and MC was reached at $\mathscr{C} = 1.1821$.

The final average ratio of the corrected MC to data kaon energy losses, resulted from the procedure described above, is 1.002 ± 0.001 (stat), with systematic deviations of the ratio not exceeding 1% for most total momentum values (see Fig. 5.13 on the next page). However up to 3-4% systematic deviations are observed at very low total momentum ($p < 0.23$ GeV/c), which are due to the imperfections of the momentum correction procedure (see section 5.13 on page 135). Only a very small fraction ($\sim 1\%$ - see section 5.6.1 on page 106) of kaons in data have such low total momentum, and therefore the overall systematic effect of the deviation on the measured ϕ meson invariant yield is small.

5.7. Straight Tracks Reconstruction

This section explains reconstruction of *straight tracks*, which are partially found full tracks containing hits in layers 1-6 only (see Fig. 2.10 on page 61). This was the 1st step of the specialized kaon reconstruction, performed on every event passing the event selection (see section 4.4 on page 78). The tracks are called straight because the layers 1-6 are positioned in a region of a very weak magnetic field (see section 2.2.5.3 on page 62), and therefore the tracks have a very low curvature [16].

Straight tracks were reconstructed separately in each arm of the PHOBOS spectrometer following the sequence of steps given below:

1. The set of allowed straight tracks layer patterns (see section 5.3 on page 98) was identified by going through the list of the layer patterns selected to be used in the specialized kaon reconstruction (see Table 5.2 on page 101), setting in each one

[16] Even though the curvature was very low, it was important to take it into account during the joining (see section 5.9 on page 120) of the straight and the Hough (see section 5.8 on page 113) tracks to reduce the number of resulting joined tracks to a level manageable by the computing resources (see section 3.1 on page 65) available for the current work.

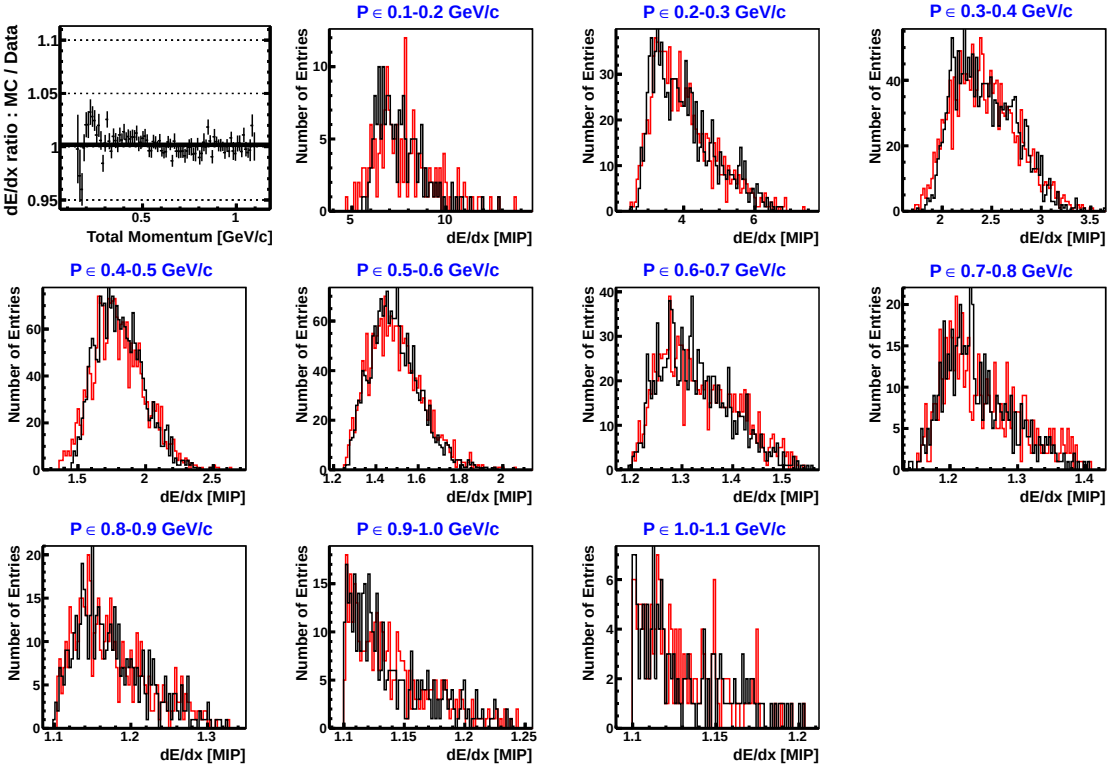

Figure 5.13.: Top-left plot shows the MC to data ratio of the kaon average most probable energy losses after the MC energy losses were scaled down by the factor of $\mathscr{C} = 1.1821$ (the black line is a fit of the ratio with a constant function). The remaining plots show the comparison of the shape of the data (red) and MC (black) kaon average most probable energy losses in ranges of the reconstructed total momentum.

bits corresponding to layer numbers 7-16 to zero, and choosing all the unique resulting layer patterns.

2. For each straight track layer pattern selected in step 1 a *seed layer pair* was identified as the two smallest layer numbers enabled in the pattern. Then all the unique pairs were chosen. Straight tracks were reconstructed separately for each such seed layer pair.

3. During the data taking the positions of RHIC beam orbits were measured and saved into a file. The reconstruction of every event started with looking up the beam orbit for the run, during which the event was recorded. The RHIC beam orbits are well approximated with a straight line over the length of the event vertex range used for the data analysis.

4. Two hit tracks were created from all the hit pairs in the currently used seed layer pair from the list found in step 2, so that the 1st hit was taken from the 1st seed

layer and the 2nd one was taken from the 2nd seed layer. Each such track was approximated with a straight line and was assigned a vertex position on the line with the smallest distance to the beam orbit line found in step 3.

5. Starting from the 2nd seed layer number plus one, steps 6, 7, 8, and 9 were performed for all layer numbers $n \leq 6$.

6. Every track from the list of tracks created so far was added a hit (let us call it $\mathscr{H}_+$) in layer n, provided n is greater than the maximal layer number m in which the track has a hit (let us call it $\mathscr{H}$), if hits $\mathscr{H}_+$ and $\mathscr{H}$ have θ-angle and φ-angle with respect to the track vertex such that

$$|\theta(\mathscr{H}_+) - \theta(\mathscr{H})| < \Delta\theta, \qquad |\varphi(\mathscr{H}_+) - \varphi(\mathscr{H})| < \Delta\varphi.$$

   If more than one hit could be added to the track, the necessary number of the track copies were made, and each hit satisfying the conditions just given was added to one of the copies. Parameters $\Delta\theta$ and $\Delta\varphi$ were different depending on the layer number m.

   Selection of parameters $\Delta\theta$ and $\Delta\varphi$. The parameters were chosen based on the MC simulation of single kaon events described in section 5.4 on page 101 performed for the set of layer patterns summarized in Table 5.3 on the next page. Namely, RMS of the $\theta(\mathscr{H}_{k+}) - \theta(\mathscr{H}_k)$ distribution was calculated for each used (kaon charge × layer pattern) combination and for each layer number k separately, where $\mathscr{H}_k$ is a hit produced by a simulated kaon in layer k and $\mathscr{H}_{k+}$ is a hit in a layer with the smallest layer number greater than k in which the kaon has a hit. The parameter $\Delta\theta$ corresponding to layer k was set to be 5 times the maximal RMS value of the distributions $\theta(\mathscr{H}_{k+}) - \theta(\mathscr{H}_k)$ among all the used (kaon charge × layer pattern) combinations. Parameter $\Delta\varphi$ was calculated in an analogous way to $\Delta\theta$, but using $\varphi(\mathscr{H}_{k+}) - \varphi(\mathscr{H}_k)$ distributions instead.

7. Every track created in step 6 was checked to have a layer pattern containing (see section 5.3.1 on page 98 for explanation) one of the layer patterns found in step 1 after the layer patterns had all of their bits in layers greater than m unset, where m is the maximal layer number in which the track has a hit. If the condition was not satisfied, the track was omitted from further consideration.

8. The hit positions of every track passing the step 7 selection were fitted with a straight line and checked to have the fit probability greater than 0.0005. If the condition was not satisfied, the track was omitted from further consideration.

9. If the total number of tracks created so far was more than 1000 and the last layer number n hits from which were added to the tracks (see description of steps 5 and 6) was greater than 3, then every track passing the step 8 selection was checked to have not more than 3 hits shared with some other track. If two such tracks

K^+	K^-
1111-1101-1111-0000	1111-1101-1110-1110
0011-1101-1111-1010	1110-1101-1111-0000
1111-1101-1111-1010	1111-1101-1111-1010
0011-1111-1111-1010	0011-1111-1110-1110
1111-1110-1110-1011	0011-1101-1110-1011
1111-1111-1111-1011	1111-1101-1111-1011
1110-1001-1011-1111	1111-1111-1111-1011
1100-1101-1111-1111	1111-1111-1110-1111
1111-1101-1111-1111	1010-1001-1111-1111
	1111-1101-1111-1111

Table 5.3.: Layer patterns used to calculate $\Delta\theta$ and $\Delta\varphi$ parameters of the straight tracks reconstruction. The set of layer patterns was used for historical reasons.

were found, the one with smaller fit probability found in step 8 was omitted from further consideration.

10. This step is analogous to step 9, except that no condition was imposed on the number of tracks created so far and the maximal number of allowed shared hits between two tracks was set to one.

The average efficiency of the straight line tracking thus implemented measured on single kaons, resulting from the realistic ϕ meson decays MC simulation (see section 5.2 on page 94), embedded into real data events with MC energy losses corrected as explained in section 5.6.2 on page 108, was 97-100%, depending on a (kaon charge × layer pattern) combination (see Table 5.2 on page 101). The average time spent per event by this part of the specialized kaon reconstruction in the used data vertex z-coordinate range was 0.77 seconds which was 4.2% of the total reconstruction time.

5.8. Hough Tracks Reconstruction

This section explains reconstruction of *Hough tracks*, which are partially found full tracks containing hits in layers 9-16 only (see Fig. 2.10 on page 61). This was the 2nd step of the specialized kaon reconstruction, performed on every event passing the event selection (see section 4.4 on page 78). The tracks are called Hough since the tracking idea is based on the algorithm of parameterizable patterns recognition using the "Hough transform"[244, 245].

5.8.1. Hough Transform Pattern Recognition

The concept of the pattern recognition employing the Hough transform utilizes a *voting scheme* the following way:

1. Overall pattern is broken into a set of subpatterns in such a way that each subpattern can be described by the same set of parameters as the overall pattern.
2. Parameters of each subpattern are determined. Conversion of the subpatterns into the space of their parameters is the *"Hough transform"*.
3. Overall parameter space is discretized into an N-dimensional table of bins, where N is the number of parameters used to describe the pattern.
4. One entry per each subpattern set of parameters is added to a corresponding bin of the table. Therefore each subpattern *votes* for some set of parameters, which (from its "point of view") describes the whole pattern.
5. The parameters of the overall pattern are determined as the average of the parameters falling into the bin (or adjacent bins) with the maximum number of counts.

The scheme can also be used to group subpatterns, which are parts of same overall pattern. Namely, if the difference in parameters of some subpatterns is significantly larger than what could be accounted for by the noise in the system, it is an evidence that the subpatterns are not parts of the same pattern.

5.8.2. Implementation

To motivate the implementation, let us first consider the simplest case of a particle moving perpendicular to the lines of a uniform magnetic field. The trajectory of the particle in such case is going to be a circle in a plane perpendicular to the field vector. It is known from geometry that for any three points on a plane, which are not located on the same line, it is possible to draw a circle through the points and only one such circle exists. Therefore any three points on the particle trajectory fully define it. Once the particle path is know, so is the direction of the particle momentum in any point. Moreover, the curvature of the circle uniquely defines the total momentum of the particle.

Layers 9-16 of the PHOBOS spectrometer are positioned in a non-uniform magnetic field (see section 2.2.5.3 on page 62), however the majority of the layer sensors is located in a roughly constant field of 2 Tesla. The field direction is approximately perpendicular to the spectrometer plane. The acceptance of the spectrometer along the φ-angle is small, namely $[-0.15, +0.15]$ and $[\pi - 0.15, \pi + 0.15]$ radians in positive and negative arm of the spectrometer correspondingly, and therefore all the charged kaons, which produce enough hits in the spectrometer detectors to be reconstructed, move almost in one plane nearly perpendicular to the magnetic field.

As can be seen, the real life reconstruction conditions are close to the perfect ones [17]. It motivates using a Hough transform for reconstructing tracks in layers 9-16 of the

[17] It must be possible to prove mathematically rigorously that any three points on a charge particle trajectory in a static magnetic field fully define the former, and so the general idea of the trajectory reconstruction discussed here is applicable to any static magnetic field and any orientation of the trajectory with respect to it (in a case of a more complicated configuration than the one in the PHOBOS detector, one would have to allow for a correspondingly larger number of parameters describing a particle trajectory). However, I do not know of anybody having provided such a proof.

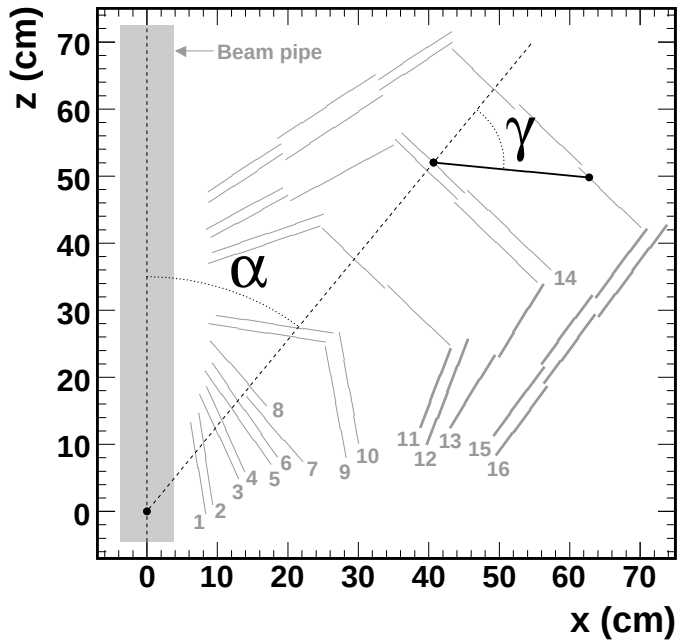

Figure 5.14.: The parameters which were used to approximately fix the coordinates of the three stick points are angles α and γ and vertex z-coordinate (this figure is a modified version of the one taken from [212]).

PHOBOS spectrometer. In this case the pattern is the particle trajectory, and a subpattern is a set of three points on the trajectory, which were chosen to be the event vertex and some two consecutive hits produced by the particle. Any such subpattern will be called a *stick* in the following algorithm description. The parameters which describe any (sub)pattern are the θ-angle at which the particle was produced, its charge q, and the reciprocal of its total momentum $1/p$. The Hough transformation here is the conversion of a stick three points coordinates into a set of parameters $(\theta, q, 1/p)$. The coordinates of the three stick points were described *for a given pair of spectrometer layers* by (see Fig. 5.14):

- event vertex z-coordinate v_z
- the θ-angle of the projection of the 1st stick hit onto the $y = 0$ plane, i.e. α-angle on the figure
- the angle between (all the projections were made onto the $y = 0$ plane)
  - the line connecting the event vertex and the projection of the 1st stick hit
  - the line connecting the projection of the 1st stick hit and the projection of the 2nd stick hit,

  i.e. γ-angle on the figure.

For any v_z in the range of event vertex z-coordinates used for the data analysis in this thesis (see section 6.1.2.2 on page 141), angles α and γ uniquely define positions of both hit projections of a stick onto the $y = 0$ plane, as the lines connecting the stick points (see Fig. 5.14 on the previous page) could have only one intersection with each spectrometer layer in which there is a hit of the stick [18].

5.8.2.1. Hough Tables

The Hough transformation was implemented as a set of look up *Hough tables*.

The Hough tables used in the specialized kaon reconstruction were different from those used in the standard PHOBOS reconstruction. The main reasons for that are:

- The measurement of the ϕ meson invariant yield using PHOBOS data was made possible by extending the reconstruction in to the forward region of the spectrometer (see section 5.1 on page 89), where the hit density is very high. The design of the Hough tables was critical for limiting the number of possible track candidate hit combinations (which otherwise would be essentially infinite from a practical point of view) to be considered by the next steps of the specialized kaon reconstruction .

- The goal was to reconstruct kaons only with rather low total momentum values, at which the kaon identification using the dE/dx vs p method (see section 5.12.2 on page 134) is possible, and this fact was used extensively to suppress the reconstruction of other kinds of particles (not charged kaons). Without the suppression the total CPU reconstruction time necessary to finish the data analysis would be prohibitively high. The suppression was the sole existence purpose of some of the tables.

The following Hough tables were used:

$\boldsymbol{\theta(\alpha,\gamma,\mathrm{dE/dx})}$: θ-angle associated with a stick as a function of α, γ, and $dE/dx = (dE/dx_1 + dE/dx_2)/2$, where dE/dx_1 and dE/dx_2 are the dE/dx values of the two hits of the stick, calculated as explained in section 5.5 on page 103, treating the two hits as a 2-hit track. Table size was $20 \times 20 \times 40$ bins.

$\boldsymbol{(1/\mathrm{p})(\alpha,\gamma,\mathrm{dE/dx})}$: $1/p$ value associated with a stick as a function of α, γ, and dE/dx. Table size was $20 \times 20 \times 40$ bins.

$\boldsymbol{\varphi(\varphi_1,\varphi_2)}$: φ-angle associated with a stick as a function of φ-angle of the two hits of the stick φ_1 and φ_2. Table size was 20×20 bins.

[18] The only exception could originate from small overlaps of some sensors in the same layer, which make two intersections of the lines with their corresponding layer possible. It introduces extra small noise into the reconstruction, in addition to deviation of the system from the perfect one, multiple scattering, and fluctuations of energy losses of charged particles as they propagate through the material of the PHOBOS spectrometer.

$(\mathbf{1/p})(\mathbf{dE/dx_1}, \mathbf{dE/dx_2})$: $1/p$ value associated with a stick as a function of dE/dx_1 and dE/dx_2. Table size was 20×20 bins.

The 1st idea used in the Hough table design was to add some redundant information to the tables in such a way that only sticks compatible with being produced by a kaon would have corresponding entries in the tables. If an empty bin of such a table corresponds to a stick, then the stick can be discarded from being subsequently used in the reconstruction. For example, if in addition to the parameters α and γ a dE/dx value associated with a stick is added, then one essentially implements the dE/dx vs p kaon identification method on a stick level, since α and γ alone are enough to determine the stick total momentum. Consequently, if a given $(\alpha, \gamma, dE/dx)$ combination corresponds to an empty bin in the Hough table, the corresponding stick could not belong to a kaon trajectory and can be neglected. As an other example, it is unlikely that two hits of the same stick would have very different φ-angle or dE/dx values, therefore if no entry is found in a Hough table for a value for one hit versus the value for the other hit, then the stick could be omitted during reconstruction.

The 2nd design idea was to check for consistency in the extra information between different sticks of a track candidate. Since it is unlikely for different sticks of the same track to have very different p, dE/dx , θ-angle or φ-angle, track candidates with large errors on the parameters, determined by considering any stick of a track as an independent measurement of the parameters, could be discarded.

Each table only allowed the difference between the y-coordinate of the 1st and the 2nd hit of a stick to be less than a certain value, summarized in Table 5.4. If not the stick was rejected from being used in the reconstruction of Hough tracks.

Layer Number	9	10	11	12	13	14	15	16
Max Δy (cm)	1.5	2.5	3.0	3.0	3.0	3.0	3.0	3.0

Table 5.4.: Maximal allowed difference between the y-coordinate of the 1st and the 2nd hit of any stick.

Filling of the Hough tables. Hough tables were filled using the single kaon event MC simulations (see section 5.4 on page 101) separately for each (kaon charge × layer pattern) combination (see Table 5.2 on page 101). For every such combination a separate set of tables was filled for each of the 200 vertex bins in the range $[-35, +15]$ cm and for each of the two consecutive bits, corresponding to layers 9-16, enabled in the layer pattern of the combination [19]. The tables for a given (kaon charge × layer pattern) combination were filled by going through the list of all the generated single kaon MC events, selecting only those which were generated with the same kaon charge and with a layer

[19] Such consecutive bits define the numbers of the layers, hits from which are to be used to create sticks utilized in tracking. For example, if the layer pattern is 0000-0000-1101-0001, then the layer pairs used are (9,10), (10,12), and (12,16).

pattern which contains (see section 5.3.1 on page 98) the layer pattern of the currently filled set of Hough tables. Each table cell contained the mean and the standard deviation of the corresponding sample of sticks from the MC simulations used to fill the table. The ranges of a table variables were determined before filling the table by looking at all the single MC kaons to be used to fill the table and finding the extreme values of each variable.

5.8.2.2. Hough Tracks Creation Procedure

Reconstruction of Hough tracks was done separately for every (kaon charge × layer pattern) combination. The proper set of tables to be used in the reconstruction was chosen based on the OneTrackVertex z-coordinate of an event, which was found as described in section 4.3.2 on page 77.

The sequence of steps followed during reconstruction is given below:

1. For each layer pair, corresponding to two consecutive bits enabled in the layer pattern, drawing the 1st hit from the first layer and the 2nd hit from the second layer, all the possible two hit combinations were made. A stick was made from every such hit combination if the Hough transformation (implemented as described in section 5.8.2.1 on page 116) is defined on the stick. Or putting it simply, a stick was made if it was possible to compute its parameters using all the four Hough tables [20]. Each stick parameter was assigned a value and an error equal to the mean value and the standard deviation of the parameter Hough table cell corresponding to the stick.

2. The sticks were joined in to *chains*, starting with the sticks corresponding to the smallest layer numbers and adding new ones one by one. Each new stick added to a chain was required to have its first hit equal to the second hit of the last stick the chain had before the addition.

3. If after an addition of a stick to a chain, the later was 3 or more sticks long, the truncated average energy loss of the chain was calculated by correcting all of the hit energy losses for an angle of incidence, selecting the ∼70% of the lowest hit energy losses of the chain, and calculating their mean and "RMS" as

$$(dE/dx)_{\text{mean}} = \frac{\sum_{i=1}^{N}(dE/dx)_i}{N \cdot \Delta E_{MIP}},$$

$$(dE/dx)^2_{\text{RMS}} = \frac{\sum_{i=1}^{N}\left((dE/dx)_i - (dE/dx)_{\text{mean}}\right)^2}{N \cdot \Delta E^2_{MIP} \cdot (dE/dx)_{\text{mean}}},$$

where $(dE/dx)_i$ is the corrected for an angle of incidence energy loss of a hit i, N is the number of such used hit energy losses, and ΔE_{MIP} (for a definition, see

[20] There are two tables computing $1/p$ value for a stick resulting in two versions of the parameter. Both versions were found and saved.

section 4.2 on page 74) was set to a fixed number of 80 keV. The angle of incidence (denoted here as α) correction was done by multiplying a hit energy loss by $\cos(\alpha)$. No correction for a sensor thickness was done, and so in the above formulas $(dE/dx)_i$ have units of energy, and therefore the calculated mean and "RMS" of a chain are dimensionless variables. The angle α was estimated from a fit of all the chain hits projections onto the $y = 0$ plane with a parabola, and calculating the angle of incidence between the parabola and a hit sensor. A chain was removed from the list of Hough track candidates if $(dE/dx)_{\text{RMS}} > 1.0$ or if

- $(dE/dx)_{\text{mean}} < 1.0$ for ϕ meson $p_t > 0.39$ GeV/c data analysis,
- $(dE/dx)_{\text{mean}} < 1.4$ for ϕ meson $p_t < 0.13$ GeV/c data analysis.

4. After each addition of a stick to a chain, value and "error" of a parameter a of the chain were assigned according to:

$$a = \frac{\sum_{i=1}^{N} \frac{a_i}{\sigma^2_{a_i}}}{\sum_{i=1}^{N} \frac{1}{\sigma^2_{a_i}}}, \tag{5.6}$$

$$\sigma^2_a = \frac{1}{N^2} \sum_{i=1}^{N-1} \left(\frac{a_{i+1} - a_i}{\sqrt{\sigma^2_{a_{i+1}} + \sigma^2_{a_i}}} \right)^2, \tag{5.7}$$

where N is the number of sticks in the chain, and a_i and $\sigma^2_{a_i}$ are the parameter a value and variance corresponding to a stick number i of the chain. In Eq. 5.6 and 5.7 a is one of the parameters θ, $1/p$, or φ, calculated using Hough tables $\theta(\alpha, \gamma, dE/dx)$, $(1/p)(\alpha, \gamma, dE/dx)$, and $\varphi(\varphi_1, \varphi_2)$ correspondingly (see section 5.8.2.1 on page 116) [21,22]. As can be seen, if a chain consisted of one stick only, any parameter a of the chain was just equal to the corresponding stick parameter with a vanishing error.

5. A stick S was added to a chain C if the following compatibility conditions between the two were satisfied:
   - $\Delta\theta < \Delta\theta_{\text{max}}$,
   - $\Delta(1/p) < \Delta(1/p)_{\text{max}}$,
   - $\Delta\varphi < \Delta\varphi_{\text{max}}$,
   - $\delta(1/p) < \delta(1/p)_{\text{max}}$,

   where

$$\Delta a = \frac{|a_C - a_S|}{\sqrt{\sigma^2_{a_C} + \sigma^2_{a_S}}}, \qquad \delta(1/p) = \frac{|(1/p)_{LSC} - (1/p)_S|}{\sqrt{\sigma^2_{(1/p)_{LSC}} + \sigma^2_{(1/p)_S}}},$$

[21] There was an exception in Eq. 5.6 for parameter $1/p$, i.e. if the first hit of a stick was in layer 9, it was skipped during the sums calculation, except the cases when the stick was the only one in a chain.

[22] Parameter $1/p$ calculated for a stick using a $(1/p)(dE/dx_1, dE/dx_2)$ Hough table, was not assigned for any chain.

a was defined above in the list item number 4, a_C and a_S are the parameters a of the chain and of the stick respectively, σ_{a_C} and σ_{a_S} are the parameter a errors of the chain and of the stick correspondingly, $(1/p)_{LSC}$ and $(1/p)_S$ are $1/p$ values calculated respectively for the **L**ast **S**tick [23] of the **C**hain C and the stick S using a $(1/p)(dE/dx_1, dE/dx_2)$ Hough table, $\sigma_{(1/p)_{LSC}}$ and $\sigma_{(1/p)_S}$ are their corresponding errors, $\Delta\theta_{\max} = 3.0$, $\Delta(1/p)_{\max} = 5.5$, $\Delta\varphi_{\max} = 1.5$, and $\delta(1/p)_{\max} = 2.5$.

6. The final chains were required to satisfy the following conditions:

$$\sqrt{\frac{1}{N}\sum_{i=1}^{N}\left(y_i^{(1)} - y_i^{(2)}\right)^2} < 1.5 \text{ cm},$$

$$\sqrt{\frac{1}{N-1}\sum_{i=1}^{N-1}\left(\left(y_{i+1}^{(1)} - y_{i+1}^{(2)}\right) - \left(y_i^{(1)} - y_i^{(2)}\right)\right)^2} < 2.5 \text{ cm},$$

$$\sqrt{(2\sigma_\theta)^2 + (\sigma_{1/p} - \sigma_\theta)^2} < 1.5,$$

where $y_i^{(1)}$ and $y_i^{(2)}$ are the 1st and the 2nd hits of the stick number i of a chain, and the other variables were defined above in the list item number 4. If any of the above conditions failed to be true for a chain, the chain was deleted from the final list of Hough tracks.

5.9. Joining Of Straight And Hough Tracks

At this step of the track reconstruction, compatible straight (see section 5.7 on page 110) and Hough (see section 5.8 on page 113) tracks were *joined* together to produce full track candidates.

The following sequence of steps was performed in the implementation of the joining procedure:

1. Truncated mean dE/dx was calculated for all straight and for all Hough tracks as explained in section 5.5 on page 103. Those are the dE/dx values used in the algorithm description below. The same dE/dx calculation method was also used for full (joined) tracks.

2. In the tracking designed for the ϕ meson $p_t < 0.13$ GeV/c data analysis, all the straight tracks with $dE/dx < 1.4$ were removed from further reconstruction. No such removal was done in the tracking designed for the ϕ meson $p_t > 0.39$ GeV/c data analysis.

3. All Hough chains satisfying the following conditions:
   - $dE/dx < 1.0$ for ϕ meson $p_t > 0.39$ GeV/c data analysis

[23] I.e. the one which shares a hit with the stick S and has the highest layer numbers of its hits.

- $dE/dx < 1.4$ for ϕ meson $p_t < 0.13$ GeV/c data analysis

were removed from further reconstruction [24].

4. Track joining was done separately for every possible (kaon charge × layer pattern) *combination*. At every such combination joining was done between:
   - all the straight tracks which had a layer pattern that contained the combination layer pattern in layers 1-6,
   - all the Hough tracks which had the same kaon charge as the combination and a layer pattern that contained the combination layer pattern in layers 9-16.

   It was also required that the final joined tracks had a layer pattern which contained the combination layer pattern, which was necessary to make sure that the joined tracks could be fit at a later stage of the specialized kaon reconstruction (see section 5.10 on page 123).

5. Let us introduce the following selection criteria:

$$|X_{\text{obs}} - X_{\text{exp}}| < n_\sigma \cdot \sigma_{\text{exp}}, \tag{5.8}$$

   where X_{obs} is an observed value of some variable, X_{exp} and σ_{exp} are the expected mean and the width (RMS) of the distribution of the variable for correctly reconstructed tracks estimated based on MC simulations, and n_σ is the maximum allowed difference $|X_{\text{obs}} - X_{\text{exp}}|$ expressed in units of σ_{exp}.

   The criteria was applied during joining of a straight track and a Hough chain into a full track on the following variables:
   - dE/dx of the Hough chain as a function of the chain total momentum,
   - dE/dx of the full track as a function of the chain total momentum,
   - the difference between the straight track and the Hough chain θ-angles as a function of the straight track θ-angle, the chain total momentum, and the z-coordinate of the event OneTrackVertex,
   - the difference between the straight track and the Hough chain dE/dx as a function of the straight track θ-angle, the chain total momentum, and the z-coordinate of the event OneTrackVertex,
   - χ^2_{ry} as a function of the straight track θ-angle, the chain total momentum, and the z-coordinate of the event OneTrackVertex. χ^2_{ry} is the reduced chi-squared of:
     - y-coordinates of hits of the chain,
     - y-coordinate of the event OneTrackVertex (denoted below as y_{otv}),

[24] The difference between this step and seemingly the same cuts explained on page 118 is the method of calculating Hough chains dE/dx values.

with respect to the straight line

$$y(l) = \frac{p_y}{\sqrt{p_x^2 + p_z^2}} \cdot l + y_{\text{otv}},$$

where l is the length (from the OneTrackVertex to the point of interest) of the linear spline of the chain projection onto the $y = 0$ plane. So,

$$\chi^2_{ry} = \frac{1}{N} \sum_{i=1}^{N} \frac{(y(l_i) - y_i)^2}{\sigma^2_{yi}},$$

where y_i is the y-coordinate of the hit number i, l_i is the length l (discussed above) to the projection of the hit number i onto the $y = 0$ plane, N is the number of hits in the chain, and σ_{yi} is equal to the vertical size of the silicon sensor pad corresponding to hit i divided by $\sqrt{12}$.

The functional dependence of the variables on their arguments was implemented as a set of tables of dimensionality equal to the number of the arguments. Each table cell contained information about the mean and the width of the variable distribution in the cell (corresponding to X_{exp} and σ_{exp} in Eq. 5.8 on the preceding page). The tables were filled by running the straight line and the Hough tracks reconstruction (as well as an unconditional joining of the two types of tracks) on single kaon MC events (see section 5.4 on page 101). The n_σ parameter was chosen to be 4.0 for all the discussed variables. A straight line track and a Hough chain were allowed to be joined into a full track only if the Eq. 5.8 on the preceding page selection criteria was satisfied for all the variables.

If an argument of some variable fell outside of its range in the corresponding implementation table [25], the following

- $X_{\text{exp}} = 0$, $\sigma_{\text{exp}} = +\infty$,
- $X_{\text{exp}} = 0$, $\sigma_{\text{exp}} = +\infty$,
- $X_{\text{exp}} = 0.007$, $\sigma_{\text{exp}} = 0.0075$,
- $X_{\text{exp}} = -0.016$, $\sigma_{\text{exp}} = 0.075$,
- $X_{\text{exp}} = 2.3$, $\sigma_{\text{exp}} = 2.4$.

default values were used (the order corresponds to the list of the used variables given above).

The parameters of a resulting from a successful joining full track were assigned as the θ- and the φ-angles of the input straight track, and the total momentum and the charge sign of the input Hough chain.

6. In the very end of the joining procedure, one more dE/dx versus total momentum (denoted here as p) selection was applied on the full joined tracks:

[25] Chain total momentum: 200 bins in the 0.001-10 GeV/c range, straight track θ-angle: 20 bins in the 0-π range, and z-coordinate of an event OneTrackVertex: 5 bins in the $[-35, +15]$ cm range.

- for ϕ meson $p_t > 0.39$ GeV/c data analysis:
  - $dE/dx > 1.10$ if $p < 0.7$ GeV/c
  - $dE/dx > 1.05$ if $p \geq 0.7$ GeV/c
  - $dE/dx > (4 - 8 \cdot p)$ if $p < 0.25$ GeV/c, where p is in GeV/c
  - $dE/dx > (19/7 - 20/7 \cdot p)$ if $p \geq 0.25$ GeV/c, where p is in GeV/c
- for ϕ meson $p_t < 0.13$ GeV/c data analysis: $dE/dx > 1.4$

5.10. Track Fitting

At this stage of the specialized kaon reconstruction the joined tracks (see section 5.9 on page 120) were *fit*, the purpose of which was twofold:

- to estimate precisely the momentum and the origin point (vertex) of a reconstructed track,
- to evaluate quantitatively the quality of the track.

Track fitting was done separately for every possible (kaon charge × layer pattern × PHOBOS spectrometer arm) *combination*.

The production point and the momentum vector of a particle will be called the *particle parameters* [26]. The fitting procedure was implemented as a minimization (see section 5.10.5 on page 131) of the chi-squared of the hit positions of a track with respect to a *track model*, which is an estimate of the average trajectory of a particle having the same parameters as the track:

$$\chi^2 = \sum_{i,j} T_i(d_i) \cdot \mathrm{cov}^{-1}(i,j) \cdot T_j(d_j), \tag{5.9}$$

where the indices i and j denote the hits of the track, the summation is done for all the hits of the track, d_i is the distance between the projections onto the $y = 0$ plane of the hit i and of the track model trajectory (see section 5.10.3 on page 126), $T_i(d_i)$ is the transformation (see section 5.10.2 on page 125) applied on the distance d_i, and $\mathrm{cov}^{-1}(i,j)$ is the inverted covariance matrix of the variables $T_i(d_i)$ (see section 5.10.4 on page 128). The track parameters at which the minimum χ^2 value was reached were assigned as the parameters of the corresponding reconstructed particle. The fit probability (see section 5.10.6 on page 132), corresponding to the found minimum χ^2 value, served as a quantitative measure of the quality of the track.

[26] As well, the parameters of the particle, which corresponds to a track, will be termed the *track parameters*.

5.10.1. Fitting Of Hit Energy Losses Of A Track

The fitting procedure originally included as well a calculation of the chi-squared of the hit energy losses of a track with respect to the average ones, which were estimated by performing MC simulations of a physical particle with the same parameters as the track. However, since it was discovered that the MC did not reproduce correctly the hit energy losses observed in data (see section 5.6 on page 106), it was decided to not use the energy losses information during fitting to avoid any unnecessary biases in the reconstruction of the total momentum of a track. In addition, any mismatch between the MC and the data energy losses causes the minimum value of χ^2 to be reached for different track parameters in the fit of the hit positions of a data track versus the fit of the hit energy losses of the track, which causes the majority of the data tracks to have very low fit probability. The later leads to a good efficiency of a tracking using the combined fitting of the hit positions and of the hit energy losses of tracks when applied on MC simulated events. However, the efficiency of such tracking when applied on data would be very low. It is possible to correct for the mismatch between the data and the MC energy losses (see section 5.6), however after that one would have to:

- Recreate all the covariance matrices used in the fitting, which is a time consuming procedure requiring about a month of computing time on ∼600 CPUs (the energy loss mismatch was discovered after all the needed covariance matrices were created).

- Create at least one more set of the covariance matrices with appropriately different correction of the MC energy losses to estimate the systematic error associated with the correction procedure (that is an other month of using all the PHOBOS computing resources).

- Run both versions of the tracking (with both sets of the covariance matrices) on data. However, one reconstruction of the PHOBOS Cu+Cu $\sqrt{s_{\mathrm{NN}}} = 200$ GeV data (with the final version of tracking used in this thesis, which requires less computing resources than the one with a combined fit of the hit positions and of the hit energy losses) takes 3-4 months using all of the PHOBOS computing resources plus a significant part of such resources of other RHIC experiments (when they are idle and therefore available for other experiments) to reconstruct the vertex range ($v_z \in [-5,+15]$ cm) used for the intermediate ϕ meson transverse momentum ($p_t > 0.39$ GeV/c) data analysis and about the same amount of time to reconstruct the vertex range ($v_z \in [-25,-5]$ cm) used for the lowest ϕ meson transverse momentum ($p_t < 0.13$ GeV/c) data analysis [27]. And that was an unaffordable amount of not only computing but also personal time which had to be invested, while other more urgent parts of the data analysis had to be finished and understood.

Therefore, the decision was made to use only the hit positions of tracks in the final fitting procedure.

[27] Here v_z is the z-coordinate of the OneTrackVertex (see section 4.3.2 on page 77) of an event.

5.10.2. Transformation

Let us consider two random variable vectors $\vec{\xi}$ and $\vec{\eta}$ (each vector has n variables) such that $\vec{\xi} = C\vec{\eta}$, where C is a constant $n \times n$ matrix. If $D_{\vec{\xi}}$ and $D_{\vec{\eta}}$ are the covariance matrices of the variables $\vec{\xi}$ and $\vec{\eta}$, then as well known from statistics [246]:

$$D_{\vec{\xi}} = C D_{\vec{\eta}} C^{\mathsf{T}},$$

where T denotes finding the transpose of a matrix. If $\vec{\xi}$ is a vector of independent variables, each of which has a Gaussian distribution with the zero mean and the unit width, then

$$\chi^2_n = \left(\vec{\xi}\right)^{\mathsf{T}} \vec{\xi} = \left(\vec{\eta}\right)^{\mathsf{T}} D^{-1}_{\vec{\eta}} \vec{\eta}, \tag{5.10}$$

where variable χ^2_n has (by definition) the chi-squared distribution with n degrees of freedom. Since a sum of independent Gaussian distributed random variables is also Gaussian distributed [28] [246], then each variable in the vector $\vec{\eta}$ in such case has a Gaussian distribution. Even if some random variables $\vec{x}$, one has to deal with in practice, are not Gaussian distributed, it is always possible to find such a *transformation* function $\vec{\eta} = T(\vec{x})$ that all the variables in $\vec{\eta}$ are Gaussian distributed. Actually, it is possible to transform (using some function $y = f(x)$) any continuously distributed random variable α with the Probability Density Function (PDF) $p_\alpha(x)$ in such a way that the transformed variable β would have any desirable PDF $p_\beta(y)$. For that one could use the following relation [246]:

$$p_\beta(y) = p_\alpha(f^{-1}(y)) \cdot \left| \frac{d f^{-1}(y)}{dy} \right|, \tag{5.11}$$

or, equivalently:

$$p_\beta(y) dy = p_\alpha(x) dx,$$

where $y = f(x)$ and $dy = \frac{df(x)}{dx} dx$, and then solve (numerically) the following equation:

$$\int_{-\infty}^{x} p_\alpha(z) dz = \int_{-\infty}^{y} p_\beta(z) dz + \text{constant}, \tag{5.12}$$

which is what was done to fit the hit energy losses of a track before such fit was removed from the final tracking algorithm (the constant in Eq. 5.12 could be found by setting some initial condition).

Let us get back to the practical case to which this theory was applied. In this case $\vec{x}$ are some used in the fitting parameters (positions, or energy losses, or both) of all the hits of a track, and $\vec{\eta}$ are the transformed (such that every variable in $\vec{\eta}$ is Gaussian distributed with a zero mean) parameters of the hits. Any track hit parameter corresponds to a random process, for example, to a (multiple) scattering or to an energy loss in silicon. In addition, the same random processes also occur in the RHIC beam pipe. Therefore the working hypothesis (which was confirmed by practical applications of

[28] Of course, a product of a constant with a Gaussian distributed random variable has a Gaussian distribution as well.

its conclusions) is that, even though the hit positions and energy losses are dependent random variables [29], one can always find such a linear combination $\vec{\xi} = C\vec{\eta}$ that the resulting random variables $\vec{\xi}$ (which would necessarily have Gaussian distributions with a zero mean) are independent. It is obviously possible to adjust elements in the C matrix such that all the variables in $\vec{\xi}$ have as well a unit width. The hypothesis is necessary to make sure that Eq. 5.10 would indeed produce a random variable with a chi-squared distribution with n degrees of freedom.

As it turned out, the distances d_i in Eq. 5.9 on page 123 have already distributions close to Gaussians, therefore Eq. 5.12 was not solved and approximate versions of the transformations were used (to minimize the CPU time needed to compute the transformations):

$$T_i(d_i) = \frac{d_i - \mu_i}{\sigma_i},$$

where μ_i and σ_i are the sample mean and width of the variable d_i for kaon tracks with their vertex z-coordinate, θ-angle, and $1/p$ within small ranges of the parameters as determined by MC simulations [30]. In practice, μ_i and σ_i were found for each covariance matrix bin (see section 5.10.4 on page 128) as the mean and the width of the d_i distribution of all the MC kaon tracks used to estimate the bin covariance matrix (see Eq. 5.9) elements, and, in particular, that means that the transformations were found separately for every possible (kaon charge × layer pattern × PHOBOS spectrometer arm) combination and for every covariance matrix bin of such a combination.

It must be obvious by now, that Eq. 5.9 and Eq. 5.10 are equivalent if distances d_i are chosen as a measure of the hit positions of a track.

5.10.3. Track Model

The track model was implemented by numerically integrating the differential equation of motion (without any energy losses) of a charged particle in a static magnetic field in a vacuum:

$$\frac{d\vec{p}}{dt} = q\left(\vec{v} \times \vec{B}(\vec{\rho})\right),$$

where $\vec{p}$ and $\vec{v}$ are the momentum and the velocity vectors of the particle respectively, q is its electric charge, and $\vec{B}(\vec{\rho})$ is the magnetic field vector in the point $\vec{\rho}$. The equation of motion could be rewritten, considering the particle trajectory length s (starting from the origin point of the particle) instead of the time t as the trajectory curve parameter, as [247, 248]:

$$\frac{d^2\vec{r}}{ds^2} = \frac{q}{p}\left(\frac{d\vec{r}}{ds} \times \vec{B}(\vec{r})\right),$$

where $\vec{r}(s)$ is the equation of the particle trajectory, and p is the total momentum of the particle. The later equation could be in turn rewritten as a system of two first order

[29] The position and the average energy loss of a hit depend on the amount of the (multiple) scattering and on the energy losses in the hits produced by the corresponding particle earlier than the hit.

[30] Here the θ-angle is the angle between a kaon momentum vector and the z-axis, and p is the total momentum of the kaon.

differential equations:

$$\begin{aligned} \frac{d\vec{r}}{ds} &= \vec{\varrho}, \\ \frac{d\vec{\varrho}}{ds} &= \frac{q}{p}\left(\vec{\varrho} \times \vec{B}(\vec{r})\right), \end{aligned} \tag{5.13}$$

which was solved numerically using the fourth-order Runge-Kutta-Nyström method [247, 248]. Note, that in the above equations $|\vec{\varrho}| = 1$, and $p = \text{const}$.

To calculate the distance d_i in Eq. 5.9 on page 123 for a given track and a track model corresponding to given particle parameters, the following sequence of steps was performed:

1. The track length s_i from the event vertex to the hit i was calculated approximating the track with a linear spline with the hit positions serving as the spline nodes. The later is how s_i was calculated during the generation of covariance matrices used for the track fitting (see section 5.10.4 on the following page). However due to an error in the data analysis code, discovered in the process of writing this thesis, the distance s_i was calculated starting from the origin of the PHOBOS coordinate system during the actual fitting of most tracks [31]. This error is expected to reduce somewhat the overall tracking efficiency due to not completely correctly estimated fit probability of tracks (see section 5.10.6 on page 132), which is not a problem since, as soon as the efficiency and occupancy correction (see section 6.3.1 on page 150) is determined correctly, the final result on the ϕ meson invariant yield will be correct as well. The error could also effect the momentum resolution of ϕ mesons, which is not a problem either, since the analysis includes a momentum resolution correction (see section 6.3.3 on page 153). The error could make the tracking efficiency to be vertex z-coordinate dependent, but that is not a problem too, since the efficiency and occupancy correction was done by studying single embedded ϕ meson events, which have the same vertex z-coordinate distribution as the data events, and so the relative weight of any vertex range in both types of events is the same, and therefore the average efficiency and occupancy correction (in a wide vertex range used for the data analysis) was estimated correctly even if the tracking efficiency does depend on vertex z-coordinate of an event. If the PHOBOS trigger is not equally efficient as a function of vertex z-coordinate of events, then the error could effect the final result if there is also a centrality dependence of the ϕ meson reconstruction efficiency, but the effect is expected to be small, since, as can be seen from Fig. 6.6 on page 150, the dependence of the ϕ meson reconstruction efficiency on centrality is weak, nevertheless it was checked directly by redoing the efficiency and occupancy correction with

[31] The mistake was that I forgot to copy the track vertex information from the straight tracks to the full tracks during the joining of straight and Hough tracks of an event. It is ironic that I made the error since an almost identical bug, which I found and reported to the PHOBOS collaboration in 2007, is present in the standard PHOBOS reconstruction code and never got fixed. And what makes it even more disappointing is that my code was correct originally but I introduced the bug during an optimization of the algorithm.

the number of ϕ mesons per event correctly (i.e. in agreement with dN/dy values in Table 7.2 on page 188) dependent on centrality and finding only negligible changes in the final results on ϕ meson invariant yield. Moreover, a systematic error due to a possible dependence of the results on vertex z-coordinate of events was in addition taken into account as described in section 6.5.1.3 on page 163.

2. As a result of the numerical solution of Eq. 5.13, the trajectory was represented as a set of points $(\varsigma_j, \vec{\varrho}_j)$, which will be called the *solution points*, where ς_j is the trajectory length (from the initial point $(0,0,\mathcal{V}_z)$ of the trajectory to the solution point j) calculated by approximating the trajectory with a linear spline with the solution points serving as the spline nodes. At this step, such a solution point number j_i was found that $|s_i - \varsigma_{j_i}|$ is minimal.

3. A circle [32] was drawn through the projections (onto the $y = 0$ plane) of the trajectory points with numbers $\{j_i - 1, j_i, j_i + 1\}$ [33], and d_i was assigned as the distance between the circle and the projection of the hit i.

5.10.4. Covariance Matrices

5.10.4.1. Creating Covariance Matrices

The covariance matrices were created separately for every possible (kaon charge × layer pattern × PHOBOS spectrometer arm) *combination*.

The variation in the amount of multiple scattering as well the fluctuations of the energy losses experienced by a particle, as it travels through the PHOBOS spectrometer, depend on the total momentum and on the direction of the travel of the particle. Therefore the elements of the covariance matrix in Eq. 5.9 on page 123 depend on the particle parameters with the strongest dependencies being on the origin z-coordinate of the particle v_z, its total momentum p, and the angle θ between the momentum vector of the particle and the z-axis. To take into account the dependencies, a separate estimate of the covariance matrix was found (for a given combination) in each bin of the following 3-dimensional histogram of the particle parameters (we will say that the histogram is *associated* with the combination):

- 64 bins of v_z in the range $[-35, +15]$ cm,
- 64 bins of θ in the range $[0.01, \pi - 0.01]$ rad,
- 64 bins of $1/p$ in the range $[0.02, 10.0]$ $(\mathrm{GeV/c})^{-1}$.

Sets of the $(v_z, \theta, 1/p)$ particle parameters were generated with uniform distributions in each such bin. A corresponding MC simulation of a single kaon was performed for

[32] The magnetic field could be considered to be uniform in a small space region with a size of $\sim(\varsigma_{j+1} - \varsigma_j)$.

[33] If point j_i happen to be the last or the first point of the trajectory, points $\{j_{\max} - 2, j_{\max} - 1, j_{\max}\}$ and $\{1,2,3\}$ were used instead correspondingly.

each such set of the particle parameters using GEANT. The other origin coordinates of such kaons were $v_x = v_y = 0$ and the ϕ-angles of the kaons were generated with uniform distributions in the range $[-0.1, +0.1]$ rad and $[\pi - 0.1, \pi + 0.1]$ rad for the positive and the negative spectrometer arm respectively. The following GEANT parameters were changed from their default values for the simulations:

"GEN"	=	10	:	user supplied particle (one particle in one event)
"DCAY"	=	0	:	no decay in flight
"PAIR"	=	0	:	no pair production
"DRAY"	=	0	:	no delta-ray production
"ANNI"	=	0	:	no positron annihilation
"PHOT"	=	0	:	no photoelectric effect
"HADR"	=	0	:	no hadronic interactions
"COMP"	=	0	:	no Compton scattering
"BREM"	=	0	:	no bremsstrahlung
"LOSS"	=	3	:	restricted Landau fluctuations plus delta ray production
"MULS"	=	2	:	multiple scattering according to Moliere

A simulation of a kaon was considered to be successful if the produced MC kaon had a layer pattern which contained the layer pattern of the combination for which the covariance matrices were generated at that time. The sets of parameters were generated until 4000 successful kaon simulations were completed. However, if no successful simulations were performed for the first 400 sets of the parameters or if the fraction of successful simulations in the first 5000 set of the parameters was below 5%, the corresponding bin was considered to be outside of the PHOBOS spectrometer acceptance and no covariance matrix was associated with the bin. To determine the hit positions of a simulated kaon, the following procedure was followed (to make sure that any effects associated with the hit reconstruction procedure, described in section 4.2 on page 74, would be correctly reflected in the evaluated covariance matrix):

1. All the hits of every such single kaon MC event were reconstructed the same way as for data events (see section 4.2).

   The caveat here is that energy losses of kaons are not correctly simulated in the PHOBOS MC (see section 5.6 on page 106), and the problem was discovered after the covariance matrices were created. So the reconstructed hit positions of a kaon in the MC would differ slightly from such positions of a kaon with the same parameters in data. There are two reasons of that:

   a) The first reason (and there is nothing one could it about without implementing a very time consuming fix to the PHOBOS MC) is that since kaons loose energy faster in MC than in data, the MC kaons would have higher trajectory curvature than kaons with the same parameters in data. This reason is important since it affects the low momentum kaons which are used for the data analysis in this thesis. The size of the effect depends on how large are the changes in positions of hits due to it in comparison to the variance of the

positions due to the multiple scattering. This problem is present as well in the standard PHOBOS reconstruction.

b) The second reason is the following: to produce a hit, only such spectrometer sensor pads energy losses are merged which pass a noise threshold cut and, since in the MC the energy losses are higher, more pads would be included on average into the same hit. However, the position of a hit in spectrometer is determined by weighting the positions of the merged pads, which were used to produce the hit, with their energy losses, and if more pads are merged, the position would be somewhat different. The importance of the effect depends on how large the difference in the position of a hit of a given kaon due to the difference in energy losses is in comparison to the variance of the hit position due to the multiple scattering. Therefore, in the best case scenario it would be desirable to recreate all the covariance matrices with the corrections to the MC energy losses applied before the hit reconstruction, with subsequent re-reconstruction of the data, which, however, would take at least 6 months of computing time and but still would not address the first problem explained above in 1a. The same problem is present in the standard PHOBOS tracking in an even bigger form, i.e. not only the difference in energy losses between data and MC is not taken into account, but also any possible effects of the hit merging are ignored (during the covariance matrix generation all the MC energy losses are merged to produce hits). In addition, the covariance matrices are computed with respect to MC tracks without multiple scattering instead of the track model trajectories.

2. The reconstructed hits of an event were matched to the MC hits of the kaon and used for the covariance matrix estimation.

The covariance matrix elements of a bin were estimated as

$$\mathrm{cov}(i,j) = \frac{1}{4000}\sum_{k=1}^{4000} T_i(d_i^{(k)})T_j(d_j^{(k)}),$$

where k is the number of a successfully simulated kaon, $d_i^{(k)}$ is the distance between the kaon hit i and the track model trajectory with the same parameters as the kaon found as explained in section 5.10.3 on page 126, T_i is the transformation function applied on $d_i^{(k)}$ (see section 5.10.2 on page 125).

5.10.4.2. Selecting Covariance Matrix Bin

As it was pointed out in section 5.10.4.1 on page 128, a separate set of covariance matrices was created for every possible (kaon charge × layer pattern × PHOBOS spectrometer arm) *combination*. We will say that a particular layer pattern was *employed* for fitting of a track, if the covariance matrices of the combination [34] containing the layer pattern

[34] Of course, such combination must in addition have the arm and the kaon charge corresponding to the fitted track.

were used for the χ^2 calculation during the fit of the track.

A given track could often be fit employing several different layer patterns (those that are contained in the layer pattern of the track), see section 5.10.5. To determine the covariance matrix of what bin had to be utilized to fit a track employing a particular layer pattern, the event OneTrackVertex z-coordinate v_z and the track θ and $1/p$ parameters determined at the joining step (see section 5.9 on page 120) of the specialized kaon reconstruction were used. The later means that it was found into what bin of the histogram (associated with the combination of the employed layer pattern, see section 5.10.4.1 on page 128) the parameters v_z, θ, and $1/p$ fell and the covariance matrix assigned to that bin was utilized. If the bin happened to be outside of the PHOBOS detector acceptance, no fitting was performed employing the corresponding layer pattern.

5.10.5. χ^2 Minimization

The minimization of a track χ^2 (see Eq. 5.9 on page 123) was performed using *Powell's conjugate directions gradient descent method* [249]. The minimization procedure was the following:

1. From the list of all the layer patterns implemented in the specialized kaon reconstruction (see Table 5.2 on page 101) for the product of

   $$(\text{the track charge}) \cdot (\text{the event magnet polarity}),$$

   such layer patterns were chosen that were contained in the layer pattern of the track.

2. The χ^2 minimization was done employing (see section 5.10.4.2 on the facing page) each of the chosen layer patterns for which the covariance matrix bin selection method returned a bin within the PHOBOS detector acceptance (let us call each such χ^2 minimization a *fitting attempt*). The fitting attempt (let us call it the *best*) which resulted in the smallest fit probability (see section 5.10.6 on the next page) was used to determine the final parameters assigned to the track. If it was not possible to perform even one fitting attempt on the track, the later was considered to be invalid and was discarded from any further consideration in the specialized kaon reconstruction.

3. The track parameters minimized during every fitting attempt were the origin z-coordinate v_z of the particle corresponding to the track, the reciprocal of its total momentum $1/p$, and the angle θ between the momentum vector of the particle and the z-axis. The values of the parameters at which the χ^2 minimum was reached in the best fitting attempt were assigned to the track as a result of the fitting procedure. The initial guesses of the parameters were the event OneTrackVertex z-coordinate and the track θ and $1/p$ parameters determined at the joining step (see section 5.9 on page 120) of the specialized kaon reconstruction correspondingly.

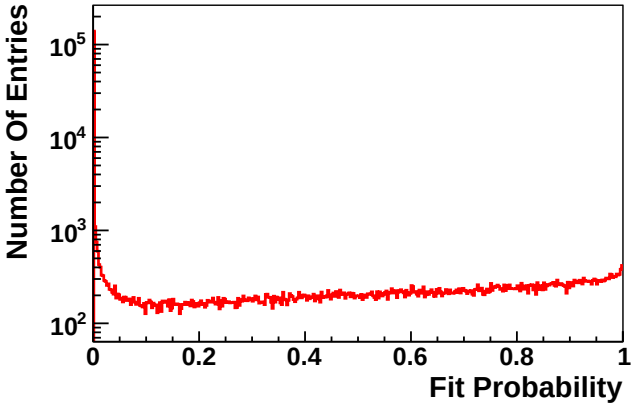

Figure 5.15.: Distribution of the fit probability (let us call it p_{fit}) of the reconstructed (using the specialized kaon reconstruction) tracks in Cu+Cu $\sqrt{s_{\text{NN}}} = 200$ GeV data. The histogram on this figure has 400 bins and the fit probability cut applied during the final track selection (see section 5.12 on the next page) was $p_{\text{fit}} > 1/400$. The tracks which did not pass the cut were composed mostly of random combinations of hits produced by different particles. See section 5.10.6 for details.

4. The track φ-angle assumed in the track model during minimization was the one determined at the joining step of the specialized kaon reconstruction. As well, vanishing values of the particle origin x- and y-coordinates were assumed.

5. The tolerance parameter of the minimization algorithm was 10^{-3} and the tolerance of the auxiliary linear (1-dimensional) minimization was set to 2×10^{-4}.

5.10.6. Fit Probability

The probability that a correctly reconstructed track would have the minimum χ^2 value resulting from the fit of the track greater than the found one is called the *fit probability*. In the later definition, a track is considered to be correctly reconstructed if all the hits assigned to it were produced by the same primary physical particle produced in a nuclear collision. The distribution of the fit probability is expected to be uniform in the $[0,1]$ range if the value calculated using Eq. 5.9 on page 123 has indeed a true χ^2 distribution.

Actually, it is true for any random variable α with a PDF $p_\alpha(x)$ that the random variable β which is

$$f(x) = \int_x^\infty p_\alpha(z)dz, \tag{5.14}$$

where x is distributed with a PDF $p_\alpha(x)$, has a uniform distribution in the $[0,1]$ range. It

can be easily proven using Eq. 5.11 on page 125 that the PDF of β is

$$p_\beta(y) = p_\alpha(f^{-1}(y)) \cdot \left| \frac{df^{-1}(y)}{dy} \right| = p_\alpha(f^{-1}(y)) \cdot \left| \frac{1}{\frac{df(y)}{dy}} \right| = p_\alpha(f^{-1}(y)) \cdot \left| \frac{1}{-p_\alpha(f^{-1}(y))} \right| = 1,$$

since the function $f(x)$ is monotonously increasing (and therefore reversible), $p_\alpha(x) \geq 0$ as a PDF, and $df(x)/dx = -p_\alpha(x)$.

In reality, during the calculation of the variable Eq. 5.9, a number of approximations (described in the previous sections) were made and so the variable has a distribution close to the true χ^2_n (with an appropriate number of degrees of freedom n) but not exactly one. However, the calculation of the fit probability was done using Eq. 5.14 with $p_\alpha(z) \equiv p_{\chi^2_n}(z)$ during the data analysis. Therefore, the fit probability distribution of correctly reconstructed tracks in data is expected to be close to uniform but not exactly such. In addition, several fitting attempts (see section 5.10.5 on page 131) were performed on some some fraction the tracks in data, and consequently the fit probability of correctly reconstructed tracks is expected to have a bias towards unity, which is exactly what is observed (see Fig. 5.15 on the facing page).

5.11. Skipping Events Requiring Too Much Computer Memory To Reconstruct

Events which required more than 1.9×10^6 kb of resident memory (i.e ~ 1.62 Gb of RAM) or more than 9.7×10^6 kb of virtual memory (i.e. ~ 9.25 Gb of total memory including the disk *swapping/paging*) were skipped in the specialized kaon reconstruction. The total fraction of such events was $\lesssim 2 \times 10^{-3}$ and therefore the corresponding systematic error would add only a tiny amount to the systematic error, estimated as described in section 6.5 on page 160, and therefore was ignored.

5.12. Final Track Selection

5.12.1. Track Ambiguity Resolution

An *ambiguity* between two tracks is by definition when two tracks either share too many hits or have insufficient number of hits in different spectrometer layers. The maximum allowed number of shared hits by any two tracks was set to two since, as it was pointed out in section 5.8.2 on page 114, any three points on a particle trajectory (in a static magnetic field) should be enough to fully define it, and so if in addition to the event vertex there are two other common points (hits) which belong to two different tracks, the tracks must be reconstructions of the same particle trajectory. The minimum allowed number of hits in different spectrometer layers for any two tracks was set to five [35].

[35] This condition was inherited from the standard PHOBOS track reconstruction. However, I personally do not see any reason why two different tracks could not have even all of their hits in the same spectrom-

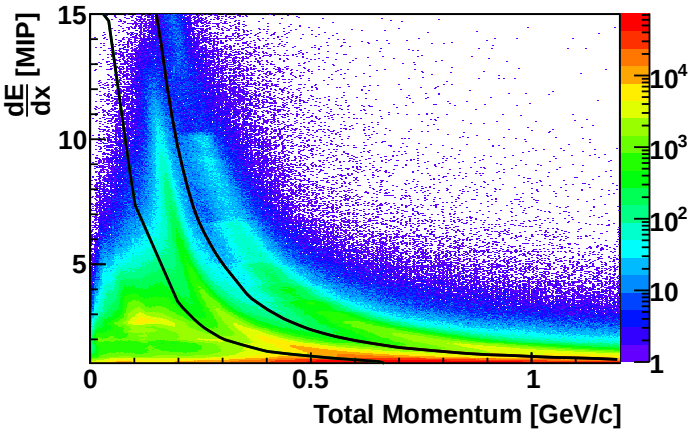

Figure 5.16.: dE/dx vs p cuts used to identify kaons among other charged particles. The data shown on the plot correspond to the positive magnet polarity Cu+Cu 200 GeV data with no centrality selection applied.

If any two tracks were found to be ambiguous, the one with a higher fit probability (see section 5.10.6 on page 132) was chosen and the other was discarded. The track ambiguity resolution was done in two steps:

1. First, the resolution was done separately for every possible (kaon charge × layer pattern × PHOBOS spectrometer arm) combination.

2. Then, the resolution was done among all the tracks reconstructed within one spectrometer arm.

5.12.2. Kaon Identification

The most copiously produced in a heavy ion collision long-lived charged particles are electrons, muons, pions, kaons and (anti)protons. Particle identification for the current work was done using dE/dx vs total momentum p information from the PHOBOS spectrometer silicon detectors. Due to lower dE/dx resolution, smaller number of hits per track and smaller relativistic rise of energy losses from MIP values at high $\beta\gamma$ in silicon in comparison to gases, PHOBOS spectrometer does not allow to distinguish between pions, electrons and muons in comparison, for example, to other experimental detectors utilizing dE/dx vs p information from Time Projection Chamber (TPC) for particle identification [169, 250, 251]. Therefore the task of charged kaon identification is reduced to separating kaons from pions and (anti)protons.

Charged particles lose energy as they traverse a material due to ionization and atomic excitation at rate which depends on their velocity [169]. Or, equivalently, at a fixed value of the total momentum of a particle, its energy loss pace dE/dx depends on the particle mass. Since a particle trajectory curvature in a magnetic field, being the directly

eter layers, and so the condition is questionable and could be removed.

Point Number	1	2	3	4	5	6	7
p (GeV/c)	0.0	0.10	0.200	0.250	0.300	0.350	0.400
dE/dx (MIP)	20.0	7.444	3.439	2.544	2.015	1.753	1.520
Point Number	8	9	10	11	12	13	N/A
p (GeV/c)	0.450	0.500	0.550	0.600	0.650	0.670	N/A
dE/dx (MIP)	1.416	1.330	1.247	1.186	1.117	1.100	N/A

Table 5.5.: Lower bound (dE/dx,p) linear interpolation knot points used for kaon identification.

measured in the PHOBOS spectrometer quantity, is determined by the value of its total momentum, and pions, kaons and (anti)protons have different mass, it is the dE/dx vs total momentum p information that could be used to identify kaons among other reconstructed charged particles.

dE/dx values were calculated as described in section 5.5 on page 103 and the total momentum values resulted from fitting of tracks as described in section 5.10 on page 123.

5.12.2.1. Parameters of dE/dx vs Total Momentum Selection

The dE/dx vs p cuts used to identify kaons among other charged particles in this thesis are shown on the Fig. 5.16 on the facing page. The cuts were implemented as a requirement that a (dE/dx,p) point for a given track to be above the lower bound curve and below the upper bound curve shown on the figure. The lower and upper bound curves were implemented as a linear interpolation of a set of points, chosen in such a way as to correspond to the local minimum in the dE/dx distribution at a set of fixed total momentum values. The knot points used for the interpolation are summarized in Tables 5.5 and 5.6. The lines connecting the first two and the last two knots of both upper and lower bounds were extended to infinity to define the bounds outside of the ranges of the corresponding knot interpolation points. No reconstructed tracks with $p \notin [0,2]$ GeV/c range or with $dE/dx < 1.05$ were identified as kaons.

5.13. Correcting Total Momentum Values

The track model (see section 5.10.3 on page 126) used for fitting of reconstructed tracks was implemented without taking into account energy losses by charged particles as they traverse the material of the PHOBOS detector. Since in reality such losses are present, curvature of particle trajectories in data is higher than in the track model at the same value of total momentum. Since the total momentum of a particle in the specialized kaon reconstruction is essentially determined from a comparison of the reconstructed trajectory curvature to the one in the track model, that leads to an underestimated reconstructed total momentum of particles in data. The effect is expected to be the

Point Number	1	2	3	4	5	6	7	8	9	10
p (GeV/c)	0.0	0.18	0.2079	0.240	0.26	0.29	0.36	0.400	0.441	0.493
dE/dx (MIP)	34.0	11.4	8.801	6.93	6.2	5.24	3.70	3.21	2.80	2.420
Point Number	11	12	13	14	15	16	17	18	19	20
p (GeV/c)	0.550	0.600	0.650	0.700	0.750	0.800	0.850	0.900	0.950	1.000
dE/dx (MIP)	2.135	1.954	1.807	1.673	1.593	1.515	1.440	1.387	1.360	1.317
Point Number	21	22	23	24	25	26	27	28	29	30
p (GeV/c)	1.050	1.100	1.150	1.200	1.287	1.360	1.480	1.636	1.786	1.9
dE/dx (MIP)	1.280	1.260	1.234	1.194	1.170	1.160	1.146	1.138	1.125	1.1

Table 5.6.: Upper bound (dE/dx,p) linear interpolation knot points used for kaon identification.

strongest for low total momentum particles since for them the energy loss rate and the fraction of the total energy lost are the highest. Fig. 5.17 on the facing page shows the average ratios of the reconstructed to the MC total momentum in single kaon events (see section 5.4 on page 101) corresponding to all the possible (kaon charge × layer pattern) combinations. As can be seen, the ratios deviate from unity for total momentum values below $\sim$ 200 MeV/c and this is the region where the correction to the reconstructed total momentum values was applied in data using the ratios shown on the figure [36]. Application of the correction does not make a significant difference on the final result since only $\lesssim$ 0.7% of all the reconstructed tracks in data have total momentum values below 200 MeV/c. The correction was implemented as a 3D linear interpolation of the ratio of reconstructed (let us denote it as p) to MC total momentum estimated in bins of a 3D-histogram with the axes $1/p$, v_z, and θ, where v_z is the z-coordinate of a MC single kaon event, and θ is the reconstructed θ-angle of the kaon. The correction was implemented separately for every possible (kaon charge × layer pattern) combination.

[36] The caveat here is again that the energy losses are not simulated correctly in the PHOBOS MC and so the ratios shown on Fig. 5.17 are too low in comparison to what they would have been if the simulations were able to reproduce the data perfectly.

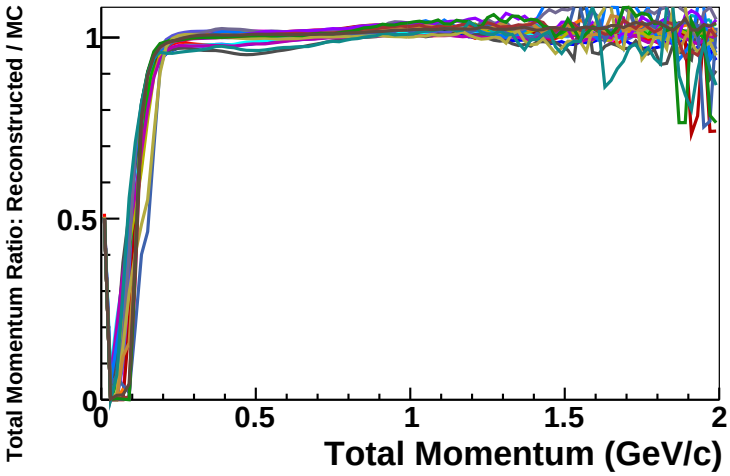

Figure 5.17.: The average ratios of the reconstructed to the MC total momentum as a function of the reconstructed total momentum in single kaon events. See section 5.13 on page 135 for details.

6. Reconstruction Of ϕ Meson Invariant Yield

In a nutshell, ϕ meson invariant yield was reconstructed by:

1. measuring the number of ϕ mesons decaying into K^+K^- pairs in intervals of transverse momentum, rapidity, and collision centrality using the event mixing technique - see section 6.1 on the following page

2. correcting the number for
   - reconstruction efficiency and effects of high hit density (*"occupancy"*) - see section 6.3.1 on page 150
   - trigger efficiency - see section 6.3.2 on page 152
   - momentum resolution - see section 6.3.3 on page 153
   - effects of dead channels in the spectrometer - see section 6.3.4 on page 157
   - branching ratio of the $\phi \rightarrow K^+K^-$ decay channel - see section 6.4.1 on page 159
   - the width of the transverse momentum and rapidity intervals - see section 6.4.1 on page 159

3. averaging the results received for positive and negative magnet polarity data - see section 6.4.1 on page 159

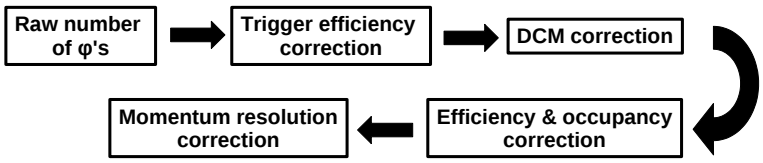

Figure 6.1.: Order of steps performed to correct the raw yield of ϕ mesons . Location of the scalings for $\phi \rightarrow K^+K^-$ branching ratio, the number of events, the width of the transverse momentum and rapidity intervals and the width of transverse momentum bin is not important, since they can be performed at any time.

6.1. Event Mixing

6.1.1. General Description Of Event Mixing Technique

Event mixing is a technique of statistical estimation of number of some correlated physical processes occurring with some probability in one measurement (*"event"*) which in addition to the physical processes unavoidably includes measurement of uncorrelated background. Event mixing involves combining information from one event with information from another event to produce another pseudo-event. If any two events are independent there assumed to be no correlation between the two parts of the pseudo-events. By applying the same analysis method on real data events one estimates both the number of occurred correlated physical processes and uncorrelated background measurements. And by applying the analysis method on the pseudo-events one estimates the number of uncorrelated background measurements only. The difference between the measurement resulting from applying the analysis method on real data events and a properly normalized measurement from applying the method on pseudo-events gives an estimation on number of occurred correlated physical processes only in the given set of data events.

6.1.2. Procedure

In the current analysis an event is one collision of Cu+Cu nuclei. The correlated physical process is a production of a ϕ meson decaying subsequently into a K^+K^- pair. K^+K^- pairs, which are not products of a ϕ meson decay, are the uncorrelated background.

The analysis method involves combining each K^+ with each K^- in a given event and a calculation of the pairs' invariant mass. Only kaons which passed the final track selection were used 5.12. The procedure was repeated for all the events which passed the event selection 4.4 resulting in the *data invariant mass distribution*. By combining information about K^+ from one event with information about K^- from another event for a number of data events, the shape of background contribution to the data invariant mass distribution was estimated. By subtracting from the data invariant mass distribution the properly scaled background invariant mass distribution, the total number of ϕ mesons in the data was estimated.

6.1.2.1. Definitions Of Some Variables

For convenience of explaining the details of the implemented event mixing procedure, let us define the following variables:

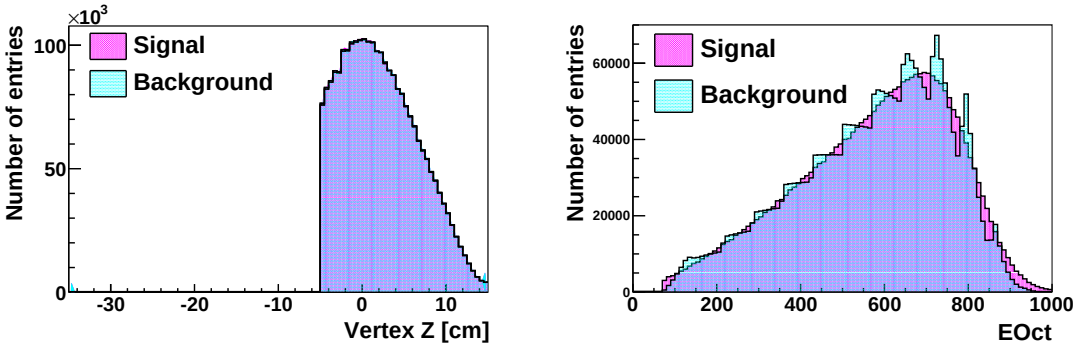

(a) Signal and background v_z distributions

(b) Signal and background *EOct* distributions

Figure 6.2.: An example of signal and background v_z (a) and *EOct* (b) distributions: Cu+Cu 200 GeV, 0-60%, positive magnet polarity, all intermediate p_t values.

v_z	vertex z-coordinate
p_t^{ϕ}	ϕ meson transverse momentum
$p_t^{K^+K^-}$	K^+K^- pair transverse momentum
$y^{K^+K^-}$	K^+K^- pair rapidity
$m_{inv}^{K^+K^-}$	K^+K^- pair invariant mass
m_K	K^+ / K^- mass
m_{ϕ}	vacuum ϕ meson mean mass
Γ_{ϕ}	vacuum ϕ meson decay width
EOct	measure of energy deposited in the octagon detector (see section 4.5.1)

6.1.2.2. Event Mixing Details

To estimate background shape correctly using the event mixing technique it is essential that for every data event the same (not necessarily integer) number of background K^+K^- pairs is generated with the same single particle K^+ and K^- distributions as in the data event.

Since acceptance of the PHOBOS detector (and consequently the single particle K^+ and K^- distributions) depends strongly on v_z , it was essential to only allow mixing of events with close v_z values (i.e. $|v_{z1} - v_{z2}| \leq 0.0625$ cm) and to require that the resulting background v_z distribution is the same as the data v_z distribution. Background v_z value was defined as an arithmetic mean of v_z values of the two events from which K^+ and K^- were selected for mixing, i.e. $v_z = 0.5 \cdot (v_{z1} + v_{z2})$. An example of signal and background v_z distributions is shown on Fig. 6.2(a).

Single particle K^+ and K^- distributions depend also on event centrality. For example, the average transverse momentum increases as centrality changes from peripheral to more central events. Therefore it was important to only allow mixing of events with similar centrality and to require that the resulting background *EOct* distribution is the same as the data *EOct* distribution. For Cu+Cu collisions centrality scales better

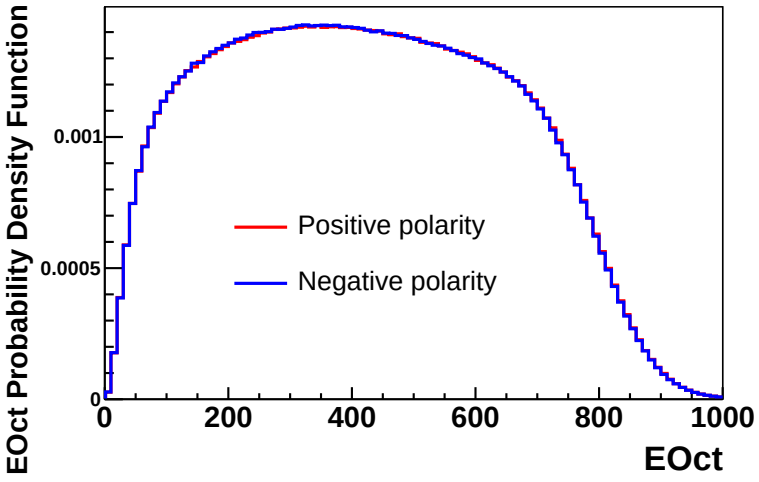

Figure 6.3.: *EOct* distributions of all used events for the intermediate p_t ϕ meson invariant yield measurement.

with *EOct* variable 4.5 therefore it was required that $|EOct_1 - EOct_2| \leq 113$ for any mixed events. In addition since there were little events with the highest *EOct* values (Fig. 6.3), if $EOct_1 > 955$ and $EOct_2 > 955$ then the two events were allowed for mixing [1]. Background *EOct* value was defined as an arithmetic mean of *EOct* values of the two events from which K^+ and K^- were selected for mixing, i.e. $EOct = 0.5 \cdot (EOct_1 + EOct_2)$. An example of signal and background *EOct* distributions is shown on Fig. 6.2(b).

To ensure that the final data and background v_z vs *EOct* distributions have the same shape:

1. A *background to signal ratio*, which here means the average number of background $m_{inv}^{K^+K^-}$ entries per one signal $m_{inv}^{K^+K^-}$ entry, was set to a fixed number (100).

2. A 2D-histogram of data v_z vs *EOct* values was filled with v_z and *EOct* values from every K^+K^- pair contributed to the data invariant mass distribution.

3. The generation was done until the following conditions were satisfied [2]:

    - the number of entries in each background v_z vs *EOct* histogram bin does

[1] The condition is is provided here for completeness, since it was present in the data analysis code. As it will be explained below, only events with $EOct < 1000$ were used in the final data analysis, therefore any two events with $EOct_1 > 955$ and $EOct_2 > 955$ are automatically allowed for mixing by condition $|EOct_1 - EOct_2| \leq 113$.

[2] The initial requirement was that the number of entries in each bin of background v_z vs *EOct* histogram is equal to the background to signal ratio times the number of entries in the corresponding bin of the data v_z vs *EOct* histogram. However, it was shown that it changes the results very little when one switches from one requirement to the other. The advantage of the used set of requirements was that it reduced the event mixing time significantly (for example, for 0-60% range of centrality positive magnet polarity data the reduction was from ~3 days to ~8 hours).

not exceed the background to signal ratio times the number of entries in the corresponding bin of the data v_z vs *EOct* histogram,

- the total number of entries in the background histogram is equal to 99% of the background to signal ratio times the total number of entries in the signal histogram.

Again the background v_z vs *EOct* histogram was filled with v_z and *EOct* values from every K^+K^- pair contributed to the background invariant mass distribution.

To treat the positive and negative magnet polarity data in a symmetric way, at positive polarity K^+ was selected 1st and K^- was selected 2nd in every event mixing iteration. At negative polarity the selection order was the opposite. By checking the event number and the run number of any two event to be mixed, it was made sure that no K^+K^- pair was selected for mixing from the same event. The event mixing was ran separately on positive and negative polarity data.

MC simulations have demonstrated that both K^+ and K^- could only be reconstructed:

- for $p_t^\phi \leq 0.13$ GeV/c if both kaons hit different arms of the PHOBOS spectrometer
- for $p_t^\phi \geq 0.13$ GeV/c if both kaons hit the same arm of the PHOBOS spectrometer

Therefore it was required that in both data and background in every K^+K^- pair both kaons are reconstructed in the same arm for intermediate p_t^ϕ range (i.e. 0.39 GeV/c $\leq p_t^\phi \leq$ 1.69 GeV/c) and in different arms for the lowest p_t^ϕ (i.e. $p_t^\phi \leq 0.13$ GeV/c).

The data used for the analysis was a mixture of different triggers which could bias single particle K^+ and K^- distributions. To take it into account it was required that any K^+K^- pair could only be drawn in the event mixing from two events with the same trigger.

And at last, the following selections were applied on events and K^+K^- pairs:

- -5 cm $\leq v_z \leq$ +15 cm for the means in intermediate p_t^ϕ range
- -25 cm $\leq v_z \leq$ -5 cm for measurement at the lowest p_t^ϕ
- selection on Centrality Bin (for example, for the 0-60% centrality range data analysis the selection was: 5 $\leq$ Centrality Bin $\leq$ 17, see Table 4.1 on page 83)
- $0 \leq EOct \leq 1000$
- $0.0 \leq y^{K^+K^-} \leq 1.0$ for intermediate p_t^ϕ range ($0.3 \leq y^{K^+K^-} \leq 1.0$ for the lowest p_t^ϕ)
- $2m_K \leq m_{inv}^{K^+K^-} \leq 2m_K + 48\Gamma_\phi$

6.1.2.3. Sorting Events

The step preceding the event mixing was to sort all the used events (i.e. events with at least one reconstructed kaon) in ascending order of v_z . The input of this step was a list of files, each containing information about a subset of such events. It was necessary to split all the events into a number of event subsets due impossibility to load all them at once into a computer RAM. The sorting was necessary to allow the event mixing to finish in a realistic time, since it greatly sped up selection of a 2nd random event within a narrow narrow v_z range around a randomly chosen 1st one.

6.1.2.4. Parallel Processing Of Event Mixing Requests

As can be seen from the description of the event mixing details 6.1.2.2, it is not known in advance how many mixing attempts have to be made to successfully satisfy the needed conditions. Also, probability of randomly generating K^+K^- pairs in different regions of the possible phase space vary greatly, so an efficient event mixing has to generate pairs very non-uniformly. As alternative, traditionally one could generate the mixed events entries using independent batch jobs and then only select the needed ones. The problems with that approach are:

1. It would require absolutely unaffordably large disc space to safe the not needed background entries.

2. For every new data set the exact amount of needed entries would have to be figured out with a trial and error method.

3. The need to safe the background entries to disk would make the process extremely slow (hard drive access time is about 1000 larger than for RAM).

The solution was to use the Parallel Information Processing 3.2 system developed for this work. The setup involved one master job, which managed ~100 slave jobs which actually generated mixed event background entries. The master job would create a set of tasks describing where (i.e. with what parameters) and how many background entries need to be generated, based on the progress made up to some moment in time. The number of tasks would also be adjusted according to the progress made in the previous iteration. The tasks would be sent to the slave jobs over network one by one, until they are all finished. Background would be generated randomly by slaves but only needed entries would be kept, and the rest would be discarded immediately. The results are then sent back to the master job, which goes through the list, selects the needed background entries, and then creates a new set of background generation tasks. The process is repeated until the final conditions are met. Since input list of reconstructed data events is split into a number of files, for each event mixing task a random pair of input files is selected. The approach solves all the problems of a traditional approach:

1. There is no need for large free disk space since very little information is saved in the very end.

2. The algorithm adjusts itself automatically to any input data and to any set of parameters.

3. The process is fast since it is not slowed down by writing large amount of information to disk.

6.1.2.5. Output

The data and generated event mixing background entries were used to fill 3D-histograms of $m_{inv}^{K^+K^-}$ vs $y^{K^+K^-}$ vs $p_t^{K^+K^-}$, which were used subsequently to calculate invariant mass distributions for any used in the data analysis p_t range by selecting the corresponding range of $p_t^{K^+K^-}$ bins and by summing over all the $y^{K^+K^-}$ bins.

6.2. Background Subtraction And ϕ Invariant Mass Peak Fitting

To subtract background and extract from data the number of reconstructed ϕ mesons, the data invariant mass distributions were fit with the following formula:

$$
\begin{aligned}
&f(m_{inv}^{K^+K^-}) = && (6.1)\\
&A\cdot\mathfrak{B}(m_{inv}^{K^+K^-})+ && \text{(part 1: event mixing background)}\\
&B\cdot\exp(-C\cdot(m_{inv}^{K^+K^-}-2m_K))+ && \text{(part 2: residual background parametrization)}\\
&D\cdot\mathbb{B}^{E,F}(m_{inv}^{K^+K^-})\cdot\exp(-G\cdot(m_{inv}^{K^+K^-}-2m_K)) && \text{(part 3: } \phi \text{ peak description)}
\end{aligned}
$$

where A-G are parameters, $\mathbb{B}^{E,F}(m_{inv}^{K^+K^-})$ is Breit-Wigner distribution with the mean E and the width F, and $\mathfrak{B}(m_{inv}^{K^+K^-})$ is the result of the event mixing procedure 6.1. An example of the fit result is shown on Fig. 6.4 on the next page.

6.2.1. Estimation Of ϕ Meson Peak Parameters

Parameter G describes the modification of the measured ϕ meson decay invariant mass distribution $\mathbb{B}^{E,F}(m_{inv}^{K^+K^-})$ due to the fact that PHOBOS detector has small azimuthal angle acceptance, therefore, as it was pointed out in section 6.1.2.2 on page 143, both $\phi \rightarrow K^+K^-$ kaons are reconstructed for $p_t^{\phi} \geq 0.13$ GeV/c if the kaons hit the same arm of the PHOBOS spectrometer, and this condition is more likely to be satisfied for smaller values of ϕ invariant mass since the opening angle between K^+ and K^- increases with the pair invariant mass (this statement applies to the intermediate p_t^{ϕ} data analysis, for the $p_t^{\phi} \leq 0.13$ GeV/c case the situation is the opposite, i.e. it is more likely that the kaons hit different arms of the PHOBOS spectrometer for higher values of ϕ invariant mass, therefore for $p_t^{\phi} \geq 0.13$ GeV/c we have $G > 0$ and for $p_t^{\phi} \leq 0.13$ GeV/c we have $G < 0$). MC simulations of ϕ mesons with uniform distribution of invariant mass showed that ϕ meson acceptance has decreasing exponential dependence on invariant mass, which

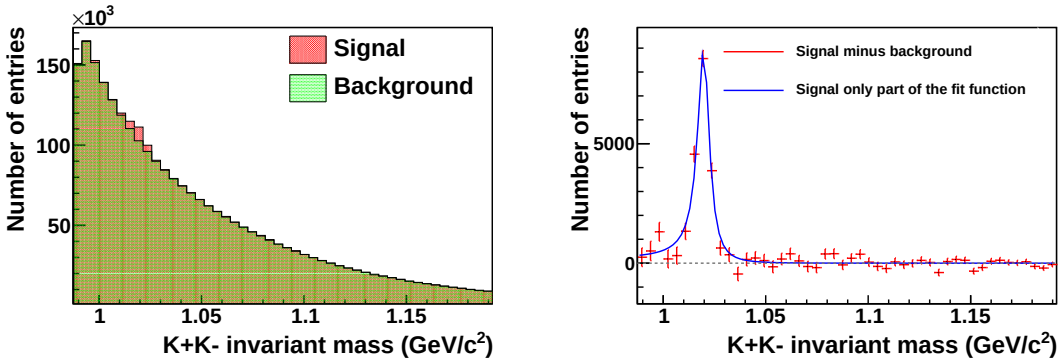

(a) Signal and background

(b) Signal minus background

Figure 6.4.: An example of background subtraction and ϕ invariant mass peak fitting: Cu+Cu 200 GeV, 0-60%, positive magnet polarity, all intermediate p_t values. Same event (red) and the sum of scaled event mixed background and residual background (shown in green, overlap of red and green on the figure looks brown) invariant mass distributions resulting from the fit as described in section 6.2 are shown on Fig. (a). Same event invariant mass distribution minus the sum of scaled event mixed background and residual background (red) and *part 3* of Eq. 6.1 fit result (blue) are shown on Fig. (b). The number of phis on the plots is 22315.02±887.50. The signal to background ratio in the bin with the highest number of ϕ mesons is ∼0.083.

explains the *part 3* of Eq. 6.1 functional form. Since the non-vanishing value of parameter G is solely due to the acceptance effects which can be properly quantified with proper MC simulations, the parameter was kept fixed during data fitting.

Parameters E-G were found by fitting (using *part 3* of Eq. 6.1 only) reconstruction results of MC simulations 5.2 of single $\phi \rightarrow K^+K^-$ events. It was predicted that ϕ meson mean and width would be modified inside hot dense strongly interacting medium of QGP (see section 1.4.3 on page 43). Such modification of the ϕ meson width was possibly observed by the STAR collaboration, however these results are not conclusive since they could be explained by uncertainties in the amount of material between the Time Projection Chamber (STAR TPC) active volume and the primary collision vertex and residual geometry misalignment [252]. In addition studying possible ϕ meson in medium modifications using $\phi \rightarrow K^+K^-$ decay channel is limited by the final collision stage rescattering effects of strongly interacting kaons. It was shown (see Fig. 7.10 on page 199) that for PHOBOS data the fit probability of fitting the ϕ peak almost does not change between the following two cases:

- parameters E and F are allowed to be varied during fitting
- parameters E and F are fixed during fitting

which shows that even if there are ϕ meson in medium modifications of its mean and

width, they are too small to be able statistically differentiate them from the case of no modifications at all. Therefore parameters E and F were kept fixed during data fitting.

6.2.2. Estimation Of Residual Background Parameters

Not all the effects could be properly taken into account using the event mixing technique 6.1 if the total number of data events available for analysis is limited.

The PHOBOS detector has a small θ-angle acceptance especially at the lowest end of the analyzed v_z range. To demonstrate why it creates difficulties for the event mixing to describe background shape correctly, let us consider the following artificial example. Let us imagine that we have a detector, which is a very thin ring around the beam pipe. The θ-angle acceptance of the detector is δ-function at every v_z value, therefore any K^+K^- pair combined from the same event tracks would have zero θ-angle between the two kaons, while during the event mixing if there is any distance in v_z between two mixed events, then the θ-angle between any two kaons reconstructed in the two events will be non-vanishing. Which means that data and mixed events background will always have different invariant mass distribution even if all the tracks in data are uncorrelated. In essence, the small θ-angle acceptance creates artificial correlation between *reconstructed tracks*. Therefore after event mixed background invariant mass distribution is subtracted from the data invariant mass distribution, there will be some *residual background*, not taken into account by event mixing, left.

To quantify the residual background due to the small θ-angle acceptance of the PHOBOS detector and to demonstrate that the background is not a consequence of some other effect, a set of toy MC events was created, in which all the kaons were independent, and the following correlated distributions of parameters repeated those in real data:

EOct vs v_z vs p_{K^+}	*EOct* vs v_z vs p_{K^-}	v_z vs N_{K^+} vs N_{K^-}
EOct vs v_z vs θ_{K^+}	*EOct* vs v_z vs θ_{K^-}	
EOct vs v_z vs ϕ_{K^+}	*EOct* vs v_z vs ϕ_{K^-}	

where

N_{K^+}	number of reconstructed K^+ per event
N_{K^-}	number of reconstructed K^- per event
p_{K^+}	total momentum of K^+
θ_{K^+}	θ-angle of K^+
ϕ_{K^+}	ϕ-angle of K^+
p_{K^-}	total momentum of K^-
θ_{K^-}	θ-angle of K^-
ϕ_{K^-}	ϕ-angle of K^-

The set of correlations was chosen in such a way that all the strongest ones in data are taken into account. By disabling and enabling some of these correlations and running the event mixing and background subtraction on the produced toy MC events it was

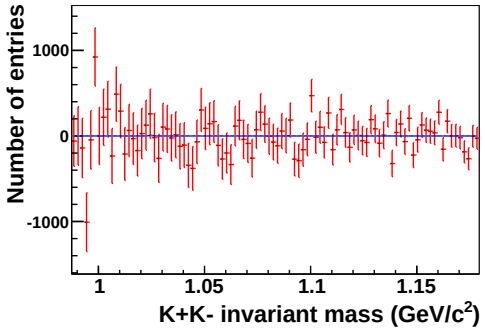

(a) Only (v_z vs N_{K^+} vs N_{K^-}) correlations from page 147 are enabled.

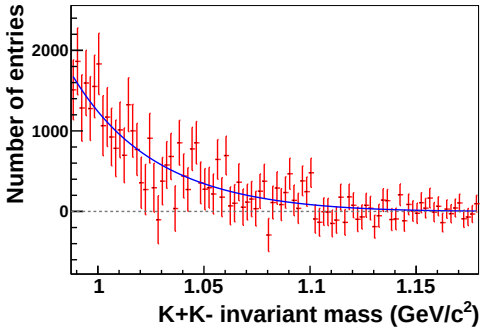

(b) Only (v_z vs N_{K^+} vs N_{K^-}), (v_z vs θ_{K^+}), (v_z vs θ_{K^-}) correlations from page 147 are enabled.

Figure 6.5.: In the intermediate ϕ meson transverse momentum data analysis residual background is solely due to the (v_z vs θ_{K^+}) and (v_z vs θ_{K^-}) correlations. The figure shows the result of event mixing (see section 6.1) and background subtraction applied on the toy MC events described in section 6.2.2 on the previous page, with exception that only some of the correlations were enabled. Fig. (a) shows the result for the case when only the (v_z vs N_{K^+} vs N_{K^-}) correlations from page 147 were enabled. Fig. (b) shows the result for the case when only the (v_z vs N_{K^+} vs N_{K^-}), (v_z vs θ_{K^+}), (v_z vs θ_{K^-}) correlations from page 147 were enabled. Further studies showed that no other correlations from page 147 could cause the event mixing procedure to be unable to reproduce the shape of background.

shown (see Fig. 6.5) that correlations

- v_z vs θ_{K^+}
- v_z vs θ_{K^-}

are solely responsible for the presence of a non-vanishing residual background. It was also demonstrated that the shape of the residual background is well described by an exponential function represented by *part 2* of Eq. 6.1.

Since it was impossible to quantify the exact values of parameters B and C in real data, the parameters were allowed to vary freely during fitting, with the initial guess of parameters coming from fitting the result of applying the event mixing 6.1 and background subtraction on the just described toy MC simulations.

The effect of a small θ-angle acceptance of the PHOBOS spectrometer is important for the intermediate p_t^{ϕ} data analysis, since (as it was pointed out on page 143) in that case both kaons resulting from a ϕ decay can be reconstructed only if they hit the same spectrometer arm. Due to this fact in the case of intermediate p_t^{ϕ} any two kaons (both in signal and in background) used to calculate invariant mass entries were reconstructed in the same spectrometer arm, which means that the opening angle between the two

kaons was small, and therefore the small modification of the angle due to the small acceptance effect was important. In case of $p_t^{\phi} \leq 0.13$ GeV/c, the two decay kaons can only be reconstructed if they hit different arms of the PHOBOS spectrometer. Due to this fact in the case of the lowest p_t^{ϕ} any two kaons (both in signal and in background) used to calculate invariant mass entries were reconstructed in different spectrometer arms, which means that the opening angle between the two kaons was large, and therefore the small modification of the angle due to the small acceptance effect was very small. Toy MC studies, described above, showed that in the case of the lowest p_t^{ϕ} event mixing described the background shape very well and the residual background was not noticeable, and therefore the corresponding term (part 2 in Eq. 6.1 on page 145) was not not used in the signal invariant mass distribution fit. Simply saying, small change to a small value creates a relatively large effect, but the same small change to a large value (as in our case) could be ignored.

6.2.3. Estimation On The Number Of Reconstructed ϕ Mesons In Data

The result of fitting the data invariant mass distribution with Eq. 6.1 are four parameters A, B, C, D and the corresponding covariance matrix.

The number of reconstructed ϕ mesons in data was determined as an integral of *part 3* of Eq. 6.1 over the whole invariant mass range, i.e. parameters A, B, C were set to be zero and the function 6.1 was integrated from $2m_K$ to $2m_K + 48\Gamma_{\phi}$.

To find the statistical error on the number of reconstructed ϕ mesons in data, the covariance matrix resulting from the data fit was used. Let us define

$$\mathscr{F} = \int_{2m_K}^{2m_K+48\Gamma_{\phi}} f(m_{inv}^{K^+K^-})\, d\, m_{inv}^{K^+K^-}$$

which depends on the values of parameters A, B, C, D. Therefore

$$d\mathscr{F} = \sum_{p=A,B,C,D} \frac{\partial \mathscr{F}}{\partial p} dp$$

$$d^2\mathscr{F} = \sum_{p,q=A,B,C,D} \frac{\partial \mathscr{F}}{\partial p} \frac{\partial \mathscr{F}}{\partial q} dp dq$$

and by taking the average over A, B, C, D

$$\sigma_{\mathscr{F}}^2 = \sum_{p,q=A,B,C,D} \frac{\partial \mathscr{F}}{\partial p} \frac{\partial \mathscr{F}}{\partial q} \mathrm{cov}(p,q). \tag{6.2}$$

Since we are only interested in the error on the integral of *part 3* of Eq. 6.1, for $p, q = A, B, C$ covariance matrix elements $\mathrm{cov}(p,q)$, $\mathrm{cov}(p,D)$, and $\mathrm{cov}(D,q)$ were set to zero and the result of Eq. 6.2 was taken to be the statistical error on the number of reconstructed ϕ mesons in data.

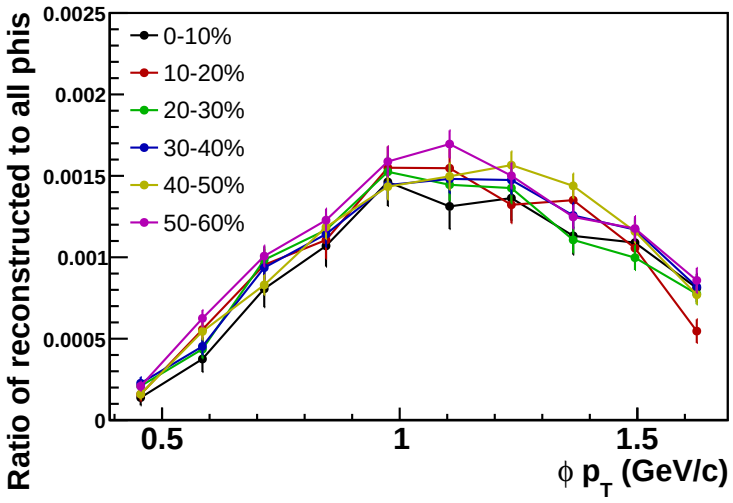

Figure 6.6.: Efficiency and occupancy correction for some of the centrality ranges (Cu+Cu 200 GeV, positive magnet polarity). Lines connect the points to guide the eye.

To estimate the number of reconstructed ϕ mesons in different transverse momentum bins, all the steps described in section 6.2 were performed in each transverse momentum bin separately.

6.3. Corrections

6.3.1. Efficiency And Occupancy Correction

Efficiency and occupancy correction was applied by dividing the raw number of reconstructed ϕ mesons in data (see section 6.2.3 on the previous page) by the fraction of reconstructed ϕ mesons embedded in to real data events. A few examples of efficiency and occupancy correction are shown on Fig. 6.6.

The procedure of finding the fraction of reconstructed ϕ mesons embedded in to real data events was the following in every p_t^{ϕ} bin:

1. For each real data event (from a list of data files used for embedding) passing the event selection 4.4, one ϕ meson was generated with uniform distributions in $p_t^{\phi} \in [0.13, 1.95]$, $y^{\phi} \in [-0.1, +1.1]$, $\varphi^{\phi} \in [-0.15, +0.15]$, and $\varphi^{\phi} \in [\pi - 0.15, \pi + 0.15]$ for intermediate p_t^{ϕ} case and with with uniform distributions in $p_t^{\phi} \in [0.0, 0.3]$, $y^{\phi} \in [+0.2, +1.1]$, and $\varphi^{\phi} \in [-\pi, +\pi]$ for the lowest p_t^{ϕ} case.

2. Each ϕ meson was isotropically decayed in to a K^+K^- pair with an invariant mass distributed according to Breit-Wigner distribution with vacuum mass and width of ϕ meson.

3. If -0.1 $\leq y^{\phi} \leq$ +1.1 (where y^{ϕ} is ϕ meson rapidity, and the range in rapidity is the ϕ meson acceptance for $v_z \in [-5,+15]$ cm) [3] and for both kaons $-0.2 \leq \varphi_K \leq +0.2$ or $\pi - 0.2 \leq \varphi_K \leq \pi + 0.2$ (i.e. both kaons are withing azimuthal angle acceptance of the PHOBOS detector spectrometer arms 2.2.5.3), then both of the decay kaons were propagated through the GEANT [223] simulation of the PHOBOS detector and the resulting hit arrays (for definition, see footnote on page 108) were saved.

4. The K^+K^- pair hit arrays were scaled to correct for the difference between energy losses in data and in PHOBOS MC simulations as explained in section 5.6 on page 106. After that the K^+K^- hit arrays were added to the real data event hit arrays. The real data event spectrometer hits were deleted and remade from the new hit arrays.

5. The ϕ meson vertex was different from the real data event vertex to take into account the vertex resolution effect on tracking efficiency. Even though v_z of every track was minimized during fitting (see 5.10.5 on page 131), the set of covariance matrices used for fitting of all the tracks in a given event was fixed and chosen based on the reconstructed event vertex, therefore some effect of vertex resolution on tracking efficiency was still present. The vertex resolution was calculated using HIJING MC simulations as a function of *EOct* and v_z , i.e. a 3D-histogram was filled with the variables Δv_z vs *EOct* vs v_z , where Δv_z is the difference between a simulated and reconstructed vertex. For ϕ meson embedded in to a every real data event a random difference between the event's reconstructed vertex and the ϕ meson vertex was assigned by generating a random number according to the MC vertex resolution histogram, using the event's v_z and *EOct* values.

6. Parameters of every ϕ meson embedding attempt were saved.

7. Full reconstruction (see chapter 5) was run on the event resulting in embedding, treating it as a real data event. The number of reconstructed ϕ mesons was found using the same event mixing technique as the one applied on real data events 6.1.

8. It was taken into account that there are some ϕ mesons in the real data events even before any embedding is done. The number was found following the same procedure as the one described above except that the actual embedding was not performed. The found number of such ϕ mesons was subtracted from the number of reconstructed ϕ mesons in the events with embedding.

9. Knowing the number of reconstructed ϕ mesons and the total number of ϕ meson embedding attempts the fraction of reconstructed ϕ mesons was found.

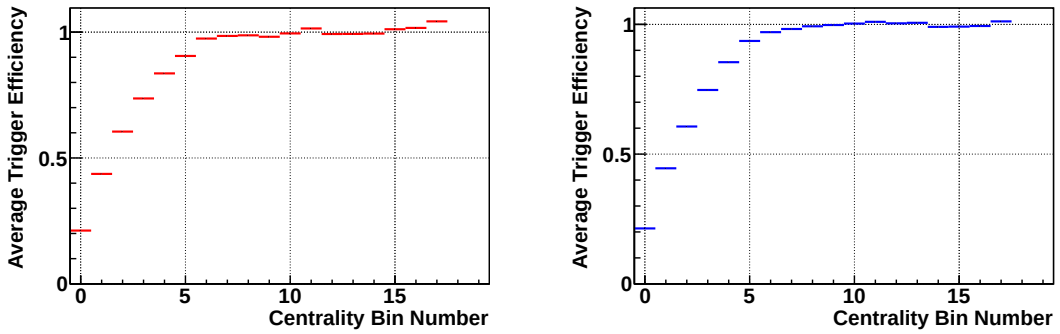

(a) positive polarity

(b) negative polarity

Figure 6.7.: Average trigger efficiency as a function of centrality bin number (see Table 4.1 on page 83) in PHOBOS Cu+Cu 200 GeV data at positive (a) and negative (b) magnet polarity.

6.3.2. Trigger Efficiency Correction

The purpose of the correction is to take into account the fact that the trigger efficiency deviates noticeably from 100% for the most peripheral events, which due to a event smaller multiplicity not always satisfy trigger conditions.

To apply the correction it was assumed that the trigger is 100% efficient for the event centrality corresponding to bin numbers 8 and above (i.e. for the 45% of the most central collisions, see Table 4.1 on page 83), which was confirmed with MC simulations (see section 4.5.3 on page 82) [4]. A histogram was filled with the number of events passing the event selection (see section 4.4 on page 78) in data corresponding to different centrality bins. Then the number of events in bins 16-17 was multiplied by a factor 5/3 and in bin 15 by a factor 5/4 to normalize to the same 5% fractional cross section. The number of events in centrality bins 8-17 was fit to a constant A, and then histogram was scaled by a factor $1/A$. The resulting histogram bin contents in bin numbers 1-7 are the average trigger efficiencies (see Fig. 6.7).

The effect of the trigger efficiencies was taken into account the following way:

- During filling of same event invariant mass and *EOct* vs v_z distributions all entries were given weight 1 for centrality bin numbers 8-17 and 1/trigger-efficiency for centrality bin numbers 1-7.

- During counting of both data and single embedded phi events, each event was counted with weight 1 for centrality bin numbers 8-17 and 1/trigger-efficiency for centrality bin numbers 1-7.

[3]The corresponding range of y^ϕ values for the lowest p_t^ϕ case was a little narrower ($0.2 \leq y^\phi \leq 1.1$) corresponding to a smaller ϕ meson acceptance for $v_z \in [-25,-5]$ cm.

[4]It is a safe assumption, since, actually, the simulations showed that the event selection (which includes the trigger) is 100% efficient for centrality bin 7 and above.

6.3.2.1. Systematic Error Due To Non 100% Efficient Trigger

Now, let us think about, what systematic effect a non 100% trigger efficiency could have on the measured invariant yield of ϕ mesons. The trigger efficiency determination procedure (see section 4.5.3 on page 82) is very simple and robust assuming, that the HIJING MC simulations describe the *EOct* distribution shape in data equally well at all collision centralities. So it will be supposed, that the trigger efficiency is known well. However, nothing is known about the invariant yield of ϕ mesons in the non-detected fraction of the collision cross-section. Since the efficiency of detecting a heavy ion collision by the trigger detectors depends on the total number of produced in the collision particles, it is reasonable to assume that the non-detected fraction of the collision cross-section corresponds to low particle multiplicities or even, in the worst case scenario, to no produced particles at all (including ϕ mesons). In the later case, $Y = \varepsilon \cdot y + (1-\varepsilon)\cdot 0 = \varepsilon \cdot y$, where Y and y are the true and the measured yields of ϕ mesons in some centrality range respectively, and ε is the average trigger efficiency in the centrality range. An so, the largest possible relative systematic error on Y is equal to $(y-Y)/Y = 1-\varepsilon$, which corresponds to an average relative systematic error of $(1-\varepsilon)/2$ and (see section 6.5.1.11 on page 174) to a resulting estimate on the error equal to $\sim 1.2534\cdot(1-\varepsilon)/2$. Therefore, the error is largest (as expected) for the most peripheral events (50-60%) used for the measurement. An addition of the error to the estimate of the total relative systematic error on the invariant yield of ϕ mesons (see section 6.5.1.10 on page 173) would only increase the later error by less than a factor of 1.02, and so the systematic error due to non 100% efficient triggering was neglected.

6.3.3. Momentum Resolution Correction

As was pointed out in 6.2.3, number of reconstructed ϕ mesons is estimated separately in different transverse momentum bins. Due to a finite resolution of momentum reconstruction some of ϕ mesons are counted in transverse momentum bins different from the ones corresponding to their true p_t^{ϕ} . It is explained below how this effect was corrected for.

Let us denote $\Delta p_t = p_t^{rec} - p_t^{true}$ to be the absolute p_t resolution, where p_t^{rec} is the reconstructed and p_t^{true} is the true ϕ meson transverse momentum . If $G(p_t^{true}, \Delta p_t)$ is the probability density function of Δp_t values at fixed $p_t^{true} = p_t^{rec} - \Delta p_t$, then $G(p_t^{true}, \Delta p_t)\cdot d\Delta p_t$ is the fraction of ϕ mesons with p_t^{true} which will be measured at p_t^{rec}, and therefore

$$\underbrace{\left(\frac{dN}{dp_t}\right)_{rec}(p_t^{rec})}_{\text{reconstructed } \frac{dN}{dp_t} \text{ at } p_t = p_t^{rec}} = \int_{-\infty}^{+\infty} \underbrace{\left(\frac{dN}{dp_t}\right)_{true}(p_t^{rec} - \Delta p_t)}_{\text{true } \frac{dN}{dp_t} \text{ at } p_t = p_t^{rec} - \Delta p_t} \cdot G(p_t^{rec} - \Delta p_t, \Delta p_t)\cdot d\Delta p_t \quad (6.3)$$

The goal of the momentum resolution correction is to find $(dN/dp_t)_{true}$ from knowing $(dN/dp_t)_{rec}$. It was assumed that the correction is not large (i.e. ≈ 1, which was

confirmed when the correction factors were found from the procedure described below), and therefore to the 1st order correction required for $dN/dp_t = (dN/dp_t)_{true}$ is the same as the one required for $dN/dp_t = (dN/dp_t)_{rec}$.

6.3.3.1. Intermediate Transverse Momentum Values

To find the correction in question in the intermediate transverse momentum range (i.e. $p_t \in [0.39, 1.69]$ GeV/c), the following MC simulation implementation was used instead of utilizing Eq. 6.3 directly, since tests showed that this approach worked better:

1. To find $G(p_t^{true}, \Delta p_t)$, or equivalently the distribution of p_t^{rec} vs p_t^{true} values, a set of single ϕ mesons decaying into K^+K^- pairs was embedded into real data events. The embedding procedure was the same as the one described in section 6.3.1. The full reconstruction (see chapter 5) was run on the resulting events, and the reconstructed tracks were matched to the MC information about K^+ and K^- tracks resulting from the ϕ meson decays, allowing it to compare reconstructed and MC values of p_t^{ϕ} . A histogram of p_t^{rec} vs p_t^{true} values of ϕ transverse momentum was filled [5]. See Fig. 6.8(a) on page 156 for an example resulting histogram.

2. ϕ meson invariant yield at as a function of p_t at low and intermediate transverse momentum values under consideration is well described by an exponential dependence, which is confirmed by good fit χ_r^2 values and the PHENIX collaboration data [253]. It is in general to be expected for particle spectra in heavy ion collisions, which typically show an exponential dependence at low and intermediate p_t due to a thermal emission from the fireball and a power law dependence at high p_t where particles are produced in hard scattering processes. Therefore the at this step $(dN/dp_t)_{rec}$ was fitted with function $p_t \exp(A + Bp_t)$, where A and B are fit parameters. During the fit the first 2 and the last 2 points were ignored since those were expected to have an underestimated number of entries due to the fact that some p_t entries would "leak out" of the bins due to momentum resolution but little entries would "leak in" since p_t values external to the measured range fall outside of the PHOBOS detector acceptance for ϕ mesons .

3. At the next step 7×10^5 random p_t values were generated according to the previous step dN/dp_t fit function. The values were generated in a much wider range of p_t (0-2.6 GeV/c) than the range on which data $(dN/dp_t)_{rec}$ was measured (0.39-1.69 GeV/c) to take into account the possibility of entries "leaking in" into the measured range of transverse momentum due to the final momentum resolution. Every p_t entry was "smeared" according to the step 1 p_t^{rec} vs p_t^{true} histogram, i.e. for every generated p_t value the corresponding p_t^{true} slice of the histogram was selected and a random p_t^{rec} value was generated according to the distribution of reconstructed values in the slice. The generated and the "smeared"

[5] In addition, every p_t^{true} bin of the histogram was normalized to have unit integral, however it should have no effect on the final result, since it does not change the shape of p_t^{rec} distributions corresponding to each such p_t^{true} bin.

p_t values were used to fill two dN/dp_t histograms such that the bin widths and the bin centers were the same as for the data $(dN/dp_t)_{rec}$ measurements. The ratio of the two histograms was the sought momentum resolution correction. An example of an input and corresponding "smeared" dN/dp_t distributions is shown on Fig. 6.8(b), with the resulting momentum resolution correction shown on Fig. 6.8(c).

4. After the correction was applied, all the dN/dp_t values were divided by p_t at the center of every bin to find the invariant yield. To test that the correction procedure just described is appropriate, the input $1/p_t dN/dp_t$ from the previous step was compared to the result of the momentum resolution correction applied on the "smeared" dN/dp_t distribution (see Fig. 6.8(d)), with the ratio of the two shown on Fig. 6.8(e). As can be seen from Fig. 6.8(e), the resulted momentum resolution corrected $1/p_t dN/dp_t$ values come out slightly (about ∼0.2%) lower than the input $1/p_t dN/dp_t$, therefore as the final operation of the correction dN/dp_t values found in step 3 were divided by the result of the fit by a constant function of the ratio on the figure.

6.3.3.2. Lowest Transverse Momentum Values

Momentum resolution correction was done somewhat differently for the measurement at the lowest transverse momentum values (i.e. $p_t < 0.13$ GeV/c). Since the measurement was done in one p_t bin only, a direct counting of the number of ϕ mesons "leaking" in and out of the p_t bin (based on MC simulations of single ϕ mesons embedded into real data events) was employed. Let us denote as

- $N_{\text{MC: } p_t<130 \text{ MeV/c}}$
  - the number of ϕ mesons in the simulations with MC $p_t < 130$ MeV/c,
- $N^{\text{Rec: } p_t>130 \text{ MeV/c}}_{\text{MC: } p_t<130 \text{ MeV/c}}$
  - the number of ϕ mesons in the simulations with MC $p_t < 130$ MeV/c which were reconstructed with $p_t > 130$ MeV/c (we will say that such mesons *leak out* of the $p_t < 130$ MeV/c bin),
- $N^{\text{Rec: } p_t<130 \text{ MeV/c}}_{\text{MC: } p_t>130 \text{ MeV/c}}$
  - the number of ϕ mesons in the simulations with MC $p_t > 130$ MeV/c which were reconstructed with $p_t < 130$ MeV/c (we will say that such mesons *leak in* into the $p_t < 130$ MeV/c bin).

Then the momentum resolution correction is

$$\underbrace{\frac{N_{\text{MC: } p_t<130 \text{ MeV/c}}}{N_{\text{MC: } p_t<130 \text{ MeV/c}} - N^{\text{Rec: } p_t>130 \text{ MeV/c}}_{\text{MC: } p_t<130 \text{ MeV/c}}}}_{\text{correction for the leaking out } \phi \text{ mesons}} \times \underbrace{\frac{N_{\text{MC: } p_t<130 \text{ MeV/c}} - N^{\text{Rec: } p_t<130 \text{ MeV/c}}_{\text{MC: } p_t>130 \text{ MeV/c}}}{N_{\text{MC: } p_t<130 \text{ MeV/c}}}}_{\text{correction for the leaking in } \phi \text{ mesons}}.$$

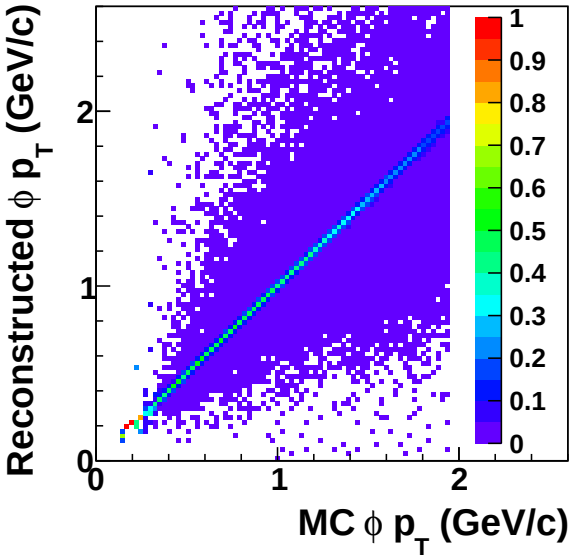

(a) Reconstructed versus MC p_t^{ϕ}

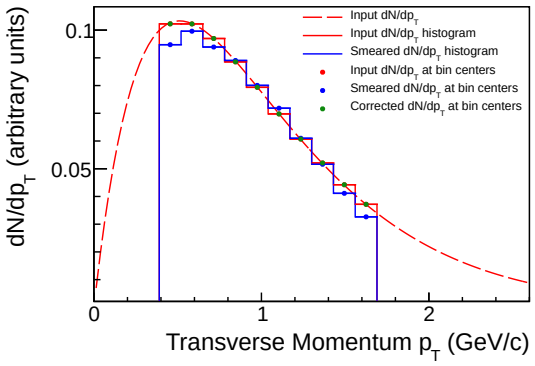

(b) Input, "smeared", and corrected dN/dp_t

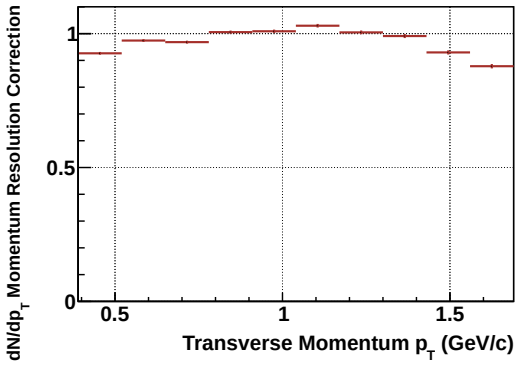

(c) Momentum resolution correction

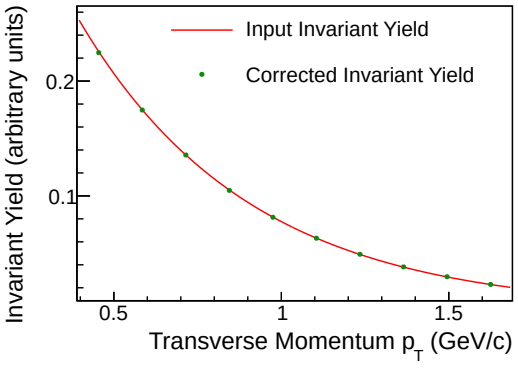

(d) Input and corrected invariant yields

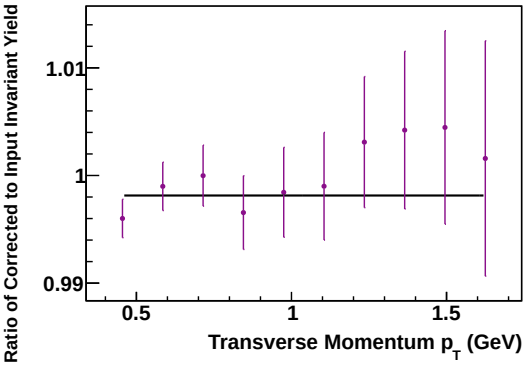

(e) Ratio of corrected to input invariant yield

Figure 6.8.: An example of momentum resolution correction, Cu+Cu 200 GeV, 0-60%. See section 6.3.3.1 on page 154 for details.

6.3.4. Dead Channel Map Correction

Some of the channels (i.e. pixels) of the PHOBOS spectrometer silicon sensors could be malfunctioning due to a manufacturing defect, radiation damage, or just due to normal wear and tear. Such channels could be either "dead" (i.e. invariably producing zero output signal), "hot" (i.e. always generating very large signal), or having having high noise level. A map of such channels (named not very well as *Dead Channel Map (DCM)*, while it would be more appropriate to call it a "Bad Channel Map") was created by marking as bad channels, which had[254]:

- average noise level above 15 keV,
- many more or many less hits than average in a particular spectrometer module,
- much higher or much lower mean energy per hit than average in a given spectrometer module.

The DCM could be used to remove (or *mask out*) the bad channels out of consideration, before the spectrometer hits used in specialized kaon reconstruction are made out of the energy loss information in all the channels.

While the bad channels are present in data, they are not modeled in PHOBOS MC simulations. Also the reconstruction of the full data set was done by using all spectrometer channels, including the bad ones. To take into account the effect of the bad channels on the final ϕ meson invariant yield result, a *DCM correction* was applied as described below.

Normally, ϕ meson dN/dp_t is determined as

$$\frac{dN}{dp_t} = \frac{T}{N\varepsilon}, \tag{6.4}$$

where N is the number of events passing the event selection (see section 4.4 on page 78), T is the raw number of ϕ mesons reconstructed in the data events corrected for trigger efficiency, and ε is the ϕ meson reconstruction efficiency (taking into account trigger efficiencies) found as described in section 6.3.1 on page 150. All the numbers are for a given ranges of centrality and p_t^{ϕ}. In Eq. 6.4, T and ε are effected by the bad spectrometer channels, and therefore need to be corrected for their effect. Since the effect of bad channels is essentially to change the number of hits (and therefore tracks) produced by some factor, both T and ε were corrected as

$$T^{\text{DCM}}_{\text{full data set}} = \frac{T^{\text{DCM}}_{\text{fractional data set}}}{T^{\text{no DCM}}_{\text{fractional data set}}} \cdot T^{\text{no DCM}}_{\text{full data set}}, \quad \text{and} \quad \varepsilon^{\text{DCM}} = \frac{T^{\text{DCM}}_{\text{MC}}}{T^{\text{no DCM}}_{\text{MC}}} \cdot \varepsilon^{\text{no DCM}}, \tag{6.5}$$

where $T^{\text{no DCM}}_{\text{full data set}}$ is the raw number of ϕ mesons in the full data set found by using all the spectrometer channels including the bad ones, $T^{\text{DCM}}_{\text{full data set}}$ is the raw number of ϕ mesons in the full data set corrected for the effect of bad channels, $T^{\text{DCM}}_{\text{fractional data set}}$ is the raw number of ϕ mesons in a subset of the full data set (~26% of all data) with all the bad channels masked out using the DCM, $T^{\text{no DCM}}_{\text{fractional data set}}$ is the raw number of ϕ mesons

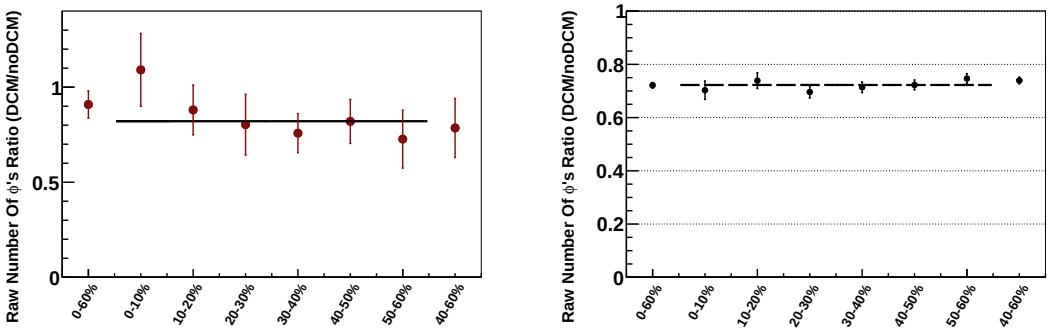

(a) DCM correction to raw number of ϕ's in data (b) DCM correction to ϕ reconstruction efficiency

Figure 6.9.: DCM correction in PHOBOS Cu+Cu 200 GeV positive polarity data ((a), first Eq. 6.5 on the preceding page, χ^2_r/ndf=2.95/5, fit-probability=0.71, correction=0.821±0.055) and single ϕ meson embedding ((b), second Eq. 6.5, χ^2_r/ndf=3.92/5, fit-probability=0.56, correction=0.723±0.009). The final correction on dN/dp_t (see Eq. 6.6) in positive polarity data is ∼1.136.

in the subset of the full data set found by using all the spectrometer channels, ε^{DCM} is the ϕ meson reconstruction efficiency corrected for the effect of bad channels, $\varepsilon^{\text{no DCM}}$ is the ϕ meson reconstruction efficiency found by using all the spectrometer channels, $T^{\text{DCM}}_{\text{MC}}$ is the raw number of embedded into data events ϕ mesons reconstructed after all the bad channels were masked out using the DCM, $T^{\text{no DCM}}_{\text{MC}}$ is the raw number of embedded into the data events (the same set of events, which was used to find $T^{\text{DCM}}_{\text{MC}}$) ϕ mesons reconstructed when all the spectrometer channels were used.

Combining Eq. 6.4 and 6.5 on the preceding page, one can get the following equation for the correction of dN/dp_t:

$$\left(\frac{dN}{dp_t}\right)_{\text{DCM}} = \underbrace{\frac{T^{\text{DCM}}_{\text{fractional data set}}}{T^{\text{no DCM}}_{\text{fractional data set}}} \Bigg/ \frac{T^{\text{DCM}}_{\text{MC}}}{T^{\text{no DCM}}_{\text{MC}}}}_{\text{Dead Channel Map correction}} \cdot \left(\frac{dN}{dp_t}\right)_{\text{no DCM}}, \tag{6.6}$$

where $(dN/dp_t)_{\text{DCM}}$ is the DCM corrected value, and $(dN/dp_t)_{\text{no DCM}}$ was calculated using all the spectrometer channels.

The correction was applied on results from positive and negative magnet polarity data separately. As an example, the two components of the correction (see Eq. 6.5 on the previous page) for positive polarity data are shown on Fig. 6.9.

6.4. Averaging Positive And Negative Magnet Polarity Data

PHOBOS Cu+Cu 200 GeV data used for this work was taken at two magnet polarities: positive and negative one (see section 2.2.5.3 on page 62). The ϕ meson invariant yield is of course independent of magnet polarity, but due to the facts that

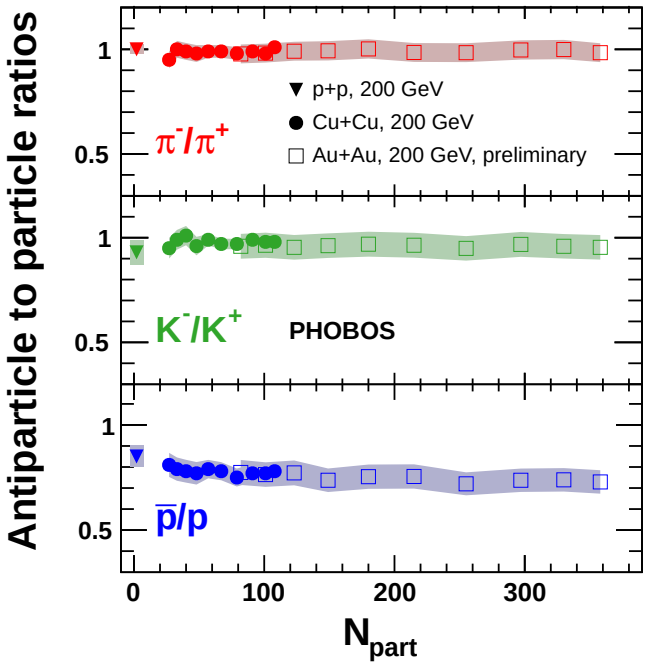

Figure 6.10.: PHOBOS measurements of particle to antiparticle ratios [255–257].

- different magnet polarities result in different acceptance for a given kind of charged particle
- the number of charged particles and their antiparticles produced in Cu+Cu collisions is not equal (which is to be expected - since the collided nuclei Cu^{+29} are positively charged, higher yield of positively charged particles over negatively charged ones has to be produced) - see Fig. 6.10

the event mixing and background subtraction (see section 6.1) was applied separately for different magnet polarity (both data and single embedded ϕ) events. The procedure of averaging the resulting invariant yields is described in 6.4.1.

6.4.1. Procedure

Let us denote as T_p and T_n raw number of ϕ mesons in positive and negative polarity data correspondingly corrected for trigger efficiency (the numbers are for a given ranges of centrality and p_t^{ϕ}). Both numbers were in addition to that:

- scaled to correspond to a yield per unit of transverse momentum and per unit of rapidity, by dividing by the width of the transverse momentum and rapidity intervals
- scaled with factors $1/(2\pi)$ and the reciprocal of $Br(\phi \rightarrow K^+K^-)$=0.489±0.005 [169], where the later is the $\phi \rightarrow K^+K^-$ branching ratio.

If N_p and N_n are the numbers of events passing the event selection (see section 4.4 on page 78), ε_p and ε_n are the ϕ meson reconstruction efficiencies (taking into account trigger efficiencies), and Y is the average number of ϕ mesons produced per event (in the considered range of centrality and p_t^{ϕ}), then

$$T_p + T_n = N_p \varepsilon_p Y + N_n \varepsilon_n Y \qquad \Longrightarrow \qquad Y = \frac{T_p + T_n}{N_p \varepsilon_p + N_n \varepsilon_n} \tag{6.7}$$

The final result was received by

1. Applying the DCM correction (see section 6.3.4 on page 157) on the raw number of ϕ mesons T_p and T_n and on the reconstruction efficiencies ε_p and ε_n.

2. Applying Eq. 6.7 to correct for efficiency and occupancy (including implicit correction for trigger efficiency, see section 6.3.2 on page 152) and to average both polarity results.

3. dN/dp_t resulting from the previous step was corrected for momentum resolution as described in section 6.3.3 on page 153.

4. Every point of such corrected dN/dp_t was divided by the $2\pi p_t$ value in the middle of the corresponding transverse momentum bin to obtain the ϕ meson invariant yield :

$$\frac{1}{2\pi p_t} \frac{d^2N}{dp_t dy}$$

6.5. Systematic Errors

6.5.1. ϕ Meson Invariant Yield Systematic Errors

6.5.1.1. General Method Description

Let us assume that we have two methods (#1 and #2) of doing a measurement of some variable Y as a function of a variable X, which differ due to some systematic effect. The two measurements might also differ statistically, in which case the statistical error is included into the systematic one to be conservative in the systematic error evaluation. Let us also assume that there is a function which fits the two measurements well and that there is a well defined procedure of averaging the two measurements. An example of fits of two such measurements as well as the fit of their average are shown on Fig. 6.11(a) on the next page. At the next step the ratio of fits of both measurements to the fit of their average is found (see Fig. 6.11(b)). After that the absolute value of the ratios deviation from unity is calculated (let us denote the deviations as $f_1(X)$ and $f_2(X)$, see Fig. 6.11(c)). Normally such deviation would serve as an estimate of the systematic error, however the fits of the two measurements might intersect in some point, which would lead to a vanishing evaluation of the error in the point. Since such a vanishing systematic error in a point is unlikely, the following procedure was used: if we denote as

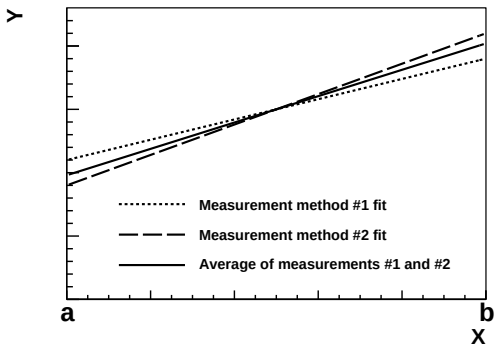

(a) Methods #1 and #2 and their average

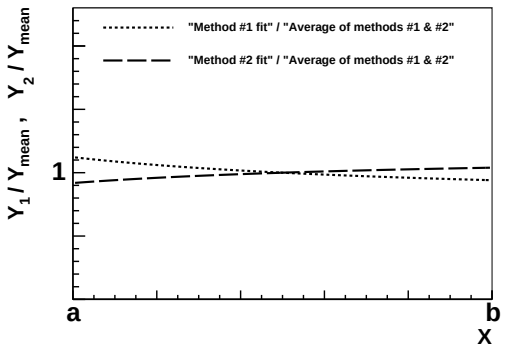

(b) Ratio of the methods #1 and #2 to their average

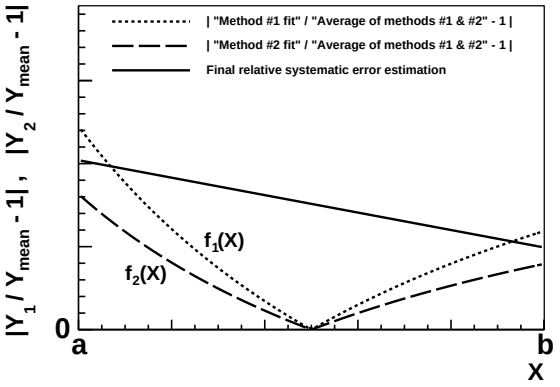

(c) Absolute value of the ratios deviation from unity

Figure 6.11.: Explanation of the ϕ meson invariant yield (Y) systematic errors estimation method. The Y relative systematic error dependence on X (transverse momentum) is estimated as a linear dependence passing through the points $(a,\ 0.5\cdot(f_1(a)+f_2(a))$ and $(b,\ 0.5\cdot(f_1(b)+f_2(b))$, where $f_i(X)=|Y_i(X)/Y_{\text{average of 1 and 2}}-1|$. See section 6.5.1.1 on the facing page for details.

Note, the pairs of figures shown in the subsequent sections, discussing particular sources of systematic errors, correspond to figures (b) and (c) shown here. In addition figures in the following sections show ratios and the errors of the data points corresponding to the fit lines.

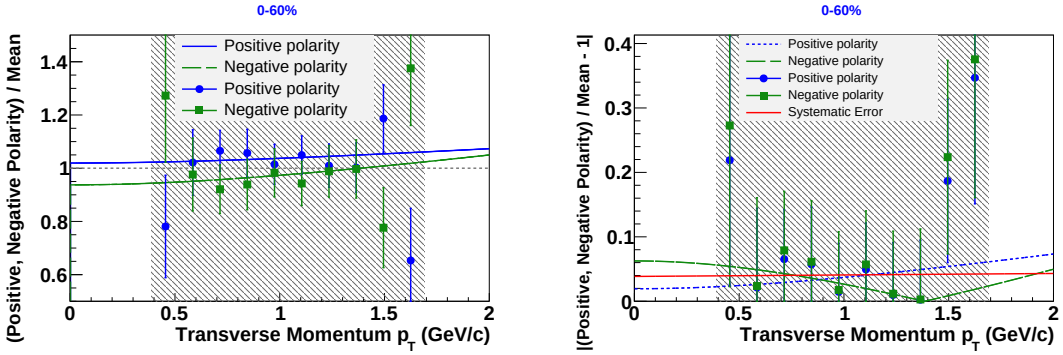

(a) Ratios of the positive and negative polarity to their average

(b) Absolute value of the ratios deviation from unity

Figure 6.12.: ϕ meson invariant yield measurement systematic error due to the uncertainty in the magnetic field map (see section 6.5.1.2 for details).

$[a,b]$ the X interval in which the measurement was made, then the dependence of the relative systematic error on X was found by connecting with a straight line the points $(a,\ 0.5\cdot(f_1(a)+f_2(a))$ and $(b,\ 0.5\cdot(f_1(b)+f_2(b))$ as shown on Fig. 6.11(c).

In our case X and Y are the ϕ meson transverse momentum and invariant yield correspondingly. The averaging procedure of measurement methods #1 and #2 is analogous to the one used for averaging positive and negative magnet polarity data (see section 6.4.1 on page 159 and Eq. 6.7):

$$\left(\frac{dN}{dp_t}\right)_{\text{eff, occ}} = \frac{T_1+T_2}{N_1\varepsilon_1+N_2\varepsilon_2}, \tag{6.8}$$

where $(dN/dp_t)_{\text{eff, occ}}$ is the efficiency and occupancy corrected value, T_1 and T_2 are the raw numbers of ϕ mesons found in measurement methods #1 and #2 correspondingly corrected for trigger efficiency, N_1 and N_2 are the numbers of events passing the event selection (see section 4.4 on page 78), ε_1 and ε_2 are the ϕ meson reconstruction efficiencies (taking into account trigger efficiencies). The value $(dN/dp_t)_{\text{eff, occ}}$ was corrected for momentum resolution as described in section 6.3.3 on page 153 and then every point of such corrected dN/dp_t was divided by the $2\pi p_t$ value in the middle of the corresponding transverse momentum bin to obtain the averaged ϕ meson invariant yield. Except during the estimation of the systematic error due to the uncertainty in the magnetic field map (see section 2.2.5.3 on page 62), no correction was done for the DCM (see section 6.3.4 on page 157), since the correction would cancel in a ratio of a method to the average of the two methods if both of them use the same magnet polarity data for the measurement.

6.5.1.2. Systematic Error Due To An Uncertainty In The Magnetic Field Map

PHOBOS magnetic field map (see section 2.2.5.3 on page 62) was measured and saved

for the positive magnet polarity only. Both during the MC simulations and in the specialized kaon reconstruction the magnetic field at the negative magnet polarity was calculated as the -1 times the magnetic field at the positive magnet polarity, which is only approximately correct. In addition the magnetic field map could have changed slightly between the measurement and the actual data taking due to installation of the PHOBOS spectrometer (and of other equipment) between the magnet poles. It is also possible that the magnetic field measurement was taken with a small systematic error due to a non perfect gaussmeter used or due to imprecise measurement of the geometric position of the gaussmeter in the process. The magnetic field measurements were taken at a limited number of points and a 3-dimensional linear interpolation was used to evaluate the field between the points, resulting in an additional source of inaccuracy. Stability of the magnet power source and some other reasons could be added to the list. Therefore a ϕ meson invariant yield measurement had a systematic error associated with the imperfect knowledge of the magnetic field. To estimate the error following the method described in section 6.5.1.1 on page 160 two methods of doing the measurement were compared: using only positive and using only negative magnet polarity data. The PHOBOS magnetic field map and therefore the systematic error are not centrality dependent, consequently the error was calculated for all centralities using the 0-60% centrality range (see section 4.5 on page 79) data only. The found systematic error was about $\sim$4% (at $p_t^{\phi} \approx$1 GeV/c), with the exact dependence on transverse momentum shown as the red line on Fig. 6.12(b) on the facing page.

6.5.1.3. Systematic Error Due To An Uncertainty In The Spectrometer Sensors Positions

Both the MC simulations and the specialized kaon reconstruction used the geometrical positions of the spectrometer sensors (see section 2.2.5.3 on page 60) to calculate the actual position of a hit from its position relative to the sensor the hit was produced in. Since the measurement of the sensor positions and their aligning procedures are not perfect, there is an associated systematic error in the ϕ meson invariant yield measurement, which was estimated using the method described in section 6.5.1.1 on page 160 by comparing the following two methods combinations of doing the measurement:

- using only the $[-5,+5]$ cm and only the $[+5,+15]$ cm vertex z-coordinate range (see Fig. 6.13(a) and Fig. 6.13(b) on the next page)
- using only the hits in the positive and only the hits in the negative arm of the PHOBOS spectrometer (see Fig. 6.13(c) and Fig. 6.13(d) on the following page).

Each of the two methods combinations produced an estimate on the systematic error in both positive and negative magnet polarity data separately. At each polarity the systematic errors from the two combinations were added in quadrature. Averaging of the systematic error at both magnet polarities is described in section 6.5.1.10 on page 173.

The geometrical positions of the spectrometer sensors and therefore the systematic error are not centrality dependent, consequently the error was calculated for all centralities using the 0-60% centrality range (see section 4.5 on page 79) data only. The found systematic error was about $\sim$15.3% (at $p_t^{\phi} \approx$1 GeV/c).

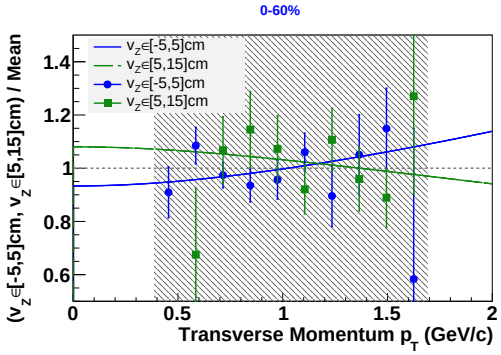

(a) Ratios of the $(-5,+5)$ cm and $(+5,+15)$ cm vertex z-coordinate intervals to their average

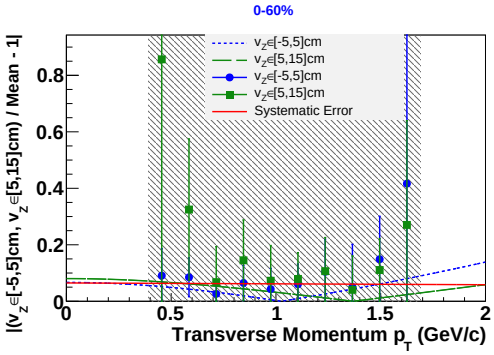

(b) Absolute value of the ratios deviation from unity

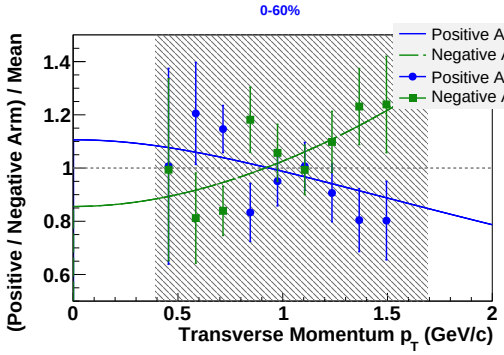

(c) Ratios of the positive and negative arm to their average

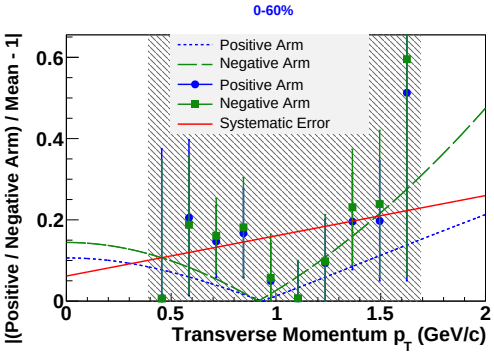

(d) Absolute value of the ratios deviation from unity

Figure 6.13.: ϕ meson invariant yield measurement systematic error due to the uncertainty in the geometric position of the spectrometer sensors in positive magnet polarity data (see section 6.5.1.3 on the preceding page for details).

6.5.1.4. Systematic Error Due To Different Choice Of Distributions Used For Efficiency And Occupancy Correction

The efficiency and occupancy correction described in section 6.3.1 on page 150 depends on the distributions of ϕ mesons embedded into real data events. The correction applied on the data utilized uniform distributions in p_t^{ϕ}, y^{ϕ} and φ^{ϕ} and used one embedded ϕ meson per event. To estimate the systematic error due to this particular choice of the distributions, the ϕ meson invariant yield results were compared to those resulting from more realistically chosen distributions of p_t^{ϕ} (see section 5.2.3 on page 95), y^{ϕ} (see section 5.2.2 on page 95) and number of embedded ϕ mesons per event (see section 5.2.4 on page 97). The general method of the systematic error evaluation arising from the two methods of doing the efficiency and occupancy correction is described in section 6.5.1.1 on page 160.

The systematic error was estimated separately for positive and negative polarity data,

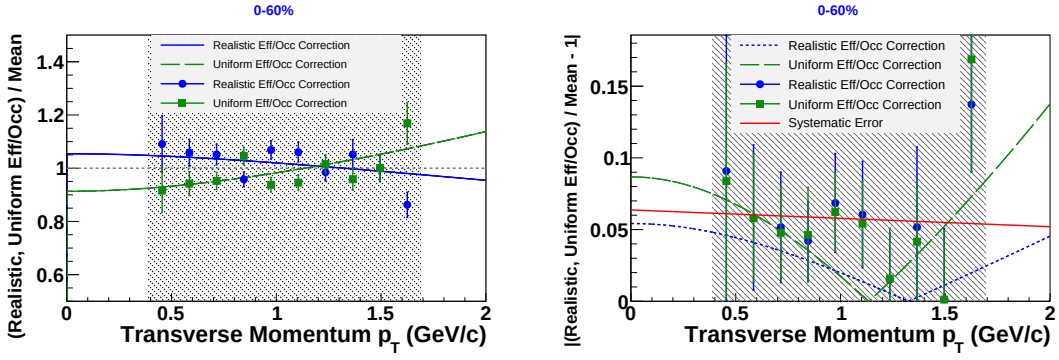

(a) Ratios of the results using uniform and realistic distributions to their average

(b) Absolute value of the ratios deviation from unity

Figure 6.14.: ϕ meson invariant yield measurement systematic error due to the choice of distributions used in efficiency and occupancy correction in positive magnet polarity data (see section 6.5.1.4 on the facing page for details).

with averaging procedure of the two described in section 6.5.1.10 on page 173. The realistic p_t^ϕ distributions and number of ϕ mesons per event are centrality dependent, however the slope parameter T characterizing the p_t^ϕ distribution (see Fig. 7.4(a) on page 191) and ϕ meson reconstruction efficiency (see Fig. 6.6 on page 150) have weak dependence on centrality, therefore if we consider the change in the efficiency and occupancy correction from the replacement of uniform embedding distributions with realistic ones as a 1st order effect, then the correction dependence on centrality would be of the 2nd order, and so was neglected [6]. Consequently the systematic error was calculated for all centralities using the 0-60% centrality range (see section 4.5 on page 79) single ϕ mesons embedding. The found systematic error was about ~6% (at $p_t^\phi \approx$1 GeV/c) [7]. Now the argument given above might be not convincing for some people, therefore the correction was compared to the one calculated using the 0-10% centrality range, resulting in about ~7% (at $p_t^\phi \approx$1 GeV/c), which provides a direct evidence

[6] Any change in efficiency and occupancy correction due to a change in the number of embedded ϕ mesons per event comes from a change of relative weights of different centrality ranges contributing to the correction. Since the dependence of the correction on centrality is weak, then the change in the correction due to the change in the weights has to be weak too.

[7] Statistical fluctuations, which are due to a limited statistics in the MC simulations, contribute a significant amount to the systematic error estimate (as well as to the estimates of systematic errors resulting from other sources). The error discussed here was also estimated using a much higher statistics single embedded ϕ meson MC simulations with the transverse momentum distributions of ϕ mesons having the parameters shown in Table 7.2 on page 188, instead of the realistic p_t^ϕ distributions described in section 5.2.3 on page 95. The resulting from the study systematic error estimate was significantly smaller, namely ~2.4% at $p_t^\phi \approx$1 GeV/c. But even that evaluation contains contributions from the statistical fluctuations in the MC simulations. However, since the error is not a large fraction of the total systematic error, in the final estimate the results of the method discussed in section 6.5.1.4 were used.

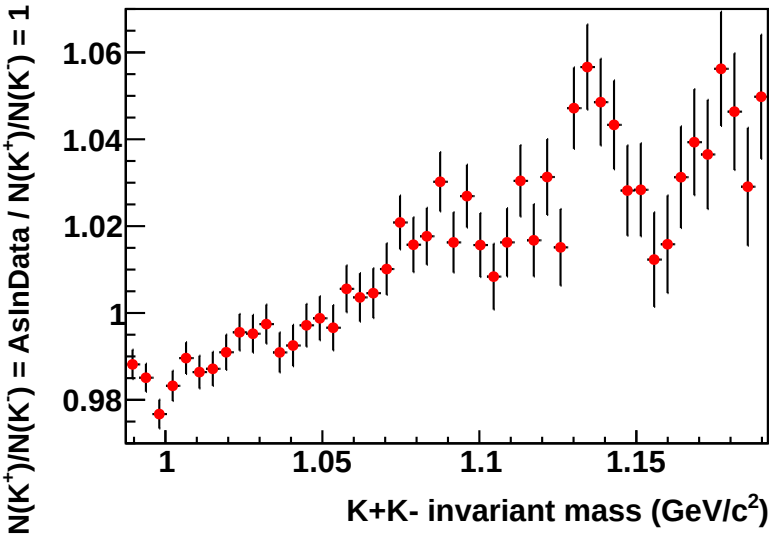

Figure 6.15.: Ratio of pure backgrounds simulated using 0-10% centrality data as input. See section 6.5.1.5 for details.

that the correction does not depend strongly on centrality [8].

As an example, the systematic error estimation for positive magnet polarity data is shown on Fig. 6.14 on the preceding page.

6.5.1.5. Systematic Error Due To Correlations Between Same Event Background Entries

When the signal (i.e. same event) invariant mass distribution is built, all possible combinations of reconstructed K^+ and K^- tracks passing the event and track selections are made. As a result if there is more than one reconstructed kaon track of the some charge and at least one reconstructed kaon track of the other charge in the same event, then at least one kaon will be used more than once to create kaon pairs to be used in invariant mass entries calculation. That leads to an implicit correlation between the entries which effects the shape of the invariant mass distribution and therefore the raw number of reconstructed ϕ mesons in data and in single ϕ meson embedding, which in turn is a source of a systematic error on the ϕ meson invariant yield .

To illustrate it, a number of realistically distributed toy MC events were simulated (see section 6.2.2 on page 147 for the description of the simulation details) for the following two cases:

- number of K^+ and number of K^- per toy event are simulated to have the same distributions as in real data,
- number of K^+ and number of K^- per toy event are always equal to one.

[8] Estimation of the systematic error directly for peripheral events would require investment of large computing resources. Based on the evidence at hand the benefit of it is dubious and not worth the effort.

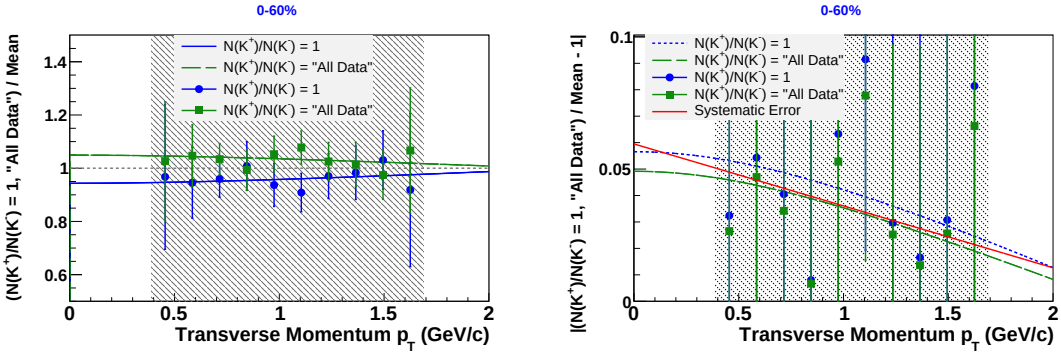

(a) Ratios of the results using $\langle N(K^+)/N(K^-)\rangle = 1$ and full data events to their average

(b) Absolute value of the ratios deviation from unity

Figure 6.16.: ϕ meson invariant yield measurement systematic error due to correlations between same event background entries in positive magnet polarity 0-60% centrality data (see section 6.5.1.5 for details).

There were no correlations between different kaon tracks in the events, and therefore the events corresponded to pure background. The ratio of the normalized to the same integral invariant mass distributions corresponding to the two cases listed above is shown on Fig. 6.15 on the facing page. As one can see, the ratio is inconsistent with unity as a function of invariant mass, which proves that the shapes of the two distributions are different.

A similar idea was used to estimate the systematic error quantitatively. Namely, following the general method of the systematic error evaluation described in section 6.5.1.1 on page 160, the following two methods of doing the measurement were compared:

1. The regular one described in sections 6.1, 6.2, 6.3 and 6.4.

2. A modified one in such a way that the measurement was done on data events with average $\langle N(K^+)/N(K^-)\rangle = 1$, where the $N(K^+)$ and $N(K^-)$ are the numbers of reconstructed K^+ and K^- tracks in an event. The modification is described in the end of the current section.

As an example, the systematic error estimation for positive magnet polarity data is shown on Fig. 6.16.

The systematic error was found separately for positive and negative polarity data, with averaging procedure of the two described in section 6.5.1.10 on page 173. The error was estimated singly also for each considered centrality range, resulting in the values summarized on Fig. 6.17 on the following page.

Making measurement on data events with $\langle \mathbf{N(K^+)/N(K^-)}\rangle = \mathbf{1}$. The measurement was done by randomly skipping some of the tracks in data events in such a way that the

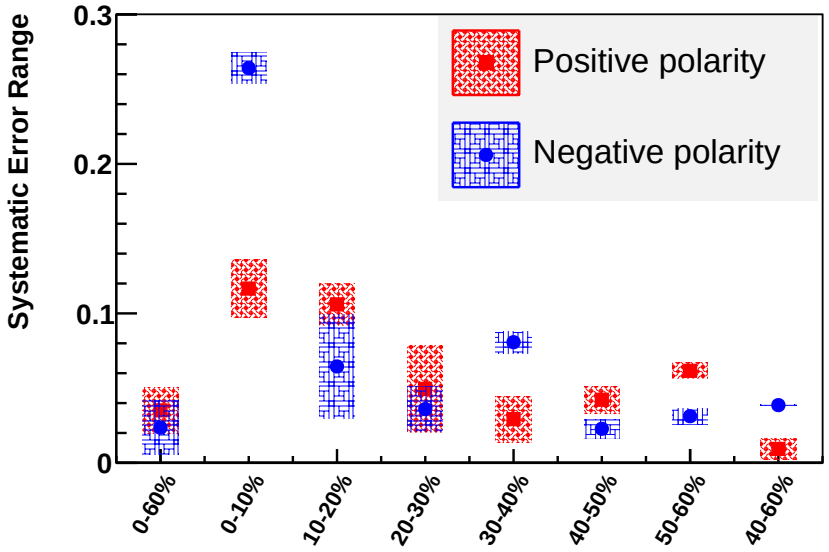

Figure 6.17.: ϕ meson invariant yield measurement systematic error due to correlations between same event background entries. Note, the points on the figure show the average error for each ("centrality range" × "magnet polarity") combination with the vertical size of the filled rectangles showing the range of the values the error assumes as a function of transverse momentum . See section 6.5.1.5 for details.

resulting average ratio of $N(K^+)$ and $N(K^-)$ per event would be unity as a function of centrality. First, the dependence of $\langle N(K^+)/N(K^-)\rangle$ on centrality was found for both positive and negative polarity data events (see Fig. 6.18 on the next page). Second, when the signal (i.e. same event) invariant mass distribution was built for data and single ϕ meson embedding MC, at negative polarity every K^+ track was ignored with probability $1/\langle N(K^+)/N(K^-)\rangle - 1$, where the average $\langle N(K^+)/N(K^-)\rangle$ was taken from Fig. 6.18(b) on the facing page at the centrality bin number of a currently processed event. At positive polarity the procedure was the same, except that all the kaon charges were reversed and the $\langle N(K^-)/N(K^+)\rangle$ was taken from Fig. 6.18(a). The result of the procedure was as if the average $\langle N(K^+)/N(K^-)\rangle = 1$ per event in data was unity as a function of centrality. In single ϕ meson embedding MC the average ratio was modified from its original value but ended up being somewhat different from unity since the original ratio in such MC was slightly different from the one in data. As can be seen, in both data and MC the raw number of reconstructed ϕ mesons at a given centrality was reduced by the factor $\langle N(K^+)/N(K^-)\rangle$ at negative polarity (and by the factor $\langle N(K^-)/N(K^+)\rangle$ at positive polarity), and therefore the ratio of the numbers (and consequently the ϕ meson invariant yield) stayed the same as in the unmodified measurement method, therefore the two methods could only differ due to the change in the background shape (and due to the statistical nature of the tracks ignoring), and therefore their comparison could be used to get (a somewhat overestimated) evaluation of the systematic error under study.

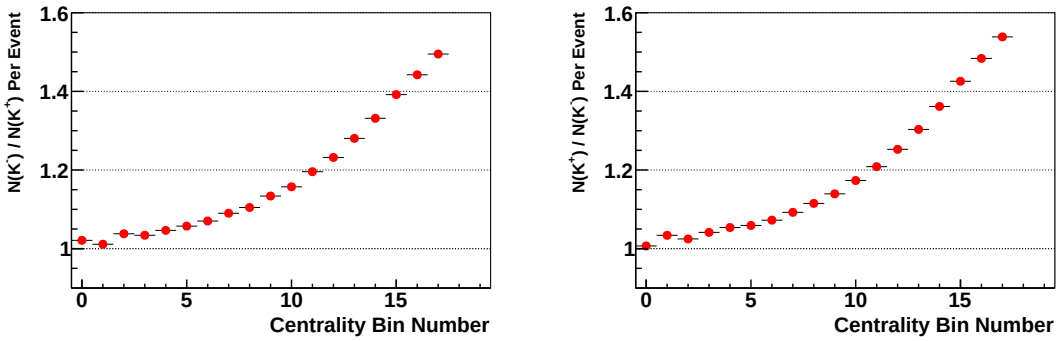

(a) positive polarity

(b) negative polarity

Figure 6.18.: Average ratio of number of reconstructed K^- to number of reconstructed K^+ per event as a function of centrality in positive magnet polarity Cu+Cu 200 GeV data (Fig. (a)). For the negative magnet polarity data the ratio was the reciprocal of the one in positive magnet polarity data (Fig. (b)). The plots for single ϕ meson embedding MC are very similar to the ones shown above. See page 167 for details.

6.5.1.6. Systematic Error Due To Choice Of Residual Background Shape Model

As it was pointed out in section 6.2.2 on page 147, residual background (due to a small vertex z-coordinate dependent θ-angle acceptance of the PHOBOS spectrometer) is well described with an exponential function of invariant mass. However, it is not the only possible function, which can be chosen for the purpose, leading to a source of a systematic error.

To estimate the error following the method described in section 6.5.1.1 on page 160 two ways of doing the measurement were compared: describing the residual background with an exponential function (as described in section 6.2 on page 145) and with a hyperbolic function (i.e. $A/(x-B)+C$).

Since the residual background is due to a geometric acceptance effect, it and therefore the systematic error under study are not centrality dependent, consequently the error was calculated for all centralities using the 0-60% centrality range (see section 4.5 on page 79) data only. The found systematic error was about ~2% (at $p_t^{\phi} \approx 1$ GeV/c). As an example, the systematic error estimation for positive magnet polarity data is shown on Fig. 6.19 on the next page. The systematic error was found separately for positive and negative polarity data, with averaging procedure of the two described in section 6.5.1.10 on page 173.

6.5.1.7. Systematic Error Due To Choice Of ϕ Meson Peak Shape Model

As it was pointed out in section 6.2 on page 145, ϕ meson peak (before modification due to the small azimuth angle acceptance of the PHOBOS spectrometer) was fitted as

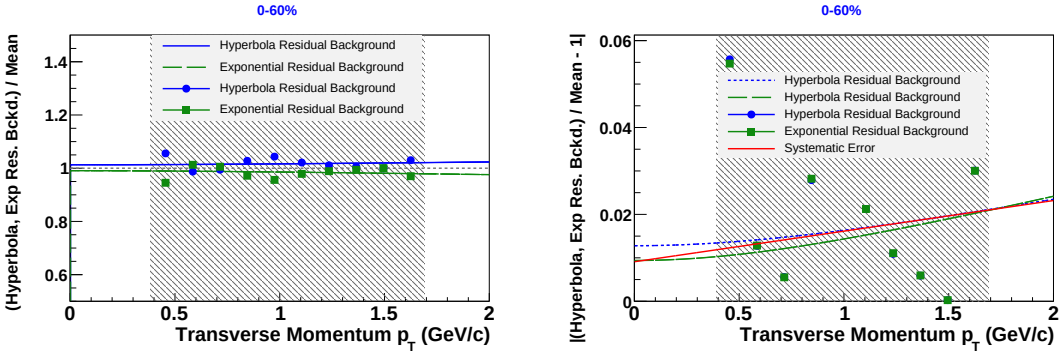

(a) Ratios of the exponential and hyperbolic fits to their average

(b) Absolute value of the ratios deviation from unity

Figure 6.19.: ϕ meson invariant yield measurement systematic error due to the uncertainty in the residual background shape model in positive magnet polarity Cu+Cu 200 GeV data (see section 6.5.1.6 on the preceding page for details).

a Breit-Wigner distribution. However, it is not the only possible function, which can be chosen for the purpose, leading to a source of a systematic error.

To estimate the error following the method described in section 6.5.1.1 on page 160 two ways of doing the measurement were compared: fitting the ϕ meson peak with a Breit-Wigner distribution (with the mean, the width and the overall scaling factor as free parameters) and with a Breit-Wigner distribution convoluted with a Gaussian distribution (with the Breit-Wigner mean, the Gaussian width and the overall scaling factor as free parameters):

$$\int_{-\infty}^{+\infty} \mathbb{B}^{E,F}(m_{inv}^{K^+K^-} - x) \cdot G^{0,\sigma}(x) \cdot dx,$$

where $\mathbb{B}^{E,F}(m_{inv}^{K^+K^-} - x)$ was defined in section 6.2 on page 145, and $G^{0,\sigma}(x)$ is the normalized to unit integral Gaussian distribution with the zero mean and width σ.

Since the possible choices of the ϕ meson peak fit functions, and therefore the systematic error under study are not centrality dependent, consequently the error was calculated for all centralities using the 0-60% centrality range (see section 4.5 on page 79) data only. The found systematic error was about ~4% (at $p_t^{\phi} \approx 1$ GeV/c). As an example, the systematic error estimation for positive magnet polarity data is shown on Fig. 6.20 on the next page. The systematic error was found separately for positive and negative polarity data, with averaging procedure of the two described in section 6.5.1.10 on page 173.

6.5.1.8. Systematic Error Due To Momentum Resolution Correction

As it was pointed out in section 6.3.3 on page 153, for the purpose of applying the momentum resolution correction, data ϕ meson dN/dp_t distribution was fitted with an

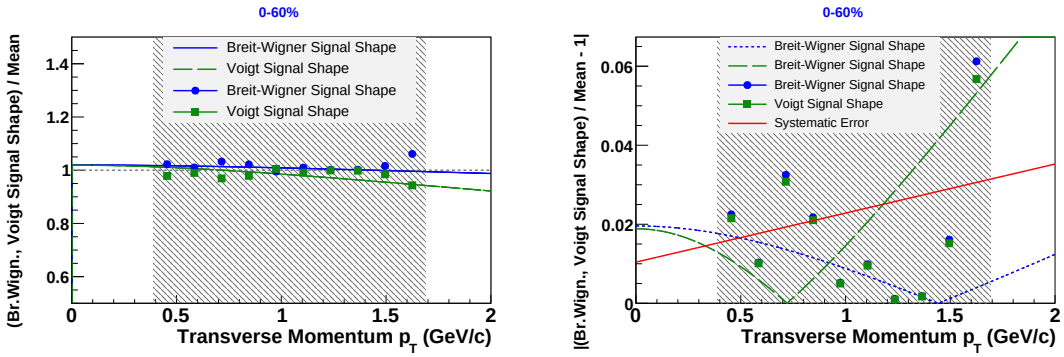

(a) Ratios of the Breit-Wigner and Voigt fits to their average

(b) Absolute value of the ratios deviation from unity

Figure 6.20.: ϕ meson invariant yield measurement systematic error due to the uncertainty in the ϕ meson peak shape model in positive magnet polarity Cu+Cu 200 GeV data (see section 6.5.1.7 on page 169 for details).

exponential function, i.e. $p_t \exp(A + Bp_t)$. However, it is not the only possible function, which can be chosen for the purpose, leading to a source of a systematic error.

To estimate the error following the method described in section 6.5.1.1 on page 160 two ways of doing the measurement were compared: fitting the ϕ meson dN/dp_t with an exponential function of p_t and with an exponential function of m_t. The second choice means the following, assuming that the distribution of ϕ mesons $1/m_t \cdot dN/dm_t$ is exponential, then after conversion of the distribution into a dN/dp_t we get the following fit function:

$$A \cdot p_t \cdot \exp\left(-\frac{\sqrt{p_t^2 + m_\phi^2} - m_\phi}{B}\right)$$

Since the possible choices of the dN/dp_t fit functions, and therefore the systematic error under study are not centrality dependent, consequently the error was calculated for all centralities using the 0-60% centrality range (see section 4.5 on page 79) data only. The found systematic error was about ~0.25% (at $p_t^\phi \approx 1$ GeV/c). As an example, the systematic error estimation for positive magnet polarity data is shown on Fig. 6.21. The systematic error was found separately for positive and negative polarity data, with averaging procedure of the two described in section 6.5.1.10 on page 173.

6.5.1.9. Systematic Error Due To Correction Of MC Energy Losses

As it was pointed out in section 5.6 on page 106, due to a disagreement between data and MC kaon energy losses, the later had to be scaled down by a factor of ~1.1821 to match energy losses in data. If the factor is chosen with some deviation from the exactly correct one, that would lead to a systematically incorrectly estimated efficiency of ϕ

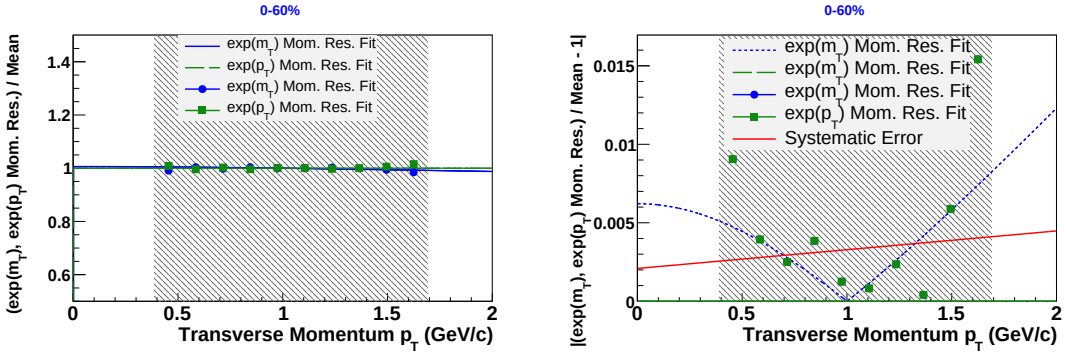

(a) Ratios of the exp(p_T) and exp(m_T) fits to their average

(b) Absolute value of the ratios deviation from unity

Figure 6.21.: ϕ meson invariant yield measurement systematic error due to the uncertainty in the momentum resolution correlation in positive magnet polarity Cu+Cu 200 GeV data (see section 6.5.1.8 on page 170 for details).

meson reconstruction from single embedded ϕ meson MC simulations and therefore to a source of a systematic error in the ϕ meson invariant yield measurement.

To estimate the error following the method described in section 6.5.1.1 on page 160 two values of the MC energy loss scaling factors were compared: ∼1.1821 and ∼1.1834. The second value was chosen based on the following argument. Studies showed that the ∼1.1821 factor produces MC energy losses which are still ∼0.2% larger than in data (see Fig. 5.13 on page 111). Before that the closest scaling factor attempted was ∼1.1795 (the scaling factor was adjusted in reducing steps, with a next attempted factor chosen based on the results of the previous ones). However, the factor of ∼1.1898 already produced MC energy losses lower than in data. That means that the correct scaling factor must be in the range [1.1821, 1.1898], therefore the second value chosen for the systematic error evaluation was $1.1821 + 0.5 \cdot (1.1821 - 1.1795) = 1.1834$.

Since the effect of the systematic error would depend on

- the average energy losses in the underlying events
- the probability of assigning a wrong hit during reconstruction to a MC kaon

in single embedded ϕ meson MC simulations and both of the effects are centrality dependent, the estimation of the systematic error was done separately for each centrality range used for the measurement. The found ranges of the systematic error assumed as a function of p_t are shown in Table 6.1 on the facing page. The error was estimated for positive magnet polarity data only, since there is no reason to believe that the effect at negative polarity would be significantly different [9]. The systematic error in negative polarity data was assumed to be (approximately) the same as in positively magnet polarity

[9]The difference between the two magnet polarity data is the following: 1) there are slightly more positively charged reconstructable particles in data than negatively charged ones, 2) the efficiency of

Centrality Range (%)	0-60	0-10	10-20	20-30
Systematic Error Range (%)	1.1-1.4	1.4-4.9	2.4-3.9	6.7-9.3
Centrality Range (%)	30-40	40-50	50-60	40-60
Systematic Error Range (%)	0.8-1.7	0.9-2.4	2.6-3.2	1.3-2.0

Table 6.1.: Ranges of values assumed as a function of p_t by the ϕ meson invariant yield systematic error due to correction of MC energy losses.

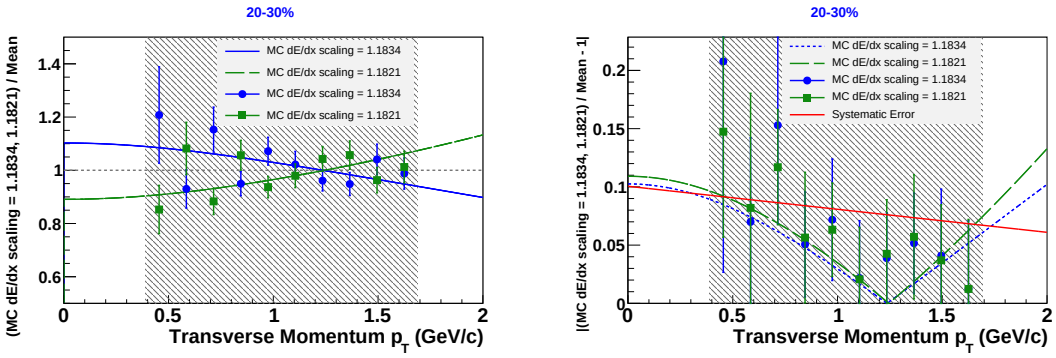

(a) Ratios of the ∼1.1821 and ∼1.1834 dE/dx scaling factors to their average

(b) Absolute value of the ratios deviation from unity

Figure 6.22.: ϕ meson invariant yield measurement systematic error due to the uncertainty in the MC energy losses scaling factor in positive magnet polarity Cu+Cu 200 GeV data (see section 6.5.1.9 on page 171 for details).

data. As an example, the systematic error estimation for the 20-30% centrality range is shown on Fig. 6.22.

6.5.1.10. Averaging Of Systematic Error In Positive And Negative Magnet Polarity Data

As it has been described above, the systematic errors from all the sources has been estimated separately for positive and negative polarity, except the one due to an uncertainty in the magnetic field map (by the nature of the error, see section 6.5.1.2 on page 162) and the one due to correction between data and MC energy losses (the error was assumed to be the same for both polarities, see section 6.5.1.9). The first step of averaging was to add all the systematic errors in quadrature within one polarity singly in each range of centrality. Then in each centrality range the total systematic error was found by averaging the errors in positive and negative polarities with weights 0.54 and 0.46 correspondingly, where the weights are the fractions of all used data with the respective magnet

reconstruction is higher for particles bending away from the beam pipe, and that direction changes to the opposite when the magnet polarity is switched. Therefore the average hit density in the underlying event should be slightly higher in negative polarity data than in positive one.

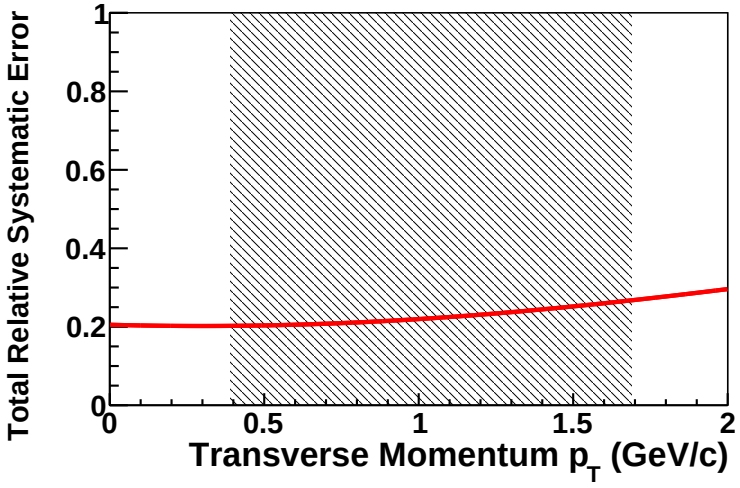

Figure 6.23.: ϕ meson invariant yield measurement total relative systematic error for the 0-60% centrality range. See section 6.5.1.10 on the preceding page for details. The extra factor of ∼1.2534, discussed in section 6.5.1.11 is already included in this figure.

polarities. The resulting relative systematic errors at each magnet polarity separately and the average of the two were approximately constant as functions of transverse momentum and collision centrality. As an example, the total systematic error for the 0-60% centrality range is shown on Fig. 6.23.

6.5.1.11. Difference Between $\langle|\Delta x|\rangle$ And $\sqrt{\langle\Delta x^2\rangle}$

The explained above ϕ meson invariant yield systematic error estimation evaluates at every step the mean absolute value of a deviation of one of two possible methods from their average (assuming that such deviations are solely due to a systematic uncertainty). However, traditionally it is the variance of a random variable that is used as a measure of the variable uncertainty. Making an assumption that the systematic error on ϕ meson invariant yield is distributed according to a normal distribution, the final error estimate was increased by a factor of ∼1.2534 since for a normally distributed x with the mean μ and width σ one has $\langle|(x-\mu)/\sigma|\rangle \simeq 0.7978\sqrt{\langle(x-\mu)^2/\sigma^2\rangle}$.

6.5.2. ϕ Meson Invariant Yield Fit Results Systematic Errors

To estimate the systematic errors on T and dN/dy, resulting from the fit ϕ meson invariant yield (in the $p_t > 0.39$ GeV/c region) with Eq. 7.1 on page 185, the following procedure was applied:

1. The systematic errors evaluation was done separately in every centrality range under study.

2. Let us denote as $f_{\text{fit}}(p_t)$ the fit result of the ϕ meson invariant yield with Eq. 7.1, and T_{fit} and $(dN/dy)_{\text{fit}}$ the corresponding fit parameters.

3. Also let us denote as p_{ti} ($i = 1-10$, see Fig. 7.1 on page 186) the transverse momentum values at which the ϕ meson invariant yield measurement was done and as $\epsilon_i^{abs.syst.}$ the absolute systematic error of the measurement at transverse momentum p_{ti}:

$$\epsilon_i^{abs.syst.} = \epsilon_i^{rel.syst.} \cdot \underbrace{\frac{1}{2\pi p_t} \frac{d^2N}{dp_t dy}\Big|_{p_t=p_{ti}}}_{\text{measured invariant yield}},$$

   where $\epsilon_i^{rel.syst.}$ is the relative measurement systematic error at transverse momentum p_{ti} estimated as explained in section 6.5.1 on page 160.

4. Such distribution $\mathscr{D}$ of T and dN/dy was found that the distribution of the Eq. 7.1 function values at each p_{ti} was a Gaussian with the mean $f_{\text{fit}}(p_{ti})$ and the width of $\epsilon_i^{abs.syst.}$. The widths of Gaussian fits to the corresponding 1-dimensional projections of $\mathscr{D}$ were assigned as the T and dN/dy systematic errors. In parallel, for each T value in $\mathscr{D}$ the corresponding $\langle p_t^{\phi} \rangle$ was calculated using Eq. 7.2 on page 187 and the $\langle p_t^{\phi} \rangle$ systematic error was estimated as the Gaussian fit width to the distribution of the calculated $\langle p_t^{\phi} \rangle$ values.

The implementation of the procedure consisted of 3 steps described below.

6.5.2.1. Step One

The first step served to generated a seed of the distribution $\mathscr{D}$ as follows:

1. Let us denote as $\mathscr{B}$ the band around $f_{\text{fit}}(p_t)$ with a width at transverse momentum p_t equal to $\epsilon^{rel.syst.}(p_t) \cdot f_{\text{fit}}(p_t)$, where $\epsilon^{rel.syst.}(p_t)$ is the relative ϕ meson invariant yield measurement systematic error at p_t estimated as explained in section 6.5.1 on page 160.

2. 10^5 random values of T and dN/dy were generated from uniform distributions in ranges $[0.5 \cdot T_{\text{fit}}, 2 \cdot T_{\text{fit}}]$ and $[0.5 \cdot (dN/dy)_{\text{fit}}, 2 \cdot (dN/dy)_{\text{fit}}]$ respectively.

3. Each such generated pair of values T and dN/dy was plugged into Eq. 7.1, resulting in a function $f(p_t)$. It was tested if the function assumed values within the band $\mathscr{B}$ for all values p_{ti} and only such T and dN/dy were kept, for which $f(p_t)$ passed the test. Fig. 6.24(a) shows an example of two functions $f(p_t)$ within the band $\mathscr{B}$ (green lines) and of two such function outside of the band (black lines). The function $f_{\text{fit}}(p_t)$ and the band $\mathscr{B}$ are shown on the figure with a red line and a pink band around it correspondingly. For each value of T using Eq. 7.2 on page 187 the corresponding value of $\langle p_t^{\phi} \rangle$ was calculated. Fig. 6.24(b) shows the distribution of T and dN/dy parameters, corresponding to functions $f(p_t)$

within the band $\mathscr{B}$, and Fig. 6.24(c) and 6.24(d) show the one dimensional distributions of such parameters. Fig. 6.24(e) shows the one dimensional distribution of the computed $\langle p_t^{\phi} \rangle$ values.

6.5.2.2. Step Two

At this step a set of histograms $\mathscr{H}_i$ was filled with the values of functions $f(p_{ti})$ corresponding to each pair of parameters T and dN/dy saved at the step one (see section 6.5.2.1 on the preceding page. After that the following was done:

1. 10^5 more random values of T and dN/dy were generated again from uniform distributions in ranges $[0.5 \cdot T_{\text{fit}},\ 2 \cdot T_{\text{fit}}]$ and $[0.5 \cdot (dN/dy)_{\text{fit}},\ 2 \cdot (dN/dy)_{\text{fit}}]$ respectively.

2. It was tested if addition of each such generated pair of parameters T and dN/dy to the already saved set of them (and refilling of the histograms $\mathscr{H}_i$ using the new set) resulted in a decreased the value of

$$\prod_{i=1}^{10} \chi_{ri}^2,$$

where χ_{ri}^2 is the reduced chi-squared of the fit of $\mathscr{H}_i$ with a Gaussian with the mean and the width fixed to $f_{\text{fit}}(p_{ti})$ and $\epsilon_i^{abs.syst.}$ correspondingly, and the integral normalization constant being the fit parameter. Only such T and dN/dy were added to the previously found set of the parameters which passed the test.

An example of the histograms $\mathscr{H}_i$ filled using the resulting set of parameters T and dN/dy is shown on Fig. 6.25 on page 180.

6.5.2.3. Step Three

As can be seen from Fig. 6.25 on page 180, the 2$^{\text{nd}}$ step of the T and dN/dy systematic errors estimation resulted in a significant excess of entries in the histograms $\mathscr{H}_i$ above their fits at the highest end of the distributions. At the 3$^{\text{rd}}$ step, the histograms $\mathscr{H}_i$ were refilled utilizing the set of T and dN/dy parameters resulted from the 2$^{\text{nd}}$ step (see section 6.5.2.2), but if using some pair of the parameters lead to an excess of a bin entry of any of the histograms above its fit (made in the end of the 2$^{\text{nd}}$ step, no refitting was done in during the 3$^{\text{rd}}$ step) in the bin, such a pair was removed from the set. An example of the refilled histograms $\mathscr{H}_i$ is shown on Fig. 6.26 on page 181. The widths of Gaussian fits of 1-dimensional distributions of T, dN/dy, and $\langle p_t^{\phi} \rangle$ (see Fig. 6.27 on page 182) in the final set were assigned as the systematic errors of the measurements of the corresponding parameters.

6.6. Closure Test

One of the tests which was done to make sure the data analysis described above is able to correctly reconstruct ϕ meson invariant yield was to apply the measurement tech-

% centrality	Polarity	Output/Input	Fit Probability
0-60	positive	0.98 ± 0.02	0.01
0-60	negative	0.99 ± 0.03	0.37
0-10	positive	1.05 ± 0.06	0.18
0-10	negative	0.98 ± 0.05	0.39
10-20	positive	1.01 ± 0.05	0.33
10-20	negative	0.96 ± 0.05	0.68
20-30	positive	0.95 ± 0.05	0.31
20-30	negative	1.04 ± 0.05	0.12
30-40	positive	0.92 ± 0.05	0.70
30-40	negative	1.04 ± 0.05	0.49
40-50	positive	0.94 ± 0.06	0.45
40-50	negative	0.94 ± 0.06	0.11
50-60	positive	0.73 ± 0.07	0.17
50-60	negative	0.91 ± 0.07	0.40

Table 6.2.: The ratio of a reconstructed (*output*) ϕ meson invariant yield in single embedded ϕ meson events with realistic distributions (see section 5.2 on page 94) to the simulated ϕ meson invariant yield (*input*) in the events is shown for different centrality ranges and different PHOBOS magnet polarities. The uncertainties on the ratio are statistical only. The ratio and the uncertainties listed in the table were found from a fit (the corresponding fit probabilities are listed as well) with a constant function of such ratio estimated for different values of ϕ meson transverse momentum. The numbers shown here correspond to the efficiency and occupancy correction evaluated by doing single ϕ meson embedding with uniform distributions in transverse momentum, rapidity, and φ-angle. Fig. 6.28(a), 6.28(b), 6.28(c), and 6.28(d) on page 183 are examples (for the 0-60% centrality range) of the figures corresponding to the numbers shown is this table. See section 6.6 for details.

nique on MC events with a known ϕ meson signal in them. Fig. 6.28 on page 183 shows an example of such test in which single embedded ϕ meson events with realistic distributions (see section 5.2 on page 94) are treated as data. Only statistical uncertainties are shown on the figure. As can be seen, the reconstructed ϕ meson invariant yield is on average within about one statistical error bar from the simulated one. The summary of the tests is shown in Table 6.2. Simulation of single embedded ϕ meson events with realistic distributions requires significant computing resources, therefore only a limited number of them was created, and so the efficiency and occupancy correction was performed using such events for the 0-60% centrality range only (Fig. 6.28(e), 6.28(f), 6.28(g), and 6.28(h)) [10]. It appears from the tests that what kind of transverse momentum distri-

[10] In this case the "data" and the MC used for the corrections are the same, consequently they are not independent and so there is a correlation between the points on Fig. 6.28(f) and 6.28(f).

% centrality	Output/Input	Fit Probability
0-60	0.96 ± 0.04	0.04
0-10	1.05 ± 0.09	0.34
10-20	1.26 ± 0.09	0.05
20-30	1.04 ± 0.10	0.50
30-40	0.99 ± 0.09	0.38
40-50	1.02 ± 0.12	0.99
50-60	0.82 ± 0.13	0.22
40-60	0.93 ± 0.09	0.73

Table 6.3.: Summary of the event mixing test performed on toy MC events with a known raw number of ϕ mesons in them. An example of the Output/Input ratio (for the 0-60% centrality range) as a function of ϕ mesons transverse momentum and the corresponding fit probability are shown on Fig. 6.29(c) on page 184. See section 6.6 for details.

bution of embedded ϕ mesons is used for efficiency and occupancy correction (a uniform distribution is compared to the one described in section 5.2.3 on page 95) does not effect systematically the reconstructed ϕ meson invariant yield, however, an estimate of the corresponding systematic error was still included into the data analysis just in case (see section 6.5.1.4 on page 164). In addition, the Kolmogorov test showed that the shapes of the reconstructed and the simulated yields are consistent at all centralities.

An other test was performed to check just the event mixing (see section 6.1 on page 140) part of the data analysis. In the test the event mixing algorithm was applied on toy MC events (see section 6.2.2 on page 147), into which a known *input* raw number (the same as the one observed in Cu+Cu $\sqrt{s_{\rm NN}} = 200$ GeV data) of ϕ mesons was added. The reconstructed (*output*) raw number of ϕ mesons was compared to the input for all the centrality ranges, for which the ϕ meson invariant yield measurement was done in the data. An example of a result of such a test is shown on Fig. 6.29 on page 184. The average output to input ratios of the raw number of ϕ mesons as well as the fit (with a constant function) probability of the ratio as a function of ϕ meson transverse momentum are summarized in Table 6.3.

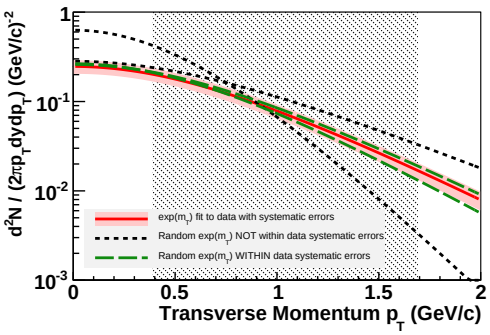

(a) Examples of Eq. 7.1 on page 185 functions within and outside the ϕ meson invariant yield systematic error band

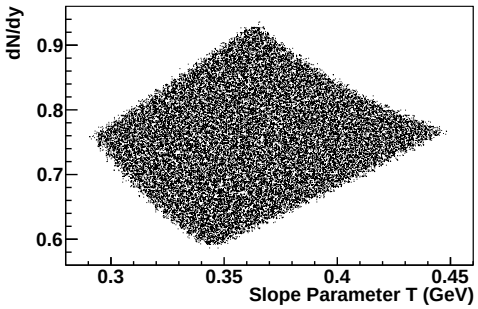

(b) Values of T and dN/dy corresponding to Eq. 7.1 functions being within ϕ meson invariant yield systematic error band

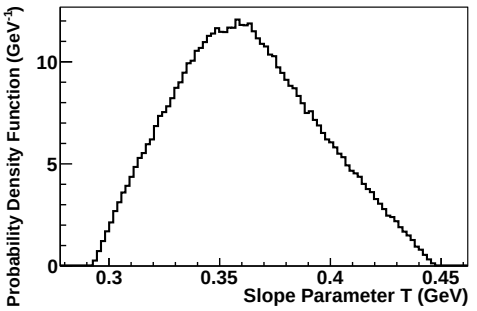

(c) Values of T corresponding to Eq. 7.1 functions being within ϕ meson invariant yield systematic error band

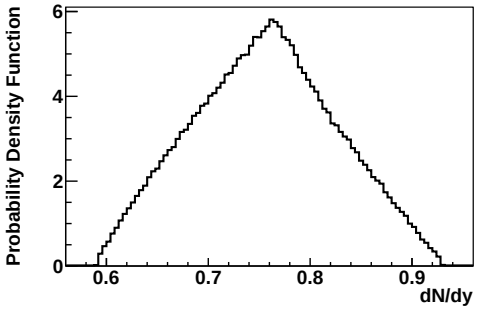

(d) Values of dN/dy corresponding to Eq. 7.1 functions being within ϕ meson invariant yield systematic error band

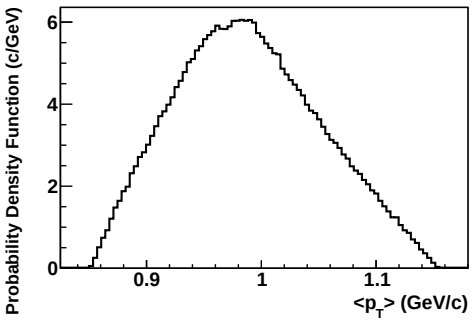

(e) Values of $\langle p_t^{\phi} \rangle$ corresponding to Eq. 7.1 functions being within ϕ meson invariant yield systematic error band

Figure 6.24.: Step one of the T, dN/dy, and $\langle p_t^{\phi} \rangle$ systematic errors estimation in 0-60% Cu+Cu 200 GeV data. See section 6.5.2.1 on page 175 for details.

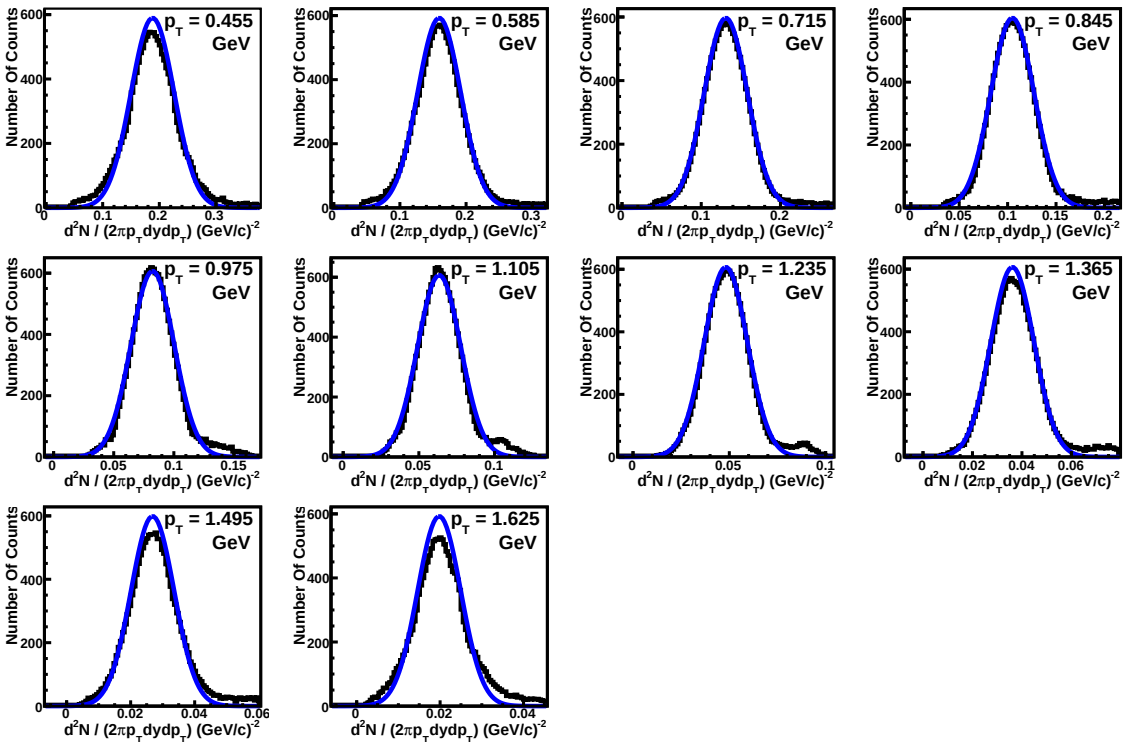

Figure 6.25.: Step two of the T, dN/dy, and $\langle p_t^{\phi} \rangle$ systematic errors estimation in 0-60% Cu+Cu 200 GeV data. The histograms $\mathscr{H}_i$ (filled using the final set of parameters T and dN/dy) are shown in black while the Gaussian fits of the histograms, performed as explained in section 6.5.2.2 on page 176, are shown in blue. Note the excess of entries in the histograms above their fits at the highest end of the distributions.

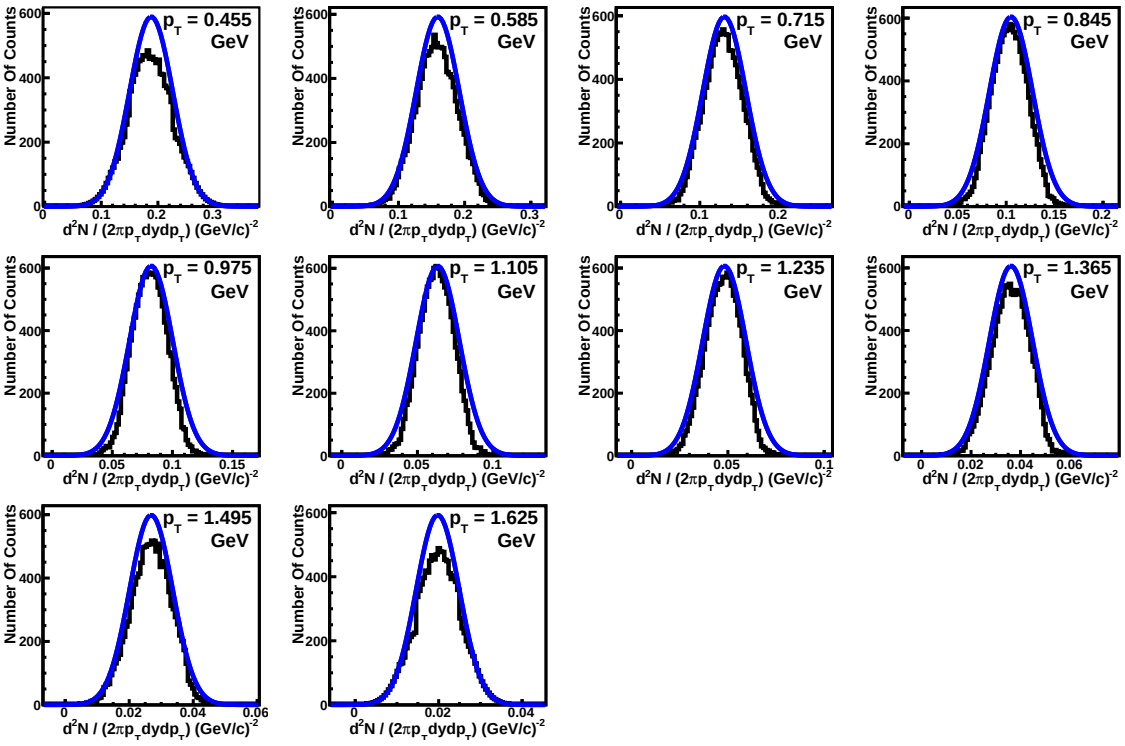

Figure 6.26.: $\mathscr{H}_i$ histograms after the step three of the T, dN/dy , and $\langle p_t^{\phi} \rangle$ systematic errors estimation in 0-60% Cu+Cu 200 GeV data. See section 6.5.2.3 on page 176 for details.

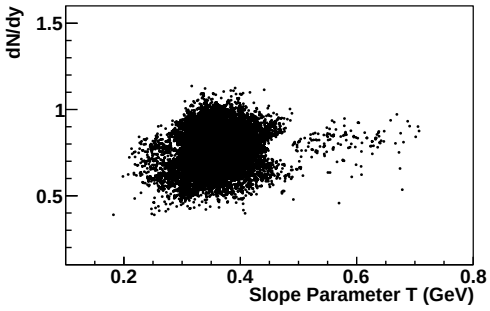

(a) dN/dy versus T distribution in the final set of the fit parameters

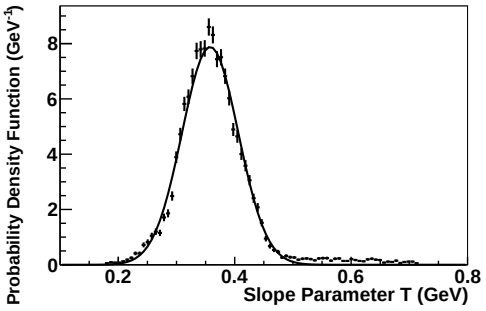

(b) T distribution (and its Gaussian fit) in the final set of the ϕ meson invariant yield fit parameters

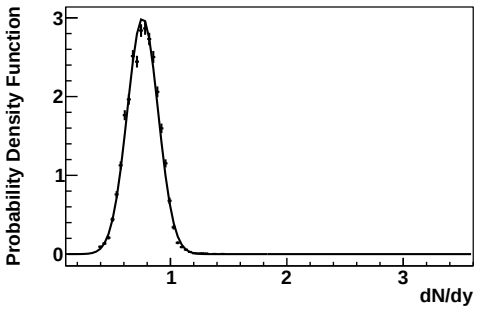

(c) dN/dy distribution (and its Gaussian fit) in the final set of the ϕ meson invariant yield fit parameters

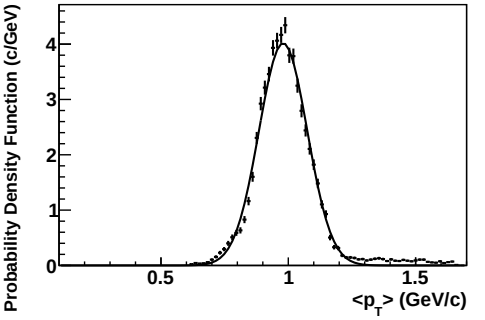

(d) $\langle p_t^{\phi} \rangle$ distribution (and its Gaussian fit) corresponding to the final set of the ϕ meson invariant yield fit parameters

Figure 6.27.: Step three of the T, dN/dy , and $\langle p_t^{\phi} \rangle$ systematic errors estimation in 0-60% Cu+Cu 200 GeV data. The final set of the ϕ meson invariant yield fit parameters mentioned in the sub-figures captions is the one which resulted from the 3rd step of the errors estimation. See section 6.5.2.3 on page 176 for details.

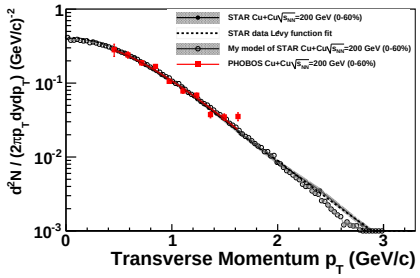

(a) 0-60%, positive magnet polarity, correction is based on uniform distributions

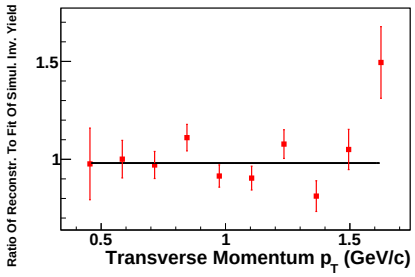

(b) 0-60%, positive magnet polarity, correction is based on uniform distributions

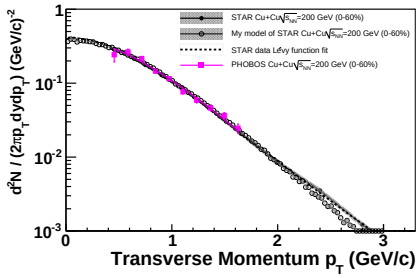

(c) 0-60%, negative magnet polarity, correction is based on uniform distributions

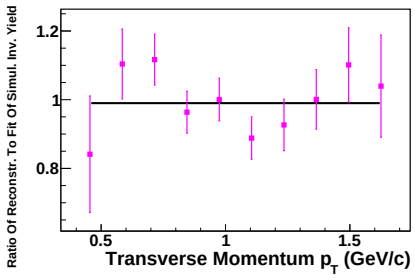

(d) 0-60%, negative magnet polarity, correction is based on uniform distributions

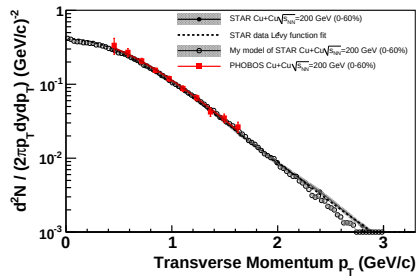

(e) 0-60%, positive magnet polarity, correction is based on STAR distributions

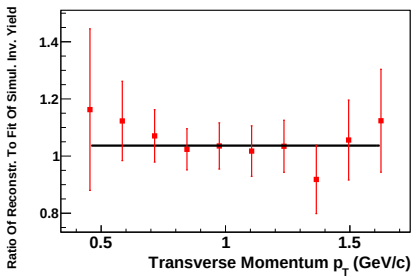

(f) 0-60%, positive magnet polarity, correction is based on STAR distributions

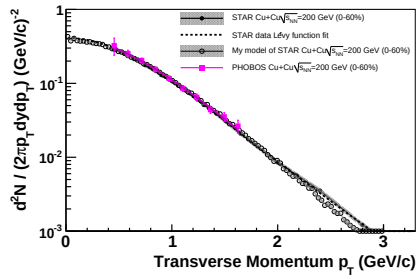

(g) 0-60%, negative magnet polarity, correction is based on STAR distributions

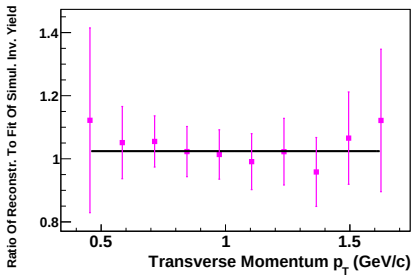

(h) 0-60%, negative magnet polarity, correction is based on STAR distributions

Figure 6.28.: An example of reconstruction of ϕ meson invariant yield in single embedded MC ϕ meson events (for which the yield is known). The red and the magenta markers show the reconstructed yield for the positive and the negative magnet polarities correspondingly. The top gray line with a few points are the published STAR results. The many gray markers line just below it is my model of the STAR results, which was used for the embedding.

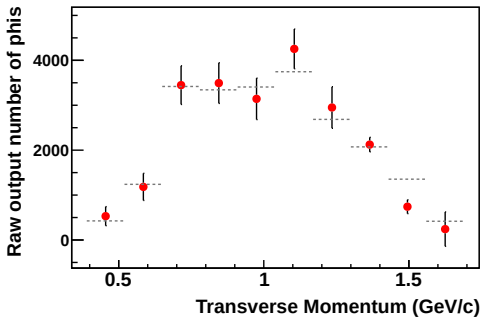

(a) The input (shown as dashed lines) and the output (shown as red markers) raw number of ϕ mesons

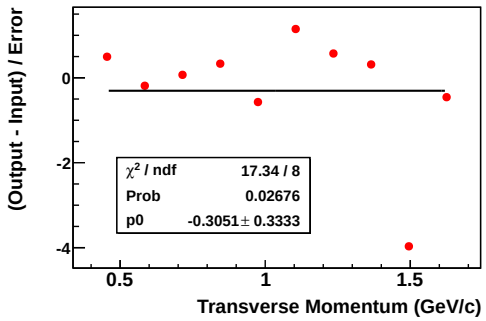

(b) The difference between the output and the input expressed in the output statistical error bars (the black line shows a fit by a constant function)

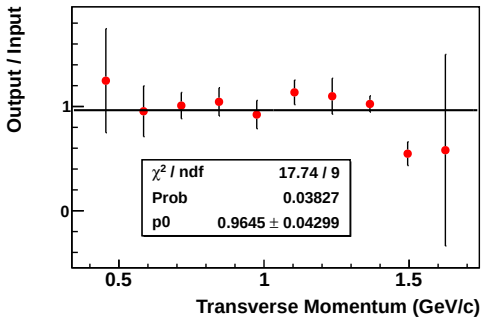

(c) The ratio of the output to the input number of ϕ mesons (the black line shows a fit by a constant function)

Figure 6.29.: An example of the event mixing test performed on toy MC events with a known raw number of ϕ mesons in them, equal to the number reconstructed in 0-60% of centrality of $\sqrt{s_{\mathrm{NN}}} = 200$ GeV data. The reconstructed number of ϕ mesons is called the *output* and the known (i.e. MC) number of ϕ mesons in the events is called the *input*. See section 6.6 on page 176 for details.

7. Results And Discussion

7.1. PHOBOS Results On ϕ Mesons Invariant Yield

The experimental results on the ϕ meson invariant yield in Cu+Cu collisions at $\sqrt{s_{\mathrm{NN}}}$ = 200 GeV arising from the data analysis procedure described in chapter 6 are shown on Fig. 7.1 on the next page. The corresponding data tables and zoomed in versions of the figures are provided in appendix A on page 233. Although numerous and extensive checks of the measurements presented in this thesis were performed by the author, the results did not go through a PHOBOS collaboration review and a publication process and therefore have to be considered preliminary.

The error bars and the boxes around the data points corresponding to the PHOBOS results on Fig. 7.1 show the size of the statistical and of the systematic uncertainties of the measurements respectively. The error bars corresponding to the STAR and the PHENIX results on the figure correspond to the statistical and the systematic errors of the respective measurements added in quadrature. The solid, dotted, and dashed lines on the figure correspond to the fits of the PHOBOS, STAR, and PHENIX results respectively. The fits are described in section 7.2.

7.2. Fitting PHOBOS Results On ϕ Meson Invariant Yield

The PHOBOS results on the ϕ meson invariant yield as a function of transverse momentum (see Fig. 7.1 on the following page) were fit using the following equation:

$$\frac{1}{2\pi p_t}\frac{d^2N}{dp_t dy} = \frac{dN/dy}{2\pi T(T+m_\phi)}\exp\left(-\frac{\sqrt{p_t^2+m_\phi^2}-m_\phi}{T}\right), \tag{7.1}$$

which follows from normalizing the Eq. 1.2 on page 23 distribution to unity and addition of an overall dN/dy scaling factor. The fit parameters were T and dN/dy while m_ϕ was fixed at 1.019456 GeV/c^2 [236]. As can be readily checked, the dN/dy parameter corresponds to the total average yield of ϕ mesons per collision, assuming that ϕ meson invariant yield dependence on transverse momentum is accurately described by Eq. 7.1 for all p_t values. During the fitting, only statistical errors of the ϕ meson invariant yield measurements were used. The quality of the fits is summarized in Table 7.1. The T and dN/dy uncertainties resulting from the fits were assigned as the statistical errors of the parameters. The average ϕ meson transverse momentum values $\langle p_t^\phi \rangle$ were calculated

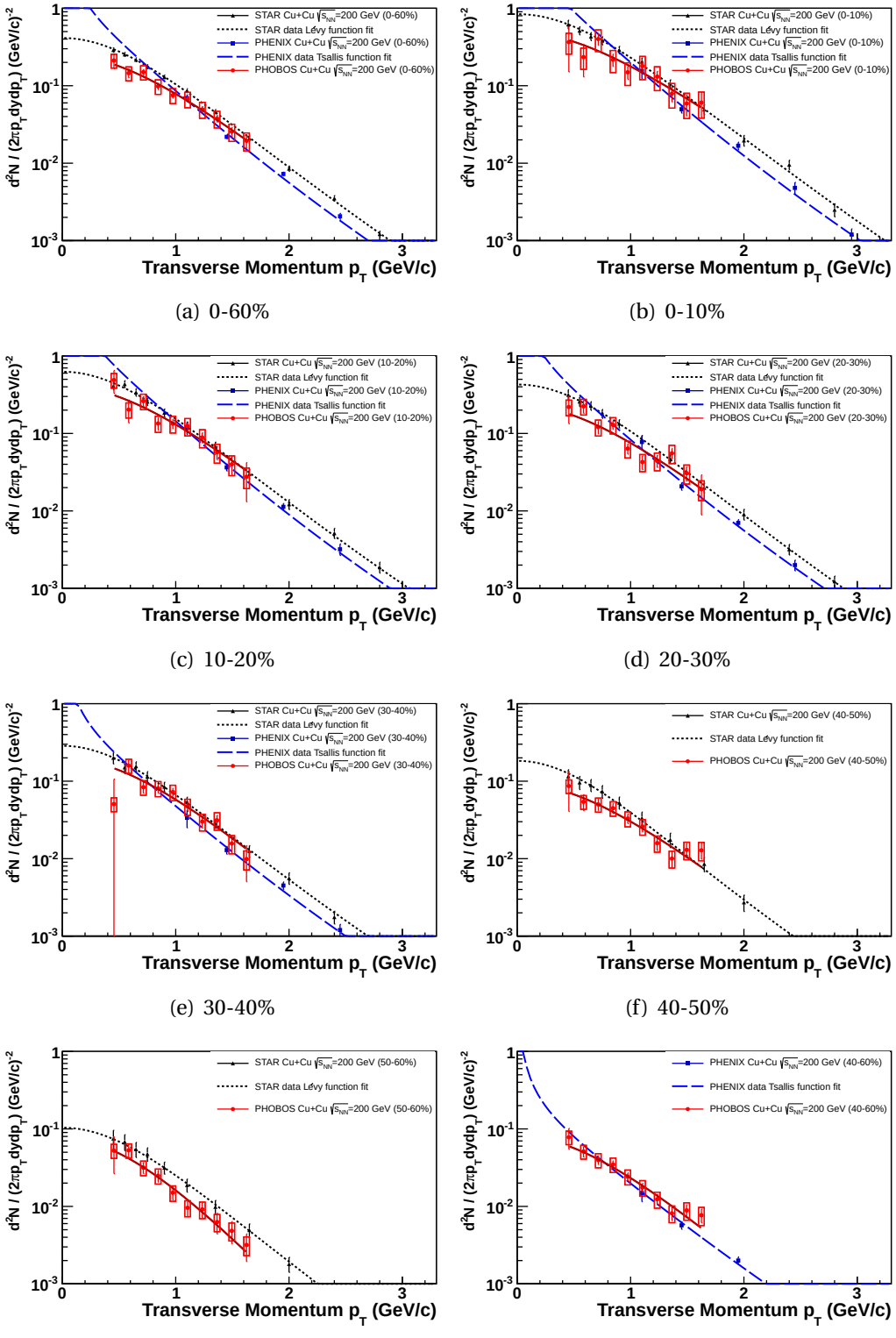

(a) 0-60% (b) 0-10%

(c) 10-20% (d) 20-30%

(e) 30-40% (f) 40-50%

(g) 50-60% (h) 40-60%

Figure 7.1.: ϕ meson invariant yield measurements in Cu+Cu collisions at $\sqrt{s_{\mathrm{NN}}}$=200 GeV in ranges of centrality. The results of the STAR [233] and the PHENIX [253] collaborations are shown in black and blue respectively. The PHOBOS collaboration results are preliminary. See section 7.1 on the previous page for details.

% centrality	χ^2 / ndf	Fit Probability
0-60	5.76 / 8	0.67
0-10	8.55 / 8	0.38
10-20	8.47 / 8	0.39
20-30	19.7 / 8	0.01
30-40	10.7 / 8	0.22
40-50	8.31 / 8	0.40
50-60	4.12 / 8	0.85
40-60	6.82 / 8	0.56

Table 7.1.: χ^2 values and the corresponding probabilities (see section 5.10.6 on page 132) of the fits of the PHOBOS results on ϕ meson invariant yield in Cu+Cu collisions at $\sqrt{s_{\mathrm{NN}}} = 200$ GeV. See section 7.2 on page 185 for details.

using Eq. 5.2 on page 97 as

$$\langle p_t^{\phi} \rangle = \int_0^{+\infty} p_t \frac{dN}{dp_t} dp_t. \tag{7.2}$$

The systematic errors of dN/dy, T, and $\langle p_t^{\phi} \rangle$ were estimated as described in section 6.5.2 on page 174. The parameter values arising from this procedure are summarized in Table 7.2 on the next page.

It is worth noting here that Eq. 1.2 and Eq. 1.3 were derived for an infinite medium in a thermodynamic equilibrium, therefore caution has to be used, while interpreting results of experimental heavy ion collisions data fits using the distributions, since the "fireball" created in such collisions has the size of only several fermis and is not in a state of full equilibrium. The pressure created in the collision region could drive the matter to collectively expand in the transverse direction (the effect called the *transverse flow* [258, 259]), and therefore the measured transverse energy could be the sum of both the thermal energy and the energy associated with the collective expansion [1,2]:

$$\langle E_T \rangle = \langle E_T^{\mathrm{thermal}} \rangle + \frac{1}{2} m v_{\mathrm{collective}}^2 \quad \Longleftrightarrow \quad T = T_{\mathrm{fo}} + \frac{1}{2} m v_{\mathrm{collective}}^2, \tag{7.3}$$

where $\langle E_T^{\mathrm{thermal}} \rangle$ is the average transverse thermal energy, $v_{\mathrm{collective}}$ is the average transverse flow velocity, and T_{fo} is the *kinetic freeze-out temperature* (the temperature at which particles in the hot hadronic gas stop colliding with each other due to a low density of the gas and start streaming freely from the collision region). The above equation for the *effective temperature* T has two unknown values T_{fo} and $v_{\mathrm{collective}}$, therefore to separate the thermal energy and the energy associated with the collective expansion, one has to perform a simultaneous fit of invariant yields of at least two different particle

[1] Since the transverse direction has 2 degrees of freedom, $\langle E_T \rangle = T$.

[2] To take into account relativistic effects, one would have to replace in Eq. 7.3 $\frac{1}{2} m v_{\mathrm{collective}}^2$ with $m c^2 (\gamma_{\mathrm{collective}} - 1)$, where $\gamma_{\mathrm{collective}} = (1 - v_{\mathrm{collective}}^2 / c^2)^{-\frac{1}{2}}$.

% centrality	dN/dy	T (GeV)	$\langle p_t^{\phi} \rangle$ (GeV/c)
0-60	$0.760 \pm 0.025 \pm 0.131$	$0.356 \pm 0.021 \pm 0.048$	$0.977 \pm 0.041 \pm 0.095$
0-10	$1.757 \pm 0.124 \pm 0.473$	$0.399 \pm 0.057 \pm 0.109$	$1.061 \pm 0.111 \pm 0.207$
10-20	$1.264 \pm 0.074 \pm 0.242$	$0.357 \pm 0.039 \pm 0.056$	$0.979 \pm 0.077 \pm 0.109$
20-30	$0.731 \pm 0.044 \pm 0.139$	$0.361 \pm 0.050 \pm 0.057$	$0.986 \pm 0.098 \pm 0.112$
30-40	$0.558 \pm 0.031 \pm 0.098$	$0.334 \pm 0.031 \pm 0.044$	$0.934 \pm 0.061 \pm 0.086$
40-50	$0.293 \pm 0.018 \pm 0.051$	$0.363 \pm 0.042 \pm 0.050$	$0.989 \pm 0.083 \pm 0.098$
50-60	$0.161 \pm 0.013 \pm 0.029$	$0.266 \pm 0.030 \pm 0.028$	$0.798 \pm 0.062 \pm 0.056$
40-60	$0.224 \pm 0.011 \pm 0.038$	$0.329 \pm 0.028 \pm 0.041$	$0.924 \pm 0.055 \pm 0.081$

Table 7.2.: The table summarizes parameters of the fits (and the corresponding $\langle p_t^{\phi} \rangle$ values) of the PHOBOS results on ϕ meson invariant yield in Cu+Cu collisions at $\sqrt{s_{\mathrm{NN}}} = 200$ GeV. The 1st number in each table cell is the parameter value, while the 2nd and the 3rd numbers are the corresponding statistical and systematic uncertainties respectively. See section 7.2 on page 185 for details.

species, similar to the analysis done in Ref. [260]. The idea of transverse flow is supported by the fact that the T_{fo} values extracted from the data are approximately constant (~ 140 MeV) while $v_{\mathrm{collective}}$ grow with the size of collided nuclei, just as the pressure induced by a collision is expected to do. Values T extracted by fitting measured transverse momentum distributions of particles using Eq. 1.2 and Eq. 1.3 differ by ~ 10 MeV [79], and the difference should be considered as the lower bound on the systematic error of T due to a theoretical uncertainty of what to call a temperature of the medium produced in relativistic heavy ion collisions.

7.3. Transition Between Confined And Deconfined States

As it was pointed out by L. Van Hove in 1982 [263], to experimentally identify a transition from a confined to a deconfined state of quarks and gluons, one could study the dependence of the parameter T (or, equivalently, of the average transverse momentum $\langle p_t \rangle$) of detected hadrons (produced in high energy hadron or nuclear collisions) as a function of the energy density or the entropy density. Transverse momentum of particles created in a heavy ion collision has contributions from both thermal emission and collective expansion in the plane perpendicular to the collision axis (see section 7.2 on page 185). According to the argument of Van Hove, the combined effect of thermal emission and collective expansion would lead to an observation of a plateau in $\langle p_t \rangle$ (and consequently, in the parameter T) dependence on entropy density [3]. The argument is reviewed below, taking into account the modern understanding of both phenomena.

The collective expansion is caused by the pressure in the quark matter formed in a

[3] Since entropy density is a monotonically increasing function of energy density, the plateau would also be observed in the $\langle p_t \rangle$ as a function of energy density dependence.

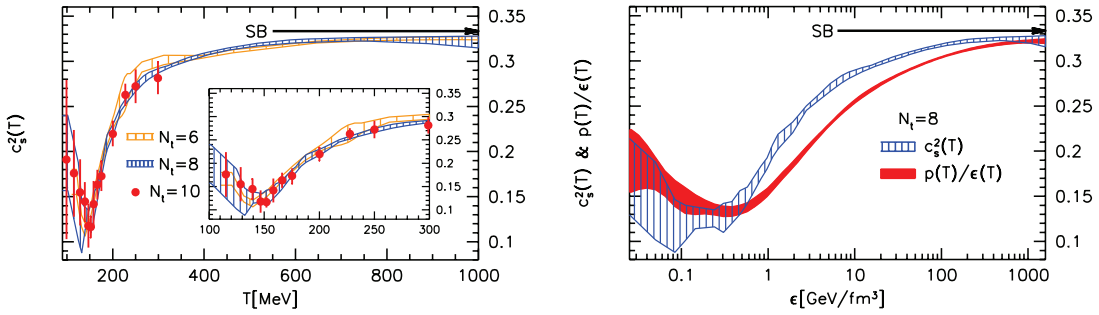

(a) c_s^2 versus temperature

(b) c_s^2 versus energy density

Figure 7.2.: Speed of sound (squared) c_s^2 in quark matter as a function of (a) temperature and (b) energy density calculated using lattice QCD with 2+1 flavors [261]. Lattice QCD calculations with 2 quark flavors result in very similar dependencies [262]. Since $c_s^2 = dp/d\varepsilon$ (where p and ε are pressure and energy density of quark matter in an equilibrium respectively), the figures above essentially plot the slope of function $p(\varepsilon)$. Therefore, pressure increase rate (as a function of energy density) has a minimum near *the lowest end* (as a function of temperature and energy density) of the transition region between confined and deconfined states of quarks and gluons (see Fig. 1.4 on page 33 and section 1.2.8 on page 30). Since See section 7.3 on the preceding page for details.

heavy ion collision. Lattice QCD calculations demonstrate (see Fig. 7.2) a *softening* of the equation of state (in the form $p(\varepsilon)$, where p and ε are pressure and energy density correspondingly) near the transition between confined and deconfined states of the matter, which means that the pressure increases in the transition region (temperature ~140-175 MeV) at a much lower rate (a factor of ~2.6) as a function of both temperature and energy density than (far) outside of the region, with the minimum rate being at temperature ~150 MeV. Therefore, one can conclude that the shape of the energy density dependence of the contribution of collective expansion into $dT/d\varepsilon$ is expected to be similar to the one shown on Fig. 7.2.

Let us now discuss the contribution of thermal emission of hadrons into the parameter T of their transverse momentum spectra. Again, lattice QCD calculations provide a prediction of the dependence of temperature T of quark matter on its energy density, from which one could estimate $d\mathsf{T}/d\varepsilon$ as a function of T and ε (see Fig. 7.3 on the following page). As can be seen, $d\mathsf{T}/d\varepsilon$ also has a strong decrease in the region of the transition between confined and deconfined states of QCD matter. The difference between $dp/d\varepsilon$ and $d\mathsf{T}/d\varepsilon$ is that while the former has a global minimum near the transition region, the minimum of the later is only local.

Combining predictions for the two contributions into $dT/d\varepsilon$, one can see that $dT/d\varepsilon$ *should have at least a local minimum near the deconfinement transition as a function*

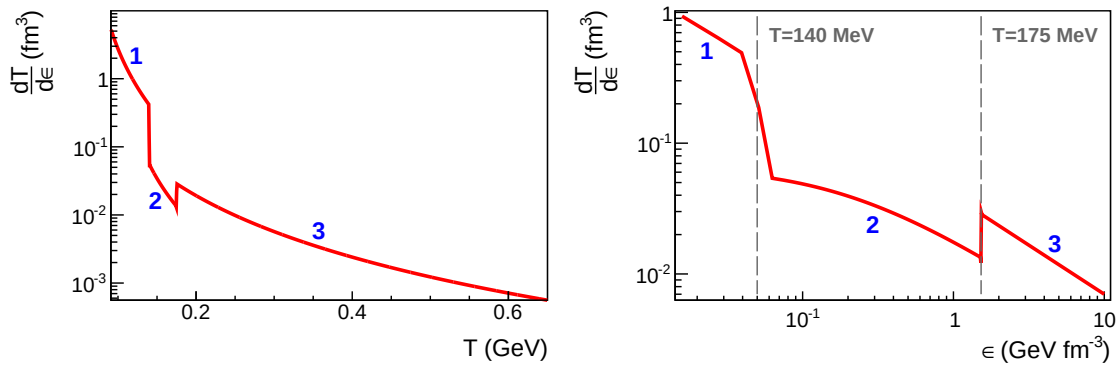

(a) $dT/d\varepsilon$ versus temperature

(b) $dT/d\varepsilon$ versus energy density

Figure 7.3.: Estimated dependencies of $dT/d\varepsilon$ on (a) T and (b) ε derived from lattice QCD results, where T and ε are temperature and energy density of QCD matter in thermodynamic equilibrium correspondingly. The dependencies were derived by approximating the ε/T^4 ratio as a function of T (see Fig. 1.4 on page 33) with a linear spline having the following nodes (the first number is T in MeV, the second number is ε/T^4 in units of $\frac{15}{\pi^2}\cdot\sigma$, where $\sigma = 85.6\ \text{fm}^{-3}\,\text{GeV}^{-3}$ is the Stefan-Boltzmann constant): $(0,0)$, $(90,0)$, $(140,1)$, $(175,12.5)$, and $(\infty,12.5)$. Three distinct ranges of the dependencies are marked on the figures. As can be seen, the rate of the temperature increase drops by about an order of magnitude as one crosses the boundary of ranges #1 and #2. The boundary corresponds to *the lowest end* (as a function of temperature or energy density) of the transition region between confined and deconfined states of quarks and gluons, while the boundary between ranges #2 and #3 corresponds to the *the highest end* of the transition region. Since the derivative $dT/d\varepsilon$ increases by about a factor of 2 on the boundary between ranges #2 and #3, then the range #2 corresponds to the lowest local rate of temperature increase. Note that in reality, the changes in $dT/d\varepsilon$ on the boundaries between the numbered ranges are smoother than what is shown on the figures (the sudden changes are an artifact of approximating the ε/T^4 ratio as a function of T with a linear spline, which intrinsically has a noncontinuous first derivative). It is interesting to notice that, the average energy densities of pions ($m_{\pi^\pm} \simeq 139.6$ MeV [169], $R_{\pi^\pm} \simeq 0.672$ fm [169], $\varepsilon_{\pi^\pm} \simeq 110\ \text{MeV/fm}^{-3}$) and protons ($m_p \simeq 938.3$ MeV [169], $R_p \simeq 0.877$ fm [169], $\varepsilon_p \simeq 332\ \text{MeV/fm}^{-3}$) correspond to the transition region between confined and deconfined states of quarks and gluons (however, it does necessarily mean that the interior of the particles has both quarks/gluons and hadron quantum fluctuations, since lattice QCD describes $\mu_B = 0$ matter, while the particles have a clearly non-vanishing net baryon charge). See section 7.3 on page 188 for details.

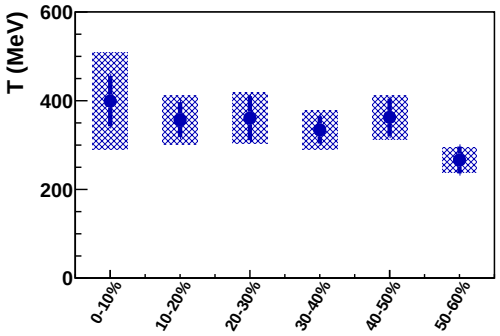

(a) slope parameter T versus centrality (the vertical sizes of the shaded areas show the estimates on the systematic errors of T, the horizontal size of the areas is arbitrary)

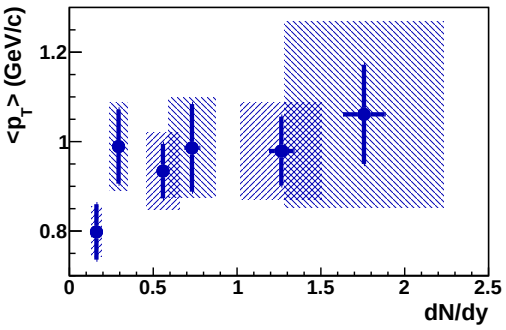

(b) $\langle p_t^{\phi} \rangle$ versus dN/dy (the horizontal and vertical sizes of the shaded areas show the estimates on the systematic errors of dN/dy and $\langle p_t^{\phi} \rangle$ correspondingly)

Figure 7.4.: The search for a transition with a latent heat or with a change in the number of degrees of freedom in the Cu+Cu collisions at $\sqrt{s_{\rm NN}}$=200 GeV as the energy density (a) or entropy density (b) are scanned to locate a plateau in the slope parameter T (or, equivalently, in the $\langle p_t^{\phi} \rangle$). See section 7.3 on page 188 for details.

of ε. An important caveat here is that the lattice QCD calculations, which were used to make the later conclusion, correspond to a vanishing baryon chemical potential, while in experimental (heavy ion collision) data, lower energy densities correspond to increasingly large values of μ_B, so a great care has to be used while comparing the theory to measurements. However, since (lattice) QCD calculations at $\mu_B \neq 0$ are not feasible at the moment, the above predictions are the closest we can get now to making exact calculations of experimental observables based on first principles. Another caveat here is that the temperature of the system created in a heavy ion collision changes over time and is not uniform in space, and so the observed hadrons are, in general, produced as emission by matter at different temperatures. In addition, after hadrons are produced in the collision, they interact with each other changing their transverse momenta and their chemical composition. The assumption, which is made here, is that a higher initial temperature of the QCD matter created in a heavy ion collision leads to a higher (or at least, not lower) average kinetic freeze-out temperature (see section 7.2 on page 185) of observed hadrons [4].

[4] If the kinetic freeze-out temperature is a constant value, which is independent of the initial temperature and energy density, then the observed slope parameter T of an hadron species depends solely on the initial pressure, and then $dT/d\varepsilon$ will have a global minimum as a function of ε near the deconfinement transition. However, let us consider the conventional cartoon picture of the evolution of a system created in a heavy ion collision: 1) primordial collisions of partons in the collided nuclei occur, 2) the partons scatter and produce new partons, 3) the partons interact with each other and reach an approximate thermal equilibrium (perhaps, QGP), 4) the system expands and cools down, 5) when the temperature reaches T_c, the QGP hadronizes, 6) hadrons interact with each other exchanging constituent quarks until

According to some theories, which are in agreement with the measurements showing that the coherent cross-section of ϕ meson interaction with non-strange hadrons is small (see section 1.4.2.2 on page 40), ϕ mesons are expected to decouple from a strongly interacting medium earlier than other particles, therefore application of the above idea to ϕ mesons can probe for the deconfinement transition at higher temperatures more directly [5]. For example, if the chemical [6] and kinetic freeze-out temperatures of ϕ mesons are higher than T_c, then by measuring the yield and the momentum distribution of ϕ mesons, one gets a direct information about the conditions at which the mesons were produced (effectively in this case, ϕ mesons could be considered as non-interacting with other hadrons). And if the freeze-out temperatures of ϕ mesons are lower than T_c, then modifications of ϕ meson spectra due to interactions at the hadronic gas stage would be smaller. In addition, ϕ mesons are not affected strongly by resonance decays due to the small number of very heavy resonances decaying into ϕ mesons [158], which is an other reason ϕ mesons provide a cleaner information about the conditions at which they are produced in heavy ion collisions.

According to the Landau's hydrodynamical model [279], dN/dy of observed hadrons is a measure of the system entropy. Also, the temperature and the baryon chemical potential of a system created in a heavy ion collision change monotonically as a function of the collision centrality (see section 1.2.8 on page 30). Consequently, the slope parameter T was studied as a function of collision centrality, as well, the average transverse momentum $\langle p_t^{\phi} \rangle$ of ϕ mesons was studied as a function of their dN/dy (see Fig. 7.4 on the preceding page). Both dependencies are consistent with being constants ($\chi^2/ndf = 3.19/5$ and $\chi^2/ndf = 3.17/5$ correspondingly [7]), which means that $dT/d\varepsilon$ as a function of energy density is consistent with having no (local) minimum and so *the deconfinement transition is not observed in the energy and the entropy density ranges corresponding to the considered centrality range of Cu+Cu $\sqrt{s_{\mathrm{NN}}}$=200 GeV collisions*. This can be explained assuming a weak dependence of energy and entropy densities on collision centrality (in the studied centrality range), which only allows to probe a narrow range of the densities for a transition.

To probe a wider range of energy and entropy densities, one could study the dependence of T and $\langle p_t^{\phi} \rangle$ of ϕ mesons as a function of $\sqrt{s_{\mathrm{NN}}}$ for a given heavy ion type at

---

the temperature of the system reaches the chemical freeze-out temperature (see footnote 6), 7) after that the hadrons only interact with exchanges of momentum until the temperature reaches the kinetic freeze-out temperature T_{fo} (see page 187), 8) after that hadrons stream freely to the experimental detectors. So one can get an impression, that the thermal emission contribution to the final slope of hadron spectra is fully determined by their freeze-out at stage 7, and that this contribution is constant. However, at all the evolution stages described above (even at the stage of QGP), hadron would be emitted from the surface at higher temperatures than T_{fo}, and not all of the hadrons would reach a full equilibrium with other hadrons, and so the average temperature of hadrons at which their momentum "freezes" will most likely grow as a function of the initial temperature of the system. Hence the assumption.

[5] Of course, this is only true if the cross-section remains small in a medium at high temperatures on the order of T_c (see section 1.2.4.1 on page 25 for a definition).

[6] At the *chemical freeze-out temperature* (by definition) particles in a hot hadronic gas stop having such (strong) interactions with each other that lead to changes of the particle species.

[7] The corresponding fit probabilities are 0.67 and 0.67.

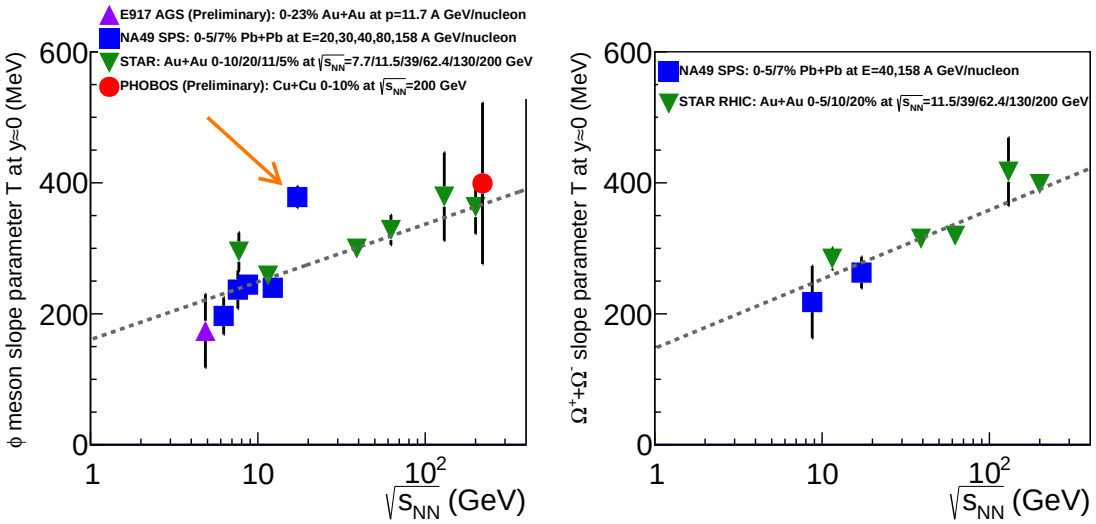

(a) ϕ meson slope parameter T versus $\sqrt{s_{\mathrm{NN}}}$ (b) $\Omega^+ + \Omega^-$ slope parameter T versus $\sqrt{s_{\mathrm{NN}}}$

Figure 7.5.: (a) Dependence of the slope parameter T of ϕ mesons on $\sqrt{s_{\mathrm{NN}}}$ in central heavy ion collisions with $A \approx 200$ (PHOBOS Cu+Cu point is added for comparison, the point is shifted for visibility to the right). The data were taken from Ref. [151, 231, 234, 264, 265]. Statistical and systematic errors were added in quadrature for all of the points except those from Ref. [151, 265]. The errors on the data points from Ref. [265] are statistical only. The data from E917 and Ref. [265] are preliminary. If the SPS data point at E=158 A GeV (marked with an arrow) is ignored, then the remaining points exhibit a smooth monotonic behavior (the dashed line on the figure is a fit with a function $T = A \cdot \ln(\sqrt{s_{\mathrm{NN}}}) + B$, χ^2/ndf=8.34/10, fit-probability=0.60), however, if the point is taken into account, the available data suggests that *either the T versus $\sqrt{s_{\mathrm{NN}}}$ dependence has a local maximum at $\sqrt{s_{\mathrm{NN}}} \sim$20 GeV or that the corresponding measurement has an unaccounted for systematic error* (with the data point included, the same fitting procedure gives fit-probability=8×10^{-7}). The situation could be clarified using the RHIC data at $\sqrt{s_{\mathrm{NN}}}$=19.6 GeV and at $\sqrt{s_{\mathrm{NN}}}$=27 GeV taken in 2011.
(b) Dependence of the slope parameter T of Ω baryons on $\sqrt{s_{\mathrm{NN}}}$ in central heavy ion collisions with $A \approx 200$. The data were taken from Ref. [264, 266–269]. For the NA49 data, statistical and systematic errors were added in quadrature for all of the points. STAR invariant yield data were fit using statistical and systematic errors added in quadrature for $\sqrt{s_{\mathrm{NN}}}$=200 GeV data and using statistical errors only for $\sqrt{s_{\mathrm{NN}}}$=62.4 GeV data. STAR data points for $\sqrt{s_{\mathrm{NN}}}$=130 GeV were taken from Table I of the corresponding publication, which presents "only statistical and $p_\perp$ dependent systematic uncertainties" (According to the publication "the $p_\perp$ independent systematic uncertainties are 10%". Since it was not completely clear to the author of this thesis what that means, $p_\perp$ independent systematic uncertainties were not included on the figures.). The errors on the data points from Ref. [269] are statistical only. The dashed line on the figure is a fit with a function $T = A \cdot \ln(\sqrt{s_{\mathrm{NN}}}) + B$, χ^2/ndf=5.74/5, fit-probability=0.33. See section 7.3 on page 188 for details.

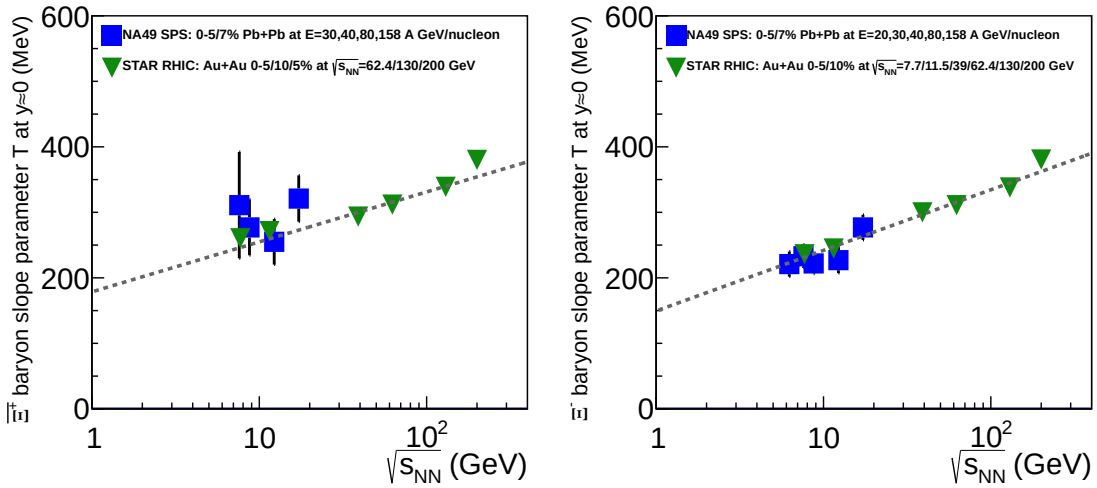

(a) $\overline{\Xi}^{+}$ slope parameter T versus $\sqrt{s_{\mathrm{NN}}}$

(b) Ξ^{-} slope parameter T versus $\sqrt{s_{\mathrm{NN}}}$

Figure 7.6.: Dependence of the slope parameter T of Ξ baryons on $\sqrt{s_{\mathrm{NN}}}$ in central heavy ion collisions with $A \approx 200$. The data were taken from Ref. [264, 266–268, 270]. The errors on the data points from Ref. [270] are statistical only. The data points for Ξ and Ω baryons were found the same way for results published in the same paper (see the caption of Fig. 7.5(b) on the previous page). The dashed line on the figures are fits with a function $T = A \cdot \ln(\sqrt{s_{\mathrm{NN}}}) + B$ (for $\overline{\Xi}^{+}$ baryons: χ^2/ndf=18.6/8, fit-probability=0.02, for Ξ^{-} baryons: χ^2/ndf=14.4/9, fit-probability=0.11). See section 7.3 on page 188 for details.

a fixed collision centrality analogously to Ref. [280, 281], where it was done for pions, kaons and protons. Unfortunately, data on ϕ meson production for collisions at atomic mass $A \approx A_{Cu} = 64$ are only available for $\sqrt{s_{\mathrm{NN}}}$=62.4 and 200 GeV, therefore the study was done for central $A \approx 200$ collisions (see Fig. 7.5(a) on the previous page). However, since T is an intensive physical quantity and QGP production is expected in central Cu+Cu collisions at $\sqrt{s_{\mathrm{NN}}}$=200 GeV (see section 1.3 on page 32), the T value of ϕ mesons measured in this thesis for the 0-10% range of centrality can be directly compared to the measurements performed in central $A \approx 200$ collisions.

In such study, it is important that the slope parameter T would be estimated using the same model out of several available ones in the topical publications (some examples are Eq. 1.2 and Eq. 1.3 on page 23, as well as exponential in $p_\perp$, $p_\perp^2$, and $p_\perp^3$ [274], Lévy function [233], Tsallis function [253], and others). The consistency in the used model choice is necessary to avoid systematic differences in the extracted T values due to inherent differences in the models. Alternatively, to make a comparison between different data sets model independent, one could study $\langle p_t \rangle$ (instead of T) of particles as a function $\sqrt{s_{\mathrm{NN}}}$. The former approach was used in this thesis and Eq. 1.2 on page 23 was the model

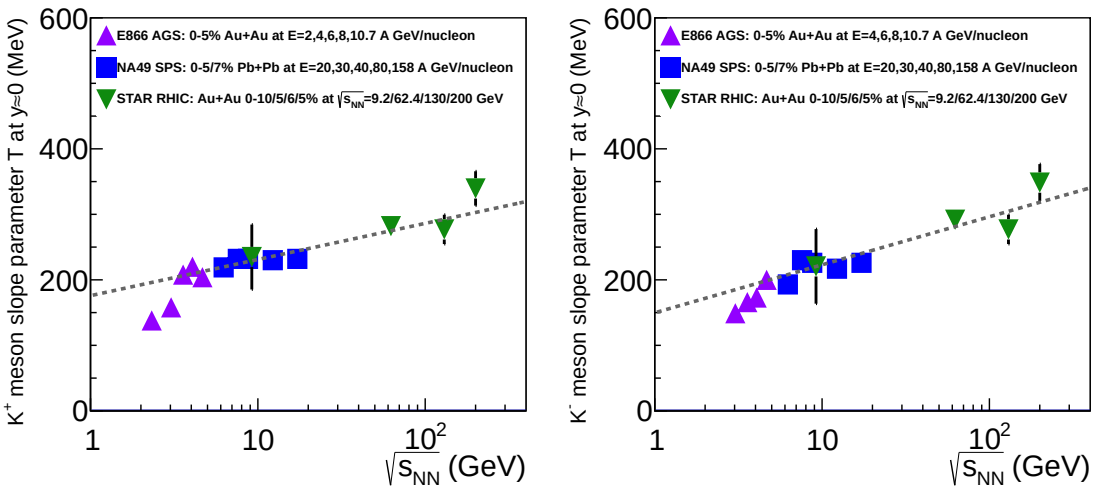

(a) K^+ slope parameter T versus $\sqrt{s_{\rm NN}}$ (b) K^- slope parameter T versus $\sqrt{s_{\rm NN}}$

Figure 7.7.: Dependence of the slope parameter T of K^+ (a) and K^- (b) mesons on $\sqrt{s_{\rm NN}}$. The data were taken from Ref. [264, 271–274]. The errors of the AGS data points are statistical only. The errors of the SPS data points at E=20 and 30 A GeV are statistical only as well. The errors of the SPS data points at E=40, 80, and 158 A GeV are statistical and systematic ones added in quadrature. The errors of the STAR $\sqrt{s_{\rm NN}}$=62.4 GeV and $\sqrt{s_{\rm NN}}$=200 GeV data points were assigned from the result of fits of the corresponding K^+ invariant yield measurements with statistical and point-to-point systematic errors added in quadrature. The error of the STAR $\sqrt{s_{\rm NN}}$=130 GeV data point was found by adding in quadrature the statistical and the systematic errors of the corresponding measurement. The dashed lines are fits (K^+: χ^2/ndf=12.0/10, fit-probability=0.28, K^-: χ^2/ndf=18.1/8, fit-probability=0.02) with a function $T = A\cdot\ln(\sqrt{s_{\rm NN}})+B$ of all of the data points except the two/three lowest AGS energies of K^+/K^- data respectively. See section 7.3 on page 188 for details.

of choice used to extract the slope parameter T from transverse momentum distributions of various particles. Particle spectra in heavy ion collisions typically show an exponential in m_T dependence at low and intermediate p_t (namely, at $p_t \lesssim 2-3$ GeV/c) due to a thermal emission from the fireball and a power law dependence at high p_t where particles are produced in hard scattering processes, therefore in a few cases the p_t range of fits was limited to the lower end of transverse momentum spectrum such that the fits would produce a reasonable fit-probability (i.e. at least 1-10%).

The resulting dependence of the slope parameter T versus $\sqrt{s_{\rm NN}}$ for ϕ mesons is shown on Fig. 7.5(a) on page 193. As can be seen, the dependence is well described with a function $T = A\cdot\ln(\sqrt{s_{\rm NN}})+B$ for all of the data points except the highest SPS

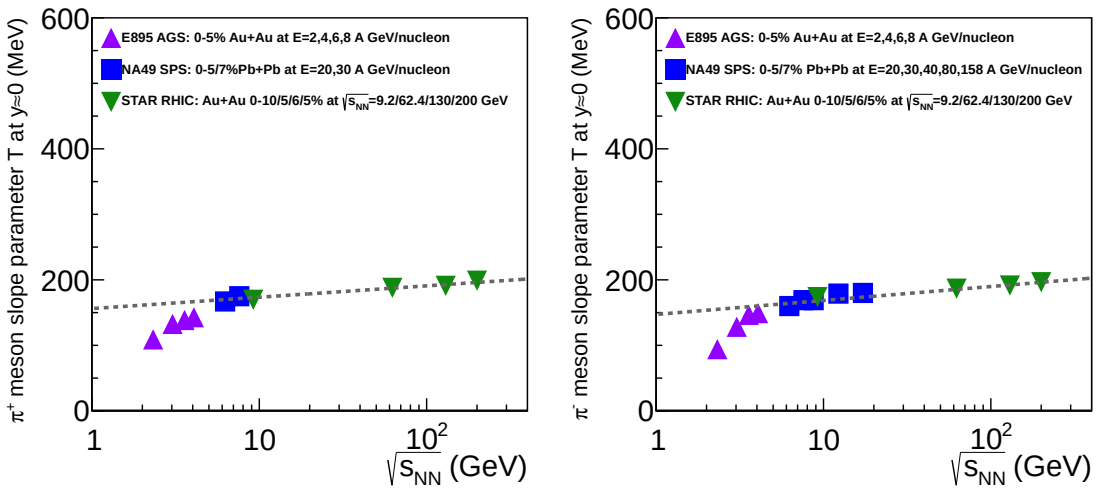

(a) π^+ slope parameter T versus $\sqrt{s_{\rm NN}}$

(b) π^- slope parameter T versus $\sqrt{s_{\rm NN}}$

Figure 7.8.: Dependence of the slope parameter T of π^+ (a) and π^- (b), on $\sqrt{s_{\rm NN}}$ in central heavy ion collisions with $A \approx 200$. The data were taken from Ref. [264, 273–277]. The errors of the E895 π^+ and π^- data points were assigned from the results of fits of the corresponding invariant yield measurements with statistical and systematic errors added in quadrature. The errors of the SPS π^+ and π^- data points at E =20 and 30 A GeV are statistical only. The errors of the SPS π^- data points at E =40, 80, and 158 A GeV correspond to statistical and systematic errors of the corresponding measurements added in quadrature. The errors of all of the STAR data points were assigned from the results of fits of the corresponding invariant yield measurements with statistical and point-to-point systematic errors added in quadrature. The dashed lines are fits (π^+: χ^2/ndf=9.47/4, fit-probability=0.05, π^-: χ^2/ndf=9.33/7, fit-probability=0.23) with a function $T = A \cdot \ln(\sqrt{s_{\rm NN}}) + B$ of all of the SPS and RHIC data points. See section 7.3 on page 188 for details.

energy. The conclusions, which can be drawn from the figure, are:

1. Since the fit function $T = A \cdot \ln(\sqrt{s_{\rm NN}}) + B$ has a monotonic dependence of its derivative on $\sqrt{s_{\rm NN}}$ (namely, $\frac{dT}{d\sqrt{s_{\rm NN}}} = \frac{A}{\sqrt{s_{\rm NN}}}$, and hence has no local or global minimum), *there is no evidence of a deconfinement transition in the data according to the ideas explained in the beginning of this section.*

2. The available data suggests that *either the T versus $\sqrt{s_{\rm NN}}$ dependence of ϕ mesons has a local maximum at $\sqrt{s_{\rm NN}} \sim$20 GeV or that the highest SPS energy measurement has an unaccounted for systematic error.* The situation could be clarified using the RHIC data at $\sqrt{s_{\rm NN}}$=19.6 GeV and at $\sqrt{s_{\rm NN}}$=27 GeV taken in 2011.

Analogous analysis was also performed for other particle species: pions (Fig. 7.8), kaons

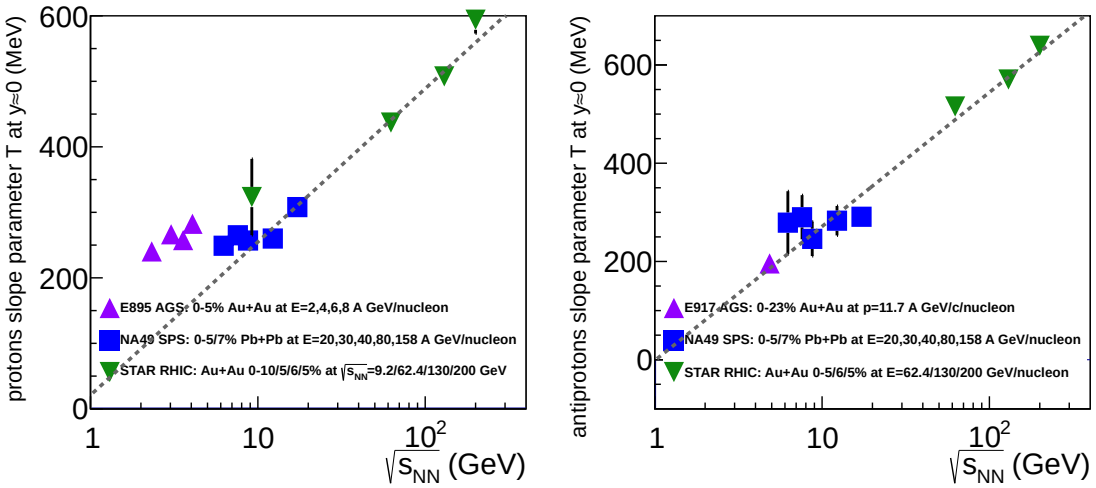

(a) p slope parameter T versus $\sqrt{s_{\rm NN}}$

(b) $\bar{p}$ slope parameter T versus $\sqrt{s_{\rm NN}}$

Figure 7.9.: Dependence of the slope parameter T of p (a), and $\bar{p}$ (b) on $\sqrt{s_{\rm NN}}$ in central heavy ion collisions with $A \approx 200$. The data were taken from Ref. [264, 273–277]. The errors of the E895 proton data points were assigned from the results of fits of the corresponding invariant yield measurements, however, it is not clear neither from Ref. [275] nor from the corresponding Ref. [278] which errors on the invariant yield were provided. The errors of all of the SPS data points are statistical only. The errors of all of the STAR data points (except for p and $\bar{p}$ at $\sqrt{s_{\rm NN}}$=130 GeV) were assigned from the results of fits of the corresponding invariant yield measurements with statistical and point-to-point systematic errors added in quadrature (only statistical errors were used in the fits of p and $\bar{p}$ invariant yields at $\sqrt{s_{\rm NN}}$=130 GeV). Nota bene: the E917 data point on Fig. (b) corresponds to a much wider centrality range than the other points on the figure (0-23% versus 0-5/6/7%) and so has to be compared to them especially cautiously. The dashed lines are fits (p: χ^2/ndf=9.14/5, fit-probability=0.10, $\bar{p}$: χ^2/ndf=15.9/7, fit-probability=0.03) with a function $T = A \cdot \ln(\sqrt{s_{\rm NN}}) + B$ of all of the data points except the AGS and the two lowest SPS energies in the protons data fit. See section 7.3 on page 188 for details.

(Fig. 7.7), (anti)protons (Fig. 7.9), Ξ (Fig. 7.6), and Ω (Fig. 7.5(b)), with the following observations:

1. The dependence of the slope parameter T on $\sqrt{s_{\rm NN}}$ for all of the studied particle species can be described with the same function $T = A \cdot \ln(\sqrt{s_{\rm NN}}) + B$ for $\sqrt{s_{\rm NN}} \gtrsim 4-9$ GeV.

2. All of the particle types have a monotonically decreasing positive slope $\frac{dT}{d\sqrt{s_{\rm NN}}}$ as

a function of $\sqrt{s_{\mathrm{NN}}}$, with the exception of protons, which have a statistically significant range ($\sqrt{s_{\mathrm{NN}}}$ ~2-9 GeV) of a much lower slope in comparison to what one could expect from extending the fit function $T = A \cdot \ln(\sqrt{s_{\mathrm{NN}}}) + B$ into the range from the ray $\sqrt{s_{\mathrm{NN}}}$ >9 GeV, where the function provides a good description of the data. And so, the proton data is consistent with having either a vanishing derivative $\frac{dT}{d\sqrt{s_{\mathrm{NN}}}}$ or a local minimum of the derivative in the range. The difficultly with the later statement is that it is not clear which errors are listed in the publications for the proton data at the AGS energies, and the SPS data only have statistical errors assigned to them (see Fig. 7.9 on the preceding page), therefore the interpretation of the data cannot be considered conclusive.

3. In the energy range $\sqrt{s_{\mathrm{NN}}} \lesssim 4-9$ GeV, pions, kaons, and (possibly) ϕ mesons have significantly higher slope $\frac{dT}{d\sqrt{s_{\mathrm{NN}}}}$ than extensions of their fit functions $T = A \cdot \ln(\sqrt{s_{\mathrm{NN}}}) + B$ into the range from the ray $\sqrt{s_{\mathrm{NN}}}$ >9 GeV.

The conclusions which can be drawn from the observations are:

- Since none of the particle species (maybe, except protons) has a local minimum in its $\frac{dT}{d\sqrt{s_{\mathrm{NN}}}}$ versus $\sqrt{s_{\mathrm{NN}}}$ dependence contrary to the expectations outlined in the beginning of the section, there is no evidence of a well defined region of energy densities which could be associated with the transition between confined and deconfined states of QCD matter.

- It is evident from Fig. 7.5(a), Fig. 7.7, Fig. 7.8, and Fig. 7.9(a) that some change in the mechanism of particle production occurs at $\sqrt{s_{\mathrm{NN}}} \approx 4-9$ GeV, however the signatures of the change are different from the expected ones.

- It is possible that the transition region is very short as a function of $\sqrt{s_{\mathrm{NN}}}$ and therefore the local minimum in the $\frac{dT}{d\sqrt{s_{\mathrm{NN}}}}$ versus $\sqrt{s_{\mathrm{NN}}}$ dependence is not observable with the available density of data points and their measurement uncertainties.

It is interesting to note in the end, that the B parameters of the fits of all the studied particles (except those of protons and antiprotons) happen to be about $150-180$ MeV (just note the value of the fit functions at $\sqrt{s_{\mathrm{NN}}}$=1 GeV), while for protons and antiprotons $B \approx 0$ MeV. However, since the fit functions $T = A \cdot \ln(\sqrt{s_{\mathrm{NN}}}) + B$ (or equivalently, $T = A \cdot \ln\left(\frac{\sqrt{s_{\mathrm{NN}}}}{B}\right)$ to avoid taking a logarithm of a dimensional variable) were chosen phenomenologically, it is not possible to say if the B values are connected to the expected values of T_c (see section 1.2.8 on page 30) or if it is just a coincidence.

7.4. In Medium Modifications of ϕ Mesons

To test for a presence of in-medium modifications of properties of the $\phi \to K^+K^-$ decay (see section 1.4.3 on page 43) in the PHOBOS Cu+Cu at $\sqrt{s_{\mathrm{NN}}} = 200$ GeV data, the data K^+K^- invariant mass distributions were fit using the following two methods (see section 6.2.1 on page 145):

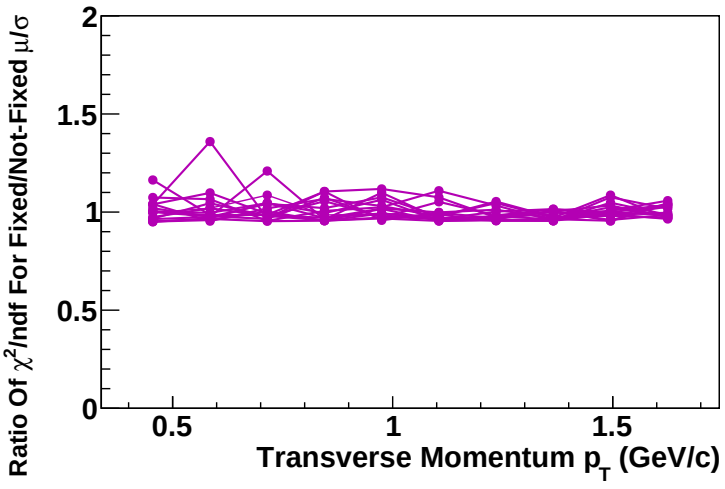

Figure 7.10.: The ratios of the reduced χ^2 values resulting from two different methods of fitting of the PHOBOS Cu+Cu data at $\sqrt{s_{\mathrm{NN}}} = 200$ GeV: 1) with the mean and the width of the ϕ meson peak varied during fitting, 2) with the mean and the width fixed during fitting. The 16 different sets of points correspond to all of the considered combinations of the data magnet polarities (2 possible values) and of the 8 examined centrality ranges (see Fig. 7.1 on page 186). See section 7.4 on the facing page for details.

- parameters E and F (the mean and the width of the ϕ meson peak) were allowed to be varied during fitting,
- parameters E and F were fixed during fitting.

If the mean or the width (or both) of ϕ mesons in $\phi \rightarrow K^+K^-$ decays is modified in a hot hadronic gas, then the second fitting method would result in significantly larger reduced χ^2 values. However, the later is not observed in the data, since the ratios of the χ^2 values arising from the two fitting methods are very close to unity (see Fig. 7.10). The ratios of the corresponding fit probabilities are consequently very close to unity as well. Therefore, one of the following conclusions is possible:

- $\phi \rightarrow K^+K^-$ decay properties are not modified in a hot hadronic gas,
- $\phi \rightarrow K^+K^-$ decay properties are modified in a hot hadronic gas, but the average lifetime of the state in Cu+Cu at $\sqrt{s_{\mathrm{NN}}} = 200$ GeV collisions is mush shorter than the ϕ meson decay time in the gas, and so only a small fraction of ϕ mesons decay inside the gas, which makes the detection of the corresponding in-medium modifications of the decay properties impossible within the experimental uncertainties. A recent (theoretical) estimate on the lifetime of the hadronic phase is 5-10 fm/c [282]. Another estimate puts the lifetime at 5-13 fm/c depending on a hadron species [283]. The width of ϕ mesons in the phase is expected to be

larger than in vacuum (see section 1.4.3.2 on page 45), which means that they would have a shorter decay time than the vacuum value of ∼46.3 fm/c (see section 1.4.2.1 on page 40). Combining the above statements, one can gather that the decay time of ϕ mesons in a hot hadronic gas is much longer than 5-13 fm/c but is limited from the above by ∼46.3 fm/c.

- $\phi \rightarrow K^+K^-$ decay properties are modified in a hot hadronic gas and a significant fraction of ϕ meson decay in the later state, but due to a strong scattering of the daughter kaons produced in the gas, their invariant mass distribution is indistinguishable from the background, and therefore ϕ mesons which decay in the gas are not reconstructed. However, if this conclusion was correct, then ϕ meson invariant yields reconstructed through the $\phi \rightarrow K^+K^-$ and through the $\phi \rightarrow e^+e^-$ channels would be inconsistent since leptons only interact electromagnetically [8] and therefore are much more weakly affected by scatterings on the gas hadrons than kaons and so (assuming that branching ratios of ϕ meson decay in a hot hadronic gas are not modified) higher fraction of ϕ mesons decaying through $\phi \rightarrow e^+e^-$ (as opposed to $\phi \rightarrow K^+K^-$) would be reconstructed resulting in a seemingly higher measured invariant yield. But the later is not the case according to a recent measurement (0-80% centrality Au+Au at $\sqrt{s_{\rm NN}}$=200 GeV) by the STAR collaboration [284], which rules out the correctness of the current conclusion (at least within the measurement uncertainties).

The PHOBOS results are consistent with the findings of other experimental groups which as well were unable to find any evidence of in-medium modifications neither of the mean nor of the width of the ϕ meson peak in relativistic heavy ion collisions using the $\phi \rightarrow K^+K^-$ decay channel [150, 151, 231–234, 285]. However, when the work on this thesis began, only the AGS and the low statistics $\sqrt{s_{\rm NN}}$=130 GeV measurements were available. And so, since the AGS collision energies were estimated to be not high enough for a transition of QCD matter into QGP, the question of possible modifications of ϕ mesons in a hot hadronic gas produced in a QGP decay was still open.

7.5. Comparison To STAR and PHENIX Results

To compare the PHOBOS results to the measurements of the ϕ meson invariant yield in Cu+Cu collisions at $\sqrt{s_{\rm NN}}$=200 GeV by the STAR [233] and the PHENIX [253] collaborations, the ratio of the measurements was estimated. To show what assumptions were made in the estimate, let us consider an example case of two variables a and b dependent on some parameter x. If

- there are two independent sets of values (let us call them, *data points*) of the variables $a_i(x_i)$ ($i = 1,\ldots,N_a$) and $b_j(x_j)$ ($j = 1,\ldots,N_b$), and

[8] The weak interactions are stronger than the electromagnetic ones only at transverse momentum transfer values of $\sim M_{Z,W^\pm}$ and could therefore be neglected at all the possible temperatures (namely, below 140-200 MeV, see section 1.2.8 on page 30) of a hadronic gas.

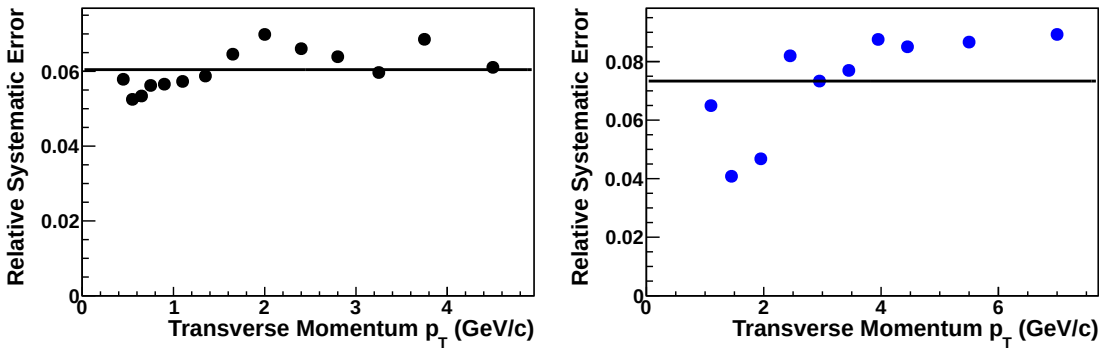

(a) STAR, 0-60%

(b) PHENIX, 0-60%

Figure 7.11.: An example of (a) STAR and (b) PHENIX ϕ meson invariant yield relative systematic errors in Cu+Cu collisions at $\sqrt{s_{\mathrm{NN}}}$=200 GeV. The lines are fits (found by assigning the unity weight to each point) of the errors by constant functions. The fits were used as parametrizations of the systematic errors during the estimation of the ratios of the STAR and the PHENIX to the PHOBOS results. See section 7.5 on the preceding page for details.

- the functions $A(x)$ and $B(x)$ with parameters p^A_n (n = 1,...,N_A) and p^B_m (m = 1,...,N_B) are fits of the two sets of data points respectively, found using the statistical uncertainties on the points $\sigma^{\mathrm{stat}}_{a_i}$ and $\sigma^{\mathrm{stat}}_{b_j}$ only,

then as a measure of agreement between the two sets of data points one could evaluate the ratio $A(x)/B(x)$ and the uncertainty on it. The statistical uncertainty on the value of the function $A(x)$ at a particular value of the argument x can be found from

$$\left(\sigma^{\mathrm{stat}}_{A(x)}\right)^2 = \sum_{n_1,n_2=1}^{N_A} \frac{\partial A(x)}{\partial p^A_{n_1}} \frac{\partial A(x)}{\partial p^A_{n_2}} \mathrm{cov}\left(p^A_{n_1}, p^A_{n_2}\right), \tag{7.4}$$

where $\mathrm{cov}(p^A_{n_1}, p^A_{n_2})$ is the covariance matrix of the function parameters. The statistical uncertainty on a value of the function $B(x)$ could be found analogously. The statistical uncertainty on the ratio $A(x)/B(x)$ of the two variables is then

$$\sigma^{\mathrm{stat}}_{A(x)/B(x)} = \left|\frac{A(x)}{B(x)}\right| \sqrt{\frac{\left(\sigma^{\mathrm{stat}}_{A(x)}\right)^2}{A^2(x)} + \frac{\left(\sigma^{\mathrm{stat}}_{B(x)}\right)^2}{B^2(x)}}. \tag{7.5}$$

Let us assume now that the data points $a_i(x_i)$ and $b_j(x_j)$ have in addition systematic uncertainties $\sigma^{\mathrm{syst}}_{a_i}$ and $\sigma^{\mathrm{syst}}_{b_j}$ associated with them correspondingly. The contribution of the systematic uncertainties into the uncertainty on $A(x)/B(x)$ depends on whether $\sigma^{\mathrm{syst}}_{a_i}$ and $\sigma^{\mathrm{syst}}_{b_j}$ affect each data point independently (the *first case*) or are a consequence of systematic errors which can change the scale of all the points $a_i(x_i)$ and $b_j(x_j)$ simultaneously (the *second case*). In the first case, the formulas above stay correct except

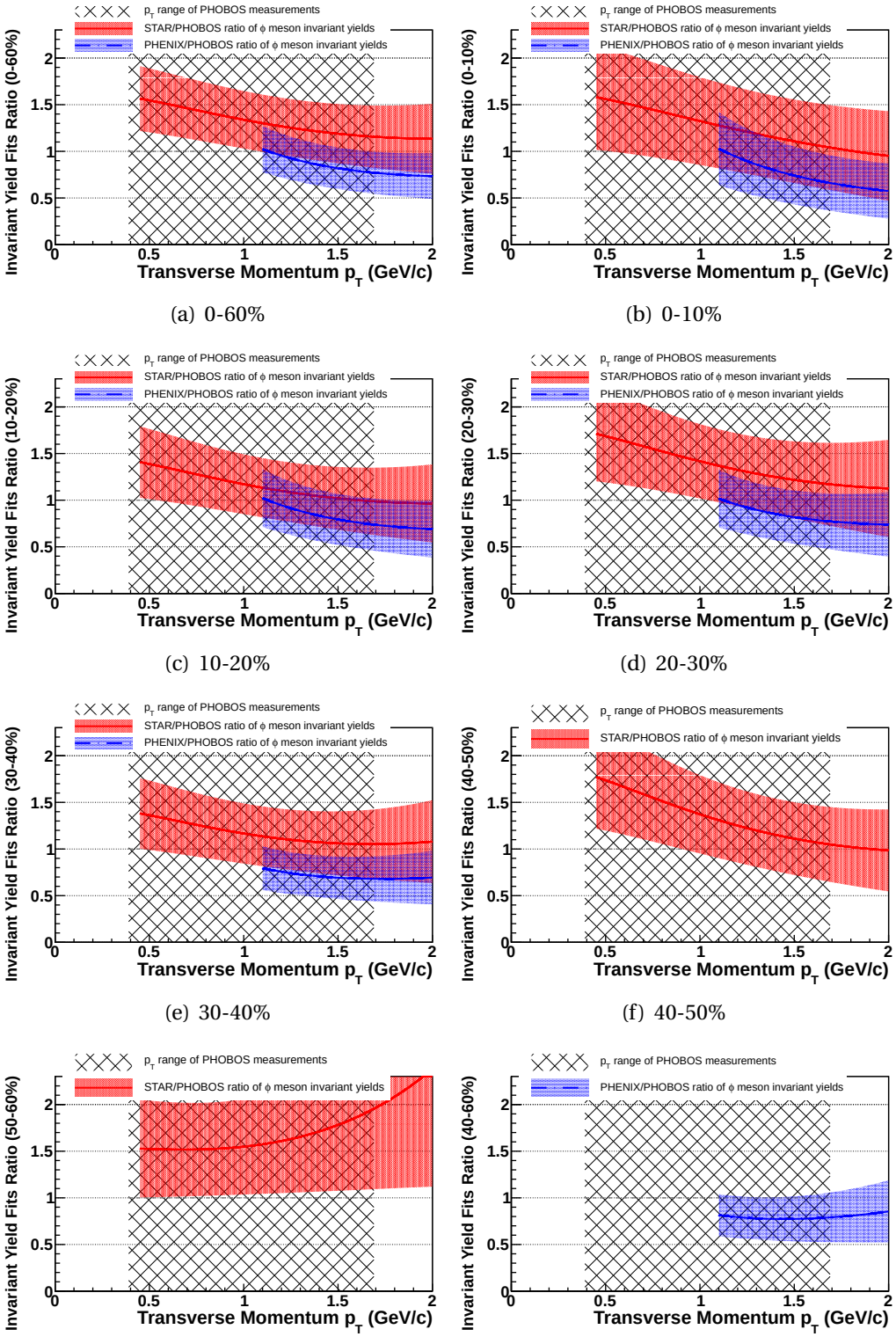

(a) 0-60%

(b) 0-10%

(c) 10-20%

(d) 20-30%

(e) 30-40%

(f) 40-50%

(g) 50-60%

(h) 40-60%

Figure 7.12.: STAR/PHOBOS and PHENIX/PHOBOS ratios of fits of the ϕ meson invariant yield measurements in Cu+Cu collisions at $\sqrt{s_{NN}}$=200 GeV in ranges of centrality. The color bands around the lines show the upper limit on the combined statistical and systematic uncertainties of the ratios. See section 7.5 on page 200 for details.

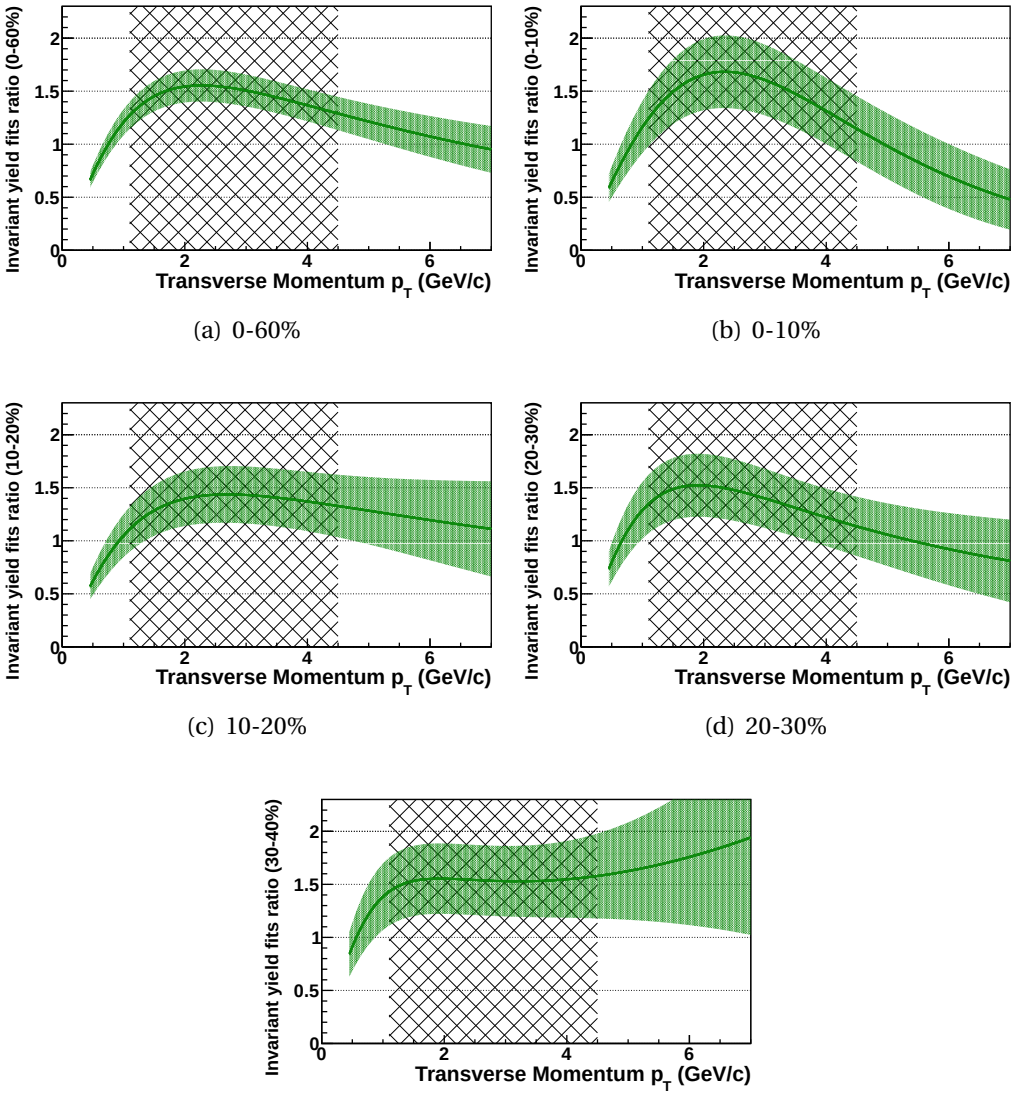

(a) 0-60%

(b) 0-10%

(c) 10-20%

(d) 20-30%

(e) 30-40%

Figure 7.13.: STAR/PHENIX/ ratio of fits of the ϕ meson invariant yield measurements in Cu+Cu collisions at $\sqrt{s_{\mathrm{NN}}}$=200 GeV in ranges of centrality. The color bands around the lines show the upper limit on the combined statistical and systematic uncertainties of the ratios. The hatched area shows the region of transverse momentum where the two measurements overlap. See section 7.5 on page 200 for details.

that during fitting of the data points, one has to use not just the statistical uncertainties but the statistical and the systematic ones added in quadrature. In the second case, one has to parametrize the systematic uncertainties of the data points (let us denote the parametrizations as $\sigma_a^{\text{syst}}(x)$ and $\sigma_b^{\text{syst}}(x)$) and add them in quadrature in Eq. 7.5, namely

$$\sigma^{\text{total}}_{A(x)/B(x)} = \left|\frac{A(x)}{B(x)}\right| \sqrt{\frac{\left(\sigma^{\text{stat}}_{A(x)}\right)^2 + \left(\sigma_a^{\text{syst}}(x)\right)^2}{A^2(x)} + \frac{\left(\sigma^{\text{stat}}_{B(x)}\right)^2 + \left(\sigma_b^{\text{syst}}(x)\right)^2}{B^2(x)}}. \tag{7.6}$$

As can be seen, in the second case the effect of the data points' systematic errors on the uncertainty in $A(x)/B(x)$ does not depend on the number of the points and is stronger than in the first case [9]. Since information on which fraction of the systematic errors affects each of the data points independently and which fraction affects the overall scale of all of the data points is not available for any of the compared measurements [10], *an upper limit* on the uncertainties on the STAR/PHOBOS and the PHENIX/PHOBOS ratios of fits of the ϕ meson invariant yield measurements was found by treating all the systematic errors as in the second case. PHOBOS results were fit as explained in section 7.2 on page 185, while the STAR and the PHENIX results were fit with the Lévy [233] and the Tsallis [253] functions respectively. To find continuous parametrizations of the STAR and the PHENIX systematic errors, the following procedure was implemented:

1. The relative systematic errors were calculated and fit with constant functions (see Fig. 7.11 on page 201 for an example).

2. Each of the fit functions found in step 1 was multiplied by the corresponding ϕ meson invariant yield fit function.

To find parametrizations of the PHOBOS systematic errors, the same procedure was followed except that continuous estimates of relative systematic errors as a function of transverse momentum were found as explained in section 6.5.1 on page 160. The resulting STAR/PHOBOS and the PHENIX/PHOBOS ratios of fits of the ϕ meson invariant yield measurements are shown on Fig. 7.12 on page 202. As can be seen, *the PHOBOS results agree with those from both the STAR and the PHENIX collaborations within the estimated uncertainties*, since the ratios on the figure deviate from the ordinate equal to unity line by less than two error bars at all transverse momentum values at which the measurements overlap. The dominant contribution to the uncertainties on the ratios comes from the PHOBOS systematic errors. For example for the 0-60% centrality range, the average uncertainty found using Eq. 7.6 is 0.32 ± 0.01 for the STAR/PHOBOS and

[9] In the first case, the effect of the systematic errors of data points on the uncertainty of their fit function values should scale as $\sim \frac{1}{\sqrt{N_p - N_{fp}}}$, where N_p is the number of points (N_a for points $a_i(x_i)$) and N_{fp} is the number of fit parameters (N_A for points $a_i(x_i)$), while in the second case, the effect of the systematic errors of data points on the uncertainty of their fit function values does not depend on N_p.

[10] Such information is not published on the web-sites of the STAR and the PHENIX experiments. Following an advice from Wit Busza, a contact attempt was made via e-mail to Helen Caines from STAR and to Rachid Nouicer from PHENIX, however no reply was received in both cases. An analysis aimed to separate the two kinds of systematic errors was not done for the PHOBOS data.

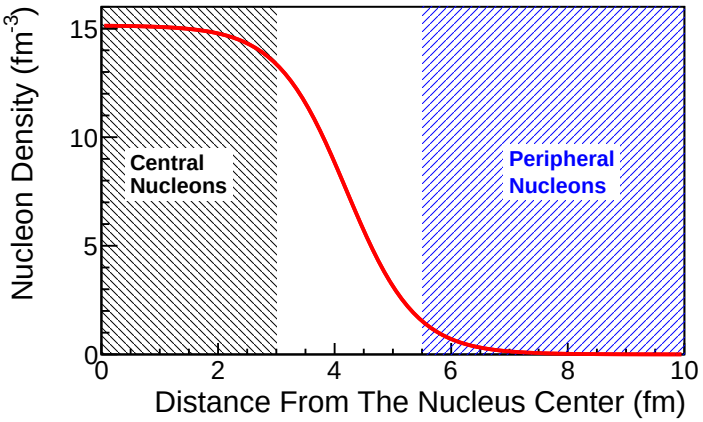

Figure 7.14.: Woods-Saxon distribution ($\rho(r) = \frac{\rho_0}{1+\exp((r-R)/a)}$) of nucleons inside a copper nucleus with parameters R=4.2 fm and a=0.596 fm [225]. The normalization parameter $\rho_0 \approx$15.145 was chosen to correspond to the average number of nucleons per nucleus in natural copper. See section 7.6 for details.

0.23 ± 0.01 for the PHENIX/PHOBOS ratios. However, if PHOBOS systematic errors are ignored, the average uncertainties drop to 0.107 ± 0.014 and 0.084 ± 0.003 correspondingly. For a comparison, the STAR/PHENIX ratio of fits of the ϕ meson invariant yield measurements (found the same way as the STAR/PHOBOS and the PHENIX/PHOBOS ratios described above) is shown on Fig. 7.13 on page 203.

7.6. Centrality Dependence Of ϕ Meson Production

To probe for conditions and for mechanism of ϕ mesons production in heavy ion collisions, one could study the dependence of the yield of ϕ mesons on collision centrality (see section 4.5 on page 79).

The centrality of a nucleus-nucleus collision determines the following mean properties of the collision:

1. the impact parameter,
2. the spacial shape (called further the *collision geometry*), the volume and the surface area of the collision region,
3. the number of nucleons participating in the collision (N_{part}),
4. the number of hard parton scattering processes occurring during the collision.

As it was pointed out in section 4.5 on page 79, the exact centrality of an event depends on what variable was used as a measure of centrality. Normally in an experiment, such variable is chosen to be a signal from some detector. However, different

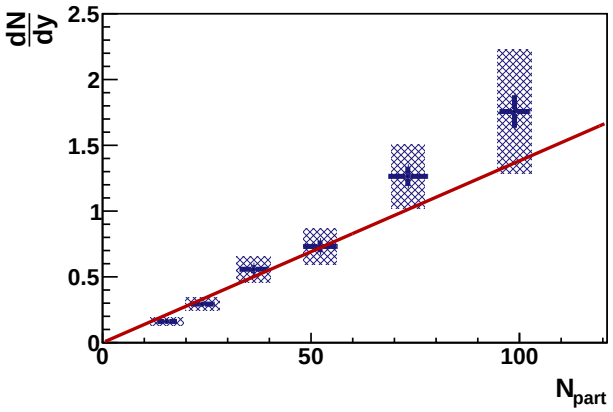

Figure 7.15.: ϕ meson dN/dy in the rapidity range $0 \leq y \leq 1$ as a function of the number of participants N_{part} as measured by PHOBOS in Cu+Cu $\sqrt{s_{\text{NN}}}$=200 GeV collisions. The horizontal blue lines show the uncertainties on N_{part}. The vertical blue lines show the statistical uncertainties on dN/dy. The vertical size of the shaded areas show the estimates on the systematic errors of dN/dy, while the horizontal size of the areas is arbitrary. The red line is the result of a fit of the dependence with a function $dN/dy = A \cdot N_{\text{part}}$ (where A is the fit parameter), arising in $A = 0.0138 \pm 0.0013$ with $\chi^2/\text{ndf} = 3.56/5$ and the corresponding fit-probability of 0.61. In the fit statistical and systematic uncertainties on dN/dy, as well as properly scaled uncertainties on N_{part} (the fit was done iteratively, the scaling factor in an iteration was the parameter A resulting from the previous iteration, the scaling factor of the first iteration was zero) were added in quadrature. See section 7.6 on the previous page for details.

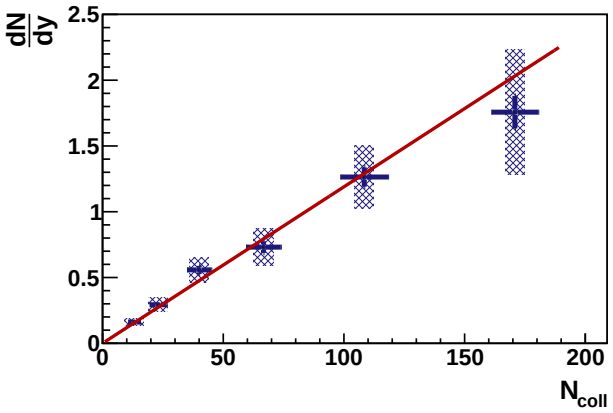

Figure 7.16.: ϕ meson dN/dy in the rapidity range $0 \leq y \leq 1$ as a function of the number of participants N_{coll} as measured by PHOBOS in Cu+Cu $\sqrt{s_{\text{NN}}}$=200 GeV collisions. The horizontal blue lines show the uncertainties on N_{coll}. The vertical blue lines show the statistical uncertainties on dN/dy. The vertical size of the shaded areas show the estimates on the systematic errors of dN/dy, while the horizontal size of the areas is arbitrary. The red line is the result of a fit of the dependence with a function $dN/dy = A \cdot N_{\text{coll}}$ (where A is the fit parameter), arising in $A = 0.0119 \pm 0.0012$ with $\chi^2/\text{ndf} = 1.01/5$ and the corresponding fit-probability of 0.96. In the fit statistical and systematic uncertainties on dN/dy, as well as properly scaled uncertainties on N_{coll} (the fit was done iteratively, the scaling factor in an iteration was the parameter A resulting from the previous iteration, the scaling factor of the first iteration was zero) were added in quadrature. See section 7.6 on the previous page for details.

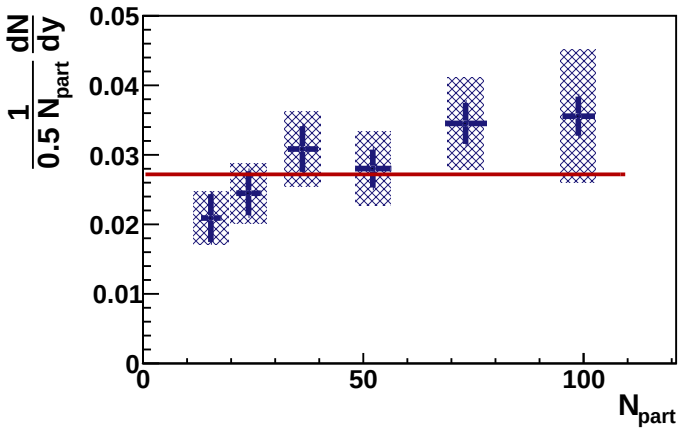

Figure 7.17.: ϕ meson dN/dy in the rapidity range $0 \leq y \leq 1$ per one pair of participating nucleons as a function of the number of participants N_{part} as measured by PHOBOS in Cu+Cu $\sqrt{s_{\text{NN}}}$=200 GeV collisions. The horizontal blue lines show the uncertainty on N_{part}. The vertical blue lines show the statistical uncertainty on $\frac{1}{0.5 \cdot N_{\text{part}}} \frac{dN}{dy}$. The vertical size of the shaded areas show the estimates on the systematic error of $\frac{1}{0.5 \cdot N_{\text{part}}} \frac{dN}{dy}$, while the horizontal size of the areas is arbitrary. The red line is the result of a fit of the dependence with a function $\frac{1}{0.5 \cdot N_{\text{part}}} \frac{dN}{dy} = A$ (where A is the fit parameter), arising in $A = 0.0272 \pm 0.0025$ with $\chi^2/\text{ndf} = 3.86/5$ and the corresponding fit-probability of 0.57. In the fit statistical and systematic uncertainties on $\frac{1}{0.5 \cdot N_{\text{part}}} \frac{dN}{dy}$ were added in quadrature. See section 7.6 on page 205 for details.

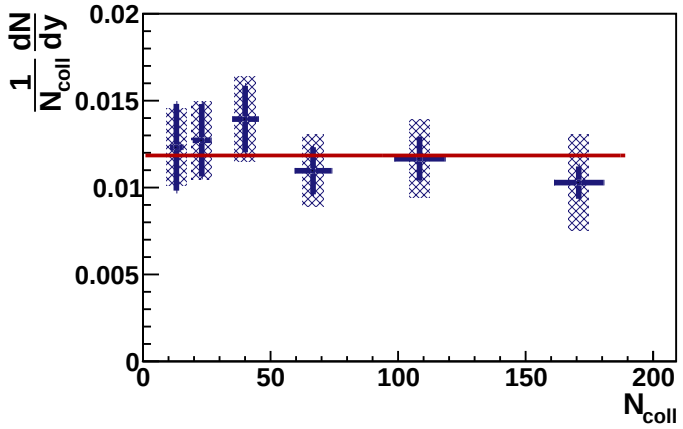

Figure 7.18.: ϕ meson dN/dy in the rapidity range $0 \leq y \leq 1$ per one collision of participating nucleons as a function of the number of participants N_{coll} as measured by PHOBOS in Cu+Cu $\sqrt{s_{\text{NN}}}$=200 GeV collisions. The horizontal blue lines show the uncertainty on N_{coll}. The vertical blue lines show the statistical uncertainty on $\frac{1}{N_{\text{coll}}} \frac{dN}{dy}$. The vertical size of the shaded areas show the estimates on the systematic error of $\frac{1}{N_{\text{coll}}} \frac{dN}{dy}$, while the horizontal size of the areas is arbitrary. The red line is the result of a fit of the dependence with a function $\frac{1}{N_{\text{coll}}} \frac{dN}{dy} = A$ (where A is the fit parameter), arising in $A = 0.0118 \pm 0.0012$ with $\chi^2/\text{ndf} = 0.97/5$ and the corresponding fit-probability of 0.96. In the fit statistical and systematic uncertainties on $\frac{1}{N_{\text{coll}}} \frac{dN}{dy}$ were added in quadrature. See section 7.6 on page 205 for details.

experiments use different detectors, and so to make their results comparable, it is necessary for each experiment to find a relationship between its detector specific centrality variable and some other variable which has to be chosen to be common for different experiments. Moreover, such common variable has to be selected in such a way that any experimental result could be compared to theoretical predictions. It has been established so historically that three different centrality variables that satisfy the above requirements are currently widely used, namely 1) the number of participants N_{part}, 2) the number of collisions N_{coll}, and 3) percentage centrality. Therefore, any dependence of some physical quantity on centrality should be represented as a function of one of the just listed variables. It is clear (and confirmed by experimental measurements) that percentage centrality could not define the yield of ϕ mesons since, for example, if one collides nuclei A+A and B+B of significantly different atomic mass, then the same percentage centrality corresponds to collisions of very different number of nucleons. Next, according to the modern theoretical point of view [286], if a cross-section of a physical process scales with N_{part}, then the cross-section is dominated by contributions from low p_T transfer interactions between partons (*"soft"* physics), and if some cross-section scales with N_{coll}, then the cross-section is dominated by high p_T transfer effects (*"hard"* physics). Consequently, if some phenomenon is dominated by thermal interactions (in our case it is ϕ mesons production due to disintegration of QGP or due to interactions in an equilibrated hadronic gas), or by low p_T transfer collisions of partons in the collided nuclei, then the phenomenon cross-section must scale with N_{part} since at RHIC energies the initial temperatures of created matter are estimated to be $T \lesssim 400$ MeV [286] and so the majority of interactions in the thermalized state are soft. And if ϕ mesons are produced predominantly in the primordial high p_T transfer collisions, then the yield of ϕ mesons must scale with N_{coll}.

Experimental data on ϕ meson dN/dy at mid-rapidity in heavy ion collisions at $\sqrt{s_{\mathrm{NN}}}$=200 GeV is currently available from PHOBOS (Cu+Cu, this thesis), PHENIX (Au+Au [232]), and STAR (Au+Au [252], Cu+Cu [233]). However, no information is available on which fraction of the systematic errors of the dN/dy measurements affects each of the data points independently and which fraction affects the overall scale of all of the data points as a function of collision centrality. Therefore, the following extreme cases were considered, in which it was assumed that 100% of the systematic errors corresponded to one of the two just mentioned possibilities (see sections 7.6.1 and 7.6.2 on page 211 correspondingly for the results).

7.6.1. Case One: 100% Uncorrelated Systematic Errors

In this case, the dependence of ϕ mesons dN/dy values at mid-rapidity in heavy ion collisions at $\sqrt{s_{\mathrm{NN}}}$=200 GeV was studied assuming that 100% of the systematic errors of the values affects each of the data points independently. This assumption is equivalent to studying the dependency with an uncertainty on each dN/dy value equal to its statistical and systematic errors added in quadrature. It was also assumed that the systematic errors on the N_{part} and the N_{coll} values are fully uncorrelated as well and so could be taken into account by adding them in quadrature after proper scaling (for details, see

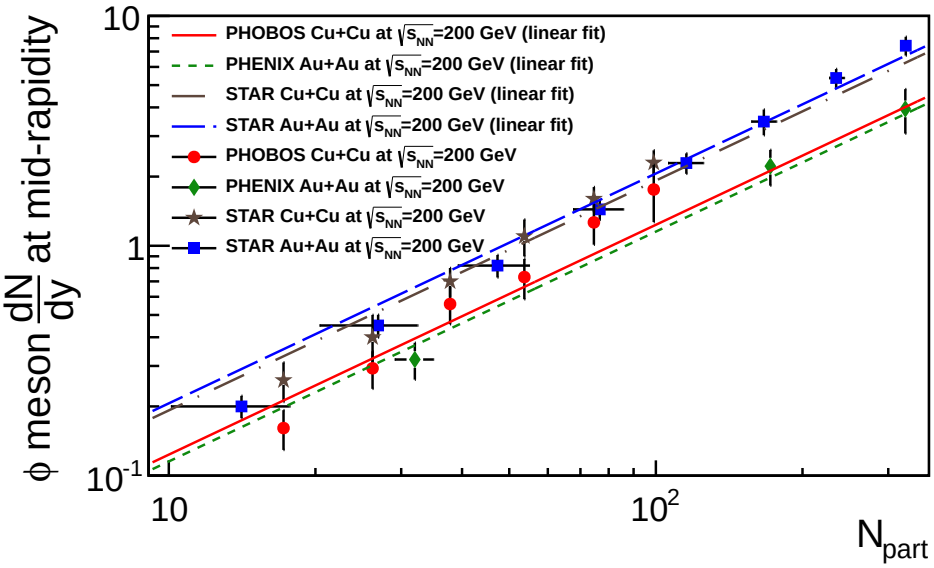

Figure 7.19.: ϕ meson dN/dy as a function of the number of participants N_{part} as measured by PHOBOS (rapidity range $0 \leq y \leq 1$), STAR [233, 252] (rapidity range $|y| < 0.5$), PHENIX [232] (pseudorapidity range $|\eta| < 0.35$) in Au+Au and Cu+Cu $\sqrt{s_{\text{NN}}}$=200 GeV collisions. The horizontal lines show the uncertainty on N_{part}. The vertical lines show the statistical and systematic uncertainties on dN/dy added in quadrature. The lines are the results of fits of the dependencies with a function $dN/dy = A \cdot N_{\text{part}}$ (where A is the fit parameter), arising in the A and χ^2/ndf values shown in Table 7.3. In the fits, statistical and systematic uncertainties on dN/dy, as well as properly scaled uncertainties on N_{part} (the fit was done iteratively, the scaling factor in an iteration was the parameter A resulting from the previous iteration, the scaling factor of the first iteration was zero) were added in quadrature. The N_{part} values and their uncertainties were taken from Ref. [232, 233]. See section 7.6.1 on the preceding page for details.

the captions of the figures referenced below) to the errors on the dN/dy values.

The dependence of dN/dy of ϕ mesons on N_{part} and on N_{coll} as measured using the PHOBOS detector is shown on Fig. 7.15 and Fig. 7.16 on page 206. As can be seen, the cross-section of ϕ mesons production near mid-rapidity scales with both N_{part} and N_{coll} within the estimated measurement uncertainties, and so the PHOBOS data alone do not allow to distinguish between the two mechanisms (soft versus hard parton interactions, see section 7.6 on page 205) of ϕ meson production in Cu+Cu collisions at $\sqrt{s_{\text{NN}}}$=200 GeV.

The dependence of dN/dy of ϕ mesons on N_{part} (see Fig. 7.19) and on N_{coll} (see Fig. 7.20 on the next page) was also studied for the STAR Au+Au [252], the STAR Cu+Cu [233], and the PHENIX Au+Au [232] data as well as for their various combina-

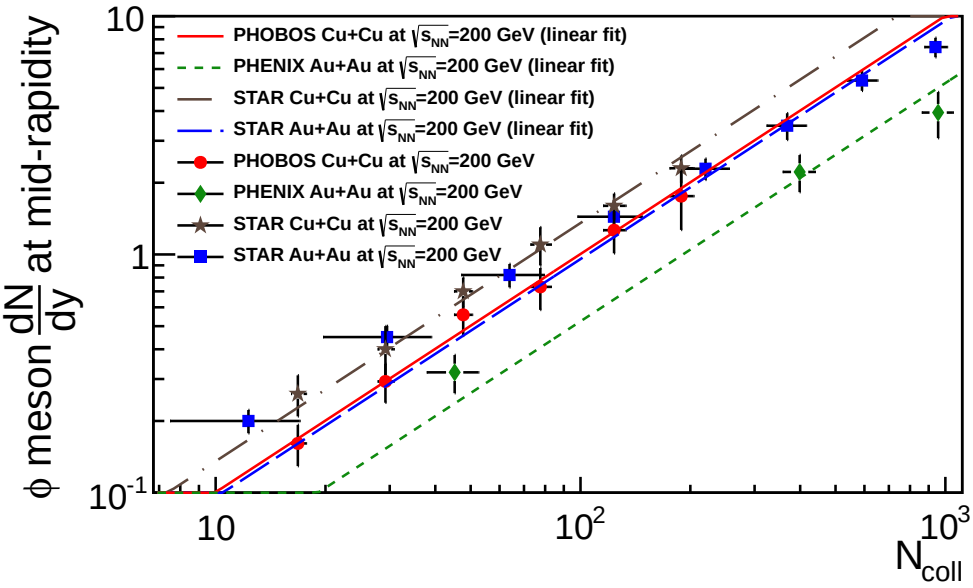

Figure 7.20.: ϕ meson dN/dy as a function of the number of collisions N_{coll} as measured by PHOBOS (rapidity range $0 \leq y \leq 1$), STAR [233, 252] (rapidity range $|y| < 0.5$), PHENIX [232] (pseudorapidity range $|\eta| < 0.35$) in Au+Au and Cu+Cu $\sqrt{s_{\text{NN}}}$=200 GeV collisions. The horizontal lines show the uncertainty on N_{coll}. The vertical lines show the statistical and systematic uncertainties on dN/dy added in quadrature. The lines are the results of fits of the dependencies with a function $dN/dy = A \cdot N_{\text{coll}}$ (where A is the fit parameter), arising in the A and χ^2/ndf values shown in Table 7.4. In the fits, statistical and systematic uncertainties on dN/dy, as well as properly scaled uncertainties on N_{coll} (the fit was done iteratively, the scaling factor in an iteration was the parameter A resulting from the previous iteration, the scaling factor of the first iteration was zero) were added in quadrature. The N_{coll} values and their uncertainties were taken from Ref. [232, 233]. See section 7.6.1 on page 208 for details.

tions with each other and with the PHOBOS data. Again, as can be seen from Table 7.3 and Table 7.4 on the facing page, each of the data sets separately (along with the combination of the STAR Au+Au and Cu+Cu data sets) is consistent with both N_{part} and N_{coll} scalings. The PHOBOS data combined with the one from PHENIX is consistent with N_{part} scaling only [11], while the PHOBOS data combined with both (Au+Au and Cu+Cu) of the STAR data sets is consistent with N_{coll} scaling only. All of the four data sets combined as well as the combination of the PHENIX data with the STAR Au+Au and Cu+Cu data sets are not consistent with neither of the two scalings.

[11] Although, the N_{coll} scaling is still possible with the fit-probability being just below 1%, one has to be careful about making conclusions based on the value since the PHENIX data set consists of only 3 points and so, such fit-probability should be considered very low.

Data	A	χ^2 / ndf	Fit Probability
PHOBOS Cu+Cu	0.0123 ± 0.0010	6.91 / 5	0.23
STAR Au+Au	0.0206 ± 0.0010	5.27 / 7	0.63
STAR Cu+Cu	0.0192 ± 0.0013	5.53 / 5	0.35
PHENIX Au+Au	0.0115 ± 0.0013	0.94 / 2	0.62
All of the 4 above data sets combined	0.0164 ± 0.0006	67.4 / 22	$2 \cdot 10^{-6}$
PHOBOS Cu+Cu and PHENIX Au+Au	0.0120 ± 0.0008	8.07 / 8	0.43
PHOBOS Cu+Cu and STAR Au+Au/Cu+Cu	0.0173 ± 0.0006	52.9 / 19	$5 \cdot 10^{-5}$
STAR Au+Au/Cu+Cu	0.0200 ± 0.0008	11.7 / 13	0.56
PHENIX Au+Au and STAR Au+Au/Cu+Cu	0.0181 ± 0.0007	38.7 / 16	$1 \cdot 10^{-3}$

Table 7.3.: χ^2 values and the corresponding probabilities (see section 5.10.6 on page 132) of the fits of the PHOBOS, PHENIX, and STAR (as well as of various their combinations) results on ϕ meson dN/dy versus N_{part}. See Fig. 7.19 for details.

Data	A	χ^2 / ndf	Fit Probability
PHOBOS Cu+Cu	0.0100 ± 0.0009	0.79 / 5	0.98
STAR Au+Au	0.0096 ± 0.0006	10.1 / 7	0.18
STAR Cu+Cu	0.0135 ± 0.0010	1.29 / 5	0.94
PHENIX Au+Au	0.0052 ± 0.0007	2.66 / 2	0.26
All of the 4 above data sets combined	0.0095 ± 0.0004	58.6 / 22	$4 \cdot 10^{-5}$
PHOBOS Cu+Cu and PHENIX Au+Au	0.0074 ± 0.0006	20.7 / 8	0.008
PHOBOS Cu+Cu and STAR Au+Au/Cu+Cu	0.0106 ± 0.0005	23.6 / 19	0.21
STAR Au+Au/Cu+Cu	0.0109 ± 0.0005	21.8 / 13	0.06
PHENIX Au+Au and STAR Au+Au/Cu+Cu	0.0093 ± 0.0004	58.0 / 16	$1 \cdot 10^{-6}$

Table 7.4.: χ^2 values and the corresponding probabilities (see section 5.10.6 on page 132) of the fits of the PHOBOS, PHENIX, and STAR (as well as of various their combinations) results on ϕ meson dN/dy versus N_{coll}. See Fig. 7.19 for details.

Consequently, the conclusion from what was said above is that the available data on ϕ meson production at mid-rapidity in heavy ion collisions at $\sqrt{s_{\mathrm{NN}}}$=200 GeV is not enough to distinguish between the N_{part} and the N_{coll} scalings, provided that the systematic errors of all the ϕ meson dN/dy values are fully uncorrelated.

7.6.2. Case Two: 100% Correlated Systematic Errors

In this case, the dependence of dN/dy values of ϕ mesons at mid-rapidity in heavy ion collisions at $\sqrt{s_{\mathrm{NN}}}$=200 GeV was studied assuming that 100% of the systematic errors affects the overall scale of all of the dN/dy values as a function of collision centrality. It

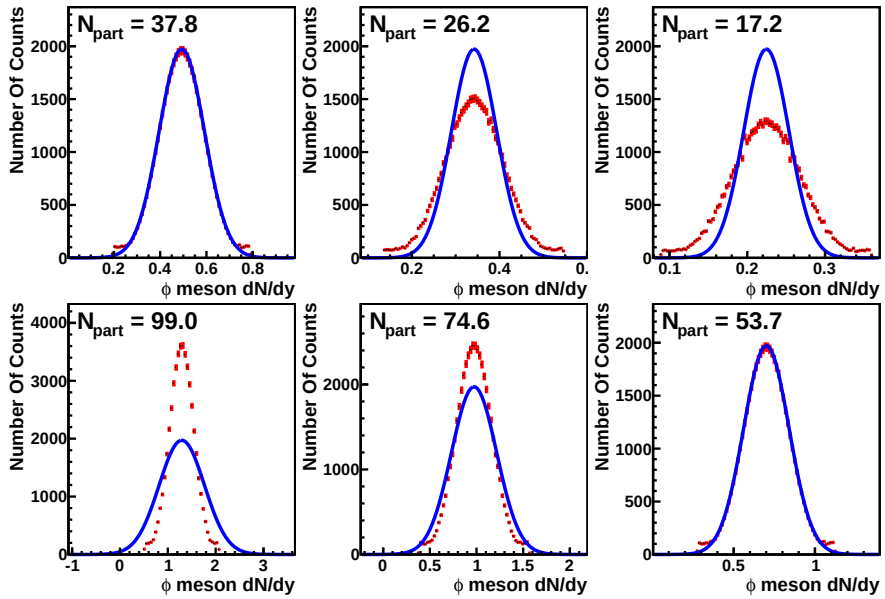

(a) Histograms $\mathscr{H}_i$ (the points with the red error bars) corresponding to each of the points of the PHOBOS Cu+Cu at $\sqrt{s_{\mathrm{NN}}}$=200 GeV data on ϕ meson dN/dy versus N_{part}. Each sub-figure also shows the Gaussian distribution (the blue lines) with the mean equal to the $\left(dN/dy\right)_{\mathrm{fit}}$=$A_{\mathrm{fit}}$·$N_{\mathrm{part}}$ value of the corresponding data point and the width equal to the systematic error of the value.

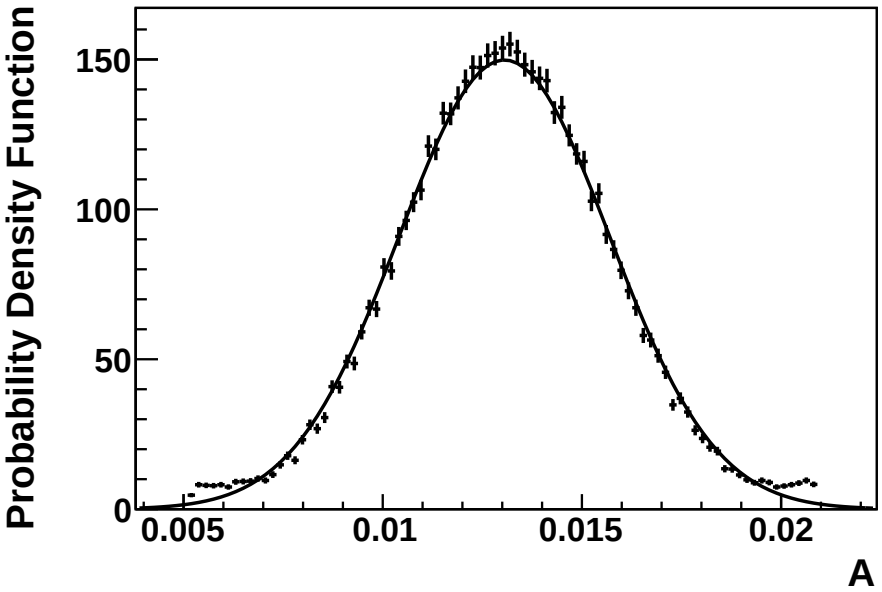

(b) Distribution of the A factors in the dependence $dN/dy = A{\cdot}N_{\mathrm{part}}$ resulting in the histograms on Fig. (a). The systematic uncertainty on the A parameter was assigned to be equal to the width of the Gaussian fit of the distribution.

Figure 7.21.: Estimation of the systematic uncertainty of the A parameter resulting from a fit of the PHOBOS data on ϕ meson dN/dy versus N_{part} with the function $dN/dy = A{\cdot}N_{\mathrm{part}}$. See section 7.6.2 on the preceding page for details.

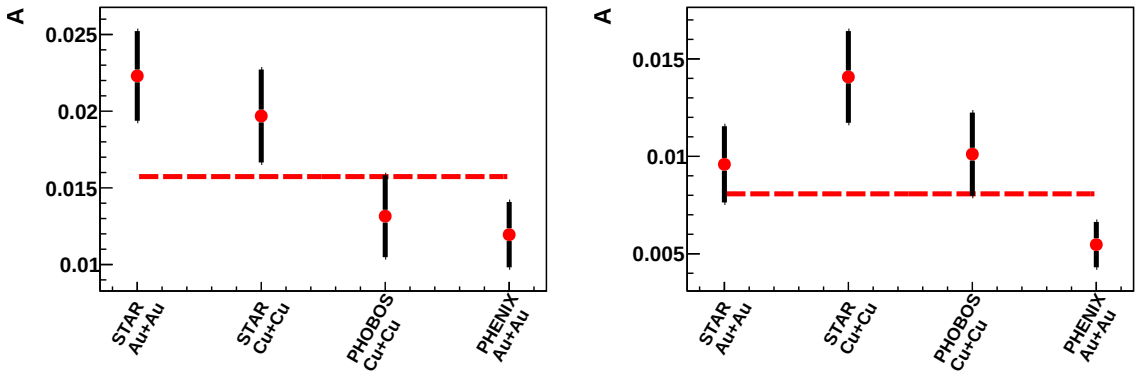

(a) A values resulting from fits of experimental data with the function $dN/dy = A \cdot N_{\text{part}}$. The dashed line fit results in $A = 0.0157 \pm 0.0013$, χ^2/ndf=10.8/3, and fit-probability=0.013.

(b) A values resulting from fits of experimental data with the function $dN/dy = A \cdot N_{\text{coll}}$. The dashed line fit results in $A = 0.0081 \pm 0.0008$, χ^2/ndf=13.0/3, and fit-probability=0.005.

Figure 7.22.: The vertical positions and the error bars of the points on the figures are equal to A_{fit} and $\Delta A_{\text{fit}}^{\text{tot}}$ respectively. Fig. (a) and Fig. (b) show the results of fitting the experimental data using functions $dN/dy = A \cdot N_{\text{part}}$ and $dN/dy = A \cdot N_{\text{coll}}$ correspondingly. If indeed ϕ meson yield in heavy ion collisions scales with N_{part} (N_{coll}), then the A values on Fig. (a) (Fig. (b)) for all of the four data sets would be consistent with each other. The red dashed lines show fits with constant functions of the A values for both of the scaling hypotheses, resulting in comparable fit-probabilities and consequently in a conclusion that *the available data do not allow to distinguish between the two scaling laws*. Nota bene: the constant function fits implicitly assume that all of the four sets of experimental data are independent, which is not completely true (for example, all of the STAR and the PHOBOS data share the same values (and so, their evaluation techniques) of N_{part} and N_{coll}, as well as it is reasonable to suppose that both of the STAR data sets were analyzed using similar methods, and so their systematic uncertainties could be correlated). See section 7.6.2 on page 211 for details.

was also assumed that the systematic errors of the N_{part} (as well as of the N_{coll}) values are fully correlated as well. However, since the dN/dy, N_{part}, and N_{coll} values result from three independent sources (dN/dy values are extracted from the yield of ϕ mesons in experimental data, while N_{part} and N_{coll} values result from the HIJING and the Glauber MC simulations respectively as described in section 4.5 on page 79), they were considered to be uncorrelated.

The following procedure was implemented to estimate the systematic uncertainties of the A factors in the $dN/dy = A \cdot N_{\text{part}}$ and the $dN/dy = A \cdot N_{\text{coll}}$ fits of the four available sets of experimental data on ϕ mesons dN/dy at mid-rapidity in heavy ion collisions at $\sqrt{s_{\text{NN}}}$=200 GeV, namely, PHOBOS (this thesis, Cu+Cu, rapidity range $0 \leq y \leq 1$), STAR [233, 252] (Au+Au and Cu+Cu, rapidity range $|y| < 0.5$), and PHENIX [232]

(Au+Au, pseudorapidity range $|\eta| < 0.35$). The procedure was the same for both the $dN/dy = A \cdot N_{\text{part}}$ and the $dN/dy = A \cdot N_{\text{coll}}$ fits and so, for clarity, will be described for the $dN/dy = A \cdot N_{\text{part}}$ fits only. The procedure implementation was analogous to the one described in section 6.5.2 on page 174 with the following differences:

- While in section 6.5.2, the x- and y-variables were ϕ meson transverse momentum and invariant yield correspondingly, in the current implementation, the variables were N_{part} and ϕ meson dN/dy at mid-rapidity respectively.

- In section 6.5.2, there were two fit parameters (T and dN/dy) drawn from ranges $[0.5 \cdot T_{\text{fit}},\ 2 \cdot T_{\text{fit}}]$ and $[0.5 \cdot (dN/dy)_{\text{fit}},\ 2 \cdot (dN/dy)_{\text{fit}}]$ correspondingly. In the current implementation there was only one fit parameter A randomly selected with a uniform distribution from the range $[0.4 \cdot A_{\text{fit}}, 1.6 \cdot A_{\text{fit}}]$, where $A_{\text{fit}} \pm \Delta A_{\text{fit}}^{\text{stat}}$ is the result of a fit of a data set with the function $dN/dy = A \cdot N_{\text{part}}$ using only statistical errors on the dN/dy values (statistical errors on the N_{part} values are negligible).

- The step, analogous to *step three* in section 6.5.2, was omitted in the current implementation.

- To take into account systematic uncertainties on N_{part} (denoted below as $\Delta N_{\text{part}}^{\text{syst}}$), instead of systematic errors on dN/dy (denoted below as $\sigma_{dN/dy}^{\text{syst}}$) the following values were used (bearing in mind independency of dN/dy and N_{part}, see above):

$$\sigma_{\text{tot}} = \sqrt{\left(A_{\text{fit}} \cdot \Delta N_{\text{part}}^{\text{syst}}\right)^2 + \left(\sigma_{dN/dy}^{\text{syst}}\right)^2}.$$

  Just as in section 7.6.1 on page 208, for all of the STAR and the PHOBOS data, the systematic errors on N_{part} (and on N_{coll}) were taken from Ref. [233], which lists the lower and the upper values of the errors. The $\Delta N_{\text{part}}^{\text{syst}}$ values above are the averages of the lower and the upper systematic errors.

An example of a set of histograms $\mathscr{H}_i$ (analogous to the ones described in section 6.5.2.2 on page 176) resulting from the procedure described above is shown on Fig. 7.21(a) on page 212, while Fig. 7.21(b) shows the corresponding distribution $\mathscr{D}_A$ of parameters A. The width of a Gaussian fit of $\mathscr{D}_A$ was assigned as the systematic error $\Delta A_{\text{fit}}^{\text{syst}}$ on the A parameter of the experimental data set, using which $\mathscr{D}_A$ was estimated.

The total uncertainty $\Delta A_{\text{fit}}^{\text{tot}}$ of the parameter A corresponding to a fit of a particular data set was found by adding in quadrature $\Delta A_{\text{fit}}^{\text{stat}}$ and $\Delta A_{\text{fit}}^{\text{syst}}$. Fig. 7.22 on the preceding page shows the values of parameters A and their total uncertainties for both of the scaling hypotheses and for all of the four experimental data sets. As can be seen, just as in case one (see section 7.6.1 on page 208), *the available data do not allow to distinguish between the N_{part} and the N_{coll} scalings of the yield of ϕ mesons in heavy ion collisions at $\sqrt{s_{\text{NN}}}$=200 GeV.*

To understand the degree of validity of the above conclusion, it is useful to think about the big picture of how the result was received and to consider a few possible variations of the analysis method. Parameters A_{fit}, resulting from fits of the data using statistical

Data Set	N_{part}	N_{coll}
PHOBOS Cu+Cu	$7 \cdot 10^{-13}$	0.09
STAR Au+Au	$4 \cdot 10^{-59}$	$1 \cdot 10^{-141}$
STAR Cu+Cu	$4 \cdot 10^{-115}$	$6 \cdot 10^{-26}$
PHENIX Au+Au	0.11	0.005

Table 7.5.: Fit probabilities of the PHOBOS (rapidity range $0 \leq y \leq 1$), STAR [233, 252] (rapidity range $|y| < 0.5$), and PHENIX [232] (pseudorapidity range $|\eta| < 0.35$) data on ϕ meson dN/dy values in Au+Au and Cu+Cu collisions at $\sqrt{s_{NN}}$=200 GeV. The column "N_{part}" corresponds to the fits of the dN/dy versus N_{part} dependencies with the function $dN/dy = A \cdot N_{part}$. The column "N_{coll}" corresponds to the fits of the dN/dy versus N_{coll} dependencies with the function $dN/dy = A \cdot N_{coll}$. All the fits here were done using *statistical errors only* on all of the values. As can be seen, the data does not allow to distinguish between the N_{part} and the N_{coll} scalings of the dN/dy values. See section 7.6.2 on page 211 for details.

errors only, were considered as the true values of the parameters A. To estimate the systematic errors, such distributions of the parameters were found that at each of the data points, the distribution of the values of the "fit" functions was as close as possible to the Gaussian distribution with the mean A_{fit} and the width equal to the full systematic error at the point.

The first evident problem here is that fits of the data using statistical errors only result in most cases in very low fit-probabilities (see Table 7.5) and so do not describe the data well [12]. And so a legitimate question here is "Would the conclusions change if the mean values of parameters A were assigned in a different way, for example, if the values shown in Tables 7.3 and 7.4 on page 211 are used instead (but the errors bars are left the same)?". A test shows that in such case the fit-probabilities listed in the captions of Fig. 7.22(a) and Fig. 7.22(b) would change to 0.025 (χ^2/ndf=9.37/3) and 0.005 (χ^2/ndf=12.6/3) correspondingly.

The second problem is obvious from Fig. 7.21(a) on page 212. As can be seen, the generated distributions of the values of the "fit" functions at some of the data points do not match the targeted Gaussian distributions, except in the middle of the considered N_{part} range. Phenomenologically, it was found that the used method of systematic error estimation is able to produce an almost perfect match between the two distributions at all of the data points if the relative systematic errors of the ordinate are approximately constant as a function of the abscissa (as it was the case during evaluations of the systematic errors on the T and dN/dy parameters, see Fig. 6.23 on page 174, but is not true for the systematic errors of the A parameters, see Fig. 7.23 and Fig. 7.24). That suggests

[12] The by-product conclusion following from a comparison of the fit-probabilities shown in Table 7.5 is that fitting of the data using statistical errors only, again does not allow to distinguish between the N_{part} and the N_{coll} scalings of the yield of ϕ mesons in heavy ion collisions at $\sqrt{s_{NN}}$=200 GeV.

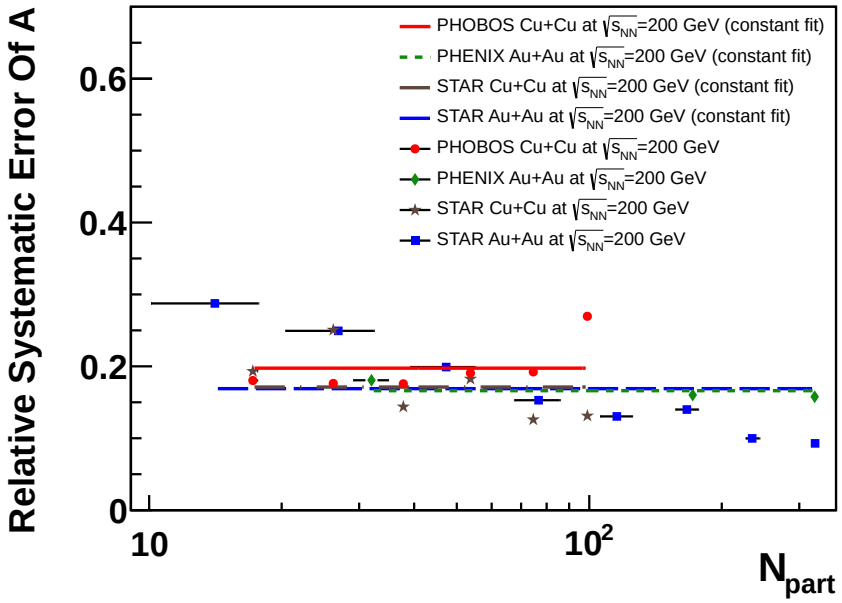

Figure 7.23.: Each point on the figure shows the relative systematic error of the parameter A (in the $dN/dy = A \cdot N_{\text{part}}$ expression) found using the corresponding single data point on dN/dy of ϕ mesons in heavy ion collisions from one of the available data set at $\sqrt{s_{\text{NN}}}$=200 GeV. The lines are constant fits of all of the points within one data set (each point was assigned an equal unity weight in the fits). The fits are estimates of the average relative systematic error of the parameter A. See section 7.6.2 on page 211 for details.

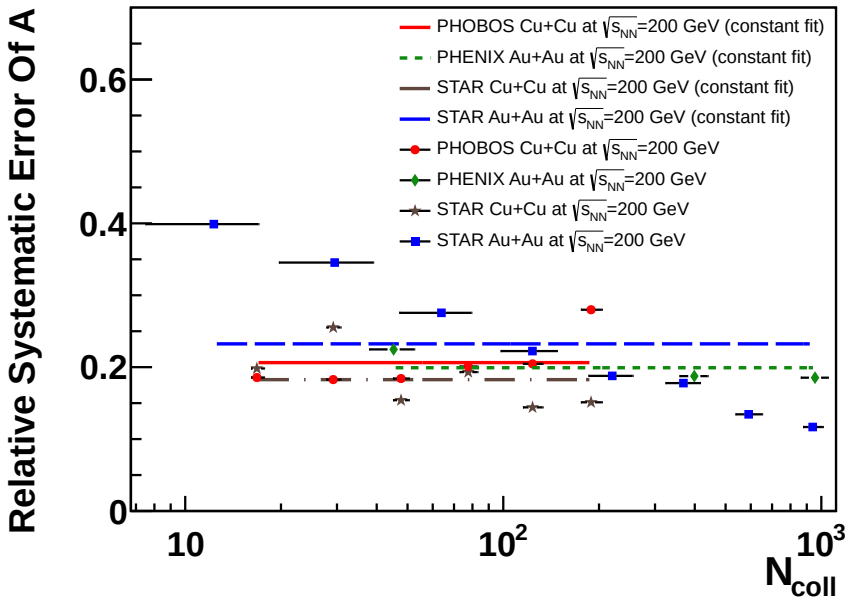

Figure 7.24.: The meaning of the points and the lines are the same for Fig. 7.23 except that parameters A were found using the $dN/dy = A \cdot N_{\text{coll}}$ expression.

that the method should produce similar results as the one in which the uncertainties $\Delta A^{\text{syst}}_{\text{fit}} = A_{\text{fit}} \cdot \langle \delta A^{\text{rel.syst}} \rangle$, where $\langle \delta A^{\text{rel.syst}} \rangle$ is the average relative systematic error of the parameters A found as explained in the captions of Fig. 7.23 and Fig. 7.24. Indeed, the fit-probabilities listed in captions of Fig. 7.22(a) and Fig. 7.22(b) would change to 0.04 (χ^2/ndf=8.14/3) and 0.01 (χ^2/ndf=11.5/3) correspondingly. However, one could also argue that the systematic error of the parameter A is mostly determined by the point with the minimal relative systematic error $\langle \delta A^{\text{rel.syst}}_{\text{min}} \rangle$ on Fig. 7.23 and Fig. 7.24 for each of the available data sets, namely $\Delta A^{\text{syst}}_{\text{fit}} \simeq A_{\text{fit}} \cdot \langle \delta A^{\text{rel.syst}}_{\text{min}} \rangle$. In such analysis, the fit-probabilities listed in captions of Fig. 7.22(a) and Fig. 7.22(b) change to 0.001 (χ^2/ndf=16.1/3) and 0.001 (χ^2/ndf=16.2/3) correspondingly.

Since the rapidity ranges of the PHOBOS ($0 \leq y \leq 1$), STAR ($|y| < 0.5$), and the PHENIX ($|\eta| < 0.35$) results are different, it is valid to question whether their results are directly comparable. However, if the assumptions described in section 5.2.2 on page 95 are correct, then the yield of ϕ mesons in the range $|y| < 0.5$ is expected to be only a factor of ~ 1.027 larger than in $0 \leq y \leq 1$, and so the systematic difference between the PHOBOS and the STAR results is much smaller than the other systematic uncertainties of the measurements, and therefore could be neglected. The *upper limit* on the systematic difference between the PHENIX and the PHOBOS results under the same assumptions is a factor of ~ 1.037, which is also negligible in comparison to other systematic uncertainties of the measurements.

Evidently, none of the above considered modifications to the analysis method produces such a pair of fit-probabilities, corresponding to the N_{part} and the N_{coll} scalings, which would allow one to make a definitive choice between the two hypotheses.

7.6.3. Conclusions

As can be seen from the discussion provided in sections 7.6.1 and 7.6.2, regardless of how systematic errors are interpreted in a comparison of the four available experimental data sets on the dependency of dN/dy of ϕ mesons on centrality in heavy ion collisions at $\sqrt{s_{\text{NN}}}$=200 GeV, it is not possible to make a conclusive statement on whether the yield of ϕ mesons in such collisions scales with the number of participants N_{part} or with the number of collisions N_{coll}. In particular, it means that it is impossible to say whether the majority of ϕ mesons are produced in a decay of equilibrated QGP (since in such case the N_{part} scaling is expected, see section 7.6 on page 205) which, as it was explained in section 1.3 on page 32, is thought to be formed at the highest RHIC collision energy.

7.7. Invariant Yield Of ϕ Mesons With $p_t < 130$ MeV

Studying production and decays of ϕ mesons at very low transverse momentum is especially interesting for the following reasons:

- Since the mesons propagate at low velocity through the medium (either a hadronic gas or a mixed state of a hadronic gas and QGP) after they are produced in heavy

ion collisions, the ϕ mesons spend more time inside the medium and therefore have higher probability to decay in it, thereby making it easier to observe any possible modification of their decay properties (see section 1.4.3 on page 43). Moreover, if the medium lifetime is short and the mean mass of ϕ mesons is modified inside the medium but the decay width is not, then studying very low transverse momentum ϕ mesons provides the only opportunity to detect directly such a modification in an experiment, since the natural mean lifetime of ϕ mesons ($\simeq$ 46.3 fm/c, see section 1.4.2.1 on page 40) is large in comparison to the radius of copper nuclei ($\sim$4.2 fm, see Fig. 7.14 on page 205), and consequently to the typical size of the interaction region of a Cu+Cu nuclear-nuclear collision, and so, unless the velocity of ϕ mesons is very low, only a small fraction of the mesons would decay inside the medium making an experimental measurement of the modification not feasible.

- The strong interaction between individual hadrons has a short range, therefore ϕ mesons could only interact with other hadrons if they are within the range. The time a ϕ meson spends in the vicinity of another hadron and, consequently, the interaction cross-section of the two hadrons are roughly inversely proportional to their relative velocity, and so low transverse momentum ϕ mesons would have higher rate of energy loss in comparison to ϕ mesons with larger transverse momentum. Whether the net result of the energy losses would reveal itself as a suppression or an enhancement of low transverse momentum ϕ mesons depends on the exact rate of the energy losses of ϕ mesons in a medium and the precise shape of their transverse momentum distribution at low p_t values. For example, if the energy loss is high and there are few [13] very low p_t ϕ mesons produced in the primordial interactions, then one would observe an apparent enhancement of the lowest transverse momentum ϕ meson yield since one would essentially detect ϕ mesons which were originally produced with higher p_t but are measured as low p_t particles due to the energy losses. Also, if there are many more primordial ϕ mesons with the lowest p_t values than with the higher ones, and the energy losses of the mesons in the medium are not as high as one would expect, then one would also observe an enhancement of the ϕ meson yield at very low transverse momentum. On the other hand, if there are significantly less very low p_t ϕ mesons than could be expected from an extrapolation of their transverse momentum distribution at higher p_t and their energy losses are very low in the medium, then an apparent effect would be a suppression of the yield of ϕ mesons at the lowest transverse momentum values. Therefore a measurement of the yield of ϕ mesons at very low p_t values provides a constrain on their energy losses in the medium in a non-perturbative regime of QCD as well as on the shape of their transverse momentum distribution.

As a reminder, the particle reconstruction and the data analysis method at the lowest (namely, $p_t < 130$ MeV/c) transverse momentum values of ϕ mesons were some-

[13] i.e. less than at higher p_t

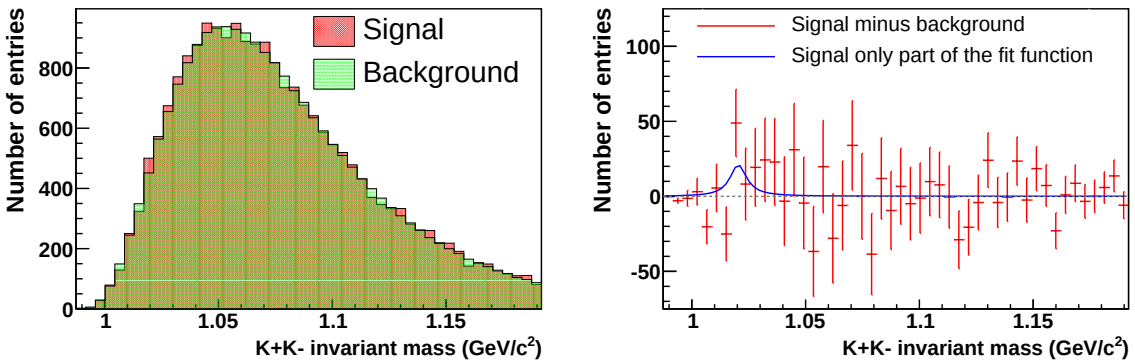

(a) Signal and background

(b) Signal minus background

Figure 7.25.: Background subtraction and ϕ invariant mass peak fitting: Cu+Cu collisions at $\sqrt{s_{NN}}$=200 GeV, 0-60%, both magnet polarities, $p_t < 130$ MeV/c. The same event (red) and the scaled event mixed background (shown in green, overlap of red and green on the figure looks brown) invariant mass distributions resulting from the fit as described in section 6.2 on page 145 are shown on Fig. (a). The same event invariant mass distribution minus the scaled event mixed background (red) and *part 3* of Eq. 6.1 on page 145 fit result (blue) are shown on Fig. (b). The number of phis on the plots is 66.5 ± 56.6. See section 7.7 on page 217 for details.

what different than for $p_t > 390$ MeV/c, as it was pointed out in chapters 5 and 6. The main differences were: 1) the vertex z-coordinates range used for the lowest p_t analysis was $v_z \in [-25,-5]$ cm instead of $v_z \in [-5,15]$ cm which was used in the case of $p_t > 390$ MeV/c, 2) for the lowest p_t data analysis, the Hough tracking part and the joining part of the track reconstruction were additionally directly optimized to reduce the CPU time required [14], 3) in the lowest p_t data analysis, K^+K^- pairs, used in the estimation of (both the signal and the background) invariant mass distributions, were combined from particles reconstructed in different arms of the PHOBOS spectrometer, while such pairs were constructed from particles reconstructed in the same arm in the case of $p_t > 390$ MeV/c, 4) there was no residual background term in the fit of invariant mass distributions in the lowest p_t data analysis, 5) the rapidity range of ϕ meson was $y \in [0.3,1.0]$ in the lowest p_t data analysis versus $y \in [0.0,1.0]$ in the case of $p_t > 390$ MeV/c. As can be seen, the two data analysis techniques were substantially different to make the estimates on the relative systematic errors performed in section 6.5.1 on page 160 not applicable in the case of the measurement of an invariant yield of the lowest p_t ϕ mesons. That and the low raw number [15] of reconstructed ϕ mesons in the

[14] The required reconstruction time per event increases exponentially in the PHOBOS detector geometry as one goes to more and more smaller values of event vertex z-coordinates.

[15] To estimate most of the systematic uncertainties as described in section 6.5.1, one has to split the full data set into subsets and to compare the results on the ϕ meson invariant yield reconstructed using each

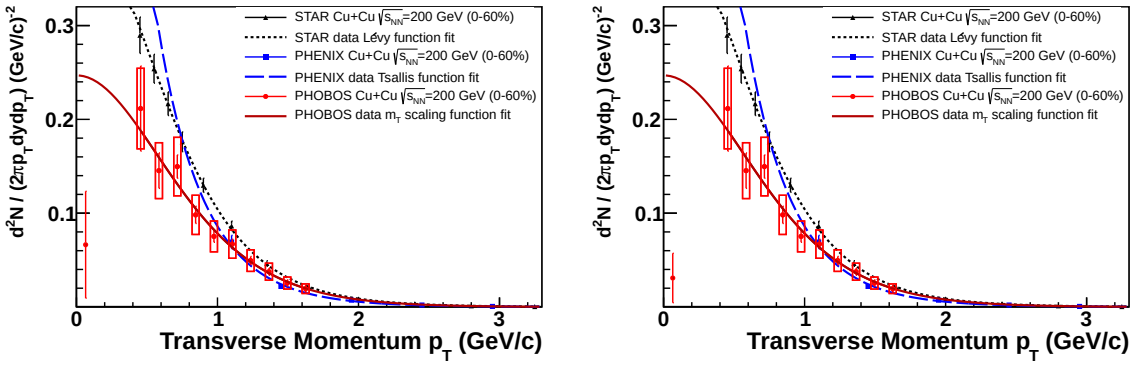

(a) Efficiency and occupancy correction was done using the transverse momentum distribution described in section 5.2.3 on page 95. Invariant yield of ϕ mesons with p_t<130 MeV/c is 0.066 ± 0.057 (GeV/c)$^{-2}$.

(b) Efficiency and occupancy correction was done using a uniform transverse momentum distribution. Invariant yield of ϕ mesons with p_t<130 MeV/c is 0.031 ± 0.026 (GeV/c)$^{-2}$.

Figure 7.26.: Invariant yield of ϕ mesons with p_t<130 MeV/c in Cu+Cu 0-60% collisions at $\sqrt{s_{NN}}$=200 GeV/c in comparison to the PHOBOS results for p_t>390 MeV/c and to the STAR [233] and the PHENIX [253] results. Fig. (a) and Fig. (b) show the results reconstructed (see section 6.3.1 on page 150) using single embedded ϕ mesons MC with a realistic and a uniform transverse momentum distributions correspondingly. The error bars of the p_t<130 MeV/c results show statistical uncertainties only. See section 7.7 on page 217 for details.

lowest p_t case are the reasons why only a lower limit on the systematic uncertainty of the invariant yield of such mesons is provided below.

Results of the reconstruction of the raw number of ϕ mesons with $p_t < 130$ MeV/c in the PHOBOS Cu+Cu $\sqrt{s_{NN}}$=200 GeV 0-60% data are summarized on Fig. 7.25 on the previous page. As can be seen from Fig. 7.25(b), the statistical uncertainties of the bin contents in the same event minus mixed events background invariant mass distribution are too large to be able to distinguish any possible modifications of the ϕ meson decay properties from statistical fluctuations, and so, following the *Occam's razor* principle, in the reconstruction of the invariant yield of ϕ mesons with $p_t < 130$ MeV/c it was assumed that the shape of the $\phi \to K^+K^-$ decay peak (for ϕ mesons produced in Cu+Cu $\sqrt{s_{NN}}$=200 GeV collisions) is the same as in vacuum. Fig. 7.26 shows the invariant yield

of the subsets separately. However, the splitting is unfeasible to do with such a low raw number of reconstructed ϕ mesons as the one in the available data set (see Fig. 7.25 on the preceding page), otherwise the systematic errors estimates would be dominated with statistical uncertainties. And so only systematic uncertainties associated with varying parameters of the MC simulations (used for various corrections applied on the raw number of ϕ mesons) could be reasonably estimated, since large enough number of MC events could be readily simulated. One of such uncertainties is estimated below and the estimate was used to set a lower limit on the overall systematic uncertainty of the measurement.

values found using two different methods of applying the efficiency and occupancy correction on the raw number of ϕ mesons in the data. The two values differ by about a factor of 2.1 (this is equivalent to ∼36% systematic deviation of each of the two values from their average), which is a drastic dissimilarity with the analogous systematic error of 1-7% found for ϕ mesons with $p_t > 390$ MeV/c (see section 6.5.1.4 on page 164). Since the reason for such a big discrepancy was not understood, and even though intuitively the result shown on Fig. 7.26(a) should be closer to the correct one (but only if the shape of the transverse momentum distribution of ϕ mesons at the lowest p_t values could be described with an extrapolation from the higher p_t values), the final estimate on the invariant yield of ϕ mesons with $p_t < 130$ MeV/c was found by averaging the results of the two reconstruction methods (using Eq. 6.7 on page 160, keeping in mind that only the efficiency and occupancy and the momentum resolution corrections are independent between the two averaged results, and explicitly writing down all the corrections):

$$Y = \frac{T \cdot d \cdot (p_1 + p_2)}{N \cdot (\varepsilon_1 + \varepsilon_2) \cdot \Delta y \cdot \Delta p_t \cdot \langle p_t \rangle \cdot \mathrm{Br} \cdot 2\pi}, \tag{7.7}$$

where Y is the average invariant yield, indices 1 and 2 correspond to the two methods of applying the efficiency and occupancy correction, $\Delta y = 0.7$ is the width of the reconstructed rapidity range of ϕ mesons, $\Delta p_t = 0.13$ GeV/c is the selected range of transverse momentum values of ϕ mesons, $\langle p_t \rangle$ is the average transverse momentum of ϕ mesons in the selected range, N is the trigger efficiency weighted number of events in the used data sample, T is the trigger efficiency weighted raw number of reconstructed ϕ mesons, d, p, and ε are the DCM, momentum resolution, and the efficiency and occupancy corrections correspondingly, and Br is the branching ratio of the $\phi \to K^+K^-$ decay in vacuum. Using Eq. 7.7 to estimate the average invariant yield and the statistical uncertainty on it and using the systematic error estimation method described in section 6.5.1 on page 160, one gets the following result on the invariant yield of ϕ mesons with $p_t < 130$ MeV/c in Cu+Cu $\sqrt{s_{\mathrm{NN}}}$=200 GeV 0-60% collisions (also shown on Fig. 7.27):

$$0.043 \pm 0.036\ (\mathrm{stat}) \pm 0.022\ (\mathrm{syst})\ (\mathrm{GeV/c})^{-2},$$

where the last number has to be regarded as a *lower limit* on the systematic error of the measurement because only one source of systematic uncertainties was considered. Since a full analysis of the systematic uncertainties was not performed for the above result, it is not possible to make any conclusions based on it, except that it seems to be an interesting measurement to be repeated on a larger data sample. *If the result is confirmed*, it would mean a strong (by about a factor of ∼6 in comparison to an extrapolation to $p_t = 0$ of the PHOBOS results at $p_t > 390$ MeV/c) suppression of the yield of ϕ mesons at the lowest transverse momentum values.

Some evidence was acquired that the results presented above could be confirmed to be correct:

- The reconstruction algorithm is capable of finding the lowest p_t ϕ mesons since such mesons are successfully reconstructed in real data events with single MC ϕ meson embedded into them.

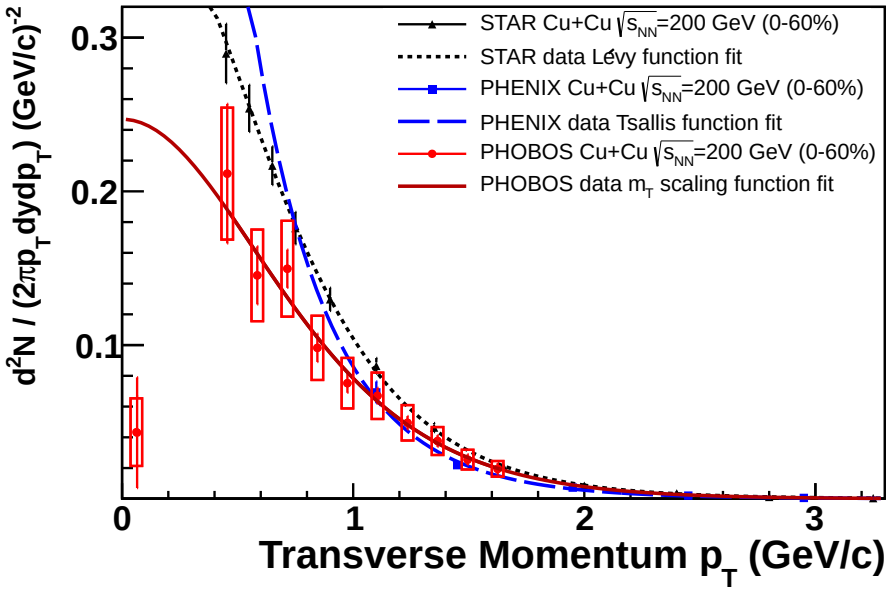

Figure 7.27.: Invariant yield of ϕ mesons with p_t<130 MeV/c in Cu+Cu 0-60% collisions at $\sqrt{s_{NN}}$=200 GeV/c in comparison to the PHOBOS results for p_t>390 MeV/c and to the STAR [233] and the PHENIX [253] results. The vertical size of the box around the p_t<130 MeV/c data point indicates the *lower limit* on the systematic uncertainty of the measurement. See section 7.7 on page 217 for details.

- In was tested on realistic toy MC events (described in section 6.2.2 on page 147), that the event mixing and background subtraction algorithm outputs raw numbers of ϕ mesons compatible within statistical uncertainties with input raw numbers of ϕ mesons at the same levels of background as in the real data events. The range of the input raw numbers of lowest p_t ϕ mesons tested was from 0 to about 400 (the later number corresponds to the expected raw number of such ϕ mesons in the PHOBOS data based on an extrapolation to $p_t = 0$ of the PHOBOS results at $p_t > 390$ MeV/c).

However, the evidence can not be considered exhaustive.

7.8. Energy Dependence Of ϕ Meson dN/dy

As it was pointed out in section 1.4 on page 35, production of strange quarks and, as a result, of ϕ mesons is expected to be enhanced in heavy ion collisions if QCD matter produced in such collisions goes through the QGP phase at some stage of its evolution. Unfortunately, the theoretical predictions are not specific about what variable should be used as a measure of the enhancement. But, it is clear, that any comparison should be done between the collision conditions in which QGP is expected to be formed and

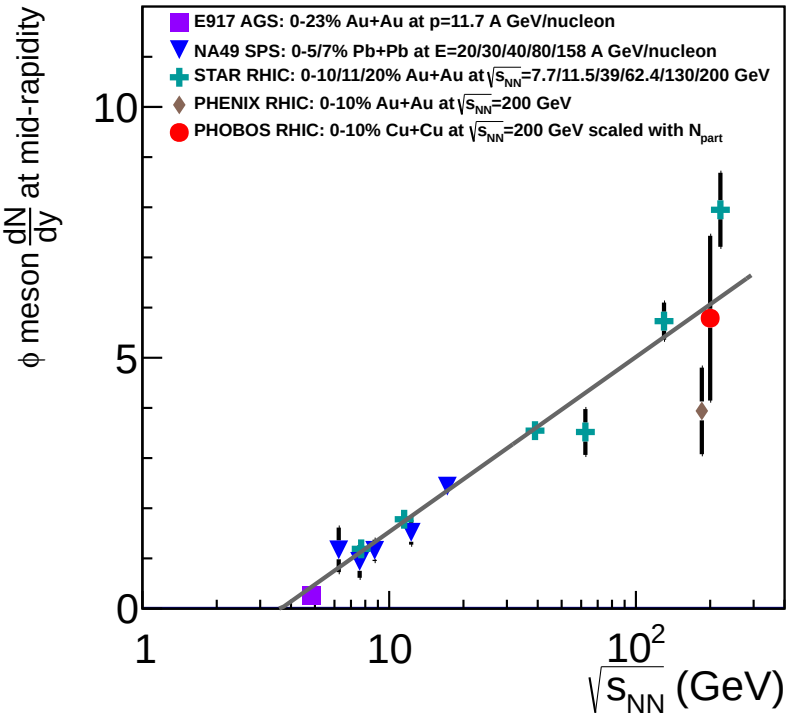

Figure 7.28.: Dependence of dN/dy of ϕ mesons on $\sqrt{s_{\mathrm{NN}}}$ in collisions of nuclei with atomic mass $A \approx 200$. The PHOBOS Cu+Cu results were scaled with the ratio of N_{part} values in 0-10% Au+Au and 0-10% Cu+Cu collision at $\sqrt{s_{\mathrm{NN}}}$=200 GeV. The data were taken from Ref. [151, 231, 232, 234, 264, 265]. Statistical and systematic errors were added in quadrature for all of the points except those from Ref. [151, 265]. The errors on the data points from Ref. [265] are statistical only. The data from E917, PHOBOS, and Ref. [265] are preliminary. The gray line shows the fit of the dependence with the function $dN/dy = a \cdot \ln \sqrt{s_{\mathrm{NN}}} + b$, where $\sqrt{s_{\mathrm{NN}}}$ is in units of GeV. The fit parameters resulting from the fit are $a = 3.03 \pm 0.09$ and $b = -1.96 \pm 0.12$, χ^2/ndf=12.0/10, fit-probably=0.28. The STAR and the PHENIX data points at $\sqrt{s_{\mathrm{NN}}}$=200 GeV were not used in the fit. See section 7.8 on the preceding page for details.

those in which matter is believed to stay in the hadronic gas state. Out of all of the heavy ion collision parameters, which can be controlled (or measured) experimentally, the center of mass energy of nucleon-nucleon collisions $\sqrt{s_{\mathrm{NN}}}$ is the one which allows to probe the widest ranges of temperature and energy density of the matter produced in the collisions. Therefore, it is logical to search for an evidence of an enhanced ϕ meson production as a function of $\sqrt{s_{\mathrm{NN}}}$. It is of a particular interest to try to identify a value or a region of $\sqrt{s_{\mathrm{NN}}}$, in which the mechanism of ϕ meson production changes, as an indication of QGP formation.

Since it is believed that QGP is not formed in collisions of individual hadrons, one

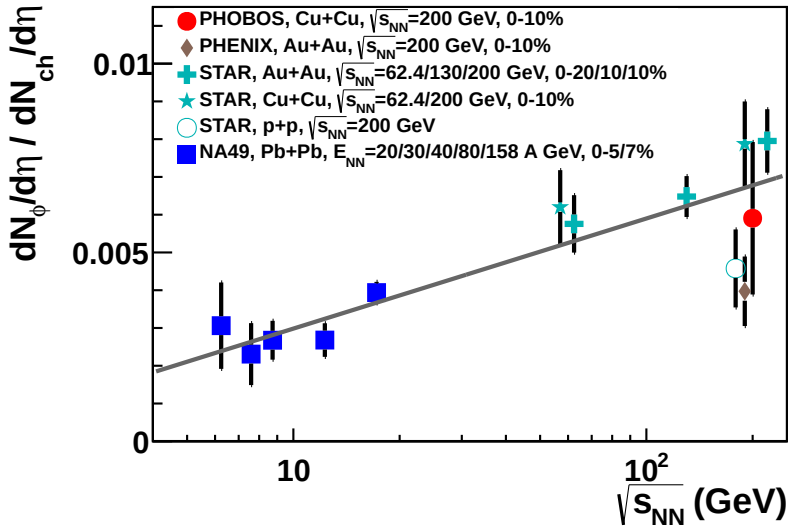

Figure 7.29.: Dependence of the ratio of $dN/d\eta$ of ϕ mesons ($dN_\phi/d\eta$) to $dN/d\eta$ of all charged particles ($dN_{\rm ch}/d\eta$) on $\sqrt{s_{\rm NN}}$ for all of the available data on ϕ meson production in heavy ion collisions [132, 231–234, 252, 264] (except those from E859 [150] and E917 [151]). The gray line shows the fit of the dependence with the function $dN/dy = a \cdot \ln\sqrt{s_{\rm NN}} + b$, where $\sqrt{s_{\rm NN}}$ is in units of GeV. The fit parameters resulting from the fit are $a = 0.00130 \pm 0.00015$ and $b = 0.0000 \pm 0.0005$ (χ^2/ndf=18.6/10, fit-probably=0.05). The pp data point at $\sqrt{s_{\rm NN}}$=200 GeV was added for comparison and was not used in the fit. The STAR Cu+Cu data point at $\sqrt{s_{\rm NN}}$=62.4 GeV as well as all the data points at $\sqrt{s_{\rm NN}}$=200 GeV (except the one from PHOBOS) were shifted somewhat along the horizontal axis for visibility. See section 7.8.2 on page 228 for details of how the positions and the uncertainties of the points were estimated.

possible way of measuring the enhancement of ϕ meson production is to study the dependence of the relative yield of ϕ mesons in collisions of nuclei of a fixed mass and at a fixed collision centrality with respect to the yield of ϕ mesons in pp or $p\bar{p}$ collisions. The problem with this approach is that measurements of the yield of ϕ mesons in pp collisions only exist at three energies $\sqrt{s_{\rm NN}}$=17.2 GeV (158 A GeV, NA49), 62.4 GeV (STAR), and 200 GeV (PHENIX, STAR), which precludes the possibility of making any conclusion using the approach about an enhancement of ϕ meson production or QGP formation. If it was known how the yield of ϕ mesons scales with centrality (which is not the case, see section 7.6 on page 205), then instead of using a pp reference, one could use the scaling to extrapolate the yield of ϕ mesons to the most peripheral collisions, which are effectively just collisions of individual nucleons, and thereby measure an enhancement of ϕ meson production. Two implicit problems with the later approach are:

- measurements of ϕ meson production at low nuclear collision energies only exist for central collisions, but any scaling law proved to be correct at much higher

collision energies (let us say at $\sqrt{s_{\rm NN}}$=200 GeV, where QGP formation is expected) is not necessarily correct at very low collision energies (where no QGP formation is believed to occur),

- even at higher collision energies, measurements of ϕ meson production exist only for collision centralities ranging from central to mid-peripheral [16], and so any scaling law determined using such measurements would not necessarily accurately predict the yield of ϕ mesons in the most peripheral collisions.

Another possible way of quantifying an enhancement of ϕ meson production is to measure the $\sqrt{s_{\rm NN}}$ dependence of the ratio of the yield of ϕ mesons to the yield of all charged particles in central nucleus-nucleus collisions. The ratio has to increase with $\sqrt{s_{\rm NN}}$ if the enhancement actually takes place, otherwise, it is the overall yield of particles, which is enhanced in heavy ion collisions, and not the one of ϕ mesons. The advantages of the approach are:

- it allows to compare experimental results on ϕ meson production for almost all of the available data (except those from E859 and E917 since it is not clear if the collaborations had any measurements done, from which one could derive the multiplicities of all charged particles),

- it allows for a comparison of collisions of nuclei with different mass (if an enhancement of ϕ meson production is indeed solely due to formation of QGP, and not due to some geometrical effect, then the enhancement should be consistent for all large enough nuclei).

Note that, since according to the Landau's hydrodynamical model [279], multiplicity of hadrons at mid-rapidity is a measure of the entropy of the system created in a heavy ion collision, this way of quantifying an enhancement of ϕ meson production effectively studies as a function of $\sqrt{s_{\rm NN}}$ a variable which is proportional to the fraction of the total system entropy which is due to ϕ mesons. One would expect that if indeed strangeness and particularly ϕ meson production are enhanced if QGP is formed at some stage of evolution of the system, then at lower energies (where no QGP formation occurs), the ratio would be either a constant or a smoothly increasing function of $\sqrt{s_{\rm NN}}$, then the slope of the dependence would increase significantly in some region of $\sqrt{s_{\rm NN}}$ which corresponds to at least partial transition of the system into QGP, and then the ratio would be again either a constant or a more slowly increasing function of $\sqrt{s_{\rm NN}}$. Fig. 7.29 on the preceding page shows the ratio of $\frac{dN_\phi/d\eta}{dN_{\rm ch}/d\eta}$ at mid-rapidity as a function of $\sqrt{s_{\rm NN}}$ as measured by the NA49, PHENIX, PHOBOS, and STAR collaborations. As can be seen, ϕ meson production is indeed enhanced at higher $\sqrt{s_{\rm NN}}$ values, however there is no evidence of any special interval of $\sqrt{s_{\rm NN}}$ in which ϕ meson production grows differently (faster) as a function of $\sqrt{s_{\rm NN}}$ than anywhere else. Rather, the ratio $\frac{dN_\phi/d\eta}{dN_{\rm ch}/d\eta}$ at mid-rapidity is a smooth increasing function of $\sqrt{s_{\rm NN}}$. The same conclusion can be drawn from studying

[16] The reason is that the experimental collision triggers of heavy ion experiments are designed to detect events with high particle multiplicities and so are not fully efficient for the very peripheral collisions.

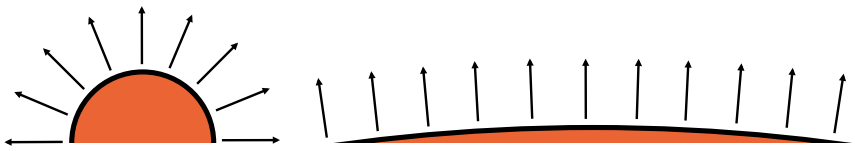

Figure 7.30.: A schematic representation of disintegration of QGP (the shaded orange circular regions, shown only partially on the figure) formed in two central heavy ion collisions: with lower $\sqrt{s_{\mathrm{NN}}}$ (on the left) and with higher $\sqrt{s_{\mathrm{NN}}}$ (on the right) values. The view for both collisions is in the transverse plane. See section 7.8.1 for details.

the dN/dy values of ϕ mesons as a function of $\sqrt{s_{\mathrm{NN}}}$ in collisions of $A \approx 200$ nuclei directly (see Fig. 7.28 on page 223) [17]. Therefore, one has to make a deduction that there is no indication in the available experimental data of any identifiable transition (of the QCD matter created in heavy ion collisions) which could be revealed as a sudden enhancement of ϕ meson production. In particular, it means that even if QGP is created in heavy ion collisions, its formation does lead to a rapid increase in the number of produced ϕ mesons. It is important to point out, that the above study only probes for the sought-for kind of transitions in the range of $\sqrt{s_{\mathrm{NN}}}$ values, in which experimental data on ϕ meson production exist, and so an existence of such a transition in the ranges of temperature and energy density corresponding to $\sqrt{s_{\mathrm{NN}}}$<4.9 GeV or to $\sqrt{s_{\mathrm{NN}}}$>200 GeV is not excluded. In addition, one could consider the possibility that ϕ mesons are produced copiously (i.e. more copiously than in a hadronic gas) relative to other hadrons in a decay of QGP, but the scattering interactions in the subsequent hadronic gas state quickly reestablish the relative ϕ mesons abundance characteristic for the state, effectively masking the signal from QGP, however in such case, quantitative reasoning and model calculations suggest that the fractional abundance of ϕ mesons among all of the produced particles would decrease as a function of $\sqrt{s_{\mathrm{NN}}}$ above the transition region (see section 7.8.1), which is not what is observed in data.

As a final note, a comparison of the measured dN/dy values of ϕ mesons to the naive extrapolation of the pre-RHIC data to $\sqrt{s_{\mathrm{NN}}}$=200 GeV (see Fig. 1.6(b) on page 36) shows that the measured yield turned out to be about an order of magnitude lower than the extrapolated one.

7.8.1. Chemical Equilibration of Hadronic Gas

The goal of this section is to discuss how likely it is that the observed fractional abundance of ϕ mesons is fully determined at the hadronic gas stage of evolution of matter

[17] The later figure does not contain any data on Cu+Cu collisions but allows to add for a comparison the preliminary Au+Au data from STAR at $\sqrt{s_{\mathrm{NN}}}$=7.7, 11.5, and 39 GeV [265]. The preliminary data necessary to estimate the $dN_{\mathrm{ch}}/d\eta$ and thereby add points corresponding to the energies to Fig. 7.29 on page 224 already exit [287], however no reply was received from the author of the talk on a request to provide the data files.

produced in heavy ion collisions, assuming that 1) the energy of the collisions is sufficient to produce QGP, and 2) that the fractional abundance of ϕ mesons in a fully equilibrated hadronic gas is lower than immediately after QGP hadronization.

Fig. 7.30 on the facing page shows a schematic representation of disintegration of QGP in two central heavy ion collisions corresponding to two different $\sqrt{s_{\rm NN}}$ values. The higher $\sqrt{s_{\rm NN}}$ value corresponds to a higher initial energy density ε of QGP, and so also to a larger system size at the moment of hadronization. It is easy to see why the later statement is correct: 1) since thermalization of partons happens very quickly (∼0.25-0.6 fm/c, see section 1.3.1 on page 32) in heavy ion collisions of high enough energy, the initial radius of an equilibrated QGP (almost) does not depend on $\sqrt{s_{\rm NN}}$ and for central collisions is equal to the radius R_o of the collided nuclei, 2) the relevant for the discussion energy density corresponds to the thermal motion of partons in the transverse plane (let us denote as ε_1 and ε_2 the energy densities corresponding to the two collision energies, where $\varepsilon_1 < \varepsilon_2$), 3) hadronization of QGP happens at some particular energy density ε_c, corresponding to the critical temperature T_c (see sections 1.2.4.1 and 1.2.8), 4) then the radii (in the transverse plane) R_{c1} and R_{c2}, corresponding to the initial energy densities ε_1 and ε_2 respectively, of produced in the heavy ion collisions QGP at the moment of hadronization can be found from (assuming that, during the QGP stage of evolution, the sum ΔE of the following two net transfers of energy is a non-decreasing function of $\sqrt{s_{\rm NN}}$: a) from the longitudinal to the transverse degrees of freedom, b) from the collective expansion to the thermal motion of partons): $\varepsilon_c \pi R_{c1}^2 = \varepsilon_1 \pi R_o^2 + \Delta E_1$ and $\varepsilon_c \pi R_{c2}^2 = \varepsilon_2 \pi R_o^2 + \Delta E_2$, where $\Delta E_1 < \Delta E_2$ are the total net energy transfers into the thermal transverse degrees of freedom for the two considered collision energies, 5) and so, as can be seen, $R_{c1} < R_{c2}$.

Larger system size at the moment of hadronization means that hadrons are emitted at that time at smaller angles with respect to each other, and so would scatter with each other more before the density and the temperature of the hadronic gas drop below the chemical freeze-out conditions. The later statement can also be considered from a purely geometrical point of view, namely, the relative increase during time dt of the area S of the hadronic gas in the transverse plane would be smaller at a given collective expansion velocity v if the system radius R at the moment of hadronization is larger, which can be seen from $S = \pi R^2$, and so $dS = 2\pi R \cdot dR = 2\pi R v \cdot dt$, and therefore $dS/S = 2(v/R) \cdot dt$. Since the energy densities ε_c and $\varepsilon_{\rm ch}$ at the moment of hadronization and at the moment of chemical freeze-out respectively are the same, regardless of the collision energy, a smaller relative increase of the area means a smaller relative decrease in the energy density, and consequently the hadronic gas phase would exist longer at a larger $\sqrt{s_{\rm NN}}$ value [18]. The same result is achieved within the **V**iscous **I**srael-**S**tewart

[18] The caveat in this reasoning that v is not a fixed value and might depend on $\sqrt{s_{\rm NN}}$, and so, as can be seen from the formula $dS/S = 2(v/R) \cdot dt$, depending on whether v grows faster or slower than R, dS/S can both increase and decrease as a function of $\sqrt{s_{\rm NN}}$. However, while R can assume any value, the magnitude of v is limited to c due to the special relativity constrains, and consequently, while the drawn conclusions are certainly correct at large enough $\sqrt{s_{\rm NN}}$ values, one can not say conclusively from the provided simplified considerations whether the conclusions are correct in the range 6 GeV$<\sqrt{s_{\rm NN}}<$200 GeV (see Fig. 7.29 on page 224). Effectively, it is assumed in this thesis that the ratio v/R is a decreasing function of $\sqrt{s_{\rm NN}}$.

Hydrodynamics a**N**d **U**rQMD (VISHNU) model [288], which also predicts that the lifetime of the hadronic gas phase is an increasing function of $\sqrt{s_{\rm NN}}$ [289]. The longer lifetime suggests that more scatterings between constituent hadrons would occur before the gas reaches chemical freeze-out conditions, and therefore at higher $\sqrt{s_{\rm NN}}$ values, the hadronic gas (during its evolution) is expected to shift further from the chemical equilibrium at temperature T_c [289], and so would have relative abundance of ϕ mesons closer to chemically equilibrated at some temperature $T < T_c$ hadronic gas, which has (by the assumption stated in the beginning of this section) smaller fractional density of ϕ mesons than such density immediately after the QGP disintegration. In summary, it means that the observed fractional density of ϕ mesons is expected to decrease as a function of $\sqrt{s_{\rm NN}}$ if the chemical composition of the observed particles was dominated by the scatterings in the hadronic gas state, which is opposite to what is observed in data (see Fig. 7.29 on page 224), and so the fractional density of ϕ mesons should be determined either mostly at the time of QGP decay (if it is formed) or by the primordial scatterings of partons in a heavy ion collision.

7.8.2. Details For Fig. 7.29 on page 224

Since the publications on ϕ meson production list dN/dy values at mid-rapidity, while the publications on charged particle multiplicities list $dN/d\eta$ values at mid-rapidity, to find the ratio of the yield of ϕ mesons to the yield of charged particles at mid-rapidity, it was necessary to convert the dN/dy values into $dN/d\eta$ values. The same conversion was needed to estimate the charged particle multiplicities at the SPS energies, which were found as sums of $dN/d\eta$ values of π^+, π^-, K^+, K^-, p, and $\bar{p}$, which in turn were found from the corresponding dN/dy values. The $dN/d\eta$ values of charged particles at mid-rapidity at all of the RHIC energies were taken from Ref. [132] (the $dN/d\eta$ values in the publication were weighted properly to find the charged particle multiplicity at mid-rapidity in the same centrality range as the corresponding dN/dy value of ϕ mesons).

To convert a dN/dy value into a $dN/d\eta$ value for a particular measurement, the following procedure was followed:

1. If the T value derived from a fit of the invariant yield data using Eq. 1.2 on page 23 was available from the respective publication, then the value was used and the total uncertainty σ_T on the value was found by adding the statistical and the systematic errors on T in quadrature. If such T value was not available, then the invariant yield data was refitted either using statistical and systematic errors on the yield added in quadrature, or using just statistical errors (depending on what kind of data tables could be found on the web-page corresponding to the publication). In the later case, σ_T was assigned to be equal to the uncertainty on T resulting from the fit.

2. The total uncertainty $\sigma_{dN/dy}$ of the dN/dy value was found by adding its statistical and systematic errors in quadrature.

3. The conversion of the dN/dy value into a $dN/d\eta$ value was done using a MC method. 100 different conversion *attempts* were performed. In each attempt, a random pair of values T_i and $(dN/dy)_i$ was selected from the Gaussian distributions with the parameters (T, σ_T) and $(dN/dy, \sigma_{dN/dy})$ respectively, where the first number is the mean and the second one is the width. Then 10^5 different values of rapidity y were randomly selected from a uniform distribution (it was shown that the shape of the rapidity distribution only effects the final result negligibly). Also 10^5 values of p_t were randomly generated using the distribution in Eq. 5.1 on page 95 with $T = T_i$. Each of the 10^5 pairs (y, p_t) was used to find a corresponding value of pseudorapidity η. Histograms of the y and η values were filled and the ratio R_i of the two histograms at $y = 0$ was found.

4. Each of the $(dN/dy)_i$ values was multiplied by R_i to find the corresponding $(dN/d\eta)_i$ value. The mean and the RMS of the 100 $(dN/d\eta)_i$ values were used as estimates on the $dN/d\eta$ value and on its uncertainty respectively.

As can be seen from the method description, the error bars on the figure are somewhat underestimated, which is not a problem since even the found uncertainties are enough to make the conclusions drawn from the figure (see section 7.8 on page 222) and full analysis of the errors would not change these conclusions.

8. Summary

A measurement of the invariant yield of ϕ mesons in Cu+Cu collisions at $\sqrt{s_{\mathrm{NN}}}$=200 GeV was performed using the PHOBOS detector at RHIC through the $\phi \rightarrow K^+K^-$ decay channel. The measurement was done as a function of transverse momentum in the range 0.39 GeV/c $< p_t <$ 1.69 GeV/c and for several collision centralities. All the measured invariant yields were averaged over the rapidity interval $0 < y < 1$. To make the measurement, it was necessary to develop a new tracking algorithm, specifically designed to reconstruct charged kaons with high efficiency in a high hit density environment.

The obtained invariant yields were fitted using the function describing the m_T-scaling distribution to extract from them as a function of centrality 1) the integrated over all the transverse momentum values yield of ϕ mesons per event at mid-rapidity, 2) the average p_t of the ϕ mesons, and 3) the inverse slope parameter T of the distribution.

The results from PHOBOS were compared to the respective measurements performed by the STAR and the PHENIX collaborations and were shown to be in agreement with both within the estimated measurement uncertainties.

An analysis of the line shape of the ϕ meson invariant mass distribution performed for various transverse momentum and centrality ranges found no evidence of any modification neither of the mean nor of the width of the distribution, suggesting that either $\phi \rightarrow K^+K^-$ decay properties are not modified in a hot hadronic gas medium or that the properties are modified but the average lifetime of the gas state produced in Cu+Cu collisions at $\sqrt{s_{\mathrm{NN}}}$=200 GeV is much shorter than the ϕ meson decay time in the medium, which results in only a small fraction of ϕ mesons decaying inside the gas and makes the detection of the corresponding in-medium modifications not feasible within the estimated experimental uncertainties.

The dependence of the yield of ϕ mesons on centrality was studies for all of the available data on ϕ mesons production in heavy ion collisions at $\sqrt{s_{\mathrm{NN}}}$=200 GeV. The goal was to shed some light on the production mechanism of the mesons in such collisions. The results show that no matter how systematic uncertainties of the measurements are interpreted, it is not possible to make a conclusive statement on whether the yield of ϕ mesons in the collisions scales with the number of participants N_{part} or with the number of collisions N_{coll}, which in turn means that the two considered mechanisms of ϕ meson production, namely via a hadronization of QGP or directly in primordial hard scattering of partons of the collided nuclei, are not distinguishable within the estimated measurement uncertainties.

Employing the ideas of L. Van Hove [263], an attempt was made to find an evidence of such a transition of QCD matter produced in heavy ion collisions, which could be as-

sociated with a latent heat or with a change in the number of degrees of freedom of the constituent particles of the matter. The study was done for the centrality dependence of the inverse slope parameter T and of the $\langle p_t \rangle$ dependence on dN/dy of ϕ mesons using PHOBOS results only, as well as for the $\sqrt{s_{\mathrm{NN}}}$ dependencies of the T parameter on $\sqrt{s_{\mathrm{NN}}}$ for various hadron species. An existence of a plateau in any of the dependencies could serve as an indication of a sought-for type of transition, however no evidence of such a plateau was found. Nevertheless, the T versus $\sqrt{s_{\mathrm{NN}}}$ dependencies show signs that the mechanism of particle production changes for temperatures and energy densities corresponding to collision energies $\sqrt{s_{\mathrm{NN}}} \simeq$4-9 GeV. An interesting observation was made, that the T versus $\sqrt{s_{\mathrm{NN}}}$ dependence of ϕ mesons either has a local maximum at $\sqrt{s_{\mathrm{NN}}} \approx$20 GeV or that the NA49 measurement of the T parameter at the highest SPS energy has an unaccounted for systematic error. The situation can be clarified using the data from the RHIC beam energy scan program at $\sqrt{s_{\mathrm{NN}}}$=19.6 GeV and at $\sqrt{s_{\mathrm{NN}}}$=27 GeV taken in 2011.

The invariant yield of ϕ mesons was also measured for transverse momentum values $p_t < 130$ MeV/c in 0-60% Cu+Cu collisions at $\sqrt{s_{\mathrm{NN}}}$=200 GeV, showing an indication of a suppression by about a factor of $\sim$6 in comparison to an extrapolation to $p_t = 0$ of the PHOBOS results at $p_t > 390$ MeV/c, however, since a full analysis of the systematic errors was not performed for the measurement, the results cannot be considered conclusive.

The dependence of the yield of ϕ mesons on $\sqrt{s_{\mathrm{NN}}}$ was studied both separately and with respect to the charged particle multiplicity at mid-rapidity. The goal was to find any evidence of a transition of the QCD matter created in heavy ion collisions which could be associated with a strong and sudden enhancement of ϕ meson production. No such evidence was observed. The data suggest however, that if the relative abundance of produced ϕ mesons is higher immediately after an hadronization of QGP than in a fully equilibrated hadronic gas, then the observed relative multiplicity of ϕ mesons cannot be determined by the strong interaction scatterings in a hadronic gas formed in a QGP decay.

A. PHOBOS ϕ Meson Invariant Yield Data Tables

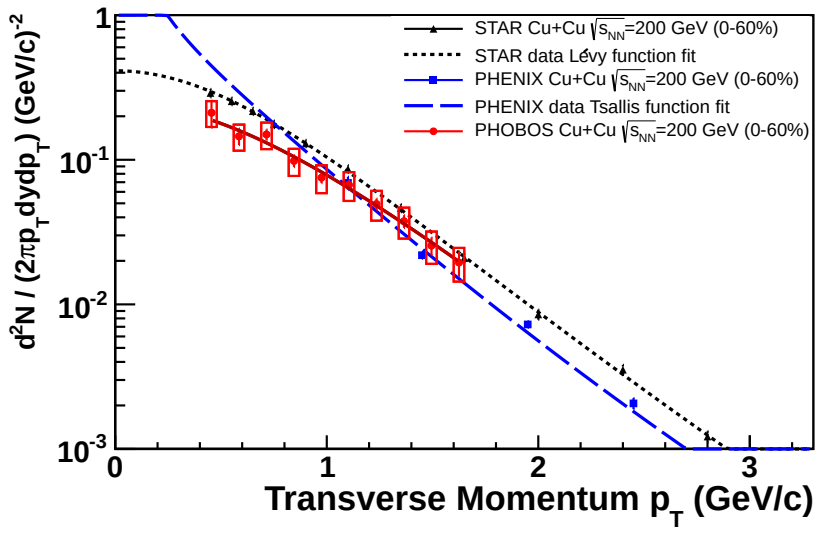

Figure A.1.: ϕ meson invariant yield in 0-60% Cu+Cu collisions at $\sqrt{s_{NN}}$=200 GeV as measured using the PHOBOS detector at RHIC.

p_t (GeV/c)	$\frac{1}{2\pi p_t}\frac{d^2N}{dp_t dy}$ ((GeV/c)$^{-2}$)	Statistical Error ((GeV/c)$^{-2}$)	Systematic Error ((GeV/c)$^{-2}$)
0.455	0.2115	0.0454	0.0429
0.585	0.1453	0.0189	0.0298
0.715	0.1497	0.0124	0.0312
0.845	0.0982	0.0092	0.0209
0.975	0.0752	0.0062	0.0164
1.105	0.0670	0.0052	0.0151
1.235	0.0494	0.0044	0.0115
1.365	0.0376	0.0038	0.0091
1.495	0.0255	0.0035	0.0064
1.625	0.0195	0.0038	0.0051

Table A.1.: ϕ meson invariant yield in 0-60% Cu+Cu collisions at $\sqrt{s_{NN}}$=200 GeV as measured using the PHOBOS detector at RHIC.

A. PHOBOS ϕ Meson Invariant Yield Data Tables

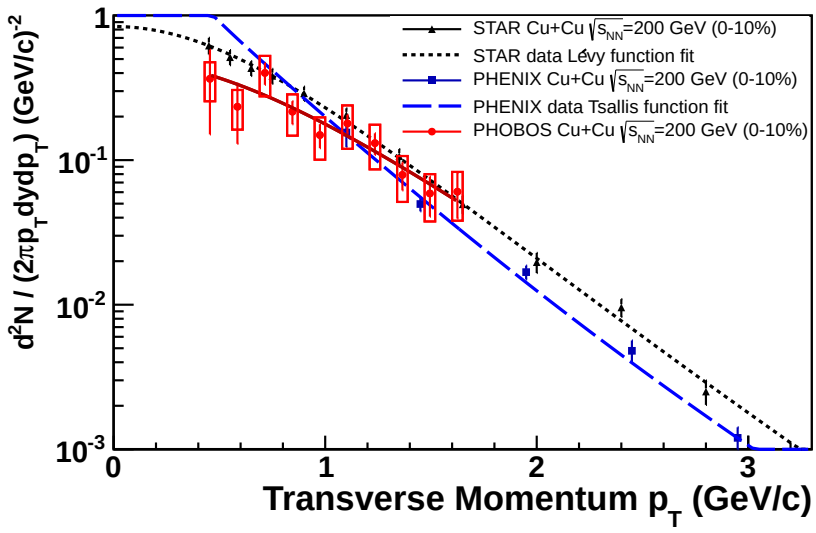

Figure A.2.: ϕ meson invariant yield in 0-10% Cu+Cu collisions at $\sqrt{s_{NN}}$=200 GeV as measured using the PHOBOS detector at RHIC.

p_t (GeV/c)	$\frac{1}{2\pi p_t}\frac{d^2N}{dp_t dy}$ ((GeV/c)$^{-2}$)	Statistical Error ((GeV/c)$^{-2}$)	Systematic Error ((GeV/c)$^{-2}$)
0.455	0.3652	0.2146	0.1100
0.585	0.2340	0.1043	0.0716
0.715	0.4009	0.0690	0.1248
0.845	0.2163	0.0393	0.0687
0.975	0.1491	0.0282	0.0484
1.105	0.1794	0.0264	0.0597
1.235	0.1310	0.0223	0.0447
1.365	0.0791	0.0173	0.0277
1.495	0.0588	0.0182	0.0212
1.625	0.0605	0.0211	0.0224

Table A.2.: ϕ meson invariant yield in 0-10% Cu+Cu collisions at $\sqrt{s_{NN}}$=200 GeV as measured using the PHOBOS detector at RHIC.

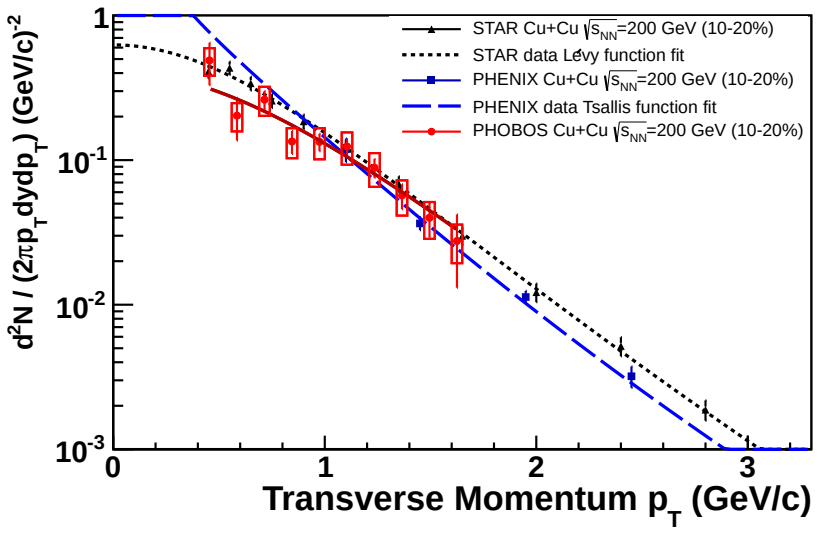

Figure A.3.: ϕ meson invariant yield in 10-20% Cu+Cu collisions at $\sqrt{s_{NN}}$=200 GeV as measured using the PHOBOS detector at RHIC.

p_t (GeV/c)	$\frac{1}{2\pi p_t}\frac{d^2N}{dp_t dy}$ ((GeV/c)$^{-2}$)	Statistical Error ((GeV/c)$^{-2}$)	Systematic Error ((GeV/c)$^{-2}$)
0.455	0.4889	0.1596	0.1059
0.585	0.2029	0.0663	0.0449
0.715	0.2619	0.0384	0.0595
0.845	0.1346	0.0243	0.0316
0.975	0.1338	0.0186	0.0325
1.105	0.1242	0.0153	0.0313
1.235	0.0886	0.0132	0.0232
1.365	0.0569	0.0111	0.0156
1.495	0.0399	0.0107	0.0114
1.625	0.0276	0.0145	0.0082

Table A.3.: ϕ meson invariant yield in 10-20% Cu+Cu collisions at $\sqrt{s_{NN}}$=200 GeV as measured using the PHOBOS detector at RHIC.

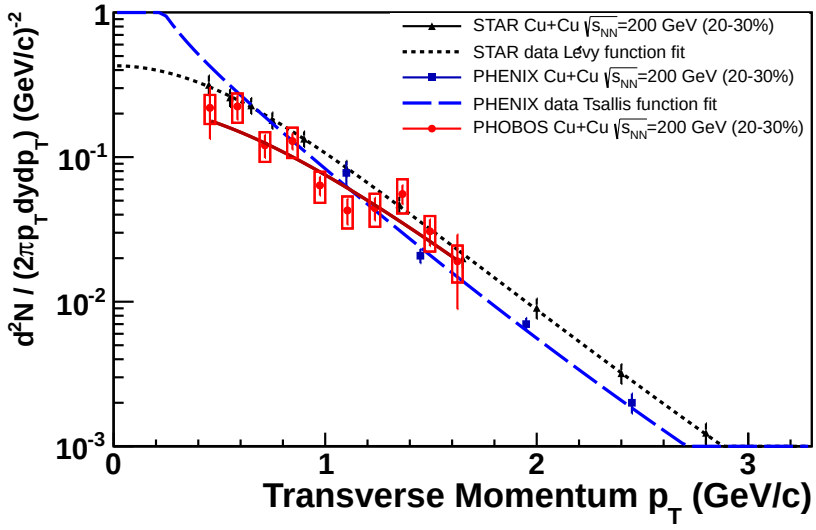

Figure A.4.: ϕ meson invariant yield in 20-30% Cu+Cu collisions at $\sqrt{s_{NN}}$=200 GeV as measured using the PHOBOS detector at RHIC.

p_t (GeV/c)	$\frac{1}{2\pi p_t}\frac{d^2N}{dp_t dy}$ ((GeV/c)$^{-2}$)	Statistical Error ((GeV/c)$^{-2}$)	Systematic Error ((GeV/c)$^{-2}$)
0.455	0.2193	0.0859	0.0498
0.585	0.2241	0.0429	0.0514
0.715	0.1207	0.0220	0.0281
0.845	0.1292	0.0165	0.0306
0.975	0.0637	0.0096	0.0155
1.105	0.0428	0.0087	0.0107
1.235	0.0444	0.0080	0.0114
1.365	0.0555	0.0084	0.0148
1.495	0.0307	0.0064	0.0085
1.625	0.0190	0.0101	0.0054

Table A.4.: ϕ meson invariant yield in 20-30% Cu+Cu collisions at $\sqrt{s_{NN}}$=200 GeV as measured using the PHOBOS detector at RHIC.

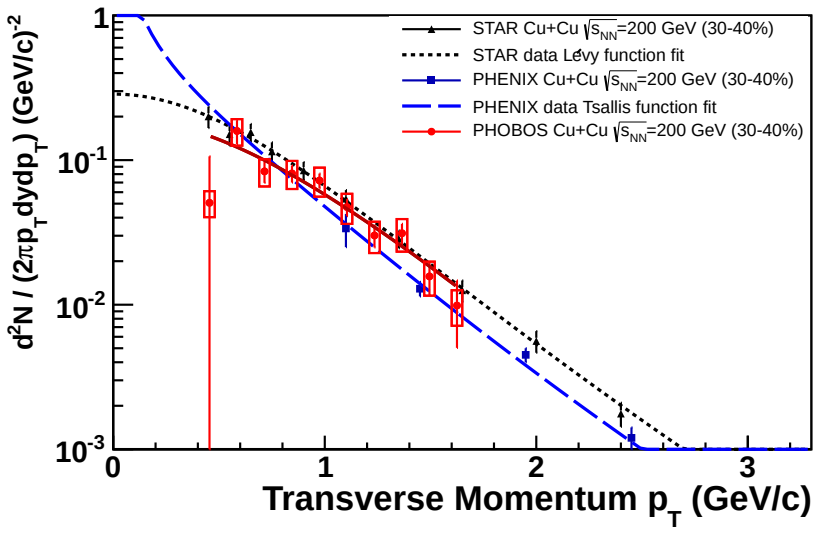

Figure A.5.: ϕ meson invariant yield in 30-40% Cu+Cu collisions at $\sqrt{s_{NN}}$=200 GeV as measured using the PHOBOS detector at RHIC.

p_t (GeV/c)	$\frac{1}{2\pi p_t}\frac{d^2N}{dp_t dy}$ ((GeV/c)$^{-2}$)	Statistical Error ((GeV/c)$^{-2}$)	Systematic Error ((GeV/c)$^{-2}$)
0.455	0.0507	0.0556	0.0103
0.585	0.1590	0.0298	0.0331
0.715	0.0836	0.0140	0.0179
0.845	0.0809	0.0109	0.0178
0.975	0.0723	0.0085	0.0164
1.105	0.0473	0.0064	0.0111
1.235	0.0301	0.0052	0.0074
1.365	0.0312	0.0051	0.0079
1.495	0.0157	0.0041	0.0042
1.625	0.0099	0.0048	0.0027

Table A.5.: ϕ meson invariant yield in 30-40% Cu+Cu collisions at $\sqrt{s_{NN}}$=200 GeV as measured using the PHOBOS detector at RHIC.

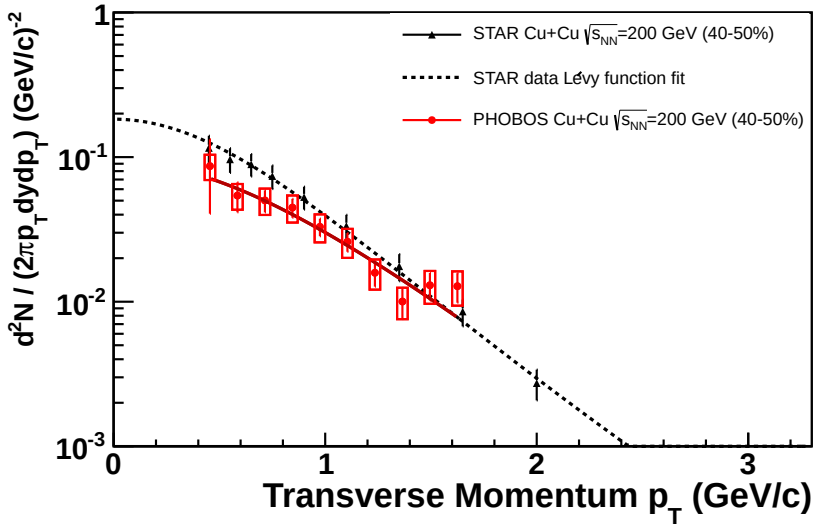

Figure A.6.: ϕ meson invariant yield in 40-50% Cu+Cu collisions at $\sqrt{s_{NN}}$=200 GeV as measured using the PHOBOS detector at RHIC.

p_t (GeV/c)	$\frac{1}{2\pi p_t}\frac{d^2N}{dp_t dy}$ ((GeV/c)$^{-2}$)	Statistical Error ((GeV/c)$^{-2}$)	Systematic Error ((GeV/c)$^{-2}$)
0.455	0.0866	0.0460	0.0172
0.585	0.0542	0.0127	0.0110
0.715	0.0502	0.0087	0.0104
0.845	0.0448	0.0067	0.0095
0.975	0.0330	0.0046	0.0072
1.105	0.0260	0.0038	0.0059
1.235	0.0159	0.0031	0.0037
1.365	0.0100	0.0024	0.0025
1.495	0.0130	0.0028	0.0033
1.625	0.0128	0.0030	0.0034

Table A.6.: ϕ meson invariant yield in 40-50% Cu+Cu collisions at $\sqrt{s_{NN}}$=200 GeV as measured using the PHOBOS detector at RHIC.

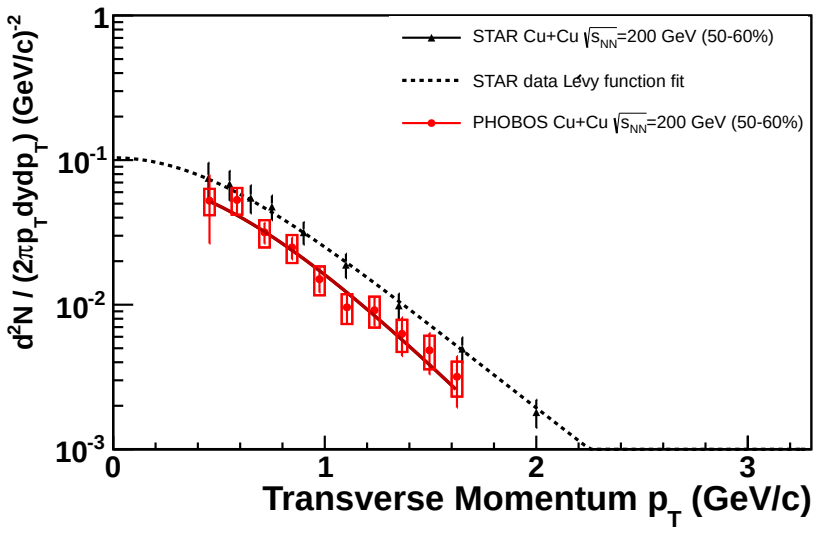

Figure A.7.: ϕ meson invariant yield in 50-60% Cu+Cu collisions at $\sqrt{s_{NN}}$=200 GeV as measured using the PHOBOS detector at RHIC.

p_t (GeV/c)	$\frac{1}{2\pi p_t}\frac{d^2N}{dp_t dy}$ ((GeV/c)$^{-2}$)	Statistical Error ((GeV/c)$^{-2}$)	Systematic Error ((GeV/c)$^{-2}$)
0.455	0.0524	0.0260	0.0108
0.585	0.0530	0.0102	0.0111
0.715	0.0317	0.0052	0.0068
0.845	0.0249	0.0043	0.0055
0.975	0.0150	0.0029	0.0034
1.105	0.0096	0.0022	0.0022
1.235	0.0092	0.0020	0.0022
1.365	0.0063	0.0019	0.0016
1.495	0.0048	0.0015	0.0013
1.625	0.0032	0.0012	0.0009

Table A.7.: ϕ meson invariant yield in 50-60% Cu+Cu collisions at $\sqrt{s_{NN}}$=200 GeV as measured using the PHOBOS detector at RHIC.

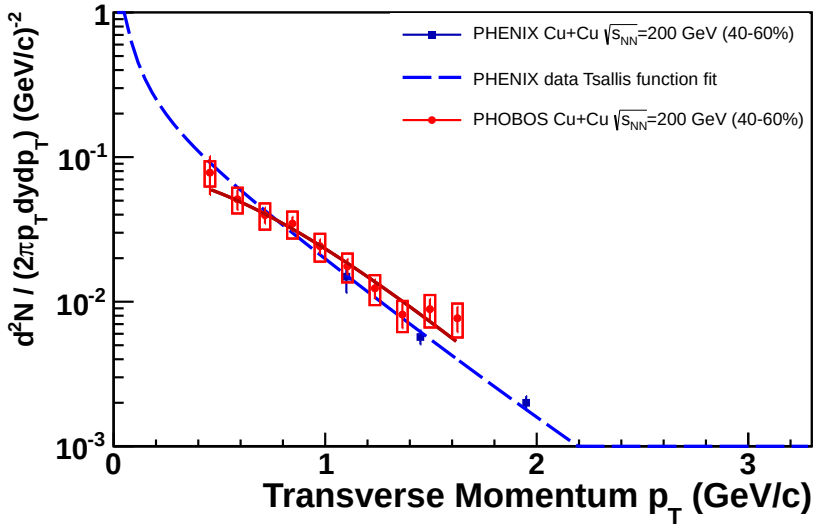

Figure A.8.: ϕ meson invariant yield in 40-60% Cu+Cu collisions at $\sqrt{s_{NN}}$=200 GeV as measured using the PHOBOS detector at RHIC.

p_t (GeV/c)	$\frac{1}{2\pi p_t}\frac{d^2N}{dp_t dy}$ ((GeV/c)$^{-2}$)	Statistical Error ((GeV/c)$^{-2}$)	Systematic Error ((GeV/c)$^{-2}$)
0.455	0.0781	0.0234	0.0155
0.585	0.0511	0.0081	0.0103
0.715	0.0397	0.0050	0.0082
0.845	0.0347	0.0040	0.0073
0.975	0.0242	0.0028	0.0053
1.105	0.0176	0.0022	0.0040
1.235	0.0124	0.0019	0.0029
1.365	0.0081	0.0016	0.0020
1.495	0.0089	0.0016	0.0022
1.625	0.0077	0.0015	0.0020

Table A.8.: ϕ meson invariant yield in 40-60% Cu+Cu collisions at $\sqrt{s_{NN}}$=200 GeV as measured using the PHOBOS detector at RHIC.

B. List of Acronyms

Facilities:

BNL Brookhaven National Laboratory (http://www.bnl.gov/)

RHIC Relativistic Heavy Ion Collider (http://www.bnl.gov/RHIC/)

STAR Solenoidal Tracker At RHIC (http://www.star.bnl.gov/)

PHENIX **P**ioneering **H**igh **E**nergy **N**uclear **I**nteraction e**X**periment (http://www.phenix.bnl.gov/)

BRAHMS **B**road **RA**nge **H**adron **M**agnetic **S**pectrometers (http://www4.rcf.bnl.gov/brahms/WWW/)

TPC Time Projection Chamber

STAR TPC Time Projection Chamber (STAR) [290]

LHC Large Hadron Collider (http://lhc.web.cern.ch/lhc/)

ATLAS A Toroidal LHC ApparatuS (http://atlas.ch/)

RACF RHIC and ATLAS Computing Facility (https://www.racf.bnl.gov/)

SLAC Stanford Linear Accelerator Center (http://www.slac.stanford.edu/)

CERN European Organization for Nuclear Research – *Conseil Européen pour la Recherche Nucléaire* (http://public.web.cern.ch/public/)

FermiLab Fermi National Accelerator Laboratory (http://www.fnal.gov/)

FAIR Facility for Antiproton and Ion Research (http://www.gsi.de/portrait/fair_e.html)

NICA **N**uclotron-based **I**on **C**ollider f**A**cility (http://nica.jinr.ru/)

SPS Super Proton Synchrotron (http://ab-dep-op-sps.web.cern.ch/ab-dep-op-sps/)

AGS Alternating Gradient Synchrotron (http://www.bnl.gov/bnlweb/facilities/AGS.asp)

JINR Joint Institute For Nuclear Research (http://www.jinr.ru/)

GSI **G**esellschaft für **S**chwer**i**onenforschung (http://www.gsi.de/)

Physics:

QCD **Q**uantum **C**hromo**d**ynamics

QGP Quark Gluon Plasma

MIP Minimum Ionizing Particle

CMB Cosmic Microwave Background

QED **Q**uantum **E**lectro**D**ynamics

CSC **C**olor **S**uper**C**onductor

CFL Color-Flavor Locked

LO Leading Order

NJL Nambu-Jona-Lasinio

PNJL Nambu-Jona-Lasinio with Polyakov loops

HBT Hanbury-Brown-Twiss

OZI Okubo-Zweig-Iizuka

QFT Quantum Field Theory

SHM Statistical Hadronization Model

VISHNU **V**iscous **I**srael-**S**tewart **H**ydrodynamics a**N**d **U**rQMD

Mathematics:

FWHM Full Width at Half Maximum

RMS Root Mean Square

PDF Probability Density Function

Computing:

RAM Random Access Memory

CPU Central Processing Unit

PIP Parallel Information Processing

LSF Load Sharing Facility

Monte Carlo Simulations:

MC Monte Carlo

HIJING Heavy Ion Jet Interaction Generator [227]
(http://www-nsdth.lbl.gov/ xnwang/hijing/)

GEANT GEANT - Detector Description and Simulation Tool
(http://wwwasd.web.cern.ch/wwwasd/geant/)

Detectors:

ZDC Zero-Degree Calorimeter

PMT **P**hoto**m**ultiplier **T**ube

T0 Time Zero Detector

ADC Analog-to-Digital Converter

Other:

DCM Dead Channel Map

DAQ Data Acquisition

ONO Oxide-Nitride-Oxide

CMN Common Mode Noise

OctProbMultVertex Octagon Probability Multiplicity Vertex

Bibliography

[1] Isaac Newton. *Principia*. 1687.

[2] Karl Schwarzschild. On the gravitational field of a mass point according to Einstein's theory. *Sitzungsber. Preuss. Akad. Wiss. Berlin (Math. Phys.)*, 1916:189–196, 1916.

[3] Karl Schwarzschild. On the gravitational field of a sphere of incompressible fluid according to Einstein's theory. *Sitzungsber. Preuss. Akad. Wiss. Berlin (Math. Phys.)*, 1916:424–434, 1916.

[4] Albert Einstein. The foundation of the general theory of relativity. *Annalen Phys.*, 49:769–822, 1916. doi: 10.1002/andp.200590044.

[5] J. Clerk Maxwell. A dynamical theory of the electromagnetic field. *Phil. Trans. Roy. Soc. Lond.*, 155:459–512, 1865.

[6] Paul A. M. Dirac. Quantum theory of emission and absorption of radiation. *Proc. Roy. Soc. Lond.*, A114:243, 1927.

[7] Enrico Fermi. Quantum theory of radiation. *Rev. Mod. Phys.*, 4(1):87, Jan 1932. doi: 10.1103/RevModPhys.4.87.

[8] H. A. Bethe. The electromagnetic shift of energy levels. *Phys. Rev.*, 72(4):339–341, Aug 1947. doi: 10.1103/PhysRev.72.339.

[9] S. Tomonaga. On a relativistically invariant formulation of the quantum theory of wave fields. *Prog. Theor. Phys.*, 1:27–42, 1946.

[10] Julian Schwinger. On quantum-electrodynamics and the magnetic moment of the electron. *Phys. Rev.*, 73(4):416–417, Feb 1948. doi: 10.1103/PhysRev.73.416.

[11] Julian Schwinger. Quantum electrodynamics. i. a covariant formulation. *Phys. Rev.*, 74(10):1439–1461, Nov 1948. doi: 10.1103/PhysRev.74.1439.

[12] R. P. Feynman. The theory of positrons. *Phys. Rev.*, 76(6):749–759, Sep 1949. doi: 10.1103/PhysRev.76.749.

[13] R. P. Feynman. Space-time approach to quantum electrodynamics. *Phys. Rev.*, 76 (6):769–789, Sep 1949. doi: 10.1103/PhysRev.76.769.

[14] R. P. Feynman. Mathematical formulation of the quantum theory of electromagnetic interaction. *Phys. Rev.*, 80(3):440–457, Nov 1950. doi: 10.1103/PhysRev.80.440.

[15] F. J. Dyson. The radiation theories of tomonaga, schwinger, and feynman. *Phys. Rev.*, 75(3):486–502, Feb 1949. doi: 10.1103/PhysRev.75.486.

[16] F. J. Dyson. The *s* matrix in quantum electrodynamics. *Phys. Rev.*, 75(11):1736–1755, Jun 1949. doi: 10.1103/PhysRev.75.1736.

[17] H. A. Bethe. Energy production in stars. *Phys. Rev.*, 55(1):103, Jan 1939. doi: 10.1103/PhysRev.55.103.

[18] H. A. Bethe. Energy production in stars. *Phys. Rev.*, 55(5):434–456, Mar 1939. doi: 10.1103/PhysRev.55.434.

[19] E. Fermi. An attempt of a theory of beta radiation. 1. *Z. Phys.*, 88:161–177, 1934. doi: 10.1007/BF01351864.

[20] S. L. Glashow. Partial Symmetries of Weak Interactions. *Nucl. Phys.*, 22:579–588, 1961. doi: 10.1016/0029-5582(61)90469-2.

[21] A. Salam. *8th Nobel Symposium on Elementary Particle Physics: Relativistic Groups and Analyticity*, page 367pp, 1968.

[22] Steven Weinberg. A model of leptons. *Phys. Rev. Lett.*, 19(21):1264–1266, Nov 1967. doi: 10.1103/PhysRevLett.19.1264.

[23] Gerard 't Hooft. Renormalization of Massless Yang-Mills Fields. *Nucl. Phys.*, B33:173–199, 1971. doi: 10.1016/0550-3213(71)90395-6.

[24] Gerard 't Hooft. Renormalizable Lagrangians for Massive Yang-Mills Fields. *Nucl. Phys.*, B35:167–188, 1971. doi: 10.1016/0550-3213(71)90139-8.

[25] J. Chadwick. Possible Existence of a Neutron. *Nature*, 129:312–+, February 1932. doi: 10.1038/129312a0.

[26] W. Heisenberg. Über den bau der atomkerne. i. *Zeitschrift für Physik A Hadrons and Nuclei*, 77:1–11, 1932. ISSN 0939-7922. URL http://dx.doi.org/10.1007/BF01342433. 10.1007/BF01342433.

[27] E. Wigner. On the consequences of the symmetry of the nuclear hamiltonian on the spectroscopy of nuclei. *Phys. Rev.*, 51(2):106–119, Jan 1937. doi: 10.1103/PhysRev.51.106.

[28] G. D. Rochester and C. C. Butler. Evidence for the existence of new unstable elementary particles. *Nature*, 160:855–857, 1947.

[29] A. Pais. Some Remarks on the V-Particles. *Phys. Rev.*, 86:663–672, 1952. doi: 10.1103/PhysRev.86.663.

[30] T. Nakano and K. Nishijima. Charge Independence for V-particles. *Prog. Theor. Phys.*, 10:581–582, 1953. doi: 10.1143/PTP.10.581.

[31] Kazuhiko Nishijima. Charge independence theory of v particles. *Progress of Theoretical Physics*, 13(3):285–304, 1955. doi: 10.1143/PTP.13.285. URL http://ptp.ipap.jp/link?PTP/13/285/.

[32] M. Gell-Mann. The interpretation of the new particles as displaced charge multiplets. *Il Nuovo Cimento (1955-1965)*, 4:848–866, 1956. URL http://dx.doi.org/10.1007/BF02748000. 10.1007/BF02748000.

[33] Marcel Froissart. First meson octet, December 18, 2007. URL http://upload.wikimedia.org/wikipedia/commons/e/e0/Meson-octet.svg. Created for Wikipedia by retired french physicist, Marcel Froissart, born in Paris on Dec. 20, 1934.

[34] Marcel Froissart. First baryon decuplet (smaller), December 18, 2007. URL http://upload.wikimedia.org/wikipedia/commons/5/53/Baryon-decuplet.svg. Created for Wikipedia by retired french physicist, Marcel Froissart, born in Paris on Dec. 20, 1934.

[35] Marcel Froissart. First baryon octet, December 19, 2007. URL http://upload.wikimedia.org/wikipedia/commons/e/ea/Baryon-octet.svg. Created for Wikipedia by retired french physicist, Marcel Froissart, born in Paris on Dec. 20, 1934.

[36] Murray Gell-Mann and Yuval Neemam. The eightfold way: a review with a collection of reprints. page 317, Sep 1964.

[37] V. E. Barnes et al. Observation of a hyperon with strangeness minus three. *Phys. Rev. Lett.*, 12(8):204–206, Feb 1964. doi: 10.1103/PhysRevLett.12.204.

[38] Murray Gell-Mann. A Schematic Model of Baryons and Mesons. *Phys. Lett.*, 8: 214–215, 1964. doi: 10.1016/S0031-9163(64)92001-3.

[39] G. Zweig. An SU(3) model for strong interaction symmetry and its breaking. pages 22–101, 1980. Published in 'Developments in the Quark Theory of Hadrons'. Volume 1. Edited by D. Lichtenberg and S. Rosen. CERN paper reports: CERN-TH-401 (17 Jan 1964, 24p.), CERN-TH-412 (21 Feb 1964, 74pp.), NP-14146.

[40] M. Fierz and W. Pauli. On relativistic wave equations for particles of arbitrary spin in an electromagnetic field. *Proc. Roy. Soc. Lond.*, A173:211–232, 1939.

[41] W. Pauli. The Connection Between Spin and Statistics. *Phys. Rev.*, 58:716–722, 1940. doi: 10.1103/PhysRev.58.716.

[42] Julian Schwinger. The theory of quantized fields. i. *Phys. Rev.*, 82(6):914–927, Jun 1951. doi: 10.1103/PhysRev.82.914.

[43] Julian Schwinger. The theory of quantized fields. ii. *Phys. Rev.*, 91(3):713–728, Aug 1953. doi: 10.1103/PhysRev.91.713.

[44] O. W. Greenberg. Spin and unitary-spin independence in a paraquark model of baryons and mesons. *Phys. Rev. Lett.*, 13(20):598–602, Nov 1964. doi: 10.1103/PhysRevLett.13.598.

[45] Yoichiro Nambu. Dynamical symmetries & fundamental fields. Proceedings of the Second Coral Gables Conference on Symmetry Principles at High Energy, Freeman, San Francisco. p133.

[46] Yoichiro Nambu. *Systematics of hadrons in subnuclear physics*. North-Holland, Amsterdam, 1966. In *Preludes in Theoretical Physics: In Honor of V. F. Weisskopf*, Edited by A. de Shalit, H. Feshback, and L. van Hove.

[47] M. Y. Han and Y. Nambu. Three-triplet model with double $su(3)$ symmetry. *Phys. Rev.*, 139(4B):B1006–B1010, Aug 1965. doi: 10.1103/PhysRev.139.B1006.

[48] J. D. Bjorken. Asymptotic sum rules at infinite momentum. *Phys. Rev.*, 179(5): 1547–1553, Mar 1969. doi: 10.1103/PhysRev.179.1547.

[49] C. G. Callan and David J. Gross. High-energy electroproduction and the constitution of the electric current. *Phys. Rev. Lett.*, 22(4):156–159, Jan 1969. doi: 10.1103/PhysRevLett.22.156.

[50] E. D. Bloom, D. H. Coward, H. DeStaebler, J. Drees, G. Miller, L. W. Mo, R. E. Taylor, M. Breidenbach, J. I. Friedman, G. C. Hartmann, and H. W. Kendall. High-energy inelastic $e-p$ scattering at 6° and 10°. *Phys. Rev. Lett.*, 23(16):930–934, Oct 1969. doi: 10.1103/PhysRevLett.23.930.

[51] M. Breidenbach, J. I. Friedman, H. W. Kendall, E. D. Bloom, D. H. Coward, H. DeStaebler, J. Drees, L. W. Mo, and R. E. Taylor. Observed behavior of highly inelastic electron-proton scattering. *Phys. Rev. Lett.*, 23(16):935–939, Oct 1969. doi: 10.1103/PhysRevLett.23.935.

[52] J. Litt, G. Buschhorn, D. H. Coward, H. Destaebler, L. W. Mo, R. E. Taylor, B. C. Barish, S. C. Loken, J. Pine, J. I. Friedman, G. C. Hartmann, and H. W. Kendall. Measurement of the ratio of the proton form factors, ge/gm, at high momentum transfers and the question of scaling. *Physics Letters B*, 31 (1):40 – 44, 1970. ISSN 0370-2693. doi: DOI:10.1016/0370-2693(70)90015-8. URL `http://www.sciencedirect.com/science/article/pii/0370269370900158`.

[53] G. Miller et al. Inelastic electron-proton scattering at large momentum transfers and the inelastic structure functions of the proton. *Phys. Rev. D*, 5(3):528–544, Feb 1972. doi: 10.1103/PhysRevD.5.528.

[54] Donald Perkins for the Gargamelle collaboration. In *Proc. XVI International Conference on High Energy Physics*, Chicago, 1972. Vol. 4, p. 189.

[55] H. Deden et al. Experimental study of structure functions and sum rules in charge-changing interactions of neutrinos and antineutrinos on nucleons. *Nuclear Physics B*, 85(2):269 – 288, 1975. ISSN 0550-3213. doi: DOI:10.1016/0550-3213(75)90008-5. URL http://www.sciencedirect.com/science/article/pii/0550321375900085.

[56] F. Ceradini et al. Multihadron production in e+ e- collisions up to 3 gev total center-of-mass energy. *Phys. Lett.*, B47:80–84, 1973. doi: 10.1016/0370-2693(73)90574-1.

[57] C. Bacci et al. Multihadronic cross-sections from e+ e- annihilation up to 3 gev center-of-mass energy. *Phys. Lett.*, B44:533–536, 1973. doi: 10.1016/0370-2693(73)90016-6.

[58] B. Bartoli et al. Electron-positron interactions at high energies. *Phys. Rev.*, D6:2374–2404, 1972. doi: 10.1103/PhysRevD.6.2374.

[59] M. Bernardini et al. The Energy Dependence of Sigma (e+ e- → Hadrons) in the Total Center-Of-Mass Energy Range 1.2-GeV to 3.0-GeV. *Phys. Lett.*, B51:200, 1974. doi: 10.1016/0370-2693(74)90215-9.

[60] G. Cosme et al. Hadronic production by e+ e- collisions at the energy 990 mev with the orsay storage ring. *Phys. Lett.*, B40:685–688, 1972. doi: 10.1016/0370-2693(72)90626-0.

[61] L. M. Kurdadze, A. P. Onuchin, S. I. Serednyakov, V. A. Sidorov, and S. I. Eidelman. Observation of multihadronic events in e+ e- collisions at the energy of 1.18-1.34 gev. *Phys. Lett.*, B42:515–518, 1972. doi: 10.1016/0370-2693(72)90120-7.

[62] David J. Gross and Frank Wilczek. Ultraviolet behavior of non-abelian gauge theories. *Phys. Rev. Lett.*, 30(26):1343–1346, Jun 1973. doi: 10.1103/PhysRevLett.30.1343.

[63] H. David Politzer. Reliable perturbative results for strong interactions? *Phys. Rev. Lett.*, 30(26):1346–1349, Jun 1973. doi: 10.1103/PhysRevLett.30.1346.

[64] S. Bethke. Experimental tests of asymptotic freedom. *Progress in Particle and Nuclear Physics*, 58(2):351 – 386, 2007. ISSN 0146-6410. doi: DOI:10.1016/j.ppnp.2006.06.001. URL http://www.sciencedirect.com/science/article/pii/S0146641006000615. arXiv:hep-ex/0606035v2.

[65] H. Fritzsch and M. Gell-Mann. In *Proc. XVI International Conference on High Energy Physics*, Chicago-Batavia, 1972. Vol. 2, p. 135.

[66] H. Fritzsch, Murray Gell-Mann, and H. Leutwyler. Advantages of the Color Octet Gluon Picture. *Phys. Lett.*, B47:365–368, 1973. doi: 10.1016/0370-2693(73)90625-4.

[67] J. J. Aubert et al. Experimental observation of a heavy particle j. *Phys. Rev. Lett.*, 33(23):1404–1406, Dec 1974. doi: 10.1103/PhysRevLett.33.1404.

[68] J. E. Augustin et al. Discovery of a narrow resonance in $e+e-$ annihilation. *Phys. Rev. Lett.*, 33(23):1406–1408, Dec 1974. doi: 10.1103/PhysRevLett.33.1406.

[69] G. S. Abrams et al. Discovery of a second narrow resonance in $e+e-$ annihilation. *Phys. Rev. Lett.*, 33(24):1453–1455, Dec 1974. doi: 10.1103/PhysRevLett.33.1453.

[70] G. Hanson et al. Evidence for jet structure in hadron production by $e+e-$ annihilation. *Phys. Rev. Lett.*, 35(24):1609–1612, Dec 1975. doi: 10.1103/PhysRevLett.35.1609.

[71] S. W. Herb et al. Observation of a dimuon resonance at 9.5 gev in 400-gev proton-nucleus collisions. *Phys. Rev. Lett.*, 39(5):252–255, Aug 1977. doi: 10.1103/PhysRevLett.39.252.

[72] F. Abe et al. Observation of top quark production in $p\bar{p}$ collisions with the collider detector at fermilab. *Phys. Rev. Lett.*, 74(14):2626–2631, Apr 1995. doi: 10.1103/PhysRevLett.74.2626.

[73] S. Abachi et al. Observation of the top quark. *Phys. Rev. Lett.*, 74(14):2632–2637, Apr 1995. doi: 10.1103/PhysRevLett.74.2632.

[74] R. Brandelik et al. Evidence for Planar Events in e+ e- Annihilation at High- Energies. *Phys. Lett.*, B86:243, 1979. doi: 10.1016/0370-2693(79)90830-X. TASSO Collaboration. DESY 79/53, Aug 1979. 18pp.

[75] M.-P. Lombardo. An Introduction to QCD at Non-Zero Temperature and Density. In W. M. Alberico, M. Nardi, & M.-P. Lombardo, editor, *Quark-Gluon Plasma and Heavy Ion Collisions*, pages 201–215, September 2002. doi: 10.1142/9789812776532_0019.

[76] Kerson Huang. *Statistical Mechanics*. John Wiley & Sons, Inc., 1987.

[77] Kenji Fukushima and Tetsuo Hatsuda. The phase diagram of dense QCD. *Reports on Progress in Physics*, 74(1):014001, 2011. URL `http://stacks.iop.org/0034-4885/74/i=1/a=014001`.

[78] David Cubero, Jesús Casado-Pascual, Jörn Dunkel, Peter Talkner, and Peter Hänggi. Thermal equilibrium and statistical thermometers in special relativity. *Phys. Rev. Lett.*, 99(17):170601, Oct 2007. doi: 10.1103/PhysRevLett.99.170601.

[79] M. C. Abreu et al. Production of rho+omega and phi in p-W and S-U collisions at 200 GeV/nucleon. *Physics Letters B*, 368(3):239 – 243, 1996. ISSN 0370-2693. doi: DOI:10.1016/0370-2693(95)01502-7. URL http://www.sciencedirect.com/science/article/pii/0370269395015027.

[80] R. Hagedorn. Multiplicities, p_t distributions and the expected hadron → quark-gluon phase transition. *La Rivista del Nuovo Cimento (1978-1999)*, 6:1–50, 1983. ISSN 0393-697X. URL http://dx.doi.org/10.1007/BF02740917. 10.1007/BF02740917.

[81] Kenneth G. Wilson. Confinement of quarks. *Phys. Rev. D*, 10(8):2445–2459, Oct 1974. doi: 10.1103/PhysRevD.10.2445.

[82] John Kogut and Leonard Susskind. Hamiltonian formulation of Wilson's lattice gauge theories. *Phys. Rev. D*, 11(2):395–408, Jan 1975. doi: 10.1103/PhysRevD.11.395.

[83] Y. Aoki, G. Endrodi, Z. Fodor, S. D. Katz, and K. K. Szabo. The order of the quantum chromodynamics transition predicted by the standard model of particle physics. *Nature*, 443:675–678, 2006. doi: 10.1038/nature05120.

[84] C. T. H. Davies. *Lattice QCD*. Institute of Physics Publishing, Bristol and Philadelphia, 2002. In *Heavy Flavor Physics*, Scottish Graduate Textbook Series (eds Davies, C. T. H. & Playfer, S. M.), pages 105-146.

[85] S. DÃijrr, Z. Fodor, J. Frison, C. Hoelbling, R. Hoffmann, S. D. Katz, S. Krieg, T. Kurth, L. Lellouch, T. Lippert, K. K. Szabo, and G. Vulvert. Ab initio determination of light hadron masses. *Science*, 322(5905):1224–1227, 2008. doi: 10.1126/science.1163233. URL http://www.sciencemag.org/content/322/5905/1224.abstract.

[86] M. A. Stephanov. QCD phase diagram: An overview. *PoS*, LAT2006:024, 2006. Plenary talk at 24th International Symposium on Lattice Field Theory (Lattice 2006), Tucson, Arizona, 23-28 Jul 2006.

[87] N. Cabibbo and G. Parisi. Exponential hadronic spectrum and quark liberation. *Physics Letters B*, 59(1):67 – 69, 1975. ISSN 0370-2693. doi: DOI:10.1016/0370-2693(75)90158-6. URL http://www.sciencedirect.com/science/article/pii/0370269375901586.

[88] Edward Shuryak. Quantum chromodynamics and the theory of superdense matter. *Physics Reports*, 61(2):71–158, 1980.

[89] Volker Koch. Introduction to Chiral Symmetry. Proceedings of the TAPS workshop, Bosen, Germany, Sept. 1995 (LBNL-38000, arXiv:nucl-th/9512029v1).

[90] M. A. Halasz, A. D. Jackson, R. E. Shrock, M. A. Stephanov, and J. J. M. Verbaarschot. Phase diagram of qcd. *Phys. Rev. D*, 58(9):096007, Sep 1998. doi: 10.1103/PhysRevD.58.096007.

[91] J. Kogut, M. Stone, H. W. Wyld, W. R. Gibbs, J. Shigemitsu, Stephen H. Shenker, and D. K. Sinclair. Deconfinement and chiral symmetry restoration at finite temperatures in su(2) and su(3) gauge theories. *Phys. Rev. Lett.*, 50(6):393–396, Feb 1983. doi: 10.1103/PhysRevLett.50.393.

[92] B.-J. Schaefer, M. Wagner, and J. Wambach. Thermodynamics of (2+1)-flavor qcd: Confronting models with lattice studies. *Phys. Rev. D*, 81(7):074013, Apr 2010. doi: 10.1103/PhysRevD.81.074013.

[93] Kenji Fukushima. Chiral symmetry and heavy-ion collisions. *Journal of Physics G: Nuclear and Particle Physics*, 35(10):104020, 2008. URL http://stacks.iop.org/0954-3899/35/i=10/a=104020.

[94] A. Andronic, D. Blaschke, P. Braun-Munzinger, J. Cleymans, K. Fukushima, L.D. McLerran, H. Oeschler, R.D. Pisarski, K. Redlich, C. Sasaki, H. Satz, and J. Stachel. Hadron production in ultra-relativistic nuclear collisions: Quarkyonic matter and a triple point in the phase diagram of qcd. *Nuclear Physics A*, 837(1-2): 65 – 86, 2010. ISSN 0375-9474. doi: DOI:10.1016/j.nuclphysa.2010.02.005. URL http://www.sciencedirect.com/science/article/pii/S0375947410003088.

[95] Philip J. Siemens. Liquid-gas phase transition in nuclear matter. *Nature*, 305 (5933):410–412, Sep 1983. doi: 10.1038/305410a0. URL http://dx.doi.org/10.1038/305410a0.

[96] G. Bertsch and Philip J. Siemens. Nuclear fragmentation. *Physics Letters B*, 126 (1-2):9 – 12, 1983. ISSN 0370-2693. doi: DOI:10.1016/0370-2693(83)90004-7. URL http://www.sciencedirect.com/science/article/pii/0370269383900047.

[97] W. Trautmann. Multifragmentation in relativistic heavy-ion reactions. 1996. arXiv:nucl-ex/9611002.

[98] D. Q. Lamb, J. M. Lattimer, C. J. Pethick, and D. G. Ravenhall. Physical properties of hot, dense matter: The bulk equilibrium approximation. *Nuclear Physics A*, 360(2):459 – 482, 1981. ISSN 0375-9474. doi: DOI:10.1016/0375-9474(81)90157-3. URL http://www.sciencedirect.com/science/article/pii/0375947481901573.

[99] B. Friedman and V. R. Pandharipande. Hot and cold, nuclear and neutron matter. *Nuclear Physics A*, 361(2):502 – 520, 1981. ISSN 0375-9474. doi: DOI:10.1016/0375-9474(81)90649-7. URL http://www.sciencedirect.com/science/article/pii/0375947481906497.

[100] Alan L. Goodman, Joseph I. Kapusta, and Aram Z. Mekjian. Liquid-gas phase instabilities and droplet formation in nuclear reactions. *Phys. Rev. C*, 30(3):851–865, Sep 1984. doi: 10.1103/PhysRevC.30.851.

[101] J. B. Natowitz, R. Wada, K. Hagel, T. Keutgen, M. Murray, A. Makeev, L. Qin, P. Smith, and C. Hamilton. Caloric curves and critical behavior in nuclei. *Phys. Rev. C*, 65(3):034618, Mar 2002. doi: 10.1103/PhysRevC.65.034618.

[102] A. B. Migdal. Superfluidity and the moments of inertia of nuclei. *Nuclear Physics*, 13(5):655 – 674, 1959. ISSN 0029-5582. doi: DOI:10.1016/0029-5582(59)90264-0. URL http://www.sciencedirect.com/science/article/pii/0029558259902640.

[103] D. A. Kirzhnits V. L. Ginzburg. *Sov. Phys. JETP*, 20:136–1348, 1965. In Russian.

[104] M. Ali Alpar David Pines. Superfluidity in neutron stars. *Nature*, 316:27–32, 1985. doi: 10.1038/316027a0. URL http://dx.doi.org/10.1038/316027a0.

[105] D. G. Ravenhall C. J. Pethick. Matter at large neutron excess and the physics of neutron-star crusts. *Annual Review of Nuclear and Particle Science*, 45:429–484, 1995.

[106] D. D. Ivanenko and D. F. Kurdgelaidze. *Astrophysics*, 1, 1965. In Russian.

[107] Franco Pacini. High-energy astrophysics and a possible sub-nuclear energy sourc. *Nature*, 209:389–390, 1966. URL http://dx.doi.org/10.1038/209389a0. 10.1038/209389a0.

[108] D. Ivanenko and D. Kurdgelaidze. Remarks on quark stars. *Lettere Al Nuovo Cimento (1969 - 1970)*, 2:13–16, 1969. ISSN 0375-930X. URL http://dx.doi.org/10.1007/BF02753988. 10.1007/BF02753988.

[109] D. D. Ivanenko and D. F. Kurdgelaidze. Quark stars. *Russian Physics Journal*, 13: 1015–1019, 1970. ISSN 1064-8887. URL http://dx.doi.org/10.1007/BF00818558. 10.1007/BF00818558.

[110] Mark G. Alford, Andreas Schmitt, Krishna Rajagopal, and Thomas Schäfer. Color superconductivity in dense quark matter. *Rev. Mod. Phys.*, 80(4):1455–1515, Nov 2008. doi: 10.1103/RevModPhys.80.1455.

[111] Bertrand C. Barrois. Superconducting quark matter. *Nuclear Physics B*, 129 (3):390 – 396, 1977. ISSN 0550-3213. doi: DOI:10.1016/0550-3213(77)90123-7. URL http://www.sciencedirect.com/science/article/pii/0550321377901237.

[112] Stephen C. Frautschi. Presented at Workshop on Hadronic Matter at Extreme Energy Density, Erice, Italy, 1978.

[113] Bertrand C. Barrois. *Nonperturbative Effects In Dense Quark Matter*. PhD thesis, California Institute of Technology, Pasadena, California, 1979. UMI-79-04847, 47pp.

[114] Mark Alford, Krishna Rajagopal, and Frank Wilczek. Color-flavor locking and chiral symmetry breaking in high density qcd. *Nuclear Physics B*, 537(1-3): 443 – 458, 1999. ISSN 0550-3213. doi: DOI:10.1016/S0550-3213(98)00668-3. URL http://www.sciencedirect.com/science/article/pii/S0550321398006683.

[115] Larry McLerran and Robert D. Pisarski. Phases of Cold, Dense Quarks at Large N_c. *Nucl. Phys.*, A796:83–100, 2007. doi: 10.1016/j.nuclphysa.2007.08.013.

[116] Giorgio Torrieri and Igor Mishustin. Nuclear liquid-gas phase transition at large nc in the van der waals approximation. *Phys. Rev. C*, 82(5):055202, Nov 2010. doi: 10.1103/PhysRevC.82.055202.

[117] Stefan B. Rüster, Verena Werth, Michael Buballa, Igor A. Shovkovy, and Dirk H. Rischke. Phase diagram of neutral quark matter: Self-consistent treatment of quark masses. *Phys. Rev. D*, 72(3):034004, Aug 2005. doi: 10.1103/PhysRevD.72.034004.

[118] Hiroaki Abuki and Teiji Kunihiro. Extensive study of phase diagram for charge-neutral homogeneous quark matter affected by dynamical chiral condensation: unified picture for thermal unpairing transitions from weak to strong coupling. *Nuclear Physics A*, 768(1-2):118 – 159, 2006. ISSN 0375-9474. doi: DOI:10.1016/j.nuclphysa.2005.12.019. URL http://www.sciencedirect.com/science/article/pii/S0375947405012728.

[119] A. Ali Khan, S. Aoki, R. Burkhalter, S. Ejiri, M. Fukugita, S. Hashimoto, N. Ishizuka, Y. Iwasaki, K. Kanaya, T. Kaneko, Y. Kuramashi, T. Manke, K. Nagai, M. Okamoto, M. Okawa, A. Ukawa, and T. Yoshié. Phase structure and critical temperature of two-flavor qcd with a renormalization group improved gauge action and clover improved wilson quark action. *Phys. Rev. D*, 63(3):034502, Dec 2000. doi: 10.1103/PhysRevD.63.034502.

[120] F. Karsch, E. Laermann, and A. Peikert. Quark mass and flavour dependence of the qcd phase transition. *Nuclear Physics B*, 605(1-3):579 – 599, 2001. ISSN 0550-3213. doi: DOI:10.1016/S0550-3213(01)00200-0. URL http://www.sciencedirect.com/science/article/pii/S0550321301002000.

[121] Zoltan Fodor and Sandor D. Katz. Critical point of qcd at finite t and Îij, lattice results for physical quark masses. *Journal of High Energy Physics*, 2004(04): 050, 2004. URL http://stacks.iop.org/1126-6708/2004/i=04/a=050.

[122] D. Toublan and John B. Kogut. The qcd phase diagram at nonzero baryon, isospin and strangeness chemical potentials: results from a hadron resonance gas model. *Physics Letters B*, 605(1-2):129 – 136, 2005. ISSN 0370-2693. doi: DOI:10.1016/j.physletb.2004.11.018. URL http://www.sciencedirect.com/science/article/pii/S0370269304015722.

[123] S. Rößner, C. Ratti, and W. Weise. Polyakov loop, diquarks, and the two-flavor phase diagram. *Phys. Rev. D*, 75(3):034007, Feb 2007. doi: 10.1103/PhysRevD.75.034007.

[124] M. Stephanov, K. Rajagopal, and E. Shuryak. Signatures of the tricritical point in qcd. *Phys. Rev. Lett.*, 81(22):4816–4819, Nov 1998. doi: 10.1103/PhysRevLett.81.4816.

[125] F Becattini and J Cleymans. Chemical equilibrium in heavy ion collisions: rapidity dependence. *Journal of Physics G: Nuclear and Particle Physics*, 34(8):S959, 2007. URL http://stacks.iop.org/0954-3899/34/i=8/a=S135.

[126] M. Stephanov, K. Rajagopal, and E. Shuryak. Event-by-event fluctuations in heavy ion collisions and the qcd critical point. *Phys. Rev. D*, 60(11):114028, Nov 1999. doi: 10.1103/PhysRevD.60.114028.

[127] A. Dumitru, U. Katscher, J. A. Maruhn, H. StÃűcker, W. Greiner, and D. H. Rischke. Thermal photons as a measure for the rapidity dependence of the temperature. *Zeitschrift fÃijr Physik A Hadrons and Nuclei*, 353:187–190, 1995. ISSN 0939-7922. URL http://dx.doi.org/10.1007/BF01295896. 10.1007/BF01295896.

[128] M. Asakawa, S. A. Bass, B. Müller, and C. Nonaka. Transverse velocity dependence of the proton-antiproton ratio as a signature of the qcd critical point. *Phys. Rev. Lett.*, 101(12):122302, Sep 2008. doi: 10.1103/PhysRevLett.101.122302.

[129] D. Toublan and J. B. Kogut. Isospin chemical potential and the qcd phase diagram at nonzero temperature and baryon chemical potential. *Physics Letters B*, 564(3-4):212 – 216, 2003. ISSN 0370-2693. doi: DOI:10.1016/S0370-2693(03)00701-9. URL http://www.sciencedirect.com/science/article/pii/S0370269303007019.

[130] J. D. Bjorken. Highly relativistic nucleus-nucleus collisions: The central rapidity region. *Phys. Rev. D*, 27(1):140–151, Jan 1983. doi: 10.1103/PhysRevD.27.140.

[131] B. Alver et al. System Size and Centrality Dependence of Charged Hadron Transverse Momentum Spectra in $Au+Au$ and $Cu+Cu$ Collisions at $sNN = 62.4$ and 200 GeV. *Phys. Rev. Lett.*, 96(21):212301, May 2006. doi: 10.1103/PhysRevLett.96.212301.

[132] B. Alver et al. Charged-particle multiplicity and pseudorapidity distributions measured with the PHOBOS detector in $Au+Au$, $Cu+Cu$, $d+Au$, and $p+p$ collisions at ultrarelativistic energies. *Phys. Rev. C*, 83(2):024913, Feb 2011. doi: 10.1103/PhysRevC.83.024913.

[133] S. A. Voloshin and A. M. Poskanzer. The physics of the centrality dependence of elliptic flow. *Physics Letters B*, 474(1-2):27 – 32, 2000. ISSN 0370-2693. doi: DOI:10.1016/S0370-2693(00)00017-4. URL http://www.sciencedirect.com/science/article/pii/S0370269300000174.

[134] P. Braun-Munzinger and J. Wambach. Colloquium: Phase diagram of strongly interacting matter. *Rev. Mod. Phys.*, 81(3):1031–1050, Jul 2009. doi: 10.1103/RevModPhys.81.1031.

[135] Jean-Yves Ollitrault. Anisotropy as a signature of transverse collective flow. *Phys. Rev. D*, 46(1):229–245, Jul 1992. doi: 10.1103/PhysRevD.46.229.

[136] B. Alver et al. System size, energy, pseudorapidity, and centrality dependence of elliptic flow. *Phys. Rev. Lett.*, 98(24):242302, Jun 2007. doi: 10.1103/PhysRevLett.98.242302.

[137] U. Heinz and P. Kolb. Early thermalization at rhic. *Nuclear Physics A*, 702(1-4):269 – 280, 2002. ISSN 0375-9474. doi: DOI:10.1016/S0375-9474(02)00714-5. URL http://www.sciencedirect.com/science/article/pii/S0375947402007145.

[138] Wojciech Broniowski, Wojciech Florkowski, Mikolaj Chojnacki, and Adam Kisiel. Free-streaming approximation in early dynamics of relativistic heavy-ion collisions. *Phys. Rev. C*, 80(3):034902, Sep 2009. doi: 10.1103/PhysRevC.80.034902.

[139] Hendrik van Hees, Vincenzo Greco, and Ralf Rapp. Heavy-quark probes of the quark-gluon plasma and interpretation of recent data taken at the bnl relativistic heavy ion collider. *Phys. Rev. C*, 73(3):034913, Mar 2006. doi: 10.1103/PhysRevC.73.034913.

[140] Miklos Gyulassy and Larry McLerran. New forms of qcd matter discovered at rhic. *Nuclear Physics A*, 750(1):30 – 63, 2005. ISSN 0375-9474. doi: DOI:10.1016/j.nuclphysa.2004.10.034. URL http://www.sciencedirect.com/science/article/pii/S0375947404011480. Quark-Gluon Plasma. New Discoveries at RHIC: Case for the Strongly Interacting Quark-Gluon Plasma. Contributions from the RBRC Workshop held May 14-15, 2004.

[141] Edward Shuryak. What rhic experiments and theory tell us about properties of quark-gluon plasma? *Nuclear Physics A*, 750(1):64 – 83, 2005. ISSN 0375-9474. doi: DOI:10.1016/j.nuclphysa.2004.10.022. URL http://www.sciencedirect.com/science/article/pii/S0375947404011340. Quark-Gluon Plasma. New Discoveries at RHIC: Case

for the Strongly Interacting Quark-Gluon Plasma. Contributions from the RBRC Workshop held May 14-15, 2004.

[142] W. Florkowski. The early thermalization and hbt puzzles at rhic. *Acta Physica Polonica B*, 41(12):2747, 2010. URL http://www.actaphys.uj.edu.pl/vol41/abs/v41p2747.htm.

[143] Ghi R Shin and Berndt MÃijller. Studies of parton thermalization at rhic. *Journal of Physics G: Nuclear and Particle Physics*, 29(11):2485, 2003. URL http://stacks.iop.org/0954-3899/29/i=11/a=004.

[144] Jean Letessier and Johann Rafelski. *Hadrons and quark gluon plasma*. Cambridge University Press, 2002. SBN-10: 0521385369, ISBN-13: 978-0521385367.

[145] Frithjof Karsch. Lattice QCD at High Temperature and Density. In Willibald Plessas and Leopold Mathelitsch, editors, *Lectures on Quark Matter*, volume 583 of *Lecture Notes in Physics*, pages 209–249. Springer Berlin / Heidelberg, 2002. URL http://dx.doi.org/10.1007/3-540-45792-5_6. 10.1007/3-540-45792-5_6.

[146] A. Taranenko and the PHENIX Collaboration. PHENIX studies of the scaling properties of elliptic flow at RHIC. *Journal of Physics G: Nuclear and Particle Physics*, 34(8):S1069, 2007. URL http://stacks.iop.org/0954-3899/34/i=8/a=S158.

[147] B. I. Abelev et al. Centrality dependence of charged hadron and strange hadron elliptic flow from $s_{nn} = 200$ gev au+au collisions. *Phys. Rev. C*, 77(5):054901, May 2008. doi: 10.1103/PhysRevC.77.054901.

[148] Dénes Molnár and Sergei A. Voloshin. Elliptic flow at large transverse momenta from quark coalescence. *Phys. Rev. Lett.*, 91(9):092301, Aug 2003. doi: 10.1103/PhysRevLett.91.092301.

[149] A. Andronic, P. Braun-Munzinger, and J. Stachel. Hadron production in central nucleus-nucleus collisions at chemical freeze-out. *Nuclear Physics A*, 772 (3-4):167 – 199, 2006. ISSN 0375-9474. doi: DOI:10.1016/j.nuclphysa.2006.03.012. URL http://www.sciencedirect.com/science/article/pii/S0375947406001485. arXiv:nucl-th/0511071v3.

[150] Y. Akiba et al. Production of φ Mesons in Central $^{28}Si + ^{196}Au$ Collisions at 14.6A GeV/c. *Phys. Rev. Lett.*, 76(12):2021–2024, Mar 1996. doi: 10.1103/PhysRevLett.76.2021.

[151] R. K. Seto et al. Production of [phi] mesons in Au—Au collisions at the AGS. *Nuclear Physics A*, 661(1-4):506 – 509, 1999. ISSN 0375-9474. doi: DOI:10.1016/S0375-9474(99)85076-3. URL http://www.sciencedirect.com/science/article/pii/S0375947499850763.

[152] S. V. Afanasiev et al. Production of [phi]-mesons in p+p, p+Pb and central Pb+Pb collisions at Ebeam=158 A GeV. *Physics Letters B*, 491(1-2): 59 – 66, 2000. ISSN 0370-2693. doi: DOI:10.1016/S0370-2693(00)01023-6. URL http://www.sciencedirect.com/science/article/pii/S0370269300010236.

[153] Johann Rafelski and Berndt Müller. Strangeness production in the quark-gluon plasma. *Phys. Rev. Lett.*, 48(16):1066–1069, Apr 1982. doi: 10.1103/PhysRevLett.48.1066.

[154] Johann Rafelski. Strangeness production in the quark gluon plasma. *Nuclear Physics A*, 418:215 – 235, 1984. ISSN 0375-9474. doi: DOI:10.1016/0375-9474(84)90551-7. URL http://www.sciencedirect.com/science/article/pii/0375947484905517.

[155] Johann Rafelski and Berndt Müller. Strangeness production in the quark-gluon plasma. *Phys. Rev. Lett.*, 56(21):2334, May 1986. doi: 10.1103/PhysRevLett.56.2334.

[156] P. Koch, B. Müller, and J. Rafelski. Strangeness in relativistic heavy ion collisions. *Physics Reports*, 142(4):167 – 262, 1986. ISSN 0370-1573. doi: DOI:10.1016/0370-1573(86)90096-7. URL http://www.sciencedirect.com/science/article/pii/0370157386900967.

[157] Simon Hands. The phase diagram of QCD. *Contemporary Physics*, 42(4):209–225, 2001. doi: 10.1080/00107510110063843. URL http://tandfprod.literatumonline.com/doi/abs/10.1080/00107510110063843.

[158] Jean Letessier Johann Rafelski. Strangeness and the Discovery of Quark-Gluon Plasma. Invited talk at 5th International Conference on Physics and Astrophysics of Quark Gluon Plasma, February 8 - 12, 2005, Salt Lake City, Kolkata, India, arXiv:hep-ph/0506011.

[159] I. Kuznetsova and J. Rafelski. Heavy flavor hadrons in statistical hadronization of strangeness-rich QGP. *The European Physical Journal C - Particles and Fields*, 51:113–133, 2007. ISSN 1434-6044. URL http://dx.doi.org/10.1140/epjc/s10052-007-0268-9. 10.1140/epjc/s10052-007-0268-9.

[160] F. Becattini. An introduction to the Statistical Hadronization Model. Lectures given at the 4th edition of the school "Quark-Gluon Plasma and Heavy Ion Collisions : past, present, future", Torino (Italy), 8-14 December 2008, arXiv:0901.3643v1 [hep-ph].

[161] P. Braun-Munzinger, J. Stachel, J. P. Wessels, and N. Xu. Thermal equilibration and expansion in nucleus-nucleus collisions at the ags. *Physics Letters B*, 344 (1-4):43 – 48, 1995. ISSN 0370-2693. doi: DOI:10.1016/0370-2693(94)01534-J.

URL http://www.sciencedirect.com/science/article/pii/037026939401534J.

[162] P. Braun-Munzinger, J. Stachel, J. P. Wessels, and N. Xu. Thermal and hadrochemical equilibration in nucleus-nucleus collisions at the sps. *Physics Letters B*, 365(1-4):1 – 6, 1996. ISSN 0370-2693. doi: DOI:10.1016/0370-2693(95)01258-3. URL http://www.sciencedirect.com/science/article/pii/0370269395012583.

[163] F. Becattini, M. Gaździcki, and J. Sollfrank. On chemical equilibrium in nuclear collisions. *The European Physical Journal C - Particles and Fields*, 5: 143–153, 1998. ISSN 1434-6044. URL http://dx.doi.org/10.1007/s100529800831. 10.1007/s100529800831.

[164] P. Braun-Munzinger, I. Heppe, and J. Stachel. Chemical equilibration in pb+pb collisions at the sps. *Physics Letters B*, 465(1-4):15 – 20, 1999. ISSN 0370-2693. doi: DOI:10.1016/S0370-2693(99)01076-X. URL http://www.sciencedirect.com/science/article/pii/S037026939901076X.

[165] F. Becattini. A thermodynamical approach to hadron production in e^+e^- collisions. *Zeitschrift für Physik C Particles and Fields*, 69:485–492, 1995. ISSN 0170-9739. URL http://dx.doi.org/10.1007/BF02907431. 10.1007/BF02907431.

[166] F. Becattini and U. Heinz. Thermal hadron production in pp and $p\bar{p}$ collisions. *Zeitschrift für Physik C Particles and Fields*, 76:269–286, 1997. ISSN 0170-9739. URL http://dx.doi.org/10.1007/s002880050551. 10.1007/s002880050551.

[167] F. Becattini and G. Passaleva. Statistical hadronization model and transverse momentum spectra of hadrons in high energy collisions. *The European Physical Journal C - Particles and Fields*, 23:551–583, 2002. ISSN 1434-6044. URL http://dx.doi.org/10.1007/s100520100869. 10.1007/s100520100869.

[168] Susumu Okubo. Consequences of quark-line (Okubo-Zweig-Iizuka) rule. *Phys. Rev. D*, 16(7):2336–2352, Oct 1977. doi: 10.1103/PhysRevD.16.2336.

[169] K Nakamura et al. Review of particle physics. *J. Phys.*, G37:075021, 2010. doi: 10.1088/0954-3899/37/7A/075021.

[170] S. Okubo. [phi]-meson and unitary symmetry model. *Physics Letters*, 5(2): 165 – 168, 1963. ISSN 0031-9163. doi: DOI:10.1016/S0375-9601(63)92548-9. URL http://www.sciencedirect.com/science/article/pii/S0375960163925489.

[171] Jugoro Iizuka. A Systematics and Phenomenology of Meson Family. *Progress of Theoretical Physics Supplement*, 37:21–34, 1966. doi: 10.1143/PTPS.37.21. URL http://ptp.ipap.jp/link?PTPS/37/21/.

[172] Jugoro Iizuka, Kunihiko Okada, and Okiyasu Shito. Systematics and Phenomenology of Boson Mass Levels. III. *Progress of Theoretical Physics*, 35(6):1061–1073, 1966. doi: 10.1143/PTP.35.1061. URL http://ptp.ipap.jp/link?PTP/35/1061/.

[173] Asher Shor. φ-Meson Production as a Probe of the Quark-Gluon Plasma. *Phys. Rev. Lett.*, 54(11):1122–1125, Mar 1985. doi: 10.1103/PhysRevLett.54.1122.

[174] H. J. Behrend, J. Bodenkamp, W. P. Hesse, D. C. Fries, P. Heine, H. Hirschmann, W. A. McNeely, A. Markou, and E. Seitz. Photoproduction of ϕ-mesons at small t-values. *Physics Letters B*, 56(4):408 – 412, 1975. ISSN 0370-2693. doi: DOI:10.1016/0370-2693(75)90331-7. URL http://www.sciencedirect.com/science/article/pii/0370269375903317.

[175] T. Ishikawa et al. ϕ photo-production from Li, C, Al, and Cu nuclei at E_γ=1.5-2.4 GeV. *Physics Letters B*, 608(3-4):215 – 222, 2005. ISSN 0370-2693. doi: DOI:10.1016/j.physletb.2005.01.023. URL http://www.sciencedirect.com/science/article/pii/S0370269305000560.

[176] Hammer H.-W. Meißner U.-G. Thomas A.W. Sibirtsev, A. ϕ-meson photoproduction from nuclei. *European Physical Journal A*, 29(2):209–220, 2006. URL http://www.scopus.com/inward/record.url?eid=2-s2.0-33748708420&partnerID=40&md5=7bc16888ccdd73e69a124f66e3452174. cited By (since 1996) 22.

[177] M. A. Shifman, A. I. Vainshtein, and V. I. Zakharov. QCD and resonance physics. theoretical foundations. *Nuclear Physics B*, 147(5):385 – 447, 1979. ISSN 0550-3213. doi: DOI:10.1016/0550-3213(79)90022-1. URL http://www.sciencedirect.com/science/article/pii/0550321379900221.

[178] Robert D. Pisarski. Phenomenology of the chiral phase transition. *Physics Letters B*, 110(2):155 – 158, 1982. ISSN 0370-2693. doi: DOI:10.1016/0370-2693(82)91025-5. URL http://www.sciencedirect.com/science/article/pii/0370269382910255.

[179] E. V. Shuryak. Physics of hot hadronic matter and quark-gluon plasma. *Nuclear Physics A*, 525:3 – 21, 1991. ISSN 0375-9474. doi: DOI:10.1016/0375-9474(91)90310-3. URL http://www.sciencedirect.com/science/article/pii/0375947491903103.

[180] Tetsuo Hatsuda. Theoretical overview –Hot and dense QCD in equilibrium–. *Nuclear Physics A*, 544(1-2):27 – 47, 1992. ISSN 0375-9474. doi: DOI:10.

1016/0375-9474(92)90563-Y. URL http://www.sciencedirect.com/science/article/pii/037594749290563Y.

[181] Abhijit Bhattacharyya, Sanjay K. Ghosh, S. C. Phatak, and Sibaji Raha. In-medium effects on the φ meson. *Phys. Rev. C*, 55(3):1463–1466, Mar 1997. doi: 10.1103/PhysRevC.55.1463.

[182] D. Lissauer and E.V. Shuryak. K meson modification in hot hadronic matter may be detected via ϕ meson decays. *Physics Letters B*, 253(1-2): 15 – 18, 1991. ISSN 0370-2693. doi: DOI:10.1016/0370-2693(91)91355-Y. URL http://www.sciencedirect.com/science/article/pii/037026939191355Y.

[183] E. Shuryak and V. Thorsson. Kaon modification in hot hadronic matter. *Nuclear Physics A*, 536(3-4):739 – 749, 1992. ISSN 0375-9474. doi: DOI:10.1016/0375-9474(92)90121-Y. URL http://www.sciencedirect.com/science/article/pii/037594749290121Y.

[184] M. Asakawa and C. M. Ko. Seeing the QCD phase transition with phi mesons. *Physics Letters B*, 322(1-2):33 – 37, 1994. ISSN 0370-2693. doi: DOI:10.1016/0370-2693(94)90487-1. URL http://www.sciencedirect.com/science/article/pii/0370269394904871.

[185] C.M. Ko and M. Asakawa. Double phi peaks as a signature for the QCD phase transition. *Nuclear Physics A*, 566:447 – 450, 1994. ISSN 0375-9474. doi: DOI:10.1016/0375-9474(94)90666-1. URL http://www.sciencedirect.com/science/article/pii/0375947494906661.

[186] Che Ming Ko and David Seibert. What can we learn from a second phi meson peak in ultrarelativistic nuclear collisions? *Phys. Rev. C*, 49(4):2198–2202, Apr 1994. doi: 10.1103/PhysRevC.49.2198.

[187] M. Asakawa and C.M. Ko. Phi meson mass in hot and dense matter. *Nuclear Physics A*, 572(3-4):732 – 748, 1994. ISSN 0375-9474. doi: DOI:10.1016/0375-9474(94)90408-1. URL http://www.sciencedirect.com/science/article/pii/0375947494904081.

[188] C. M. Ko and B. H. Sa. Phi meson production in hadronic matter. *Physics Letters B*, 258(1-2):6 – 10, 1991. ISSN 0370-2693. doi: DOI:10.1016/0370-2693(91)91199-6. URL http://www.sciencedirect.com/science/article/pii/0370269391911996.

[189] Kevin L. Haglin and Charles Gale. Properties of the [phi]-meson at finite temperature. *Nuclear Physics B*, 421(3):613 – 631, 1994. ISSN 0550-3213. doi: DOI:10.1016/0550-3213(94)90519-3. URL http://www.sciencedirect.com/science/article/pii/0550321394905193.

[190] Pin-Zhen Bi and Johann Rafelski. Decay of ϕ in hot matter. *Physics Letters B*, 262 (4):485 – 491, 1991. ISSN 0370-2693. doi: DOI:10.1016/0370-2693(91)90627-3. URL http://www.sciencedirect.com/science/article/pii/0370269391906273.

[191] Wade Smith and Kevin L. Haglin. Collision broadening of the φ meson in baryon rich hadronic matter. *Phys. Rev. C*, 57(3):1449–1453, Mar 1998. doi: 10.1103/PhysRevC.57.1449.

[192] R. Muto et al. Evidence for In-Medium Modification of the ϕ Meson at Normal Nuclear Density. *Phys. Rev. Lett.*, 98(4):042501, Jan 2007. doi: 10.1103/PhysRevLett.98.042501.

[193] M. Harrison, T. Ludlam, and S. Ozaki. Rhic project overview. *Nucl. Instrum. Meth. A*, 499(2-3):235 – 244, 2003. ISSN 0168-9002. doi: DOI:10.1016/S0168-9002(02)01937-X. URL http://www.sciencedirect.com/science/article/pii/S016890020201937X. The Relativistic Heavy Ion Collider Project: RHIC and its Detectors.

[194] RHIC Runs Overview, . URL http://www.agsrhichome.bnl.gov/RHIC/Runs/.

[195] M. Adamczyk et al. The BRAHMS experiment at RHIC. *Nucl. Instrum. Meth. A*, 499 (2-3):437 – 468, 2003. ISSN 0168-9002. doi: DOI:10.1016/S0168-9002(02)01949-6. URL http://www.sciencedirect.com/science/article/pii/S0168900202019496. The Relativistic Heavy Ion Collider Project: RHIC and its Detectors.

[196] K. Adcox et al. PHENIX detector overview. *Nucl. Instrum. Meth. A*, 499(2-3):469 – 479, 2003. ISSN 0168-9002. doi: DOI:10.1016/S0168-9002(02)01950-2. URL http://www.sciencedirect.com/science/article/pii/S0168900202019502. The Relativistic Heavy Ion Collider Project: RHIC and its Detectors.

[197] B. B. Back et al. The PHOBOS detector at RHIC. *Nucl. Instrum. Meth. A*, 499(2-3):603 – 623, 2003. ISSN 0168-9002. doi: DOI:10.1016/S0168-9002(02)01959-9. URL http://www.sciencedirect.com/science/article/pii/S0168900202019599. The Relativistic Heavy Ion Collider Project: RHIC and its Detectors.

[198] K. H. Ackermann et al. STAR detector overview. *Nucl. Instrum. Meth. A*, 499(2-3):624 – 632, 2003. ISSN 0168-9002. doi: DOI:10.1016/S0168-9002(02)01960-5. URL http://www.sciencedirect.com/science/article/pii/S0168900202019605. The Relativistic Heavy Ion Collider Project: RHIC and its Detectors.

[199] P. Thieberger, M. McKeown, and H. E. Wegner. Tests for Pulsed High Current Heavy Ion Synchrotron Injection with an MP-Tandem Van de Graaff. *Nuclear Science, IEEE Transactions on*, 30(4):2746 –2748, aug. 1983. ISSN 0018-9499. doi: 10.1109/TNS.1983.4332943.

[200] H. Hahn, E. Forsyth, H. Foelsche, M. Harrison, J. Kewisch, G. Parzen, S. Peggs, E. Raka, A. Ruggiero, A. Stevens, S. Tepikian, P. Thieberger, D. Trbojevic, J. Wei, E. Willen, S. Ozaki, and S. Y. Lee. The RHIC design overview. *Nucl. Instrum. Meth. A*, 499(2-3):245 – 263, 2003. ISSN 0168-9002. doi: DOI:10.1016/S0168-9002(02)01938-1. URL http://www.sciencedirect.com/science/article/pii/S0168900202019381. The Relativistic Heavy Ion Collider Project: RHIC and its Detectors.

[201] P. Thieberger D. B. Steski. Stripping foils at RHIC. 2009. URL www.bnl.gov/isd/documents/44095.pdf. Presented at the 24th World Conference of the International Nuclear Target Development Society (INTDS), GANIL, Caen, France, Septenlber 15-19, 2008.

[202] AGS Booster Synchrotron. URL http://www.bnl.gov/rhic/booster.asp.

[203] H.C. Hseuh. The AGS Booster vacuum systems. *Vacuum*, 41(7-9):1903 – 1906, 1990. ISSN 0042-207X. doi: DOI:10.1016/0042-207X(90)94127-C. URL http://www.sciencedirect.com/science/article/pii/0042207X9094127C.

[204] RHIC Magnets Overview, . URL http://www.bnl.gov/magnets/RHIC/RHIC.asp.

[205] B. B. Back et al. The PHOBOS detector at RHIC. *Nucl. Instrum. Meth. A*, 499: 603–623, 2003. doi: 10.1016/S0168-9002(02)01959-9.

[206] R. Bindel, E. Garcia, A. C. Mignerey, and L. P. Remsberg. Array of scintillator counters for PHOBOS at RHIC. *Nucl. Instrum. Meth. A*, 474(1):38 – 45, 2001. ISSN 0168-9002. doi: DOI:10.1016/S0168-9002(01)00866-X. URL http://www.sciencedirect.com/science/article/pii/S016890020100866X.

[207] Burak Alver. *Measurement of Non-flow Correlations and Elliptic Flow Fluctuations in Au+Au collisions at RHIC*. PhD thesis, Massachusetts Institute of Technology, 2010.

[208] R. Hollis. *Centrality Evolution of Charged Particles Produced in Ultra-relativistic Au+Au and d+Au Collisions*. PhD thesis, University of Illinois at Chicago, 2005.

[209] C. Adler, A. Denisov, E. Garcia, M. Murray, H. Stroebele, and S. White. The RHIC zero degree calorimeters. *Nucl. Instrum. Meth. A*, 470(3):488

– 499, 2001. ISSN 0168-9002. doi: DOI:10.1016/S0168-9002(01)00627-1. URL http://www.sciencedirect.com/science/article/pii/S0168900201006271.

[210] Sebastian N. White. Inelastic Diffraction at Heavy Ion Colliders. *Nuclear Physics B - Proceedings Supplements*, 146:48 – 52, 2005. ISSN 0920-5632. doi: DOI:10.1016/j.nuclphysbps.2005.02.059. URL http://www.sciencedirect.com/science/article/pii/S092056320500397X. Diffraction 2004.

[211] C. Adler, A. Denisov, E. Garcia, M. Murray, H. Strobele, and S. White. The rhic zero-degree calorimeters. *Nuclear Instruments and Methods in Physics Research Section A: Accelerators, Spectrometers, Detectors and Associated Equipment*, 499 (2-3):433 – 436, 2003. ISSN 0168-9002. doi: DOI:10.1016/j.nima.2003.08.112. URL http://www.sciencedirect.com/science/article/pii/S0168900203024069. The Relativistic Heavy Ion Collider Project: RHIC and its Detectors.

[212] C. Reed. *Studies of Nucleon-Gold Collisions at 200 GeV per Nucleon Pair Using Tagged d+Au Interactions*. PhD thesis, Massachusetts Institute of Technology, 2006.

[213] R. Nouicer et al. Silicon pad detectors for the PHOBOS experiment at RHIC. *Nucl. Instrum. Meth. A*, 461(1-3):143 – 149, 2001. ISSN 0168-9002. doi: DOI:10.1016/S0168-9002(00)01191-8. URL http://www.sciencedirect.com/science/article/pii/S0168900200011918. 8th Pisa Meeting on Advanced Detectors.

[214] B.B. Back et al. The PHOBOS perspective on discoveries at RHIC. *Nuclear Physics A*, 757(1-2):28 – 101, 2005. ISSN 0375-9474. doi: DOI:10.1016/j.nuclphysa.2005.03.084. URL http://www.sciencedirect.com/science/article/pii/S0375947405005282. First Three Years of Operation of RHIC.

[215] Willis T. Lin et al. Development of a double metal, AC-coupled silicon pad detector. *Nuclear Instruments and Methods in Physics Research Section A: Accelerators, Spectrometers, Detectors and Associated Equipment*, 389(3):415 – 420, 1997. ISSN 0168-9002. doi: DOI:10.1016/S0168-9002(97)00346-X. URL http://www.sciencedirect.com/science/article/pii/S016890029700346X.

[216] Heinz Pernegger. Layout and tests of silicon pad detectors for the PHOBOS experiment at RHIC. *Nuclear Instruments and Methods in Physics Research Section A: Accelerators, Spectrometers, Detectors and Associated Equipment*, 419(2-3):549 – 555, 1998. ISSN 0168-9002. doi: DOI:10.1016/S0168-9002(98)00833-X. URL http://www.sciencedirect.com/science/article/pii/S016890029800833X.

[217] Birger Back et al. The PHOBOS silicon pad sensors. *Nuclear Instruments and Methods in Physics Research Section A: Accelerators, Spectrometers, Detectors and Associated Equipment*, 447(1-2):257 – 263, 2000. ISSN 0168-9002. doi: DOI:10.1016/S0168-9002(00)00197-2. URL http://www.sciencedirect.com/science/article/pii/S0168900200001972.

[218] M. P. Decowski et al. Performance of the PHOBOS silicon sensors. *Nuclear Instruments and Methods in Physics Research Section A: Accelerators, Spectrometers, Detectors and Associated Equipment*, 478(1-2):299 – 302, 2002. ISSN 0168-9002. doi: DOI:10.1016/S0168-9002(01)01814-9. URL http://www.sciencedirect.com/science/article/pii/S0168900201018149.

[219] E. Garcia, R.S. Hollis, A. Olszewski, I.C. Park, M. Reuter, G. Roland, P. Steinberg, K. Wozniak, and A.H. Wuosmaa. Vertex reconstruction using a single layer silicon detector. *Nuclear Instruments and Methods in Physics Research Section A: Accelerators, Spectrometers, Detectors and Associated Equipment*, 570 (3):536 – 542, 2007. ISSN 0168-9002. doi: DOI:10.1016/j.nima.2006.10.355. URL http://www.sciencedirect.com/science/article/pii/S0168900206020390.

[220] W. Fischer et al. Vacuum pressure rise with intense ion beams in RHIC. . URL cern.ch/AccelConf/e02/PAPERS/WEPRI034.pdf. Prepared for 8th European Particle Accelerator Conference (EPAC 2002), Paris, France, 3-7 Jun 2002.

[221] W. Fischer et al. Electron clouds and vacuum pressure rise in RHIC. . URL mafurman.lbl.gov/ECLOUD04_proceedings/fischer-ecloud04-v4.pdf. Proceedings of the 31st ICFA Advanced Beam Dynamics Workshop on Electron-Cloud Effects (ECLOUD 04), April 19-23, 2004, Embassy Suites Napa Valley in Napa, California, USA.

[222] H. C. Trbojevic et al. Beam Lifetime Dependence on the Beam-Gas Interactions in RHIC. URL epaper.kek.jp/p01/PAPERS/RPAH125.PDF. Proceedings of the 2001 Particle Accelerator Confrerence, Chicago.

[223] Rene Brun, Federico Carminati, and Simone Giani. GEANT Detector Description and Simulation Tool. CERN-W5013, 1994.

[224] Fulvia Caterina Pilat. Operations and Performance of RHIC as a Cu-Cu Collider. 2005. URL http://cdsweb.cern.ch/record/927054. 21st IEEE Particle Accelerator Conference, Knoxville, TN, USA, 16 - 20 May 2005, pp.4281.

[225] C. Loizides P. Steinberg B. Alver, M. Baker. The PHOBOS Glauber Monte Carlo. 2008. arXiv:0805.4411v1 [nucl-ex].

[226] E-Mail communication with Richard Hollis on the phobos@mit.edu e-mail lists, Date: Fri, 23 Sep 2011 08:58:51 -0700 (PDT).

[227] Xin-Nian Wang and Miklos Gyulassy. hijing: A Monte Carlo model for multiple jet production in pp, pA, and AA collisions. *Phys. Rev. D*, 44(11):3501–3516, Dec 1991. doi: 10.1103/PhysRevD.44.3501.

[228] Michal Petran, Jean Letessier, Vojtech Petracek, and Jan Rafelski. Statistical Hadronization of Multistrange Particles. 2010.

[229] C. Alt et al. Strangeness from 20-A-GeV to 158-A-GeV. *J. Phys.*, G30:S119–S128, 2004. doi: 10.1088/0954-3899/30/1/011.

[230] I. G. Bearden et al. Charged meson rapidity distributions in central Au+Au collisions at $\sqrt{s_{\rm NN}}$=200 GeV. *Phys. Rev. Lett.*, 94:162301, 2005. doi: 10.1103/PhysRevLett.94.162301.

[231] C. Adler et al. Midrapidity φ production in Au+Au collisions at $\sqrt{s_{NN}} = 130$ GeV. *Phys. Rev. C*, 65(4):041901, Mar 2002. doi: 10.1103/PhysRevC.65.041901.

[232] S. S. Adler et al. Production of ϕ mesons at midrapidity in $\sqrt{s_{NN}}$=200 GeV Au+Au collisions at relativistic energies. *Phys. Rev. C*, 72(1):014903, Jul 2005. doi: 10.1103/PhysRevC.72.014903.

[233] B. I. Abelev et al. Energy and system size dependence of ϕ meson production in Cu+Cu and Au+Au collisions. *Phys. Lett.*, B673:183–191, 2009. doi: 10.1016/j.physletb.2009.02.037.

[234] J. Adams et al. ϕ meson production in Au+Au and p+p collisions at $\sqrt{s_{\rm NN}}$=200 GeV. *Physics Letters B*, 612(3-4):181 – 189, 2005. ISSN 0370-2693. doi: DOI:10.1016/j.physletb.2004.12.082. URL `http://www.sciencedirect.com/science/article/pii/S0370269305003448`.

[235] Claude Amsler et al. Review of particle physics. *Phys. Lett.*, B667:1–1340, 2008. doi: 10.1016/j.physletb.2008.07.018.

[236] S. Eidelman et al. Review of particle physics. *Phys. Lett.*, B592:1, 2004. doi: 10.1016/j.physletb.2004.06.001.

[237] H. Bethe. Theory of the passage of fast corpuscular rays through matter. *Annalen Phys.*, 5:325–400, 1930. In German.

[238] H. Bethe. Bremsformel für Elektronen relativistischer Geschwindigkeit. *Z Phys.*, 76:293, 1932. In German.

[239] F. Bloch. Zur Bremsung rasch bewegter Teilchen beim Durchgang durch die Materie. *Ann. Phys.*, 16:285, 1933. In German.

[240] F. Bloch. Bremsvermögen von Atomen mit mehreren Elektronen. *Z Phys.*, 81:363, 1933. In German.

[241] W.R. Leo. *Techniques for Nuclear and Particle Physics Experiments*. Springer, 1994.

[242] L. Landau. On the energy loss of fast particles by ionization. *J. Phys. (USSR)*, 8: 201, 1944.

[243] P. V. Vavilov. Ionization losses of high-energy heavy particles. *Sov. Phys. JETP*, 5: 749–751, 1957.

[244] P.V.C. Hough. Machine analysis of bubble chamber pictures. 1959. Proc. Int'l Conf. High Energy Accelerators and Instrumentation.

[245] Richard O. Duda and Peter E. Hart. Use of the Hough transformation to detect lines and curves in pictures. *Commun. ACM*, 15(1):11–15, 1972. ISSN 0001-0782. doi: http://doi.acm.org/10.1145/361237.361242.

[246] V. P. Chistyakov. *A Course in Probability Theory*. Nauka, Moscow, 1982. In Russian.

[247] Lars Bugge and Jan Myrheim. Tracking and track fitting. *Nuclear Instruments and Methods*, 179(2):365 – 381, 1981. ISSN 0029-554X. doi: 10.1016/0029-554X(81)90063-X. URL `http://www.sciencedirect.com/science/article/pii/0029554X8190063X`.

[248] E Lund, L Bugge, I Gavrilenko, and A Strandlie. Track parameter propagation through the application of a new adaptive Runge-Kutta-Nyström method in the ATLAS experiment. *Journal of Instrumentation*, 4(04):P04001, 2009. URL `http://stacks.iop.org/1748-0221/4/i=04/a=P04001`.

[249] William H. Press, Saul A. Teukolsky, William T. Vetterling, and Brian P. Flannery. *Numerical Recipes in C (2nd ed.): The Art of Scientific Computing*. Cambridge University Press, New York, NY, USA, 1992. ISBN 0-521-43108-5.

[250] M. Shao et al. Extensive particle identification with TPC and TOF at the STAR experiment. *Nucl. Instrum. Meth.*, A558:419–429, 2006. doi: 10.1016/j.nima.2005.11.251.

[251] Roberto Preghenella. Particle identification at the LHC with the ALICE experiment. Talk at the International School of Subnuclear Physics - 48th course - Erice, September 5, 2010.

[252] B. I. Abelev et al. Measurements of ϕ meson production in relativistic heavy-ion collisions at RHIC. *Phys. Rev.*, C79:064903, 2009. doi: 10.1103/PhysRevC.79.064903.

[253] A. Adare et al. Nuclear modification factors of phi mesons in d+Au, Cu+Cu and Au+Au collisions at $\sqrt{S_{NN}}$=200 GeV. *Phys. Rev.*, C83:024909, 2011. doi: 10.1103/PhysRevC.83.024909.

[254] E. Wenger. *Studies of High Transverse Momentum Phenomena in Heavy Ion Collisions Using the PHOBOS Detector*. PhD thesis, Massachusetts Institute of Technology, 2008.

[255] B. B. Back et al. Ratios of charged antiparticles to particles near midrapidity in Au + Au collisions at $\sqrt{s_{NN}} = 200$ GeV. *Phys. Rev. C*, 67:021901, Feb 2003. doi: 10.1103/PhysRevC.67.021901. URL http://link.aps.org/doi/10.1103/PhysRevC.67.021901.

[256] B. B. Back et al. Charged antiparticle to particle ratios near midrapidity in $p + p$ collisions at $\sqrt{s_{NN}} = 200$ GeV. *Phys. Rev. C*, 71:021901, Feb 2005. doi: 10.1103/PhysRevC.71.021901. URL http://link.aps.org/doi/10.1103/PhysRevC.71.021901.

[257] B. Alver et al. Identified charged antiparticle to particle ratios near midrapidity in Cu+Cu collisions at $\sqrt{s_{NN}} = 62.4$ and 200 GeV. *Phys. Rev. C*, 77:061901, Jun 2008. doi: 10.1103/PhysRevC.77.061901. URL http://link.aps.org/doi/10.1103/PhysRevC.77.061901.

[258] Kang Seog Lee, U. Heinz, and E. Schnedermann. Search for collective transverse flow using particle transverse momentum spectra in relativistic heavy-ion collisions. *Zeitschrift für Physik C Particles and Fields*, 48:525–541, 1990. ISSN 0170-9739. URL http://dx.doi.org/10.1007/BF01572035. 10.1007/BF01572035.

[259] Ekkard Schnedermann, Josef Sollfrank, and Ulrich Heinz. Thermal phenomenology of hadrons from 200A GeV S+S collisions. *Phys. Rev. C*, 48(5):2462–2475, Nov 1993. doi: 10.1103/PhysRevC.48.2462.

[260] I. G. Bearden et al. Collective Expansion in High Energy Heavy Ion Collisions. *Phys. Rev. Lett.*, 78(11):2080–2083, Mar 1997. doi: 10.1103/PhysRevLett.78.2080.

[261] Szabolcs Borsányi, Gergely Endrődi, Zoltán Fodor, Antal Jakovác, Sándor Katz, Stefan Krieg, Claudia Ratti, and Kálmán Szabó. The QCD equation of state with dynamical quarks. *Journal of High Energy Physics*, 2010:1–33, 2010. ISSN 1029-8479. URL http://dx.doi.org/10.1007/JHEP11(2010)077. 10.1007/JHEP11(2010)077.

[262] S. Ejiri, F. Karsch, E. Laermann, and C. Schmidt. Isentropic equation of state of 2-flavor qcd. *Phys. Rev. D*, 73:054506, Mar 2006. doi: 10.1103/PhysRevD.73.054506. URL http://link.aps.org/doi/10.1103/PhysRevD.73.054506.

[263] L. Van Hove. Multiplicity dependence of pt spectrum as a possible signal for a phase transition in hadronic collisions. *Physics Letters B*, 118(1-3): 138 – 140, 1982. ISSN 0370-2693. doi: DOI:10.1016/0370-2693(82)90617-7.

URL http://www.sciencedirect.com/science/article/pii/0370269382906177.

[264] Compilation of NA49 results, March 29, 2010. URL https://edms.cern.ch/file/1075059/1/na49_compil.pdf.

[265] Xiaoping Zhang. Probing QCD phase diagram with phi meson production in STAR BES program. Presented at 7th International Workshop on Critical Point and Onset of Deconfinement - Wuhan, China, Nov. 7-11, 2011. The data were received in a private e-mail communication on 12/30/2011 09:03 PM. URL http://drupal.star.bnl.gov/STAR/presentations/cpod/xiaoping-zhang.

[266] J. Adams et al. Multistrange Baryon Production in Au-Au Collisions at $\sqrt{s_{NN}} =$ 130 GeV. *Phys. Rev. Lett.*, 92:182301, May 2004. doi: 10.1103/PhysRevLett.92.182301. URL http://link.aps.org/doi/10.1103/PhysRevLett.92.182301.

[267] J. Adams et al. Scaling Properties of Hyperon Production in Au + Au Collisions at $\sqrt{s_{NN}} = 200$ GeV. *Phys. Rev. Lett.*, 98:062301, Feb 2007. doi: 10.1103/PhysRevLett.98.062301. URL http://link.aps.org/doi/10.1103/PhysRevLett.98.062301.

[268] M. M. Aggarwal et al. Strange and multistrange particle production in Au + Au collisions at $\sqrt{s_{NN}} = 62.4$ GeV. *Phys. Rev. C*, 83:024901, Feb 2011. doi: 10.1103/PhysRevC.83.024901. URL http://link.aps.org/doi/10.1103/PhysRevC.83.024901.

[269] Feng Zhao. Strange Baryons Production in RHIC Beam Energy Scan. Presented at APS Division of Nuclear Physics Fall Meeting 2011 - East Lansing, MI, Oct. 26-29, 2011. The data were received in a private e-mail communication on 01/06/2012 08:20 PM. URL http://drupal.star.bnl.gov/STAR/presentations/dnp2011/feng-zhao.

[270] Xianglei Zhu. Measurements of strange hadrons K^0_S, Λ, and Ξ from Au+Au collisions at $\sqrt{s_{NN}} = 7.7$, 11.5 and 39 GeV in STAR. Presented at 7th International Workshop on Critical Point and Onset of Deconfinement - Wuhan, China, Nov. 7-11, 2011. The data were received in a private e-mail communication on 12/30/2011 07:15 PM. URL http://drupal.star.bnl.gov/STAR/presentations/cpod/xianglei-zhu-0.

[271] L Ahle et al. An excitation function of K- and K+ production in Au+Au reactions at the AGS. *Physics Letters B*, 490(1-2):53 – 60, 2000. ISSN 0370-2693. doi: 10.1016/S0370-2693(00)00916-3. URL http://www.sciencedirect.com/science/article/pii/S0370269300009163.

[272] C. Adler et al. Kaon production and kaon to pion ratio in Au + Au collisions at $\sqrt{s_{NN}} = 130$ GeV. *Physics Letters B*, 595(1-4):143 – 150, 2004. ISSN 0370-2693. doi: 10.1016/j.physletb.2004.06.044. URL http://www.sciencedirect.com/science/article/pii/S0370269304009050.

[273] J. Adams et al. Identified Particle Distributions in pp and Au + Au Collisions at $\sqrt{s_{NN}} = 200$ GeV. *Phys. Rev. Lett.*, 92:112301, Mar 2004. doi: 10.1103/PhysRevLett.92.112301. URL http://link.aps.org/doi/10.1103/PhysRevLett.92.112301.

[274] B. I. Abelev et al. Systematic measurements of identified particle spectra in *pp*, d + Au, and Au + Au collisions at the STAR detector. *Phys. Rev. C*, 79:034909, Mar 2009. doi: 10.1103/PhysRevC.79.034909. URL http://link.aps.org/doi/10.1103/PhysRevC.79.034909.

[275] E895 Published Spectra Results, September 26, 2003. URL http://nuclear.ucdavis.edu/~e895/published_spectra.html.

[276] J. Adams et al. Rapidity and centrality dependence of proton and antiproton production from ^{197}Au+^{197}Au collisions at $\sqrt{S_{NN}} = 130$ GeV. *Phys. Rev. C*, 70:041901, Oct 2004. doi: 10.1103/PhysRevC.70.041901. URL http://link.aps.org/doi/10.1103/PhysRevC.70.041901.

[277] B. B. Back et al. Antibaryon production in AU+AU collisions at the AGS. URL http://www.osti.gov/bridge/product.biblio.jsp?query_id=0&page=0&osti_id=11886&Row=1&formname=basicsearch.jsp. American Physical Society Centennial Meeting, Atlanta, GA (US), 03/20/1999–03/26/1999.

[278] J. L. Klay et al. Longitudinal Flow of Protons from (2˜8)*A*GeV Central $Au + Au$ Collisions. *Phys. Rev. Lett.*, 88:102301, Feb 2002. doi: 10.1103/PhysRevLett.88.102301. URL http://link.aps.org/doi/10.1103/PhysRevLett.88.102301.

[279] Lev D. Landau. On the multiple production of particles in high energy collisions. *Izv. Akad. Nauk SSSR Ser. Fiz.*, 17:51, 1953.

[280] M.I Gorenstein, M Gazdzicki, and K.A Bugaev. Transverse activity of kaons and deconfinement phase transition in nucleus-nucleus collisions. *Physics Letters B*, 567(3-4):175 – 178, 2003. ISSN 0370-2693. doi: DOI:10.1016/j.physletb.2003.06.043. URL http://www.sciencedirect.com/science/article/pii/S0370269303009432.

[281] Bedangadas Mohanty, Jan-e Alam, Sourav Sarkar, Tapan K. Nayak, and Basanta K. Nandi. Indication of a coexisting phase of quarks and hadrons in nucleus-nucleus collisions. *Phys. Rev. C*, 68(2):021901, Aug 2003. doi: 10.1103/PhysRevC.68.021901.

[282] Ralf Rapp Min He, Rainer J. Fries. Thermal Relaxation of Charm in Hadronic Matter. May 2011. URL http://arxiv.org/abs/1103.6279. arXiv:1103.6279.

[283] S. A. Bass, A. Dumitru, M. Bleicher, L. Bravina, E. Zabrodin, H. Stöcker, and W. Greiner. Hadronic freeze-out following a first order hadronization phase transition in ultrarelativistic heavy-ion collisions. *Phys. Rev. C*, 60:021902, Jul 1999. doi: 10.1103/PhysRevC.60.021902. URL http://link.aps.org/doi/10.1103/PhysRevC.60.021902.

[284] Sonia Kabana. Highlights from the STAR experiment at RHIC. Presented at Strangeness Quark Matter 2011, Cracow, Poland, Sep. 19-24, 2011. URL http://drupal.star.bnl.gov/STAR/presentations/sqm-2011/sonya-kabana-0.

[285] C. Alt et al. Energy dependence of ϕ meson production in central Pb + Pb collisions at $\sqrt{s_{NN}} = 6$ to 17 GeV. *Phys. Rev. C*, 78:044907, Oct 2008. doi: 10.1103/PhysRevC.78.044907. URL http://link.aps.org/doi/10.1103/PhysRevC.78.044907.

[286] S. Sarkar, H. Satz, B. C. Sinha, and B. B. Sinha. *The physics of the quark-gluon plasma: introductory lectures*. Lecture notes in physics. Springer, 2010. ISBN 9783642022869. URL http://books.google.com/books?id=0bbuRAAACAAJ.

[287] Lokesh Kumar. Identified Hadron Production from the RHIC Beam Energy Scan Program. Presented at the Meeting of the Division of Particles and Fields of the American Physical Society - Providence, RI, Aug. 9-13, 2011. URL http://drupal.star.bnl.gov/STAR/presentations/dpf-2011/lokesh-kumar.

[288] Huichao Song, Steffen A. Bass, and Ulrich Heinz. Viscous qcd matter in a hybrid hydrodynamic+boltzmann approach. *Phys. Rev. C*, 83:024912, Feb 2011. doi: 10.1103/PhysRevC.83.024912. URL http://link.aps.org/doi/10.1103/PhysRevC.83.024912.

[289] Private e-mail communication with Prof. Ulrich Heinz, Ohio State University, April 30, 2012 - May 5, 2012.

[290] M. Anderson et al. The STAR time projection chamber: A unique tool for studying high multiplicity events at RHIC. *Nucl. Instrum. Meth.*, A499:659–678, 2003. doi: 10.1016/S0168-9002(02)01964-2.

Acknowledgments

First and foremost, I want to say *"Thank you"* for the continuous support to all the members of the MIT Heavy Ion Group and to the MIT Physics Department. The measurements performed in this thesis turned out to be very technically challenging to make using data from the PHOBOS detector [1]. Without the truly unparalleled accommodations, which were provided to me, the completion of this work would be impossible. In particular, I would like to thank Wit Busza, Gunther Roland, Krishna Rajagopal, and Christoph Paus for helping me to receive financial support (and teaching experience, which not many students have a chance to get) in the form of four sequential semesters of Teaching Assistant assignments at the MIT Junior Lab (courses "8.13 Experimental Physics I" and "8.14 Experimental Physics II") and for the Research Assistant assignments during the summer and IAP terms extending beyond the average period of time it takes for a graduate student to complete a thesis at MIT.

I would also like to thank Gunther Roland, Catherine Modica, Crystal Hall, and all the members of the International Students Office for their help in obtaining the necessary documents, which allowed me to maintain a legal status in the United States for the duration of my study at MIT.

In addition, I am very grateful for the efforts of, first of all, Peter Steinberg but also of Gunther Roland in defending the PHOBOS computing resources from being turned off or given away (to other research groups using the RACF facility) during the time when I was left an almost sole their user, while measurements made for this thesis required unmatched (in comparison to other analyses done by our collaboration) amounts of CPU time for particle reconstruction in the data as well as for various MC simulations. Without the computing resources, the work on this thesis would immediately come to an almost full stop with little chance of completion on any feasible time scale.

If I had to describe my research adviser, Gunther Roland, with one word, I would say *"efficient"*. He has an absolutely amazing ability to identify any possible problems with a data analysis using various mental shortcuts, cross-checks, and rules of thumb. I always thought about what Gunther had to say very carefully, since there was invariably a great deal one could learn from observing and reflecting upon how he thinks, and I just wish I had more opportunities to learn from him. Not just that, but also Gunther's advice is usually about how to fix or find a problem in a data analysis in the fastest and the simplest way. Gunther is as well very efficient in the sense that he has an astounding ability to organize work of a group of people such that they would work coherently, like a single multi-headed organism, on multiple projects, and that in turn allows to remove

[1] I was the 4^{th} (or possibly even the 5^{th}) person to attack the problem within our group and the only one to succeed.

papers from a to-publish list much faster than in a situation where different people work on different papers independently. A side-effect of such system is that one could only credit the whole group for any result, but a highly collaborative approach to scientific problems is a reality of today's high energy physics, and Gunther's abilities are a perfect fit for this reality. When I started my graduate study at MIT, I did not, in fact, understand how the system works since I was used to a different approach, and combining it with a project which other people did not dare to invest much time in, my life and work as a graduate student was pretty isolated, however, I hope that I was able to pick up the more efficient way of doing research from Gunther, although not through a hands-on experience.

More than anybody else, Wit Busza taught me the general wisdom of doing science in the US, and I only wish I had discovered his openness to share his vast experience and knowledge earlier. Wit's office door was never closed for a student to walk in and to ask for advice, and I know that my future decisions in life will be strongly influenced by those conversations. Looking back at my time at MIT, I can say that Wit is not only a scientist with a critical and enthusiastic mind but a great teacher as well, and until my level of experience matches his, whenever in doubt or if I will have to give some advise to my students (an I hope I will have some in a not too distance future) my first reaction will be to remember what Wit had to say to me about it.

In the end of 2009 and beginning of 2010, when the specialized kaon reconstruction just started to work and I was running the first attempts to reconstruct particles in the data while looking for and fixing the last remaining errors in the code, and when Gunther was very busy with the preparations for the first data from LHC, and then with the analysis of the data, I had numerous (once every 1-2 weeks) useful discussions of various pieces of the data analysis presented in this thesis with Burak Alver. A fresh, independent perspective on my ideas on how to identify and repair different problems from somebody, who was familiar with nuts and bolts of a real high energy physics data analysis, helped me to make progress in my work faster. It was especially helpful to get his view in the situations when me and Gunther disagreed on how to proceed. Essentially, I would talk to Gunther and to Burak about my plans, then think carefully about both opinions before making the final decisions. Some general strategies of data analysis I still use today were born as a results of those discussions. In addition, I am grateful for Burak's selfless help with transferring data files in March 2010, when half of the PHOBOS RACF nodes were retired.

My thesis committee, which consisted of Gunther Roland, Wit Busza, and Krishna Rajagopal, provided me with valuable comments on this thesis, the most important of which were implemented in the final draft thereby improving the quality of this work.

I am also thankful for a few useful discussions with Edward Wenger at the early stages of work on the specialized kaon reconstruction, as well as for him always answering my questions in a timely matter via instant messaging or e-mail. Kristjan Gulbrandsen and Conor Henderson were the ones who helped me a lot to get started with PHAT when I just joined PHOBOS. Also, Kristjan Gulbrandsen helped me to cross the cultural barrier after my arrival to the US, since he was always open to honest and free discussions on any topic. Whenever I bumped into a yet another bug in ROOT, Corey Reed was

always very helpful in confirming the bug and suggesting ways to work around it. I am appreciative of Barbara Wosiek's reading of and giving many useful comments on an early version of this writeup. My girlfriend, Willa Chen, read the abstract, introduction, results and conclusions, summary, and acknowledgments of this document and made numerous grammatical corrections to the text, as well as her support, help, sacrifices, and love in everyday life for the last years of work on this thesis truly knew no equal. And, of course, I am very much grateful to all members of the PHOBOS team for building and maintaining our detectors and for developing various pieces of the data analysis software, which were reused by most of the collaboration. Without these contributions, the measurements presented in this thesis would be impossible.